Planar Electromagnetic Sensors for Environmental Monitoring

A thesis presented in partial fulfilment of the requirements for the degree of
Doctor of Philosophy in Electrical Engineering
at Massey University, Palmerston North, New Zealand

MOHD AMRI BIN MD YUNUS

2011

To my wife

Norsyidah binti Khairul Anuar

Abstract

Water is the essence of life and an important nutrient for every living thing. Therefore, ninety six novel planar electromagnetic sensors based on the combination of meander sensor and interdigital sensor have been designed, fabricated, and tested for the application of water quality monitoring. Experiments were conducted to obtain the impedance characterization for each sensor, and the results were used to estimate the important parameters that influence the performance of the sensors based on the equivalent electrical circuits. The best sensors were selected based on the design with the highest electrical parameters (total effective capacitance and effective inductance). Intensive modelling and simulation of the selected best sensors are also discussed where the results were compared with the simulation results. Furthermore, the best sensors have been tested to detect nitrates contamination in distilled water using sodium nitrate ($NaNO_3$) and ammonium nitrate (NH_4NO_3) solutions with different concentrations. The sensor that consists of the series combinations of spiral meander planar sensor (with five turns) with the interdigital sensor (with large negative electrode): SECS22_1 is the best sensor to detect the presence of nitrate added into distilled water and can estimate the concentration level. Furthermore, the sensor was tested with various kinds of prepared samples and natural water samples taken from natural sources around New Zealand. The outcomes have shown a very good correlation of contamination level, translated from the qualitative and quantitative results. Using the SECS22_1 sensor, a method to estimate nitrate contamination in natural water sources using Independent Component Analysis (*ICA*) has been explained and demonstrated. This model can accurately estimate nitrate in a natural water source as shown by the results. A low-cost system has been developed based on SECS22_1, a microcontroller, a waveform circuit, signal conditioning circuits, and *LabView*. The results from the experiment have shown the low-cost system has the potential to be used as a tool for nitrate detection and water sources quality monitoring in remote places such as farms. Finally, the work and improvement for future consideration are also discussed in this research.

Acknowledgements

Praise to Allah S.W.T., the Most Gracious and the Most Merciful, whose blessing and guidance have helped me to present this thesis. There is no power nor strength save in Allah, the Highest and the Greatest. Peace and blessing of Allah be upon our Prophet Muhammad S.A.W. who has given light to mankind.

I would like to express my deepest gratitude to my supervisors Associate Professor Dr. Subhas Chandra Mukhopadhyay and Dr Gardiyawasam Amal Darshana Punchihewa for their support and supervisions. This research would not have been successful without their invaluable guidance, constant help as well as constructive criticisms and opinions throughout the research.

I would like to express my sincere thanks to my colleagues who provided guidance and assistance during the research. Also to Dr Gourab Sen Gupta, Mr Collin Plaw, and Bruce Collins, your assistance and support during my research were most appreciated.

Special thanks to my mother, wife, father, brothers, sisters, families, and Libo for their wishes, assistance, sedulous guidance, and patience. Also, thanks to all my friends and syabab, whose sacrifices had made everything is possible for me.

Last but not least, special thanks to the Ministry of Higher Education (MOHE) of Malaysia and Universiti Teknologi Malaysia for providing me with the financial support and granting leave to pursue my Ph.D degree.

Table of Contents

List of Figures

List of Tables

Abbreviations

NO_3^-	nitrate ion
SSCPXX_V	SSCP is the code for the meander sensor and interdigital sensor that are placed side by side and connected in parallel. XX is the number of the variation from 1 to 24. V is the version number of the sensors which is 1.
SSCSXX_V	SSCS is the code for the meander sensor and interdigital sensor that are placed side by side and connected in series. XX is the number of the variation from 1 to 24. V is the version number of the sensors which is 1.
SECPXX_V	SECP is the code for the meander sensor that is enclosing the interdigital sensor and the sensors are connected in parallel. XX is the number of the variation from 1 to 24. V is the version of the sensors which is 1.
SECSXX_V	SECP is the code for the meander sensor that is enclosing the interdigital sensor and the sensors are connected in series. XX is the number of the variation from 1 to 24. V is the version of the sensors which is 1.
$\vec{H}$	the magnetic field intensity
$\vec{E}$	the electric field intensity
$\vec{B}$	the magnetic flux density
$\vec{D}$	the electric flux density
$\vec{J}$	the current density
$\vec{J}^e$	the external current density
σ	the electric conductivity
v	the velocity of the conductor
ρ	the electric charge density
ε_0	the permittivity of vacuum which sets to be 8.854×10^{-2} F/m
μ_0	the permeability of vacuum equals to $4\pi\times10^{-7}$ H/m
χ_e	the electric susceptibility
χ_m	the magnetic susceptibility
ε_r	the relative permittivity
μ_r	the relative permeability
ε	the permittivity
μ	the permeability

V	the electric scalar potential
$\vec{A}$	the magnetic vector potential
Ψ	the gauge variable
ω	the angular frequency
$\widetilde{A}$	the modified magnetic vector potential
$\widetilde{V}$	the modified electric scalar potential
$NaNO_3$	Sodium Nitrate
NH_4NO_3	Ammonium Nitrate
HCl	Hydrochloric acid
NaOH	Sodium hydroxide base
MLR	Multilinear regression method
ICA	Independent component analysis
FastICA	Fixed point independent component analysis algorithm
$(NH_4)_2HPO_4$	Diammonium Phosphate
PCB	Printed circuit board

CHAPTER 1

Introduction

1.1 Problem Statement and Aim of the Research

The freshwater reserves make out about 2.53% of the total water resources, and from the freshwater reserves, human beings water for daily use that is sourced from groundwater (29.9% of freshwater reserves) and surface water (0.29% of freshwater reserve) [1]. Clean water is vital to human bodies, human health, food, and environment. It is also essential for water sports and recreation. Moreover, the survival of fish and other wildlife species also depend on clean water. The land absorbs the water that fall form the sky, then the water flow into the sea from the river, evaporate into the sky and fall back into the land, this process repeats over and again. Under normal situation, the organic pollutants are biodegraded and converted into beneficial nutrients to the aquatic life. As for the inorganic pollutants, the hazards limited because of their even dispersion in the water. Today we have to face issues, such as fulfilling the growing water demands while keeping the water clean at the same time. Civilizations have been contaminating water supplies with foreign matter (whether in liquid or solid forms) that deteriorate the quality of the water and deliberately or not, increase the amount of inorganic pollution.

This research is mainly concerned with the amount of nitrate contamination in natural water sources as popularly discussed in the health and safety field in recent times. Moreover, we are also working on detecting the contamination level caused by any substances in natural water sources. Nitrate is a natural compound present in all ecosystems. It is a form of nitrogen that is used to create vital structural proteins and enzymes which help the plant to grow and develop. However, too much nitrate is a problem, and it is difficult to remove from water due to its high solubility. Figure 1.1(a) illustrates the data for all the rivers worldwide. It can be observed from Figure 1.1(a) that there are significant changes in nitrate mg·$(NO_3)^-$−N/L concentrations between the two decades under comparison can be observed from Figure 1.1(a), while changes in the

median value are not statistically significant [2]. Several parts in Europe, particularly in regions with intensive livestock production, concentrations higher than 50 mg/L are observed frequently in 39 groundwater bodies (14%). Around 20% of EU measurement stations had concentrations in excess of the limit concentration, and 40% locations were in excess of the standard (25 mg/l) between 1996 and 1998 as can be seen in Figure 1.1(b) France and Sweden are showing an overall increase in nitrate concentrations in groundwater [3]. In New Zealand, the peak level of nitrate concentration in the rivers, taken as an average value, has increased between 1990 and 2007 by approximately 66% [4].

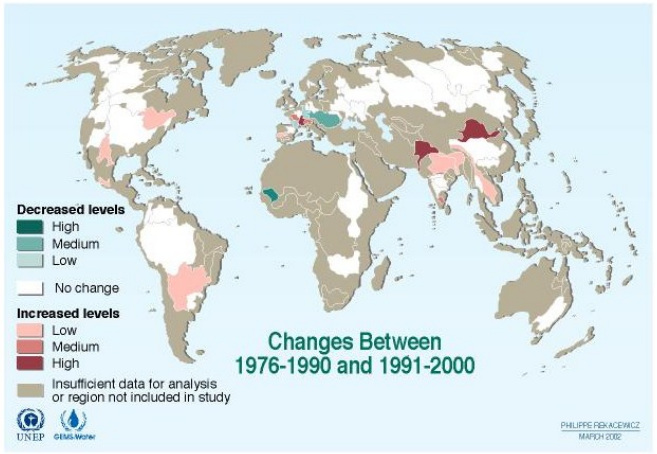

Source: United Nations Environment Programme (UNEP) - Global Environment Monitoring System (GEMS) Water Programme, 2001; National Water Research Institute Environment Canada, Ontario, 2001.

(a)

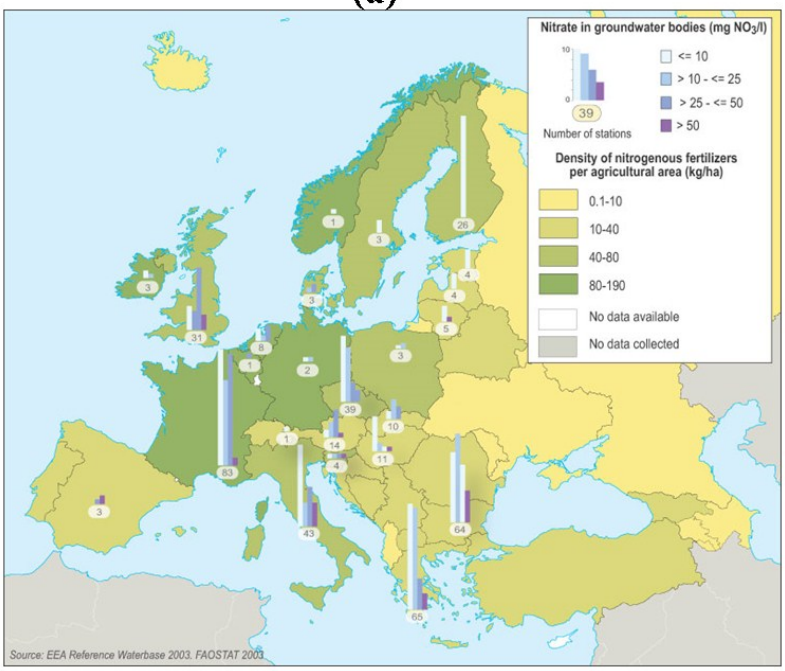

(b)

Figure 1.1: (a) Nitrate contamination of surface water in the world compared over two decades [2] (b) Nitrate contamination of groundwater in the EU, in 2003 [3]

Illness caused by nitrate poisoning can be fatal to infants; they are vulnerable to methemoglobinemia due to haemoglobin oxidation and can cause fatal consequences. It can affect the infant in a short period, sometimes even in a couple of days [5]. Livestock especially ruminants are also exposed to the same problem, they will start to show signs such like lack of coordination, labored breathing, blue membranes, vomiting, and aborted pregnancies [6]. The high amount of nitrate in surface water and groundwater because of over fertilizing can accelerate the growth of algae and weeds (eutrophication). When the algae and weeds died, the decomposition process removed oxygen from the water thus killing fish and other aquatic life [7]. According to reports from experiments, there is still inadequate information to come to a conclusion about the relationship of high nitrate intake and other human cancer like gastric cancer, thyroid cancer and thyroid disease. However, the link cannot be ruled out due to the inadequacy of data available [8, 9]. Figure 1.2 illustrates the maximum concentration in drinking water as recommended by agencies in several countries where it was mainly established for protection from methemoglobinemia [8]. The main sources of nitrate contamination are agricultural fertilizers and animal wastes, industrial wastes related to food processing, munitions, and septic tanks; especially in densely populated areas [10-12]. Another factor is the application of nitrogen-rich fertilizers to turf grass. This occurs on golf courses and in residential areas, sites where accidental spills of nitrogenous materials may accumulate, and finally, manure storage by the farmers [13].

Figure 1.2: Recommended nitrate limit by government agencies in several counties in the world (all values are presented in mg·$(NO_3)^-$−N/L unit, to convert the value into mg·$(NO_3)^-$−N/L unit, multiply by 4.33)

Nitrate detection methods for natural water sources can be divided into indirect and direct methods. Such applications of indirect methods, but not limited to, are the detection of results of nitrate reduction reaction such as nitric oxide gas followed by gasometry or potentiometry [14], diphenylamine reaction [15], chemical reaction that involved salicylic acid followed by spectrophotometer[16], detection of ammonium ion resulting from the reduction of nitrate by trichloride in hydrochloric acid [17], spectrophotometric [18], polarography and voltametry [19]. A recent indirect and in-situ detection of nitrate, as reported in [20], measures the change of LED intensity emitted through a nitrate sensitive membrane. The light intensity is measured using photo-detectors. This system has a good sensitivity with a range of 0.002 and 1000 mM and precision of 4%. However, one major drawback is that the optical path has to be properly guided and aligned, requiring a regular repositioning to maintain the accuracy. In New Zealand, the measurement of nitrate level in water sources conducted by the government agencies which publicized the data, has been conducted using absorption spectrophotometry (using a specific reagent) since for the last decades [21, 22]. Most of the indirect methods were often developed and established for laboratory standards thus making it expensive due to many components requirement. This technique involved laborious measuring steps and inevitably consumes a lot of time. These methods also require controlled working condition, and preparation of extra reagent or chemical.

The direct methods have been proven to provide much simpler solution; such applications are chromatography [23] and biosensors incorporating enzymes, antibodies, and whole cells[16]. The most popular direct method, which is also considered as low cost, is potentiometry based on ion selective electrodes (ISE) [24, 25]. The application of the method had been reported in [14]. Among the advantages of this technology are such as unsophisticated sensor fabrication process, simple monitoring instrumentation, fast and rapid response, accurate, compact and acceptably responsive even to a limited amount of sample, and suitable for continuous measurement. However, the strength of the output signal depends on the strength or concentration of the targeted ions and often requires amplification. Moreover, the output signal also susceptible to interference from untargeted ions thus a large number of reagents were necessary for the purpose of neutralization of the noise and adversely might be harmful to the environment [17, 26]. Looking at the importance of nitrate detection and the challenges which arise, the

motivation of this research is to develop a sensor which can be integrated as a low cost, convenient, and suitable for in-situ measurement system for water quality monitoring, particularly nitrate detection. Looking at the disadvantages of indirect and indirect methods, this research aims to achieve the following objectives:

1. Design and fabricate novel planar electromagnetic sensors based on the combination of meander and interdigital elements for the application of contamination and nitrate detection on natural water sources.
2. Modelling and simulation of the novel planar electromagnetic sensors based on finite element modelling (FEM).
3. Characterization of the sensors and investigation of the best sensor for the application of contamination and nitrate detections.
4. Investigation of the best method of nitrate concentration estimation in natural water sources samples between multi-linear regression method and independent component analysis.
5. Development of a low-cost system for contamination and nitrate detection based on the best sensor.

1.2 Recent Progress in Planar Electromagnetic Sensors

The field of non-destructive testing or inspections is a very broad, interdisciplinary field that produces reliable information of the material under investigation so that proper actions can be taken for the benefits of animal, environment, and human. As has been reported [27], non-destructive testing and evaluation based on electromagnetic approaches are gaining worldwide attention since it was introduced due to simplicity, fast response, convenience, and low cost. In this research, a particular electromagnetic approach of interest is the non-destructive testing or inspections based on the inductive and capacitive or electromagnetic effects. Such devices or sensors can be seen in the industrial areas [28], agriculture [29], and engineering/scientific application (e.g. land mine detection) [30], health and food monitoring [31], manufacturing [32, 33], automation [34], structure inspection [35] etc.

Perusing at a planar electromagnetic device, the sensing or/and exciting elements usually have flatten structures and separated by substrates e.g FR4, alumina etc. Several examples of planar electromagnetic systems are discussed in this section. Inductive planar electromagnetic devices have been reported in [36-45] and extension used as sensors for testing (nondestructive testing) the integrity of materials (conductive and magnetic material) [46-55]. Inductive planar sensors are also used as proximity and displacement sensors [43, 56]. A method for inspecting the integrity of different coins, which can successfully discern different types of coins using meander planar sensors has been demonstrated[57]. Capacitive planar electromagnetic sensors or commonly known as coplanar interdigital sensors have been used for many applications, some of the examples are moisture measurement in pulp [58], monitoring the impedance change caused by the growth of immobilized bacteria [59], human health confirmation based on the content of water in human skin [60], humidity sensors [61], food inspection for human safety [62-64], and estimation of material dielectric properties such as food and saxophone reeds [65-68]. Figure 1.3 illustrates an interdigital sensor and experimental setup for sheep skin property estimation as described in [69]. A sensing system based on the interdigital sensor has been developed for determining the looseness in sheep skins. A good correlation was observed between the sensor output voltage and looseness values for both before and after tanning process. The formula for calculating of looseness was developed, and on comparison with the actual looseness values, they were quite proximate [69].

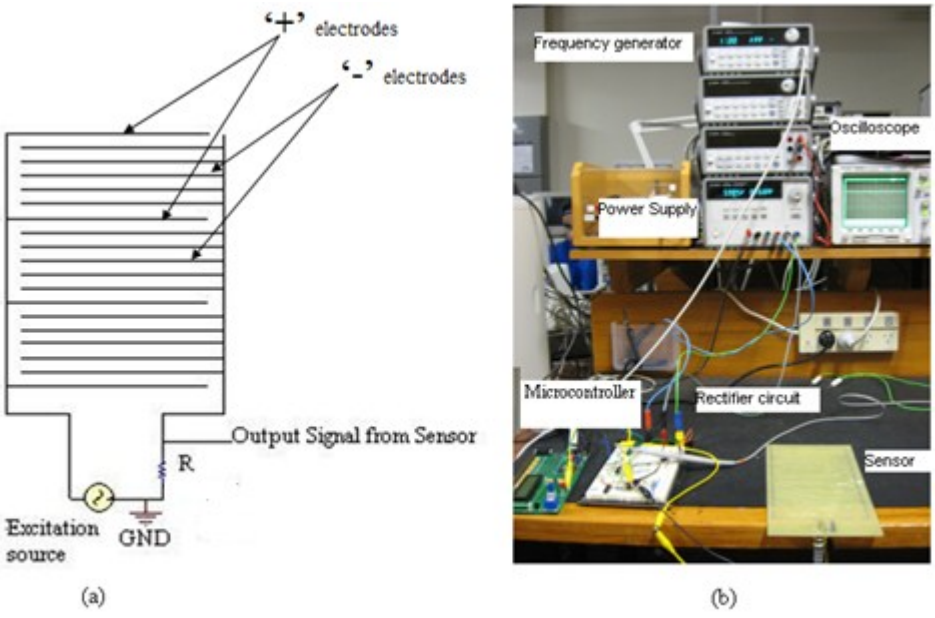

Figure 1.3: (a) Interdigital sensor (b) Experimental set-up

Another useful application of planar electromagnetic sensors is for imaging landmine, which had been reviewed by Schlicker *et.al.* [30]. The advantages of applying electromagnetic sensors array at multiple positions and different orientations for detecting landmine and unexploded ordnance to overcome the weakness of existing technologies in discriminating between harmful object and harmless clutters. The inductive and capacitive sensor array were constructed and used separately, each array has a unique single drive structures that form an electromagnetic field which penetrates deeper into the ground. The images were obtained through scans over the ground surface and then enhanced using spatial filtering. It is shown that the inductive sensor array and capacitive sensor array are clearly responsive to metal and no-metal object, respectively.

For the past ten years, the research of environmental monitoring based on planar meander and interdigital elements has followed several avenues as summarized in Table 1.1. The early work (since 2001) involved a serially closed circuit inductor-capacitor (LC) element, (Titanium Dioxide) TiO_2 coating, and flexible parallel plate capacitor which forms a passive sensor as described in the first section of Table 1.1. The sensor operates on wireless and remote query basis has been applied for environmental parameters monitoring based on complex permittivity of a surrounding medium, temperature monitoring, and pressure [70]. Later on, this work evolved into other application such as bacteria growth monitoring [71, 72], monitoring of electrical properties of biological cell solutions [73], quantifying packaged food quality [74], and real-time monitoring of water content in civil engineering materials [75, 76]. Despite of offering a good performance, this system is quite complex, considering the material properties estimation was achieved from impedance spectrum of the sensor measured using a remotely located antenna. The material properties (e.g. complex permittivity) are calculated from the impedance spectrum at the resonant frequency with the inductance and capacitance of the sensor values based on calculation of an analytical model. Moreover, looking at the current technologies, the potential of this system to be a portable or home appliance is hindered as it requires either an expensive impedance analyzer or lock in amplifier. Having a resemblance sensor design, Stanley et al. [77] and Woodard [78] employed open-circuited self-resonating planar spiralling pattern of electrically conductance material coated with active material as explained in the fourth section of Table 1.1. The results reflected that the sensors are suitable to be used in harsh condition. Nevertheless, the material used to make the sensor i.e. Silicon Nitride (Si_3N_4) is relatively expensive and only affordable by

programs funded for space exploration. Dickey et al. [79] and Oommon et al. [80] have investigated the effect of different size of pore and uniformity of the substrate (Metal Oxide) which was made as a platform base for interdigital sensor on the sensitivity and accuracy of NH_3 and relative humidity as describe in the second part of Table 1.1. Metal Oxide materials (SnO_2, Al_2O_3, and TiO_2) are relatively low cost and well-known for their manipulatable structure for gas-sensing enhancement. However, the fabrication of the sensor is laborious that requires an access to expensive facilities and considerably skilled personnel.

Several researchers [81, 82] have address the application of Inductor and Capacitor (LC) wireless sensor with Elecrolyte-Nitrate-Oxide-Silicon (ENOS) structure as an electrochemical potential-to-capacitance transductor fabricated using CMOS technology for pH measurement of liquid material such as water. These studies have made improvement of shorter response time and linear response. The main drawback is the operating frequency had to be adjusted to a proper value to minimize the unwanted response of the sensor to the sample (material under test) conductivity. In this research, our attention and interest have been drawn into to develop an electromagnetic sensor consisting both inductive and capacitive element which can be integrated as a low cost, convenient, and suitable for in-situ measurement system for water quality monitoring which will contribute to environmental monitoring.

Table 1.1: Environmental monitoring based on sensing system based on planar meander and interdigital elements

Sensor's Description	Scale	Research objective/Sensing Method	Environmental Parameters Monitored	Frequency Range	Ref
1) Inductor and Capacitor circuits (LC) connected in a loop with Ti_2O coating and flexible parallel plate capacitor.	Mili	The sensor reacts with its environment. Then, a pair of antenna loop was used to detect the resonant frequency of the sensor which estimated from the impedance/voltage spectrum of the antenna. The environmental parameters are then calculated from the resonant frequency	Complex permittivity of a surrounding medium, ε' difference (%): 2.9 to 9.1 % and ε'' difference (%): 14.4 to 37.3 %. Temperature monitoring: linear shift of 6.4 kHz/°C. Humidity: resonant frequency shift of 3.1 MHz (≈14 %) during humidity change between 0-98 %. Pressure: linear resonant frequency shift of 1.28 MHz/psi over the pressure range between 0-5 psi.	5 to 25 MHz	[70]
2) Interdigital sensor with gold electrodes deposited on Metal Oxide films which formed through an anodization process	Nano	Study the effect of uniformity on different pore size of Metal Oxide films in ammonia gas (NH_3) and relative humidity sensing. Sensor impedance was measured using an Impedance Analyzer.	Detection of NH_3 at room temperature and relative humidity.	5 kHz	[79, 80]
3) Inductor and Capacitor (LC) wireless sensor with Elecrolyte-Nitrate-Oxide-Silicon (ENOS) structure as an electrochemical potential-to-capacitance transductor fabricated using CMOS technology.	Nano	The sensor measures the electrolyte using a wireless coil where the resonant frequency of the sensor as a function of pH is determined.	pH measurement with sensitivity of 1.2 % frequency/pH.	100 to 140 kHz	[81, 82]
4) Self-resonating-open-circuited planar spiralling pattern of electrically conducted material, coated with active material such as silicon nitride and polyaniline.	Mili	The sensor is wirelessly excited by external oscillating magnetic fields. The sensor's resonant frequency is related to the deformation of the sensor's pattern, electric and magnetic properties changes of the sensor's pattern, or the electric and magnetic properties changes of the material/environment place close to the sensor.	Application in harsh condition. Gases detection such as NH_3, CO, CO_2, O_2, H_2, and CH_4. Temperature measurement. Ambient pressure.	5 to 25 MHz	[77, 78]

1.3 Recent Progress in Nitrate Detection

Extensive list of nitrate detections for biological/environmental samples e.g. plant, urine, water, etc. in the period between 1980 and 2001 can be found in [26, 83]. Furthermore, Desai et al. reviewed the improvisations of portable analytical chemistry methods of nitrate detection in terms of nonproliferation of heavy metal and acid materials [84]. This section specifically reviews the recently developed nitrate detection methods in natural waters sources in between 2001 and 2011 where the assessment of the methods is reported in the form of strength and weakness. As has been briefly discussed in section 1.2, there are direct and indirect methods of nitrate detections in natural water sources. Indirect method can further be classified into single detection technique and hybrid detection technique as shown in Figure 1.4. Hybrid detection technique involves at least two detection methods such as colorimetric and spectroscopy. Next section will discuss the direct method.

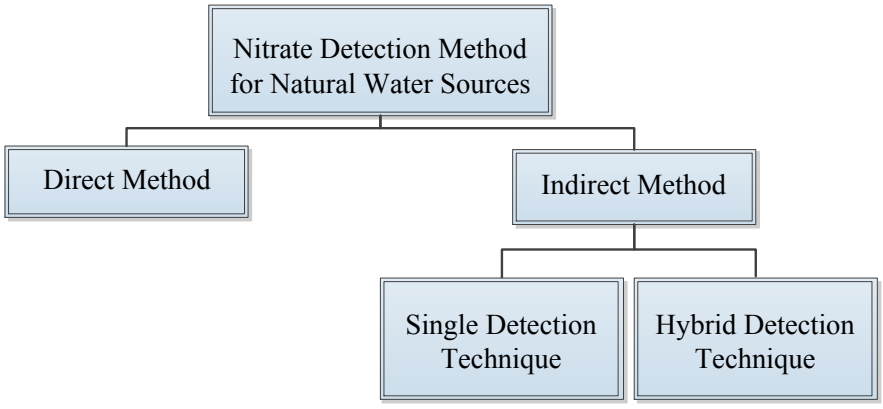

Figure 1.4: Classification of nitrate detection method for natural water sources

1.3.1 Direct Method

In the past decade, direct method of nitrate measurement in water sources involved potentiometry [25, 85-87], ion chromatographic method [88, 89], amperometric [90], electrochemical [91-97], and biosensor [20, 98-100]. A potentiomery system based on ion selective electrodes (ISE) relates the analytical concentration of the solution's analyte

with the electrical potential measured between a set of electrodes under the condition of no current flow. A typical potentiometry system consists of a working electrode and a reference electrode immersed in the sample solution and a reference solution, respectively linked with a salt bridge as illustrated in Figure 1.5. The output signal (potential difference) is measured between the working electrode and reference electrode. The working electrode is made specifically to be chemical reactive with the targeted test sample, thus the electrode's potential be subject to the concentration of the sample solution's analyte. The definition of reference potential is determined from the reference potential.

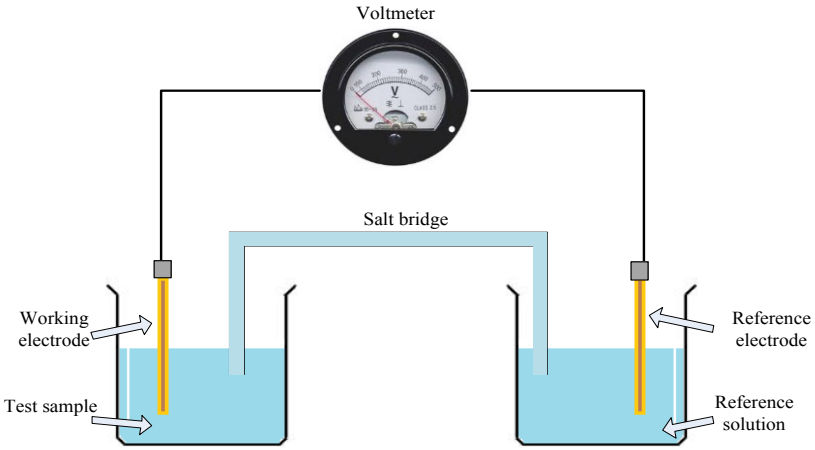

Figure 1.5: A simple potentiometric system

A potentiometric nitrate detection system based on graphite pencil doped with polypyrrole has been verified to be highly selective to nitrate [25]. Ashgari et al. [85] and Ardakani et al. [86] developed working electrodes based on nickel (II) complex coated with PVC-based membrane. Mahajan et al. [87] made a significant improvement by developing a working electrode based on zinc (II) complex coated with PVC-based membrane. Table 1.2 summarizes the maximum detection value of the nitrate detection systems based on potentiometry method.

Table 1.2: Maximum detection value for different types of potentiometry systems

Working Electrode Type	Maximum detection value in $mg\cdot(NO_3)^-N/L$	Reference
Graphite pencil doped with polypyrrole.	10 mg/L	[25]
PVC-based membrane coated tetra-coordinate nickel (II) complex.	15.5 mg/L	[85]
PVC-based membrane coated tetra-cyclotetra-decanato nickel (II) complex.	31.25 mg/L	[86]
PVC-based membrane coated Zinc (II) complex.	129.58 mg/L	[87]

As a whole, potentiometry systems offer advantages such as low cost, simple device construction, high sensitivity/response [25, 85-87], and wide pH range response [85]. However, this type of system cannot avoid the extensive preparation of extra reagent and solution [25, 85-87]. One particular potentiometric system involved the emission of a harmful gas during polypyrrole purification process [25].

Amperometry/electrochemical system retrieves information about the sample's analyte by applying a range of current/potential value while measuring the resulting potential/current. The electrodes comprise of a working electrode, an auxiliary electrode, and a reference electrode as can be seen from Figure 1.6. These methods (amperometry and electrochemical) supposedly reveal the electrochemical reactivity of an analyte.

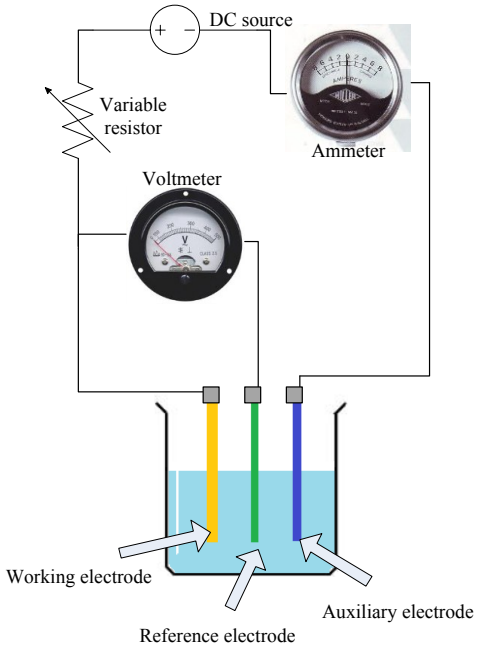

Figure 1.6: Three-electrode setup for amperometirc electrochemical system

The applications of amperometry and electrochemical cover micro-amperometirc sensor based on silver electrode incorporated with nitrate permeable ion selective membrane [90], micro-electrochemical sensor based on electro-deposition of copper electrode at boron doped diamond (BDD) [91], electrochemical system based copper deposited on paladium disk as working electrode [92], micro-electrochemical sensor based on copper-complex plated modified electrode [93], electrochemical sensor based on electro-deposition of a renewable copper layered electrode [94], micro-electrochemical

sensor based on doped polypyrrole nanowires [95], micro-electrochemical sensor based on copper-plated platinum electrode [96], and electrochemical sensor with metallic copper nanoparticle-plated polypyrrole-polystrene sulfonate thin film as working electrode [97]. Table 1.3 sums up the maximum detection value of the nitrate detection system based on amperometry and electrochemical methods. The main advantages of amperometry and electrochemical systems are as following:

1. Small, compact, and cost effective,
2. Portable and suitable for in-situ measurement, and
3. Relatively fast response and wide detection limit.

On the other hand, the common disadvantages are listed as below:

1. The repeatability and sensitivity depend on the re-activation of the working electrode every time before the actual experiment starts,
2. Require extensive process of solution reagent preparation,
3. Susceptible to interference ions such as chloride, sulphate, and phosphate, and
4. Requirement of different types of electrodes.

Table 1.3: Maximum detection value for different types of amperometry and electrochemical systems

System Type	Maximum detection value in $mg\cdot(NO_3)^-N/L$	Reference
Micro-amperometirc sensor based on silver electrode incorporated with nitrate permeable ion selective membrane.	6250 mg/L	[90]
Micro-electrochemical sensor based on electro-deposition of copper electrode at Boron doped diamond (BDD).	775 mg/L	[91]
Electrochemical system based copper deposited on palladium disk as working electrode	3.6 mg/L	[92]
Micro-electrochemical sensor based on copper-complex plated modified electrode	312.5 mg/L	[93]
Electrochemical sensor based on electro-deposition of a renewable copper layered electrode	15625 mg/L	[94]
Micro-electrochemical sensor based on doped polypyrrole nanowires	6250 mg/ L	[95]
Micro-electrochemical sensor based on copper-plated platinum electrode	1875 mg/ L	[96]
Electrochemical sensor with metallic copper nanoparticle-plated polypyrrole-polystrene sulfonate thin film as working electrode	187.5 mg/ L	[97]

Ion chromatography operates by separating ionized sample with extraction resin into individual ions based on their charge, species type, and size. The sample solutions are passed through a pressurized column where the samples solutions react with the extraction resin called as eluent. As the eluent runs through the column and drips through

the detector (commonly electrical conductivity detector), the ionized samples begin separating from the column as can be seen from Figure 1.7. Each ionic species has their own retention time which is different from the others. Therefore, the retention time will determine the ionic concentrations of different species in the sample as detected by the detector. Ion chromatographic method enhanced with artificial neural networks analysis has been used to detect nitrate in water sources as demonstrated in [88, 89]. Although this method provides a highly accurate and reliable nitrate measurement system with limit at 43.13 mg/L, it is relatively expensive and commonly known as desk application i.e. not portable and bulky.

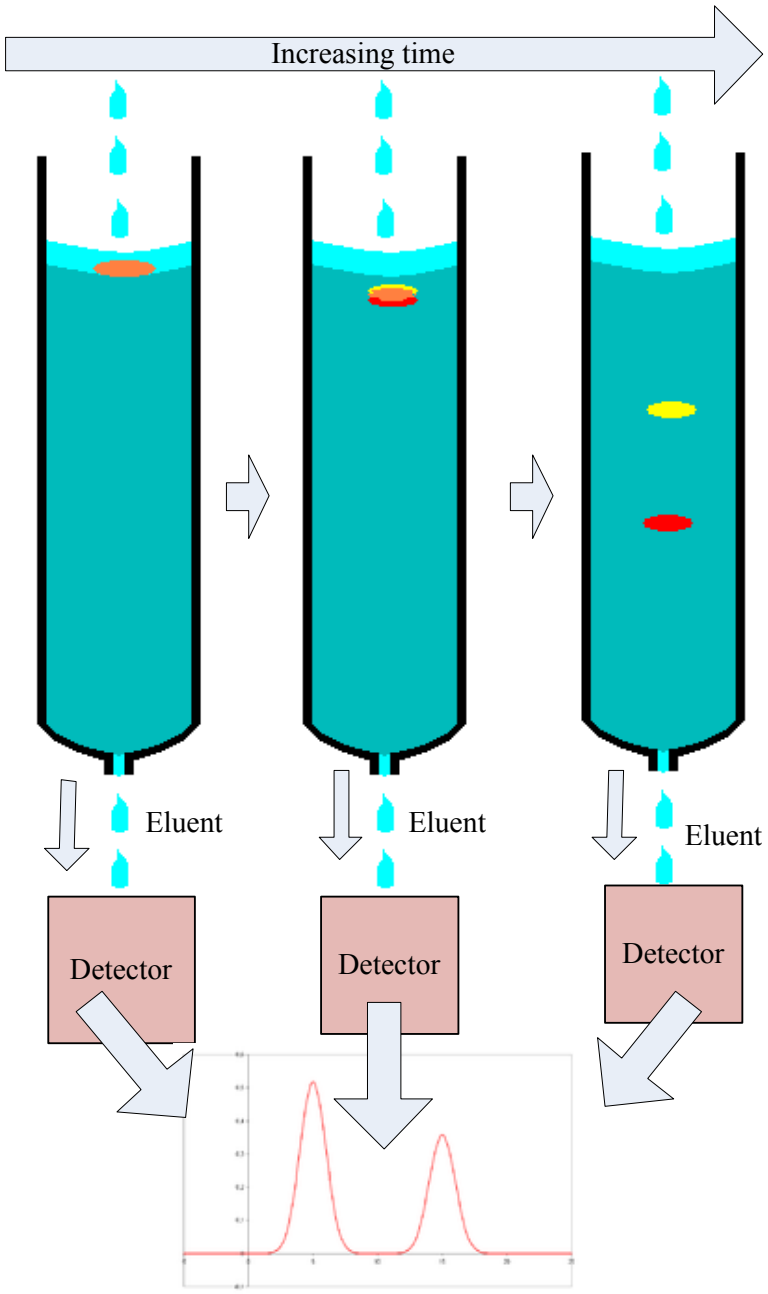

Figure 1.7: Schematic diagram of an ion chromatography

Another emerging direct method, which is receiving a lot of attention, is the application of biosensor in nitrate detection. A biosensor is basically a device which detects a certain analyte based on the integration between a biological/biological-synthesized material with a physicochemical detector component. A biosensor system encompasses three main parts: biological/biological-synthesized material, transducer, and signal conditioning circuit as summarized in Figure 1.8.

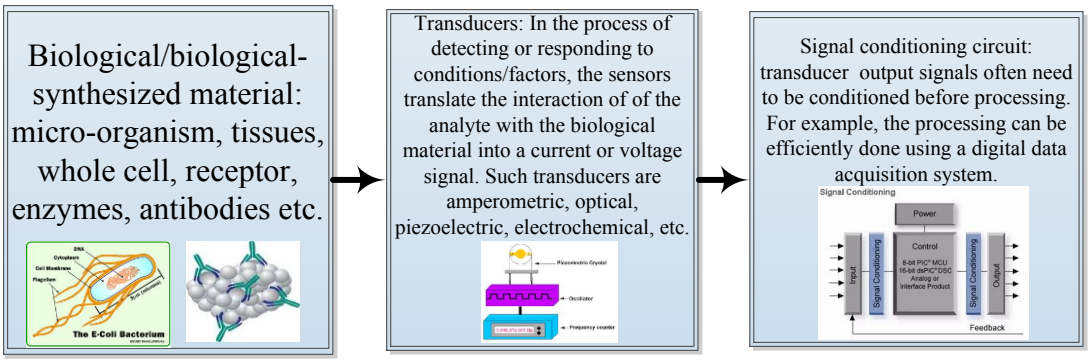

Figure 1.8: Three important parts of biological sensors

The applications of biosensor for nitrate detection have followed several occasions as summarized in Table 1.4. Biosensors applications reap the benefit of being cheap, relative small up to micro-scale [98], fast response and wide detection limit [20, 98-100], high selectivity [20, 98-100], and portable [20]. Although the benefits are considered overwhelming, certain biological element may require optimum temperature around 37 °C for optimum results [98]. Moreover, these methods are complex in terms of construction and operational procedure [99, 100]. One part of sensing elements, which is the optical path has to be properly guided and aligned, requiring a regular repositioning to maintain the accuracy [20].

Table 1.4: Biosensor applications for nitrate detection

Biological/biological synthesized material	Transducer	Maximum detection value in mg·$(NO_3)^-$−N/L	Reference
Escherichia Coli (E-Coli) bacteria as reduction agent.	Micro-amperometric.	6250 mg/L	[98]
Escherichia Coli (E-Coli) bacteria transformed into complex promoter.	Fluorescent reagent detector and fluorescence spectrometry.	5000 mg/L	[99]
Selective membrane based on a C3 symmetry amide based receptor.	Spectrophotometer.	39375 mg/L	[100]
Selective membrane base on ionophore-chromoionophore.	Portable photometry.	62500 mg/L	[20]

1.3.2 Indirect Method

A single detection indirect method of nitrate measurement in water involved flow injection analysis (FIA)-spectrofluorometer [101, 102], FIA-spectrophotometry [103-105], FIA-UV-Vis spectroscopy [106], reduction agent-spectrophotometry [107-110], and micro-scale-reduction agent-spectrophotometry [111]. The hybrid method has been mainly exploring high precision liquid chromatography (HPLC)-spectrophotometry [112-114].

An FIA method consists of four main sequential stages: distribution process, reduction process, pre-detection process, and detection process as shown in Figure 1.9. The distribution process is actually an automation process where the exact fraction of the sample from the input stream can systematically be passed to the next process so that it can be continuously operated for a relatively long period. In the reduction process, reduction agent such as copperized cadmium reduces NO_3^- into more reactive nitrite which can be quantified by the reagent assay (detection agent) in the pre-detection process. The output from reduction process is coupled with a detector agent, to form a compound which may illuminate at a certain wavelength and its intensity/absorbance level depends on the concentration level as detected by a spectrophotometer. The classical Griess method pioneered the Griess assay reagent which coupled the reactive nitrate into nitrite diotized sulfanilic acid which has a peak response at the wavelength of 560 nm [115].

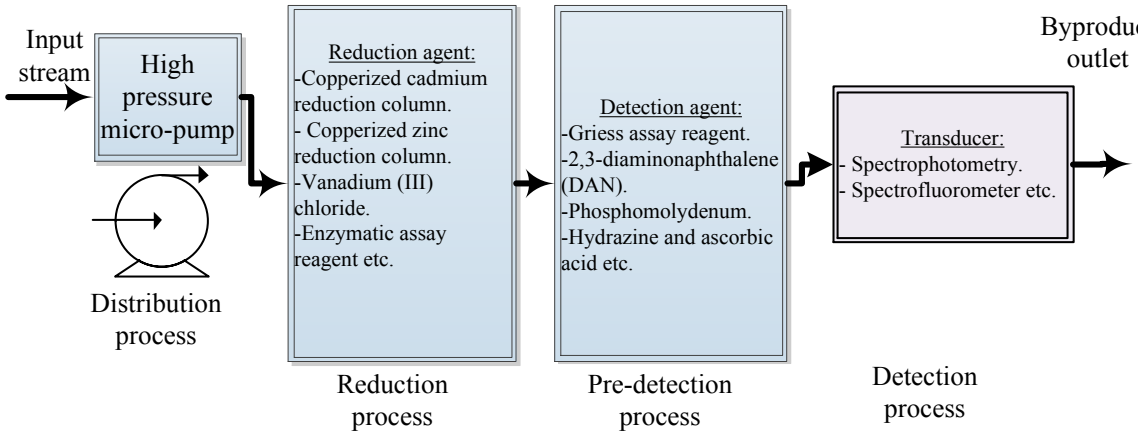

Figure 1.9: Schematic diagram of FIA method

Table 1.5 summarizes the FIA based method for nitrate detection in natural water sources and the corresponding detection limit value in mg/L. Based on the work in the literature listed here, the prevalent advantages of FIA-based method are [101-106]:

1. Can continuously be used for a relatively long period.
2. Operate with a limited amount of sample.
3. Minimal manual labour during actual experimental session benefited from automation process, and
4. Relatively fast response.

However, the disadvantages that have been noticed are:

1. Interference with major ions in the water sample such as phosphate[101].
2. Production of poisonous waste water containing cadmium [101-104].
3. Extensive preparation process of extra assay reagents, as well as safety issues in handling the assay reagents.
4. Limited life span of mechanical part such as rotary valve [101-106].
5. The consistency and reproducible depends on the controlled condition of certain process such as the sample pH value must be between 8 and 8.5 [104].

Table 1.5: FIA based applications for nitrate detection

Reduction agent	Detection agent	Transducer	Maximum detection value in $mg\cdot(NO_3)^-N/L$	Reference
Copperized cadmium reduction column.	2,3-diaminonaphthalene (DAN).	Spectrofluorometer	0.02 mg/L	[101]
Copperized cadmium reduction column.	Phosphomolydenum	Spectrofluorometer	0.025 mg/L	[102]
Cadmium granules column	Griess assay reagent	Spectrophotometer	0.1 mg/L	[103]
Improved copperized cadmium column	Azo-dye colouring agent	Spectrophotometer	5 mg/L	[104]
Enzymatic assay reagent	Griess-Ilosvay assay reagent	Spectrophotometer	250 mg/L	[105]
Copperized zinc reduction column	Ammonium ion	UV-Vis spectroscopy	500 mg/L	[106]

There are other methods that share the same concept with FIA-based but did not incorporate distribution process as explained in Figure 1.9. They explored the use of hydrazine and ascorbic based reduction agent and *chemiluminescence* detection agent

with spectrophotometry [108], spectrophotometric method based on the reaction of nitrate with brucine reagent and 3-methyl 1-2-benzothiazolinone hydrazine hydrochloride (MBTH) in sulphuric acid medium [107], spectrophotometric method based on Vanadium (III) chloride reduction agent and Griess assay reagent [109], and UV-vis spectrophotometric method based on acidic reduction process coupled with detection assay reagent of N-1-(maphtyl)-ethylenediamine dihydrochloride (NEDA) [110]. As a whole, the detection limit is found to be between 0.5 and 100 mg/L of mg·$(NO_3)^-$−N/L. Besides the points that show the pros and cons of having a distribution process, these methods share the same advantages and disadvantages of FIA-based methods.

Last but not the least, the combination methods of high precision liquid chromatography (HPLC) with spectrophotometry [112-114] have proven to provide very accurate measurement and consistency. Another possible main reason to the employment of these methods is to provide high certainty of the results. The HPLC was mainly aimed to separate NO_3^- subsequently followed by photo-chemical reaction whose absorbance level measurement is based on spectrophotometry. They also provide considerably high level of maximum detection value between 500 and 1000 mg/L of mg·$(NO_3)^-$−N/L. However, the total revenue cost of this kind of methods makes it unsuitable, and still far from portable and low cost applications.

1.4 Contributions of This Thesis

Looking at the importance of nitrate detection and the challenges arise, this research has made three important contributions.

- Firstly, the innovation from the concept of novel sensor based on the combination of planar meander and interdigital sensors has been made. The best design was presented for the application of natural water quality monitoring.
- Secondly, an analysis technique based on independent component analysis to estimate the amount of nitrate contamination in natural water sources has been demonstrated.
- Finally, the integration of the best sensor with a low cost, convenient, and suitable for in-situ measurement system for water quality monitoring has been achieved.

1.5 Organization of the Thesis

This thesis is organized into eight chapters. In Chapter 1, the problem formulation and objectives, literature review of planar sensors for environmental monitoring, literature review for nitrate detection in natural water sources, and contribution of the research are presented. Chapter 2 describes the designs of all the electromagnetic sensors that have been considered in this research. In Chapter 3, the selected sensors were simulated and evaluated using COMSOL multiphysics modelling and simulation software. The comparison of the simulation results and the experimental results are also shown in Chapter 3. The evaluation and performance parameter comparisons of the fabricated sensors in Chapter 2 have been conducted in Chapter 4. Chapter 5 includes the main experimental observation where the outcomes concluded that the best sensor consists of the series combinations of spiral meander planar sensor (with five turns) with the interdigital sensor (with large negative electrode), SECS22_1. In Chapter 6, a method based on Independent Component Analysis (*ICA*) in estimating the amount nitrate contamination in a natural water sources is discussed. Chapter 7 describes the experimental set-up and the interfacing of sensor signal to a low-cost system for the application of nitrate detection and water quality estimation. Finally, the current work and future work have been concluded and proposed, respectively, in Chapter 8.

CHAPTER 2

Description of the Sensors

2.1 General Description of the Sensors

Applications of planar electromagnetic sensors have been reported in [36-50, 52-57, 62-69, 116] where the designs can be found. In this chapter, two main types of sensors are introduced as following:

- Sensors with meander and interdigital elements placed side by side having parallel and series combinations.
- Sensors with meander surrounding interdigital element, where the interdigital element is placed in the middle having parallel and series combinations.

All the sensors were designed using Altium Designer 9 and it has been fabricated using simple printed circuit board (PCB) fabrication technology where the thickness of the PCB is 0.25 mm. All the sensors were sprayed with Wattyl Killrust Incralac to form an acrylic resin-based protective coating. Wattyl Killrust Incralac is an acrylic resin-based protective coating containing special tarnish and corrosion control additives designed especially for the protection of copper, brass and similar alloys. The thickness of the coating was set to be approximately 30 microns.

2.2 Meander and Interdigital: Side by Side

Each sensor has a BNC connector and can be connected to an external function generator which provides an alternating 10 Volt peak-to-peak sine waveform signal. There are two types of connections: parallel and series, which will be discussed in the next section.

2.2.1 Parallel Connection

Figures 2.1 and 2.2 show samples of the first variations of inductive-capacitive planar electromagnetic sensors connected in parallel: SSCP1_1, SSCP2_1, SSCP3_1, and

SSCP4_1, respectively. In this section the sensors are denoted by the generic code of SSCPXX_V.

Where, SSCP = the code for the meander sensor and interdigital sensor that are placed side by side and connected in parallel.

XX = the number of the variation from 1 to 24.

V = the version number of the sensors which is 1.

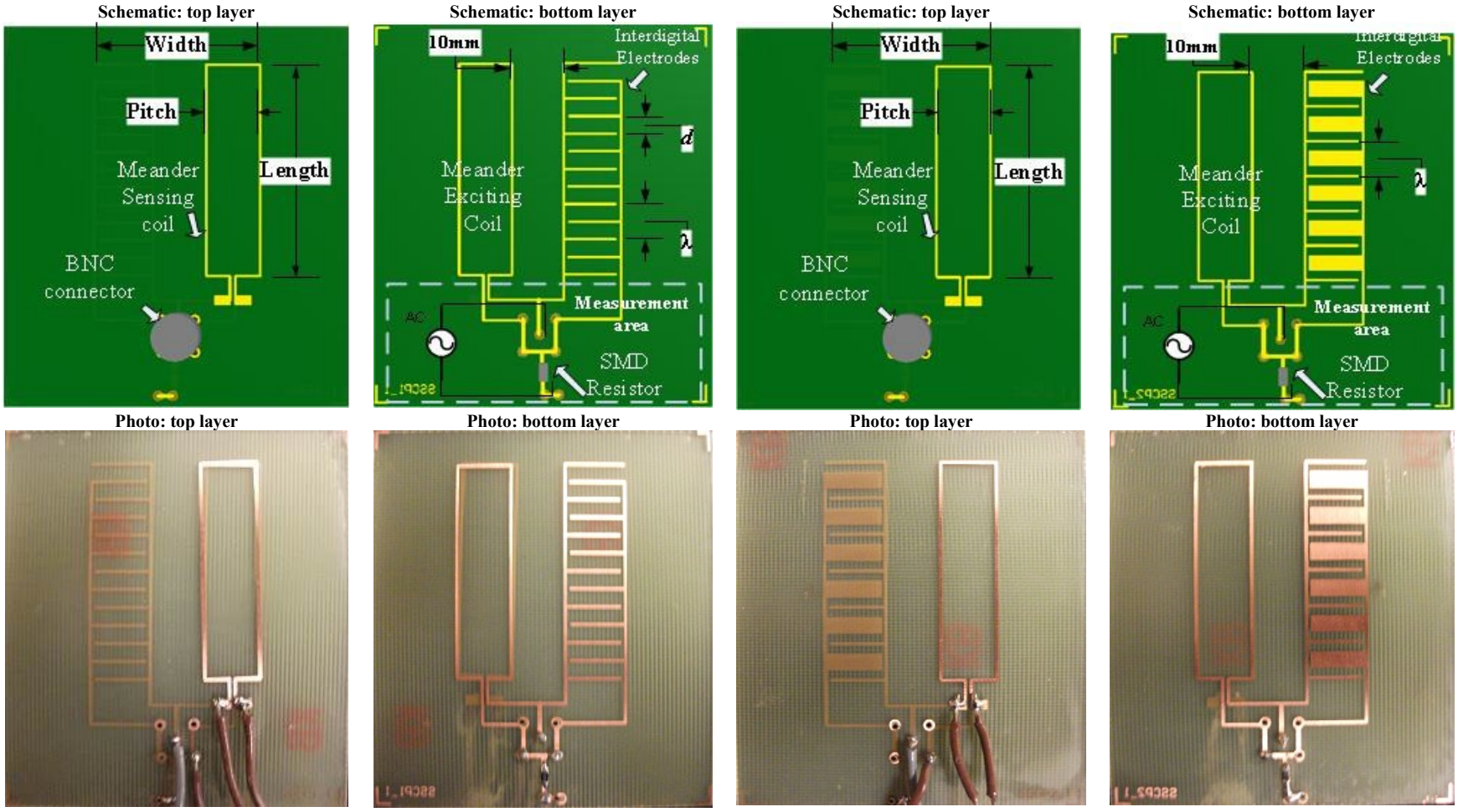

(a) SSCP1_1 (b) SSCP2_1

Figure 2.1: Schematic diagrams and pictures of (a) SSCP1_1 (b) SSCP2_1

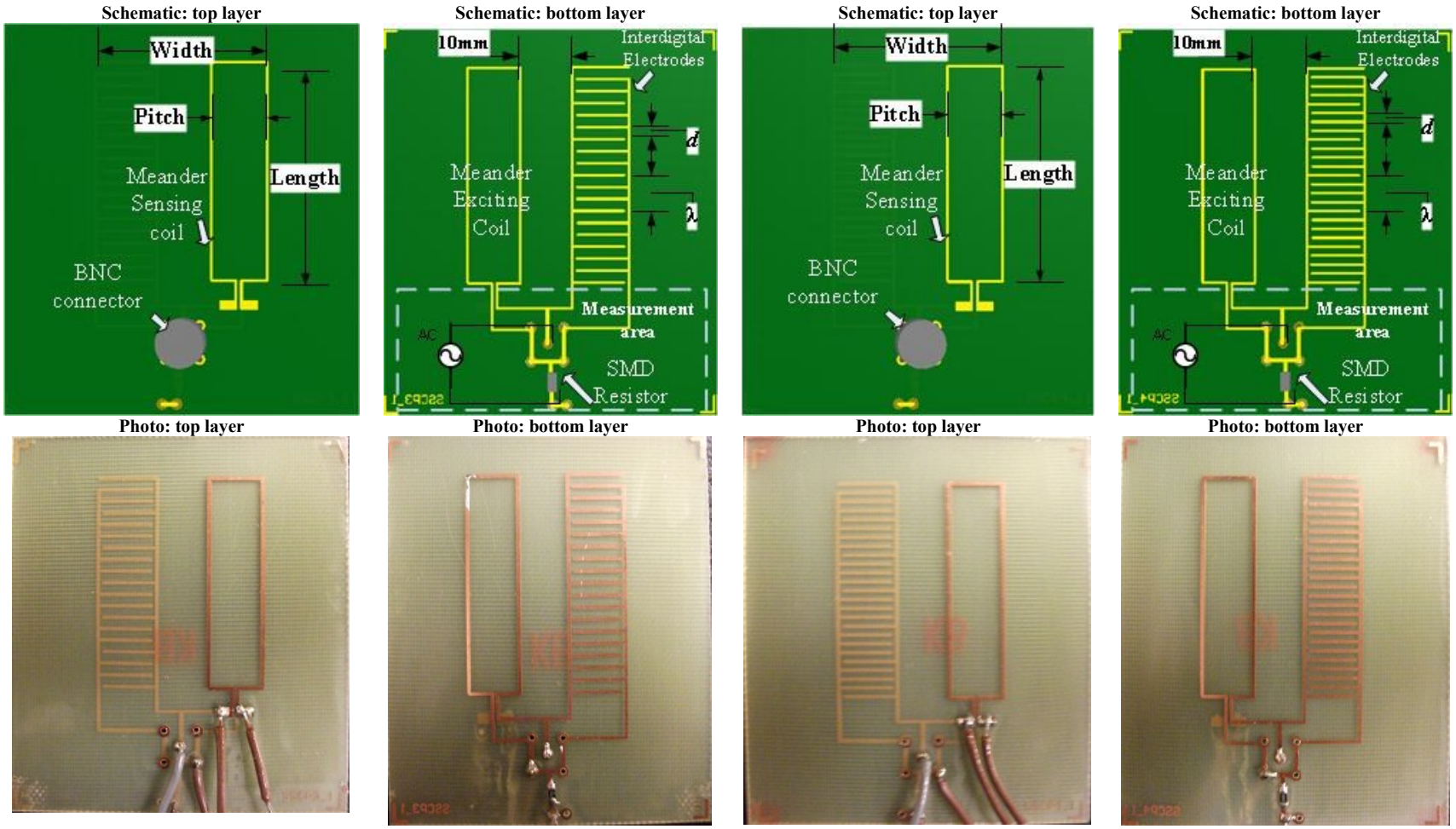

(a) SSCP3_1 (b) SSCP4_1

Figure 2.2: Schematic diagrams and pictures of (a) SSCP3_1 (b) SSCP4_1

The copper track width was set at 0.5 mm thick. The main idea of developing a combined sensor is to study the relationship between the generated electromagnetic fields with different combinations and geometries of planar electromagnetic sensors, thus finding the sensors, which have the best performance for detection of water contamination. In general, each sensor has a dimension of 30 mm × 40 mm (width × length). SSCP1_1, SSCP2_1, SSCP3_1, and SSCP4_1 consist of different interdigital designs but the same effective area of 10 mm × 40 mm, placed 10 mm apart to a meander sensor with single turn (10 mm pitch). The meander sensors part consists of two coils. The exciting coil is driven by sinusoidal current to create a magnetic field. SSCP1_1 has the first type of interdigital sensor, whose electrodes' pattern is + - + - + - +, which is an arrangement of alternative positive and negative electrodes separated by a distance of 3.3 mm. It consists of total 13 electrodes of 10 mm length and 0.5 mm width, 7 connected to exciting/driving electrodes and 5 are connected to ground. SSCP2_1 shares the same design with SSCP1_1 but it has the second type of interdigital sensor, and the negative electrodes width is 3 mm as shown in Figure 2.1(b). Negative electrodes with wider size enable a better or strong current signal off the sensor. The third interdigital type, in the design configuration of SSCP3_1, the electrodes are arranged in the pattern of + - - + - - + etc, a driving electrode followed by a series of 2 ground electrodes as shown in Figure 2.2(a). The above pattern was repeated with a driving electrode again. Each electrode is separated by a distance of 2.24 mm; each electrode is of 10 mm in length and 0.5 mm in width. The fourth interdigital sensor type in SSCP4_1 is similar to SSCP3_1, however employs electrodes pattern of + - - - + - - - + etc, where each electrode is separated by a distance of 1.67 mm as can be seen in Figure 2.2(b). The positive electrodes are driven by an ac electric potential (same source as the meander) to create an ac electric field between the positive and negative electrodes. These field pass through the material under test, thus material dielectrical properties as well as the electrode and material property affect the capacitance and the conductance between (impedance) the two electrodes. The penetration depth of the electric field is determined from the spatial wavelength, λ, which is the length between the two adjacent electrodes of same type. The penetration depth is one fourth of the spatial wavelength [32, 65, 67, 69].

SSCP5_1, SSCP6_1, SSCP7_1, and SSCP8_1 are similar to SSCP1_1, SSCP2_1, SSCP3_1, and SSCP4_1, respectively, but having a grounded backplane on the other side

of the interdigital sensor to provide shielding from external perturbation, define ground potential, and confine the electric field to the upper half-space [117]. Figure 2.4(a) and 2.4(b) show the design layouts for SSCP5_1 and SSCP6_1, respectively. From this point, two new variations of sensors are fabricated based on SSCP1_1 to SSCP8_1. The second variation and the third variation have meander sensors with three and five turns, respectively. Figure 2.4 (a) and 2.4(b) show the designs for SSCP9_1 and SSCP10_1, respectively, each having meander sensor with three turns. The distance between the turn, d_1, is set at 1.45 mm. Table 2.1 summarizes the designs of sensors in this part.

Table 2.1: Summary of SSCP1_1 to SSCP24_1

Sensor	Interdigital type,.			Meander		
	Type	Wavelength, λ (mm)	Distance between electrode, *d* (mm)	Negative backplane	Number of turns	Distance between turn, d_1 (mm)
SSCP1_1	1	6.6	3.3	No	1	N/A
SSCP2_1	2	6.6	1.8	No	1	N/A
SSCP3_1	3	6.6	2.24	No	1	N/A
SSCP4_1	4	6.6	1.67	No	1	N/A
SSCP5_1	1	6.6	3.3	Yes	1	N/A
SSCP6_1	2	6.6	1.8	Yes	1	N/A
SSCP7_1	3	6.6	2.24	Yes	1	N/A
SSCP8_1	4	6.6	1.67	Yes	1	N/A
SSCP9_1	1	6.6	3.3	No	3	1.45
SSCP10_1	2	6.6	1.8	No	3	1.45
SSCP11_1	3	6.6	2.24	No	3	1.45
SSCP12_1	4	6.6	1.67	No	3	1.45
SSCP13_1	1	6.6	3.3	Yes	3	1.45
SSCP14_1	2	6.6	1.8	Yes	3	1.45
SSCP15_1	3	6.6	2.24	Yes	3	1.45
SSCP16_1	4	6.6	1.67	Yes	3	1.45
SSCP17_1	1	6.6	3.3	No	5	0.5
SSCP18_1	2	6.6	1.8	No	5	0.5
SSCP19_1	3	6.6	2.24	No	5	0.5
SSCP20_1	4	6.6	1.67	No	5	0.5
SSCP21_1	1	6.6	3.3	Yes	5	0.5
SSCP22_1	2	6.6	1.8	Yes	5	0.5
SSCP23_1	3	6.6	2.24	Yes	5	0.5
SSCP24_1	4	6.6	1.67	Yes	5	0.5

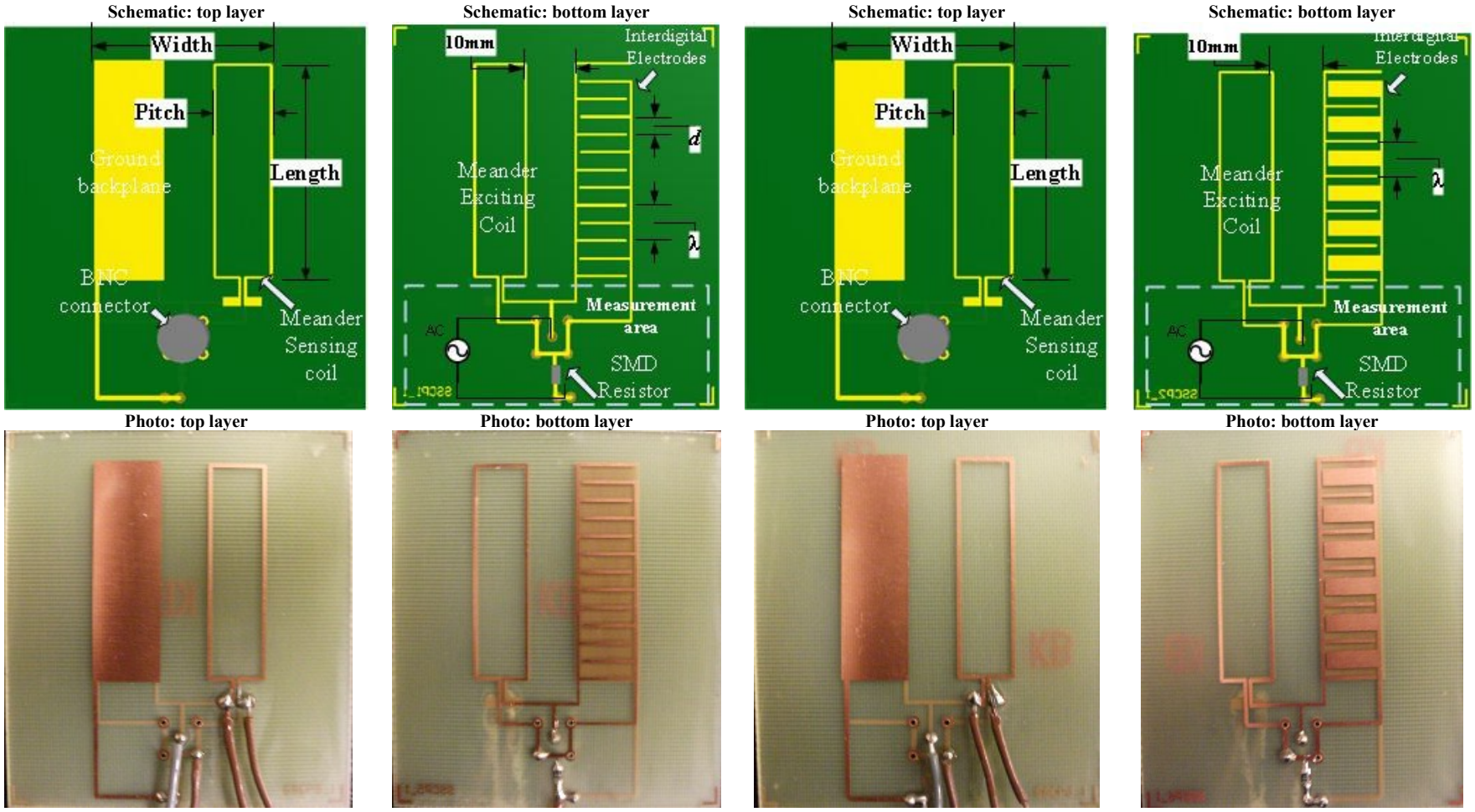

(a) SSCP5_1 (b) SSCP6_1

Figure 2.3: Schematic diagrams and pictures of (a) SSCP5_1 (b) SSCP5_1

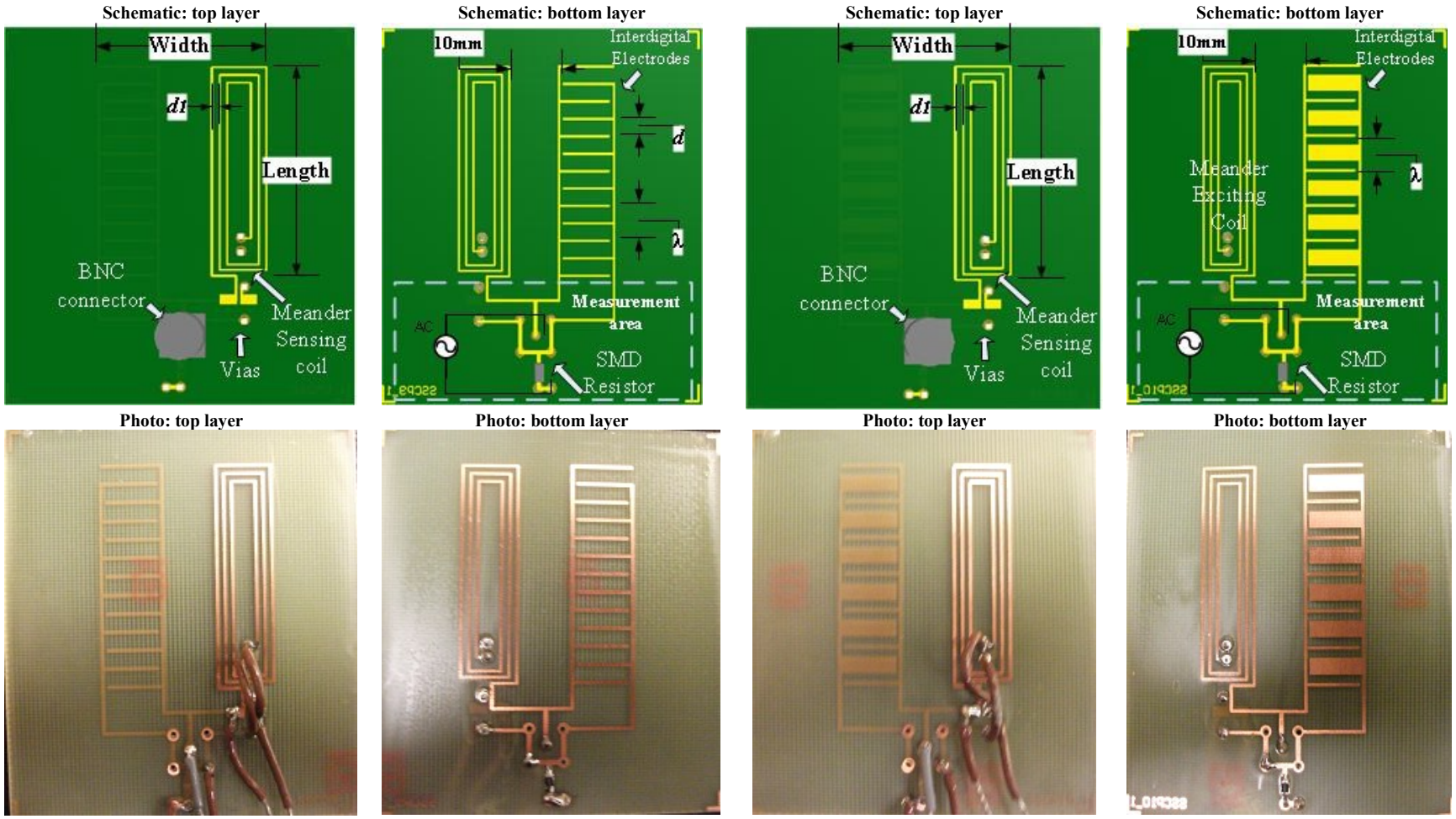

(a) SSCP9_1 (b) SSCP10_1

Figure 2.4: Schematic diagrams and pictures of (a) SSCP9_1 (b) SSCP10_1

2.2.2 Series Connection

The series connected meander and interdigital sensors, placed side by side: SSCS1_1, SSCS2_1, SSCS3_1, SSCS4_1, SSCS5_1, SSCS6_1, SSCS7_1, SSCS8_1, SSCS9_1, SSCS10_1, SSCS11_1, SSCS12_1, SSCS13_1, SSCS14_1, SSCS15_1, SSCS16_1, SSCS17_1, SSCS18_1, SSCS19_1, SSCS20_1, SSCS21_1, SSCS22_1, SSCS23_1, and SSCS24_1 are similar to SSCP1_1, SSCP2_1, SSCP3_1, SSCP4_1, SSCP5_1, SSCP6_1, SSCP7_1, SSCP8_1, SSCP9_1, SSCP10_1, SSCP11_1, SSCP12_1, SSCP13_1, SSCP14_1, SSCP15_1, SSCP16_1, SSCP17_1, SSCP18_1, SSCP19_1, SSCP20_1, SSCP21_1, SSCP22_1, SSCP23_1, and SSCP24_1, respectively. Sensors SSCS1_1 to SSCS24_1 are connected in series. Figures 2.5(a) and 2.5(b) depict the designs of SSCS22_1 and SSCS24_1, respectively. The series connection between meander sensor and interdigital sensor can be seen from the measurement area (bottom layer schematic diagram) of Figures 2.5(a) and 2.5(b). In this section the sensors are denoted by the generic code of SSCSXX_V.

Where, SSCS = the code for the meander sensor and interdigital sensor that are placed side by side and connected in series.

XX = the number of the variation from 1 to 24.

V = the version number of the sensors which is 1.

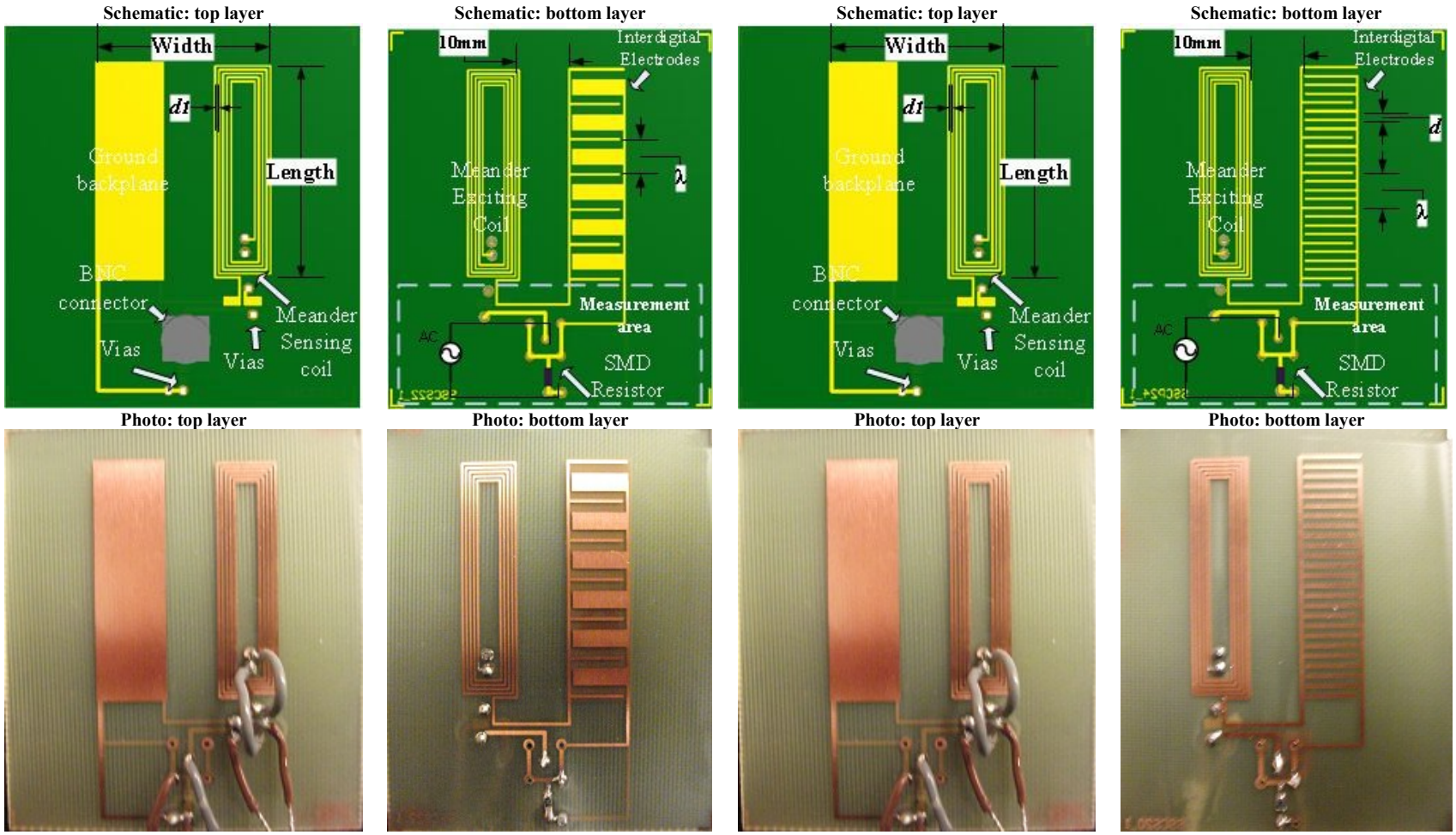

(a) SSCS22_1 (b) SSCS24_1

Figure 2.5: Schematic diagram and picture of (a) SSCS22_1 (b) SSCS24_1

2.3 Meander Enclosing Interdigital

In this section, each sensor consists of a meander coil spiralling inwards in rectangular form and the inner end is connected to an interdigital sensor completing a serial connection. The meander type of coil is connected in parallel and in series with the interdigital coil and an ac voltage is applied across the combination of the coils. The meander coil will produce a magnetic field and the interdigital coil will produce an electric field. So the combination of meander and interdigital coils will produce a combination of electric and magnetic field.

2.3.1 Parallel Connection

Figures 2.6 and 2.7 sample of the first variations of inductive-capacitive planar electromagnetic sensors connected in parallel: SECP_1, SECP_2, SECP_3, and SECP_4, respectively. In general, each sensor has a dimension of 26 mm × 54 mm (width × length). SECP1_1, SECP2_1, SECP3_1, and SECP4_1 consist of type 1 interdigital, type 2 interdigital, type 3 interdigital, and type 3 interdigital, respectively (each intergital has the same effective area of 10 mm × 40 mm), placed in the middle of a meander sensor with three turns. The distances between the sensors are kept at 2.5 mm. The meander sensor only consists of the exciting part.

SECP5_1, SECP6_1, SECP7_1, and SECP8_1 are similar to SECP1_1, SECP2_1, SECP3_1, and SECP4_1, respectively, but having a grounded backplane on the other side of the interdigital sensor (top layer). Figures 2.8(a) and 2.8(b) show the design layouts for SECP7_1 and SECP8_1, respectively.

The rest of the sensors are fabricated based on SSCP1_1 to SSCP8_1. The second variation and the third variation have meander sensors with three and five turns, respectively. Figures 2.9(a) and 2.9(b) show the designs for SECP10_1 (three turns) and SECP17_1 (five turns), respectively. Table 2.2 summarizes the designs of sensors in this part. In this section the sensors are denoted by the generic code of SECPXX_V.

Where, SECP = the code for the meander sensor that is enclosing the interdigital sensor and the sensors are connected in parallel.

XX = the number of the variation from 1 to 24.

V = the version number of the sensors which is 1.

Table 2.2: Summary of SECP1_1 to SECP24_1

Sensor	Interdigital type,.			Meander		
	Type	Wavelength, λ (mm)	Distance between electrode, *d* (mm)	Negative backplane	Number of turns	Distance between turn, d_1 (mm)
SECP1_1	1	6.6	3.3	No	3	2.0
SECP2_1	2	6.6	1.8	No	3	2.0
SECP3_1	3	6.6	2.24	No	3	2.0
SECP4_1	4	6.6	1.67	No	3	2.0
SECP5_1	1	6.6	3.3	Yes	3	2.0
SECP6_1	2	6.6	1.8	Yes	3	2.0
SECP7_1	3	6.6	2.24	Yes	3	2.0
SECP8_1	4	6.6	1.67	Yes	3	2.0
SECP9_1	1	6.6	3.3	No	4	1.35
SECP10_1	2	6.6	1.8	No	4	1.35
SECP11_1	3	6.6	2.24	No	4	1.35
SECP12_1	4	6.6	1.67	No	3	1.35
SECP13_1	1	6.6	3.3	Yes	4	1.35
SECP14_1	2	6.6	1.8	Yes	4	1.35
SECP15_1	3	6.6	2.24	Yes	4	1.35
SECP16_1	4	6.6	1.67	Yes	4	1.35
SECP17_1	1	6.6	3.3	No	5	1
SECP18_1	2	6.6	1.8	No	5	1
SECP19_1	3	6.6	2.24	No	5	1
SECP20_1	4	6.6	1.67	No	5	1
SECP21_1	1	6.6	3.3	Yes	5	1
SECP22_1	2	6.6	1.8	Yes	5	1
SECP23_1	3	6.6	2.24	Yes	5	1
SECP24_1	4	6.6	1.67	Yes	5	1

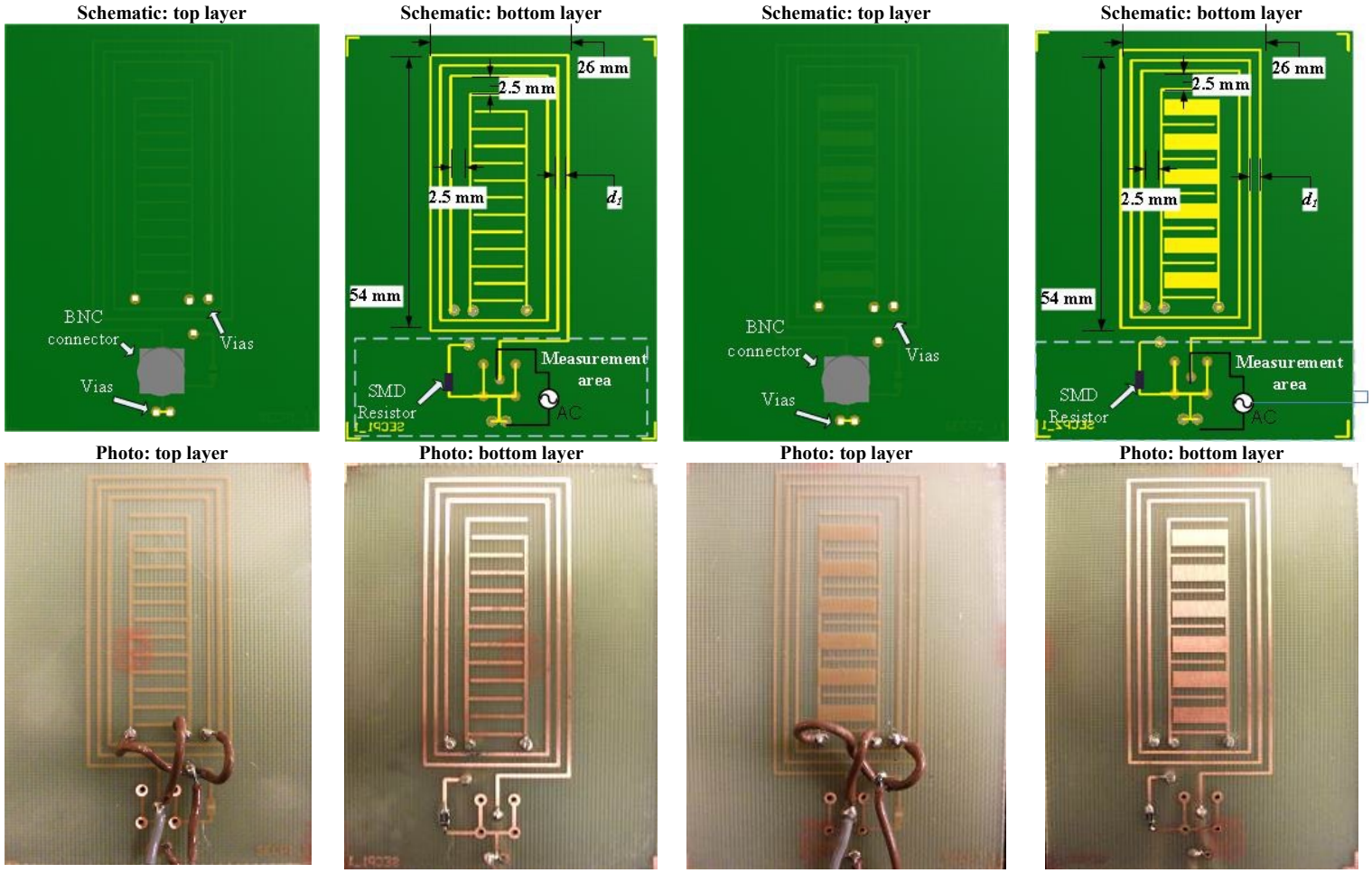

(a) SECP1_1 (b) SECP2_1

Figure 2.6: Schematic diagrams and pictures of (a) SECP1_1 (b) SECP2_1

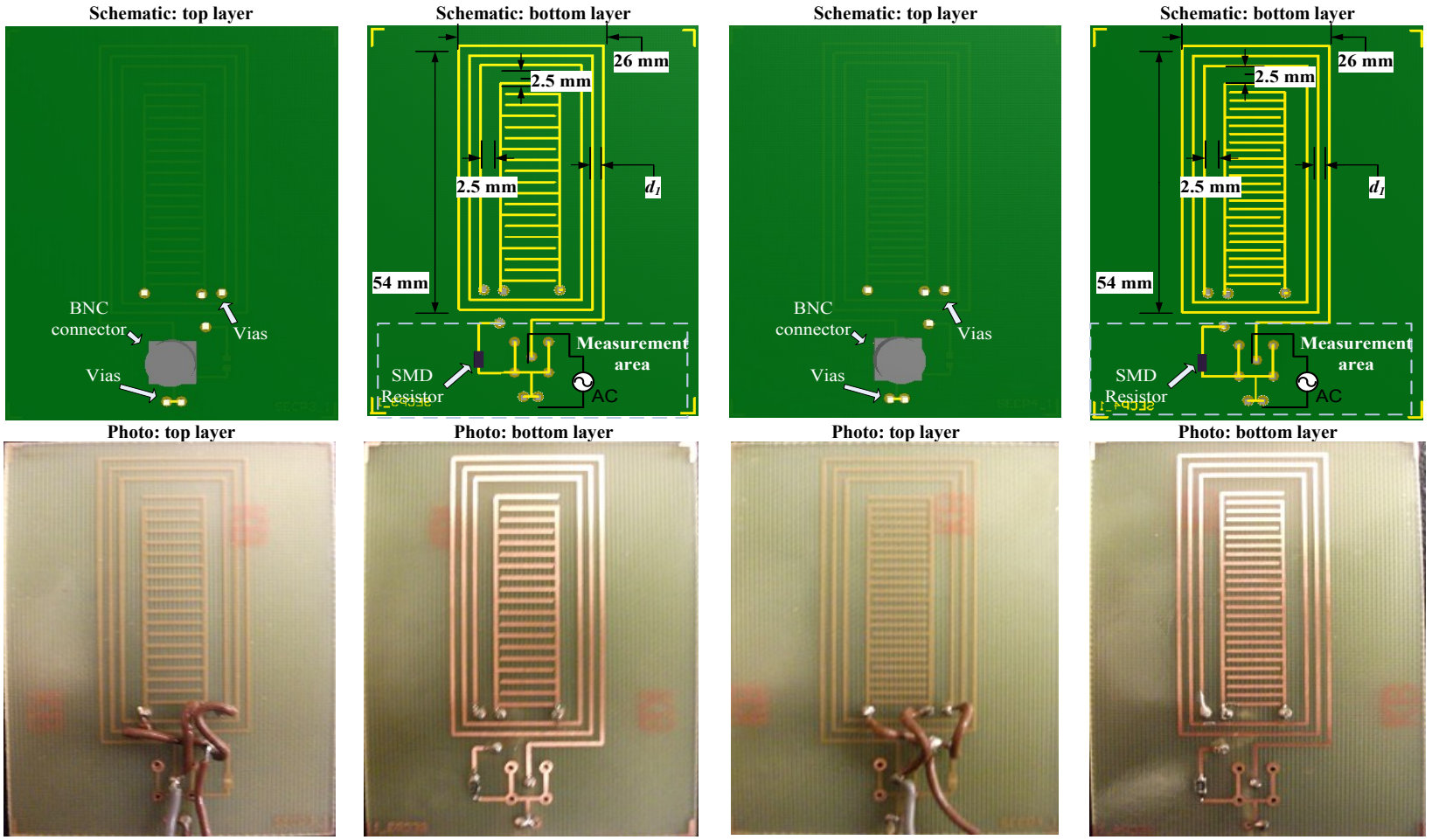

(a) SECP3_1 (b) SECP4_1

Figure 2.7: Schematic diagrams and pictures of (a) SECP3_1 (b) SECP4_1

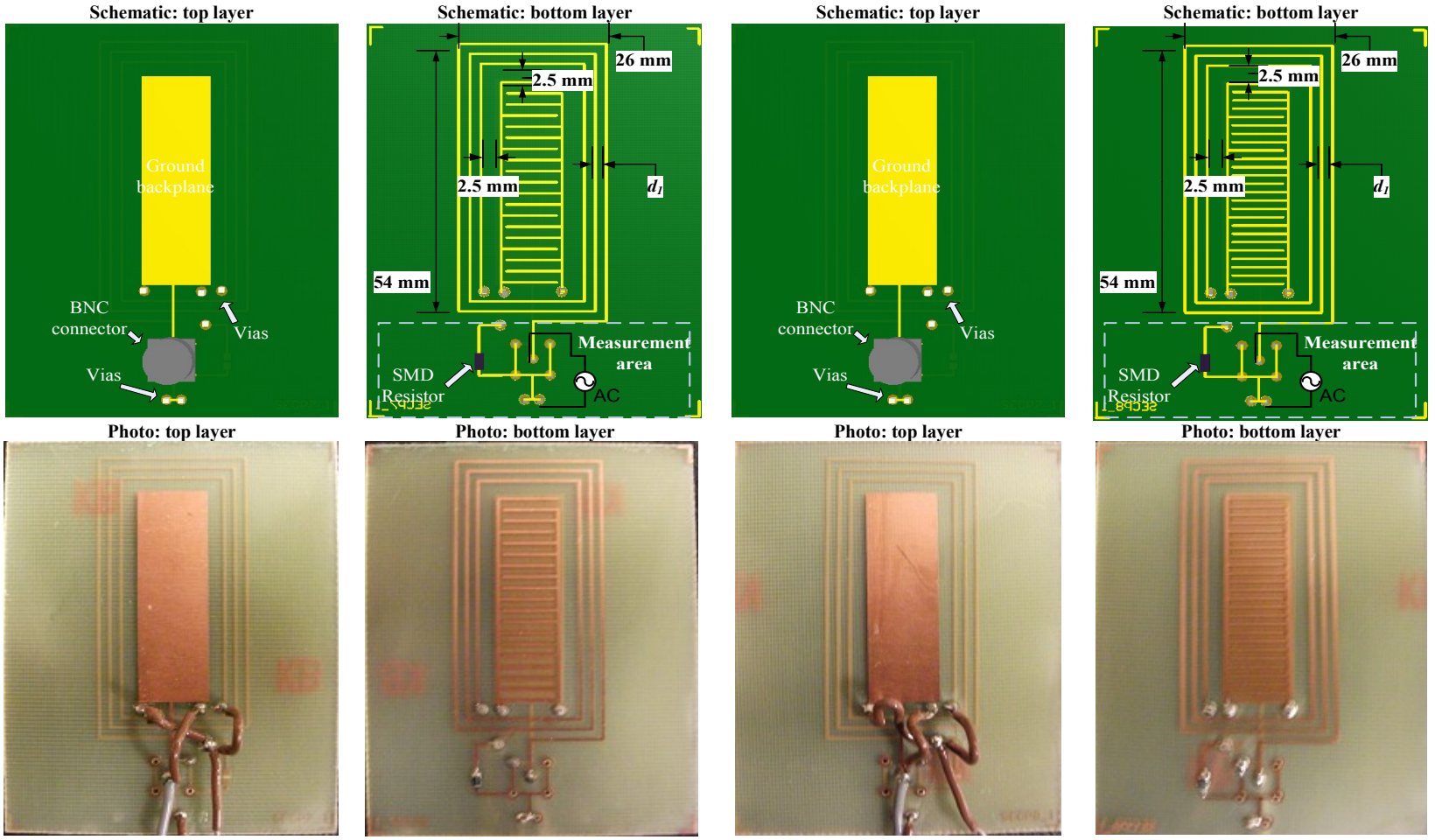

(a) SECP7_1 (b) SECP8_1

Figure 2.8: Schematic diagrams and pictures of (a) SECP7_1 (b) SECP8_1

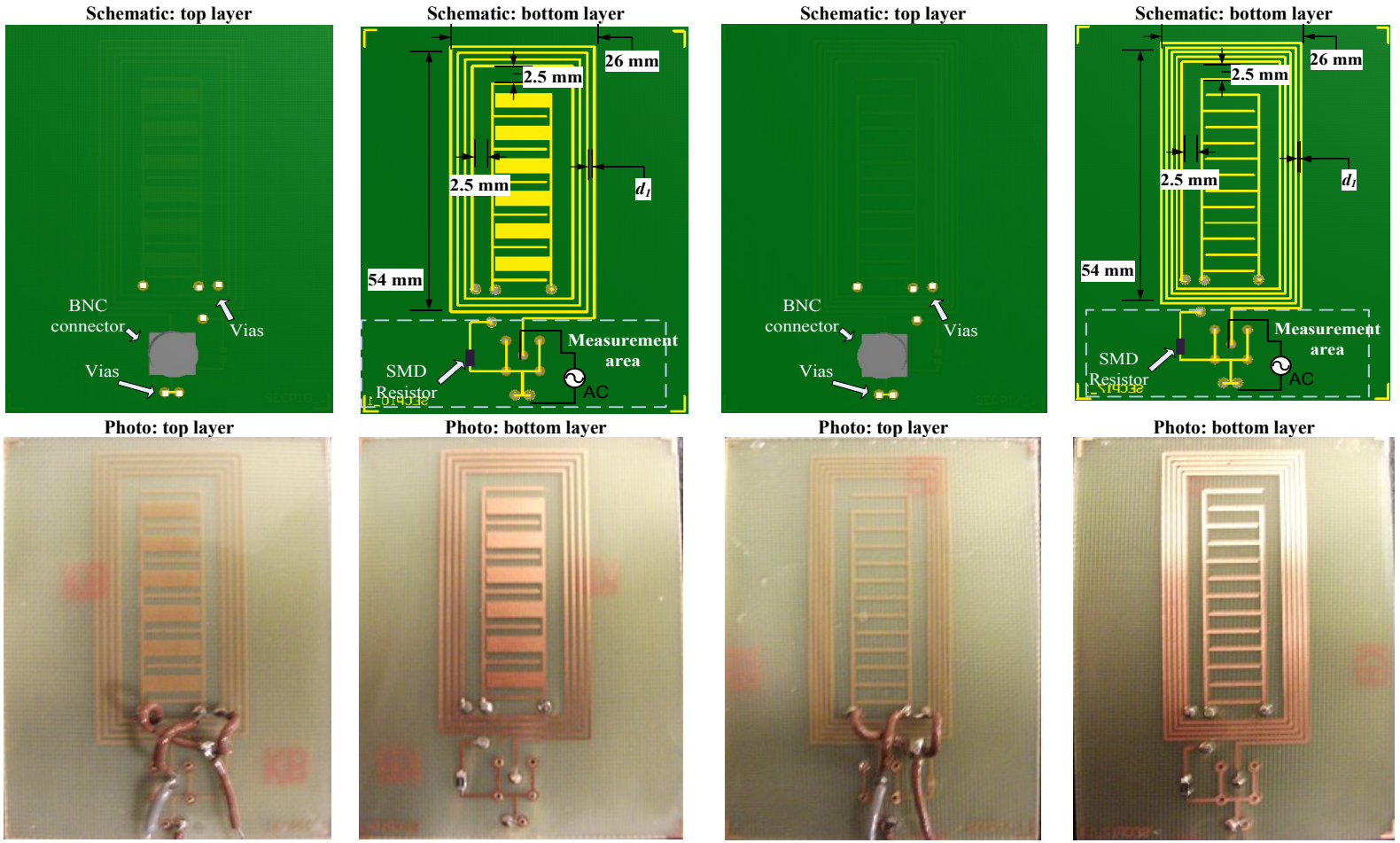

(a) SECP10_1 (b) SECP17_1

Figure 2.9: Schematic diagrams and pictures of (a) SECP10_1 (b) SECP17_1

2.3.2 Series Connection

The meander enclosing interdigital sensors, which are connected in series are: SECS1_1, SECS2_1, SECS3_1, SECS4_1, SECS5_1, SECS6_1, SECS7_1, SECS8_1, SECS9_1, SECS10_1, SECS11_1, SECS12_1, SECS13_1, SECS14_1, SECS15_1, SECS16_1, SECS17_1, SECS18_1, SECS19_1, SECS20_1, SECS21_1, SECS22_1, SECS23_1, and SECS24_1 are similar to SECP1_1, SECP2_1, SECP3_1, SECP4_1, SECP5_1, SECP6_1, SECP7_1, SECP8_1, SECP9_1, SECP10_1, SECP11_1, SECP12_1, SECP13_1, SECP14_1, SECP15_1, SECP16_1, SECP17_1, SECP18_1, SECP19_1, SECP20_1, SECP21_1, SECP22_1, SECP23_1, and SECP24_1, respectively. Sensors SECS1_1 to SECS24_1 are connected in series. Figures 2.10(a) and 2.10(b) depict the designs of SECS22_1 and SECS24_1, respectively. The series connection between meander sensor and interdigital sensor can be seen from the measurement area (bottom layer schematic diagram and photo pictures) of Figures 2.10(a) and 2.10(b). In this section the sensors are denoted by the generic code of SECSXX_V.

Where, SECS = the code for the meander sensor that is enclosing the interdigital sensor and the sensors are connected in series.

XX = the number of the variation from 1 to 24.

V = the version number of the sensors which is 1.

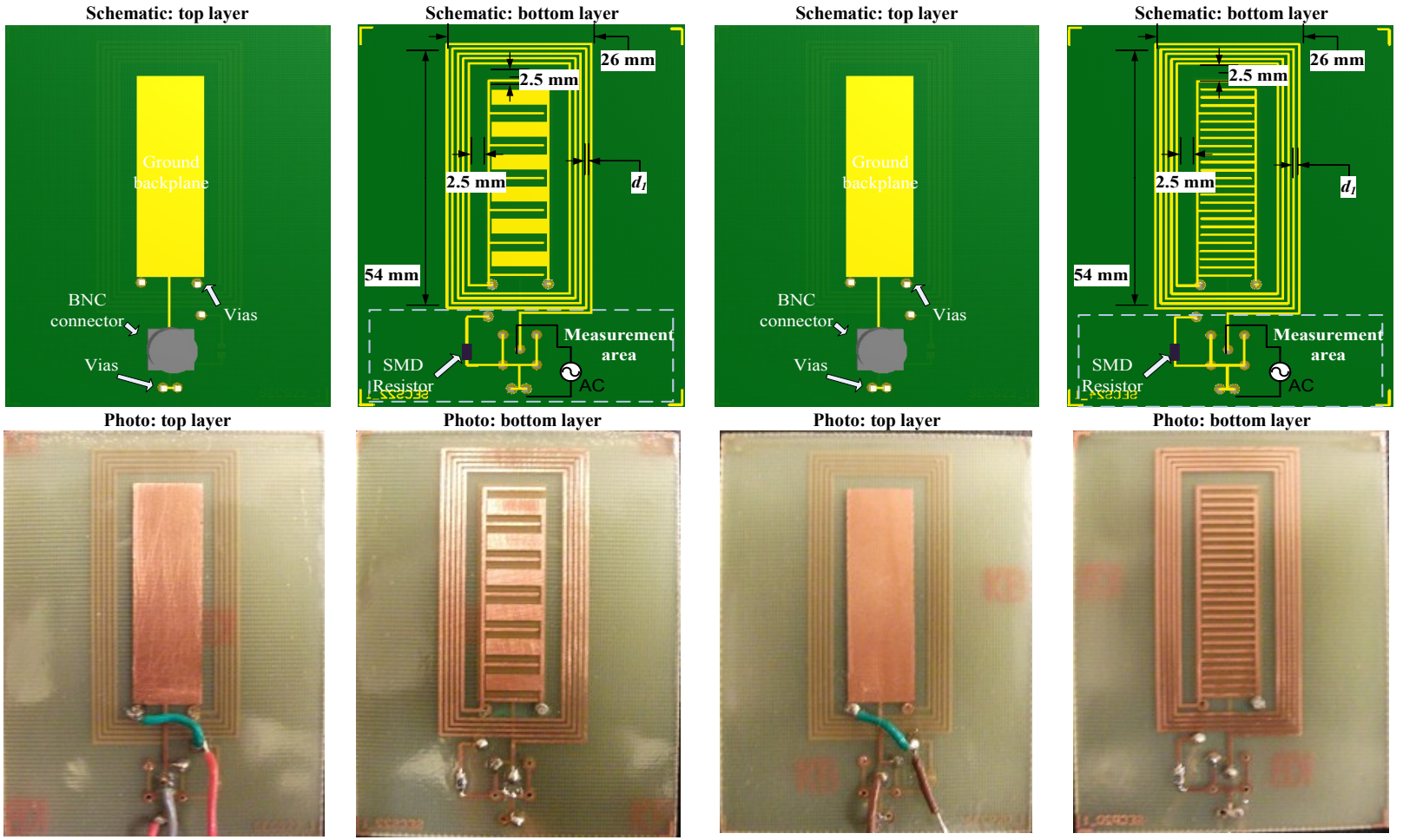

(a) SECS22_1 (b) SECS24_1

Figure 2.10: Schematic diagrams and pictures of (a) SECS22_1 (b) SECS24_1

2.4 Principle of Measurement

The electrical equivalent circuits of SSCP1_1 to SSCP24_1 and SSCS1_1 to SSCS24_1 sensors are shown in Figures 2.11(a) and 2.11(b), respectively. Each sensor is connected to a function generator. Where,

R_g = the output resistance of the function generator with a nominal value of 50 Ω.

R_{mp} = the real part resistance of the exciting coil (meander) for SSCP1_1 to SSCP24_1.

X_{mp} = the imaginary part reactance of the exciting coil (meander) for SSCP1_1 to SSCP24_1.

R_{ms} = the real part resistance of the sensing coil (meander) for SSCP1_1 to SSCP24_1.

X_{ms} = the imaginary part reactance of the sensing coil (meander) for SSCP1_1 to SSCP24_1.

R_{ip} = the real part resistance of the interdigital sensor for SSCP1_1 to SSCP24_1.

X_{ip} = the imaginary part reactance of the interdigital sensor for SSCP1_1 to SSCP24_1.

$R_{mp'}$ = the real part resistance of the exciting coil (meander) for SSCS1_1 to SSCS24_1.

$X_{mp'}$ = the imaginary part reactance of the exciting coil (meander) for SSCS1_1 to SSCS24_1.

R_{is} = the real part resistance of the interdigital sensor for SSCS1_1 to SSCS24_1.

X_{is} = the imaginary part reactance of the interdigital sensor for SSCS1_1 to SSCS24_1.

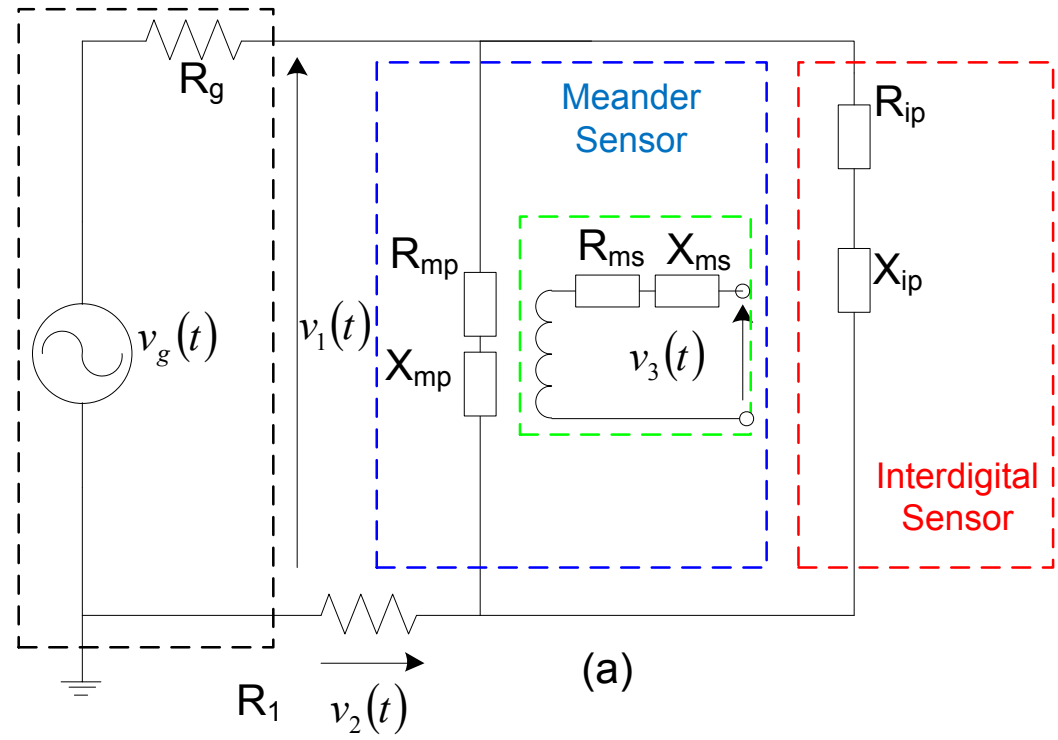

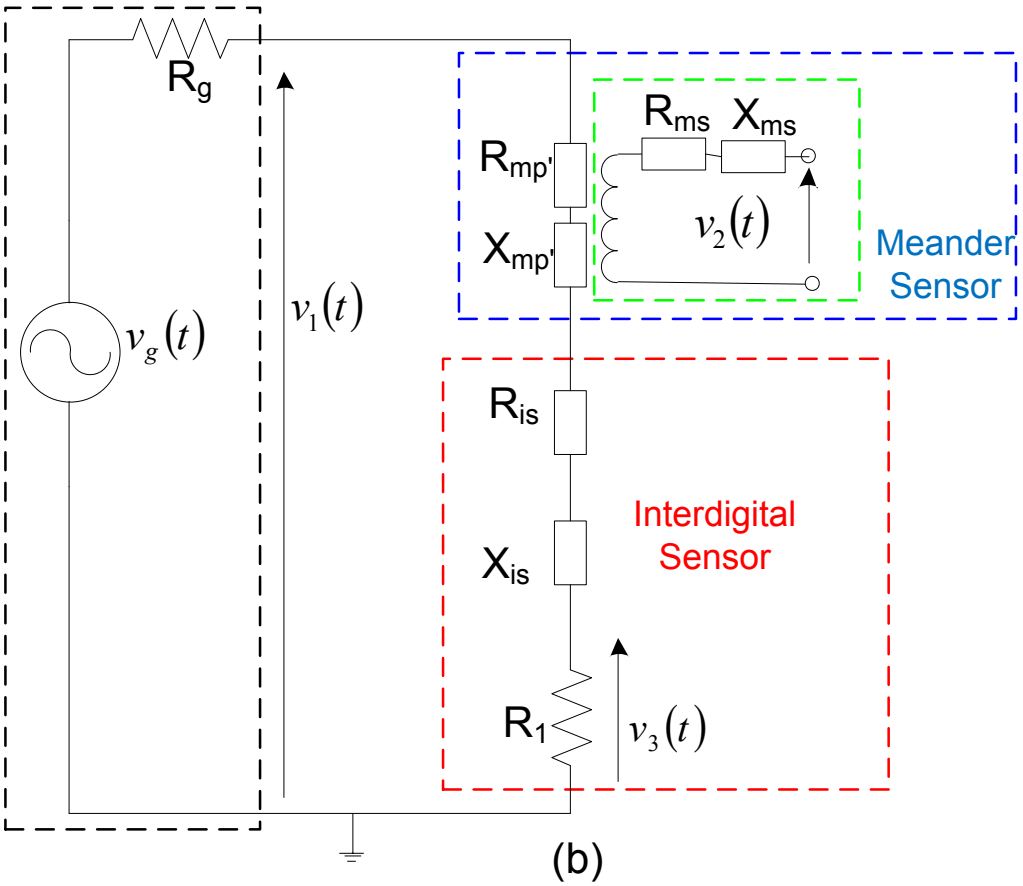

Figure 2.11: The Equivalent circuits for (a) SSCP1_1 to SSCP24_1 (b) SSCS1_1 to SSCS24_1

The electrical equivalent circuits of SECP1_1 to SECP24_1 and SECS1_1 to SECS24_1 sensors are shown in Figures 2.12(a) and 2.12(b), respectively. Where,

R_g = the output resistance of the function generator with a nominal value of 50 Ω.

R_{mp} = the real part resistance of the exciting coil (meander) for the sensors connected in parallel.

X_{mp} = the imaginary part reactance of the exciting coil (meander) for the sensors connected in parallel.

R_{ms} = the real part resistance of the sensing coil (meander).

X_{ms} = the imaginary part reactance of the sensing coil (meander).

R_{ip} = the real part resistance of the interdigital sensor for the sensors connected in parallel.

X_{ip} = the imaginary part reactance of the interdigital sensor for the sensors connected in parallel.

$R_{mp'}$ = the real part resistance of the exciting coil (meander) for the sensors connected in series.

$X_{mp'}$ = the imaginary part reactance of the exciting coil (meander) for the sensors connected in series.

R_{is} = the real part resistance of the interdigital sensor for the sensors connected in series.

X_{is} = the imaginary part reactance of the interdigital sensor for the sensors connected in series.

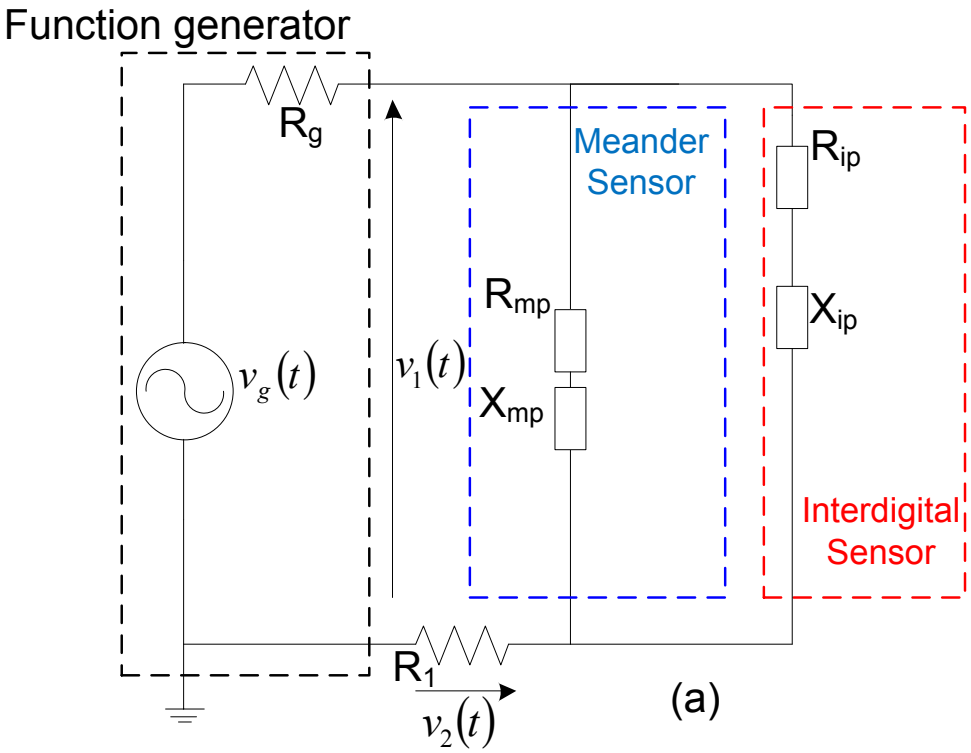

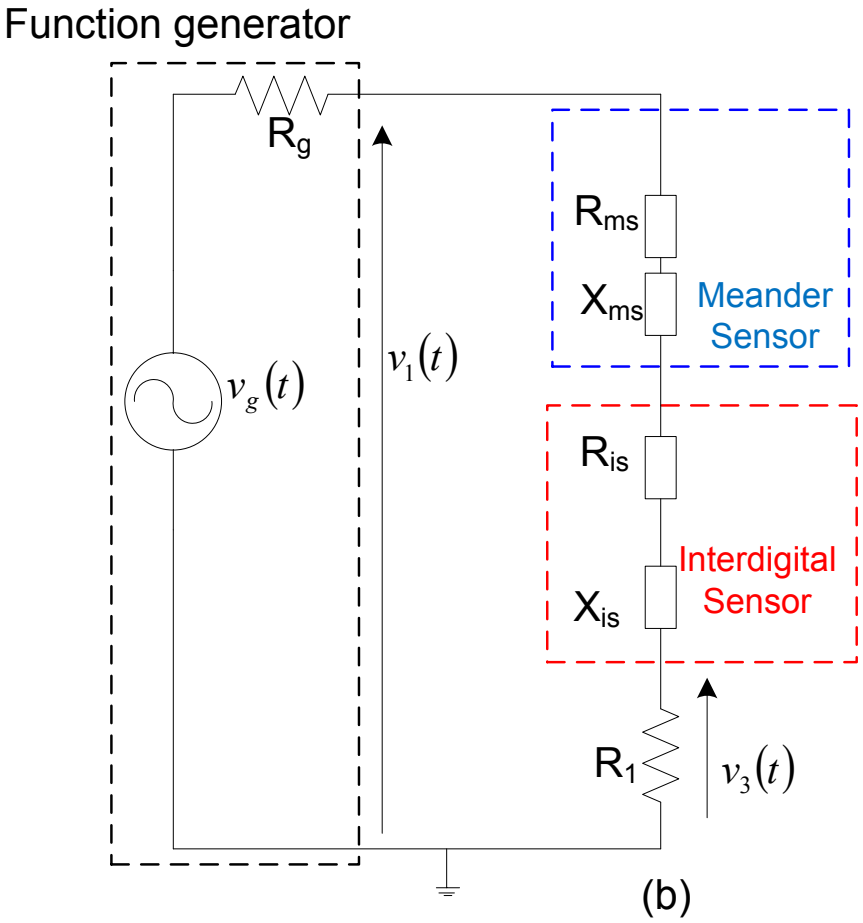

Figure 2.12: The equivalent circuits for (a) SECP1_1 to SECP24_1 (b) SECS1_1 to SECS24_1

For the circuits in Figures 2.11(a) and 2.12(a), the real part (R_{total}) and imaginary (X_{total}) part, can be calculated from:

$$I_1 = V_2 \angle 0° / R_1 \qquad \textbf{2.1}$$

where, I_1 = the rms value of total current that flows through the sensor and

V_2 = the voltage across the surface mount resistor.

R_1 = the series surface mount resistor used to measure the total current through both sensors.

In this case, R_1 value was selected as 100 Ω. Introducing Eq. 2.1 into Eq 2.2 giving Z_{total_p} (the total impedance).

$$Z_{total\_p} = V_1 \angle \theta_1 / I_1 \angle 0° \qquad \textbf{2.2}$$

therefore, R_{total_p} and X_{total_p} are given by:

$$R_{total\_p} = Z_{tota\_p} \cdot \cos(\theta_1) - R_1 \qquad \textbf{2.3}$$

$$X_{total\_p} = Z_{total\_p} \cdot \sin(\theta_1) \qquad \textbf{2.4}$$

where, V_1 = the rms values of input voltage.

θ_1 = the phase difference between $v_1(t)$ with $v_2(t)$ in degree, taking $v_2(t)$ as reference.

For the sensors in Figure 2.11(b) and 2.12(b), R_1 denotes the series surface mount resistor connected to the sensors with the nominal value of 120 kΩ. Hence, R_{total_s} and X_{total_s} can be calculated from:

$$I_1 = V_3 \angle 0^\circ / R_1 \qquad \textbf{2.5}$$

where, I_1 = the rms value of current through the sensor.

V_3 = the voltage across the surface mount resistor. Introducing Eq. 2.5 into Eq 2.6, giving Z_{total_s} (the total impedance)

$$Z_{total\_s} = V_1 \angle \theta_1 / I_1 \angle 0^\circ \qquad \textbf{2.6}$$

θ_1 = the phase difference between $v_1(t)$ with $v_3(t)$ in degree, taking $v_3(t)$ as reference. therefore, R_{tota_s} and X_{total_s} are given by:

$$R_{total\_s} = Z_{tota\_s} \cdot \cos(\theta_1) - R_1 \qquad \textbf{2.7}$$

$$X_{total\_s} = Z_{total\_s} \cdot \sin(\theta_1) \qquad \textbf{2.8}$$

2.5 Conclusion

In total, 96 planar electromagnetic sensors have been fabricated in this research resulted from the different designs of the sensors (meander and interdigital) and the combination of the sensors (meander and interdigital). Design, basic operation, and principle of measurements have been discussed for all 96 sensors. The printed circuit board technology has proven to be a simple and reliable method to construct the sensors. The used of Incralac coating not only provides protection to the sensors but also opens the way for the investigation of planar electromagnetic sensors for environmental monitoring.

CHAPTER 3

Modelling of Sensors: Finite Element Method Simulation

3.1 Introduction

Finite element modelling (FEM) under COMSOL© software offers a powerful numerical tool for solving engineering problems based on partial differential equations. The development of FEM element software capable of modelling electromagnetic phenomenon has given a good insight in characterizing the sensors. In this section, 3D simulations of the sensors using quasi-static time harmonic analysis were established to see the coupling of electric and magnetic fields, calculate the sensors impedances, and the effect of material property changes to sensor's output (impedance: real part and imaginary part). The summary of the modelling steps can be listed as:

- Choosing the 3D, electric and induction current mode
- Drawing the sensor geometry
- Generating the mesh
- Setting the electrical properties parameters and values in the subdomains
- Setting the boundary condition
- Setting the expressions to calculate the impedance of the sensors
- Solving the model to find the electromagnetic fields distribution and calculate the total impedance

COMSOL simulation of planar meander sensor and interdigital sensor can be found from [118] and [119], respectively. This chapter will investigate the capability of the COMSOL© to simulate the selected novel planar electromagnetic sensors having the combination of meander and interdigital sensor.

3.2 Governing Equations

The Maxwell's equations for certain boundary conditions can be applied to the problem of macroscopic level electromagnetic analysis field of study. For quasi-static time harmonic analysis, the governing Maxwell's equations, which explain the Electromagnetic phenomena, can be written as [120]:

$$\nabla \times \vec{H} = \sigma\left(\vec{E} + v \times \vec{B}\right) + \frac{\partial \vec{D}}{\partial t} + \vec{J}^{e} \qquad \textbf{3.1}$$

$$\nabla \times \vec{E} = -\frac{\partial \vec{B}}{\partial t} \qquad \textbf{3.2}$$

$$\nabla \cdot \vec{B} = 0 \qquad \textbf{3.3}$$

$$\nabla \cdot \vec{D} = \rho \qquad \textbf{3.4}$$

$$\nabla \cdot \vec{J} = 0 \qquad \textbf{3.5}$$

where, , $\vec{H}$ = the magnetic field intensity.

$\vec{E}$ = the electric field intensity.

$\vec{B}$ = the magnetic flux density.

$\vec{D}$ = the electric flux density.

$\vec{J}$ = the current density.

$\vec{J}^{e}$ = the external current density.

σ = the electric conductivity.

v = the velocity of the conductor.

ρ = the electric charge density.

Eq. 3.1 and 3.2 are also commonly known as Maxwell-Ampere's law for quasi-static time-harmonic analysis and Faraday's law, respectively. Gauss' law for the electric and magnetic forms are given by Eq. 3.3 and 3.4, respectively. Finally, Eq. 3.5 is the equation of continuity.

All the materials, which constitute the models (sensors and any samples presence), are assumed to be linear and isotropic, therefore, giving constitutive relations that describe the macroscopic properties of the materials as:

$$\vec{\mathrm{D}} = \varepsilon_0(1+\chi_e)\vec{\mathrm{E}} = \varepsilon_0\varepsilon_r\vec{\mathrm{E}} = \varepsilon\vec{\mathrm{E}} \qquad \textbf{3.6}$$

$$\vec{\mathrm{B}} = \mu_0(1+\chi_m)\vec{\mathrm{H}} = \mu_0\mu_r\vec{\mathrm{H}} = \mu\vec{\mathrm{H}} \qquad \textbf{3.7}$$

Where, ε_0 = the permittivity of vacuum equals to 8.854×10^{-2} F/m.

μ_0 = the permeability of vacuum which sets to be $4\pi\times10^{-7}$ H/m.

χ_e = the electric susceptibility.

χ_m = the magnetic susceptibility.

ε_r = the relative permittivity.

μ_r = the relative permeability.

ε = the permittivity.

μ = the permeability.

The formulation of the problems starts with the definitions of the potentials given by the following equations:

$$\vec{\mathrm{B}} = \nabla\times\vec{\mathrm{A}} \qquad \textbf{3.8}$$

$$\vec{\mathrm{E}} = -\nabla\mathrm{V} - \frac{\partial\vec{\mathrm{A}}}{\partial t} \qquad \textbf{3.9}$$

where $\vec{\mathrm{A}}$ is the magnetic vector potential. From Eq. 3.8 and 3.9, the electric and magnetic potentials are not uniquely defined from the electric and magnetic fields. Substituting Eq. 3.6, 3.7, 3.8 and 3.9 into Eq. 3.1 yields:

$$\left(j\omega\sigma - \omega^2\varepsilon_0\varepsilon_r\right)\vec{\mathrm{A}} + \nabla\times\left(\mu_0^{-1}\mu_r^{-1}\times\vec{\mathrm{A}}\right) - \sigma\mathrm{v}\times\left(\nabla\times\vec{\mathrm{A}}\right) + \left(\sigma + j\omega\varepsilon_0\varepsilon_r\right)\nabla\mathrm{V} = \vec{J}^e \qquad \textbf{3.10}$$

where ω is the angular frequency. The new equation of continuity replacing Eq. 3.5 can be obtained by taking the divergence of Eq. 3.10 and can be written as:

$$-\nabla\cdot\left(\left(j\omega\sigma-\omega^2\varepsilon_0\varepsilon_r\right)\vec{\mathrm{A}}-\sigma\mathrm{v}\times\left(\nabla\times\vec{\mathrm{A}}\right)+\left(\sigma+j\omega\varepsilon_0\varepsilon_r\right)\nabla\mathrm{V}\right)=0 \qquad \textbf{3.11}$$

Eq. 3.10 and 3.11 describe the system of equations as second-order equation in time. The time-harmonic analysis can handle this case without much difficulty. At this point, there are 4 physical variables: the electric scalar potential V and three components of the magnetic vector potential Ax, Ay and Az. Here, we can also see that the solution for the system of equations is not unique.

A gauge transformation is introduced to reduce the equations in the system of equation by putting a constraint consisting of a gauge variable $\Psi=-j\mathrm{V}/\omega$. The gauge transformation begins with the introduction of two new potentials:

$$\tilde{\mathrm{A}}=\vec{\mathrm{A}}+\nabla\Psi=\vec{\mathrm{A}}-\frac{j}{\omega}\nabla\mathrm{V} \qquad \textbf{3.12}$$

$$\tilde{\mathrm{V}}=\mathrm{V}-\frac{\partial\Psi}{\partial\mathrm{t}}=\mathrm{V}-\frac{\partial\left(-\frac{j}{\omega}\mathrm{V}\right)}{\partial\mathrm{t}}=\mathrm{V}-\mathrm{V}=0 \qquad \textbf{3.13}$$

Replacing the previous A and V potentials with the new potentials $\tilde{\mathrm{A}}$ and $\tilde{\mathrm{V}}$ into Eq. 3.10 and 3.11, respectively, gives us a unique equation for the subdomains:

$$\left(j\omega\sigma-\omega^2\varepsilon_0\varepsilon_r\right)\tilde{\mathrm{A}}+\nabla\times\left(\mu_0^{-1}\mu_r^{-1}\times\tilde{\mathrm{A}}\right)-\sigma\mathrm{v}\times\left(\nabla\times\tilde{\mathrm{A}}\right)=J^e \qquad \textbf{3.14}$$

Therefore, the magnetic flux density and electric field intensity are expressed with respect to $\tilde{\mathrm{A}}$, resulting:

$$\vec{\mathrm{B}}=\nabla\times\tilde{\mathrm{A}} \qquad \textbf{3.15}$$

$$\vec{\mathrm{E}}=-\frac{\partial\tilde{\mathrm{A}}}{\partial t} \qquad \textbf{3.16}$$

Finally, after the gauge transformation only three physical variables are required which are the three components of magnetic vector potentials $\widetilde{A}_x$, $\widetilde{A}_y$, and $\widetilde{A}_z$.

3.2.1 Boundary Condition

On the boundaries of the outer surface and PCB (printed circuit board) for every sensor model, the continuity condition was considered. The equations of continuity are written as following:

$$n \times \left(\vec{H}_1 - \vec{H}_2\right) = 0 \qquad \textbf{3.17}$$

$$n \cdot \left(\vec{J}_1 - \vec{J}_2\right) = 0 \qquad \textbf{3.18}$$

where n is the outward normal, Eq. 3.17 explains that the tangential component of the magnetic field intensity is continuous and Eq. 3.18 shows that the normal component of the conducting current must be continuous in the case of eddy current field. Considering the practical aspect for the copper track, the impedance boundary condition is applied. The equation is given by:

$$n \times \vec{H} + \sqrt{\frac{\varepsilon - j\frac{\sigma}{\omega}}{\mu}} \cdot n \times \left(\vec{E} \times n\right) = 0 \qquad \textbf{3.19}$$

The other boundaries are the external surfaces of the sensor's environment where the magnetic vector potential is discontinued, given as following:

$$n \times \vec{A} = 0 \qquad \textbf{3.20}$$

and the normal current are also discontinued, giving the equation:

$$n \cdot \vec{J} = 0 \qquad \textbf{3.21}$$

Exceptions were set for two boundaries, each replacing Eq. 3.21 with electric potential condition (V_0) or current input condition (I_0) and electric ground condition ($V = 0$). The induced current in the sensor is calculated by the integration of normal current density on the surface area of the sensor near the ground point which can be written as:

$$I = \int_S \vec{J}.\mathrm{ds} \qquad \textbf{3.22}$$

where ds is a surface element of the surface S. The induced voltage across the sensor is calculated over a number of finite elements. The general approximation is given by:

$$V_{induced} = \sum_{i=1}^{M} \frac{\left(E_x \cdot i_x + E_y \cdot i_y + E_z \cdot i_z\right)_i .N}{A_i} \qquad \textbf{3.23}$$

where, N stands for the number of turns in the conductor (not the number of meander spiral turn). E_x, E_y, and E_z are the electric filed for x, y, and, z component, respectively given in V/m^2 unit, at the i^{th} element. i_x, i_x, and i_z are the current directions at x, y, and, z, respectively, at the i^{th} element Ai is the cross section area at the i^{th} element, given in m^2.

3.2.2 Subdomain Equation

By default, for every sensor model, there are four physical variables: the scalar electrical potential $\tilde{V}$ and the three components of magnetic vector potentials ($\tilde{A}$) $\tilde{A}_x$, $\tilde{A}_y$, and $\tilde{A}_z$. The sensor models can be divided into four subdomains, which are PCB copper tracks, insulating layer (Polytetrafluoroethylene or Teflon), environment (air/ pure water) [121, 122], and Incralac coating film. Incralac is an acrylic coating for copper and bronze. It consists of a solution of methyl methacrylate copolymer incorporating benzotriazole [121, 123, 124]. The domain properties for the sensor models are given in Table 3.1.

Table 3.1: Subdomain parameters of planar electromagnetic sensors.

Subdomain	1	2	3	4
name	PCB copper tracks	PCB insulating layer	Air/Water	Incralac coating film
σ	5.998×10^{7}	0.004	0.8/0.8	1.45×10^{-12}
ε_r	1	4.5	1/82	9
μ_r	1	1	1/1	1
J^e	0	0	0/0	0
v	0	0	0/0	0

3.3 Characterization of the Sensors via Simulation

In order to simulate the characteristic of the sensors and to study the effect of different design parameters such as connection type (parallel or series), number of meander turns, and interdigital design, simulations were accomplished using COMSOL 3.5a on a PC with 2.93 GHz Quad-Duo core processor and 6 GB RAM. The selected sensors are described in this section. A set of illustrations as shown in Figure 3.1(a) depicts the top view (left-hand side) and bottom view (right-hand side) of the parallel combination sensors: SSCP1_1 (case A in Figure 3.1(a)), SSCP17_1 (case B in Figure 3.1(a)), SSCP5_1 (case C in Figure 3.1(a)), SSCP21_1 (case D in Figure 3.1(a)), and SSCP22_1 (case E in Figure 3.1(a)) the sensors consist of meander and interdigital sensors which are placed side by side at 10 mm distance. Table 3.2 summarizes the description of the sensors.

Another set of illustrations as shown in Figure 3.1(b) depict the top view (left-hand side) and bottom view (right-hand side) of series combination sensors: SECS17_1 (case A in Figure 3.1(b)), SECS21_1 (case B in Figure 3.1(b)), and SECS22_1 (case C in Figure 3.1(b)). Each sensor consists of a meander coil spiralling inwards in rectangular form, and the inner end is connected to an interdigital sensor completing a serial connection. Table 3.3 summarizes the description of the sensors.

Table 3.2: Parameters of planar electromagnetic sensors combined in parallel

Sensor type	Parameters			
	Pitch (mm)	Length (mm)	Number of turn (N)	Wavelength, λ (mm)
SSCP1_1	10	40	1	6.6
SSCP5_1	Similar with SSCP1_1 except a ground plane situated on the back of interdigital sensor.			
SSCP17_1	10	40	5 (each turn is 0.5 mm apart)	6.6
SSCP21_1	Similar with SSCP17_1 except a ground plane situated on the back of interdigital sensor.			
SSCP22_1	Similar with SSCP21_1 except the negative electrodes are of 3 mm width.			

Table 3.3: Parameters of planar electromagnetic sensors combined in series

Sensor type	Parameters			
	Length (mm)	Width (mm)	Number of turn (N)	Wavelength, λ (mm)
SECS17_1	10	40	5 (each turn is 0.5mm apart)	6.6
SECS21_1	Similar with SECS17_1 except a ground plane situated on the back of interdigital sensor			
SECS22_1	Similar with SECS21_1 except the negative electrodes are of 3 mm width.			

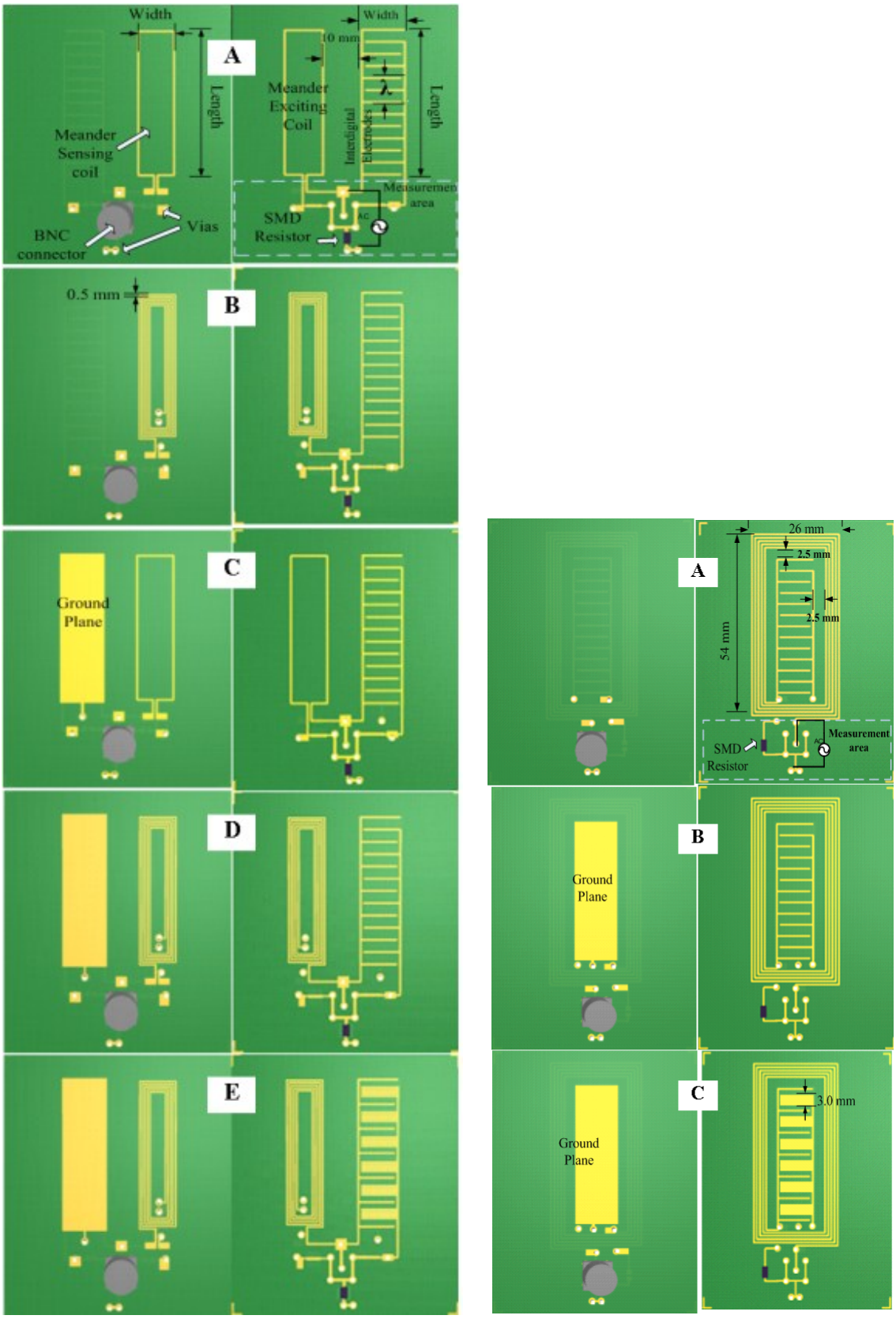

(a) (b)

Figure 3.1: (a) Schematic diagrams of planar sensors connected in parallel (b) Schematic diagrams of planar sensors connected in series

3.3.1 Sensors' Description for Characterization Simulation

The complete descriptions of the selected sensors have been discussed in the previous section. The geometrical configurations of the selected sensors (SSCP1_1 and SECS1_1) are shown in Figure 3.2. All sensors are drawn based on the dimensions taken from Figure 3.1, Table 3.2, and Table 3.3. The quasi-statics electromagnetic equation set of the COMSOL 3.5a electromagnetic module is used for the model in time-harmonic analysis type [120]. Both magnetic and electric properties sets are considered meaning that vector potential $\tilde{A}$ and the scalar electric potential $\tilde{V}$ are the physical unknowns to solve which derived after using a gauge transformation [120] as described in section 3.2. $\tilde{A}$ and $\tilde{V}$ are set to be vector and linear elements, respectively. Eq 3.14 is set to be the subdomain equation.

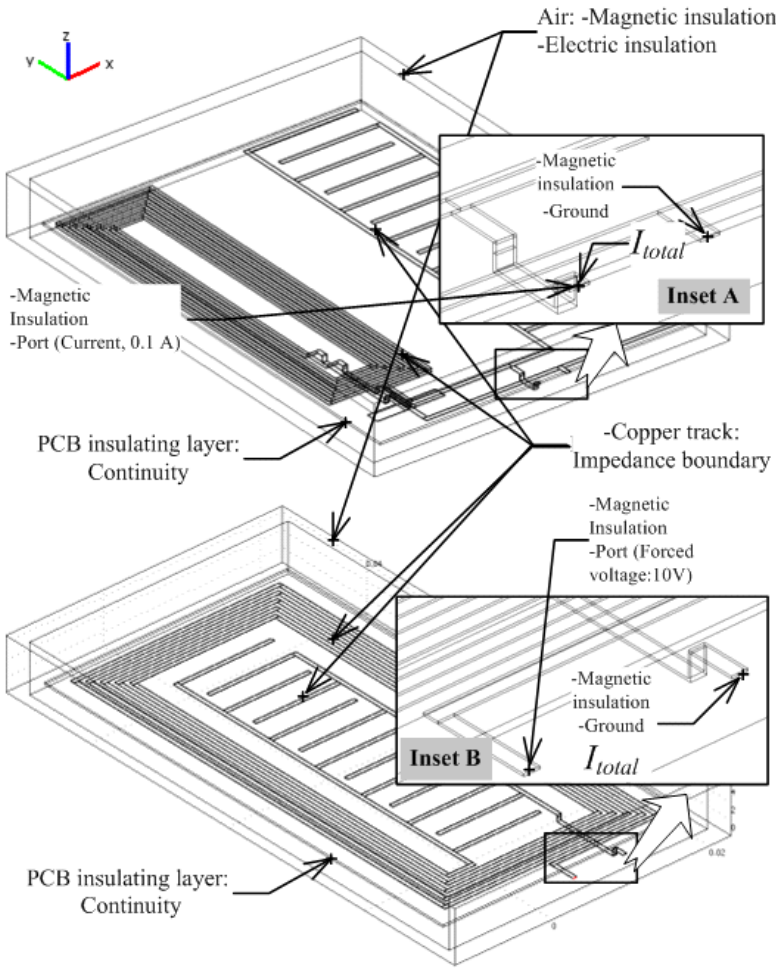

Figure 3.2: 3D-drawing and the boundary condition of SSCP1_1 and SECS1_1

The sensor models can be divided into four subdomains, which are PCB copper tracks, insulating layer (Polytetrafluoroethylene or Teflon), environment (air/ pure water) [121, 122], and Incralac coating film as shown in Figure 3.1. Incralac is an acrylic coating for copper and bronze. It consists of a solution of methyl methacrylate copolymer incorporating benzotriazole [121, 123-125]. All the subdomains use the same and unique system Eq. 3.14. The environment domain properties for the sensor models are set as air as given in Table 3.1.

The PCB copper tracks are subjected to impedance boundary condition, given by Eq. 3.19. Insulating layer dielectric is treated with continuity boundary equations given by Eq. 3.17 and 3.18. The magnetic insulation and electric insulation equations are as given by Eq. 3.20 and Eq. 3.21, respectively. The other boundaries for parallel and serial combination sensors are the input and output boundaries as shown in inset A and B of Figure 3.2. The input boundary requires magnetic insulation equation and port boundary condition. Magnetic insulation equation and ground is applied on the opposite end of the input (output).

For the sensors combined in parallel, the current port boundary condition gives the total impedance of the sensor which derived from Eq. 3.22 and Eq. 3.23, the total impedance is given by:

$$Z_{total\_p} = \frac{1}{Y_{11}} = \frac{V_{induced}}{I} \qquad \textbf{3.24}$$

As for serial combined sensors, the forced voltage boundary condition gives the total impedance of the sensors which is derived from Eq. 3.22 and Eq. 3.23. The total impedance is governed by:

$$Z_{total\_s} = Z_{11} = \frac{V_{induced}}{I} \qquad \textbf{3.25}$$

3.3.2 Characterization of Simulation Results

The simulation results for the parallel sensors are shown in Figure 3.3 where the absolute impedance value was calculated from Eq. 3.24. As a whole, the total impedance increases as the frequency is increasing. From the simulation results, it is concluded that all the parallel sensors possess inductive characterization. SSCP17_1, SSCP21_1, and SSCP22_1 have higher impedance values compared to SSCP1_1 and SSCP5_1 as the latter have less number of turns (total coil resistance).

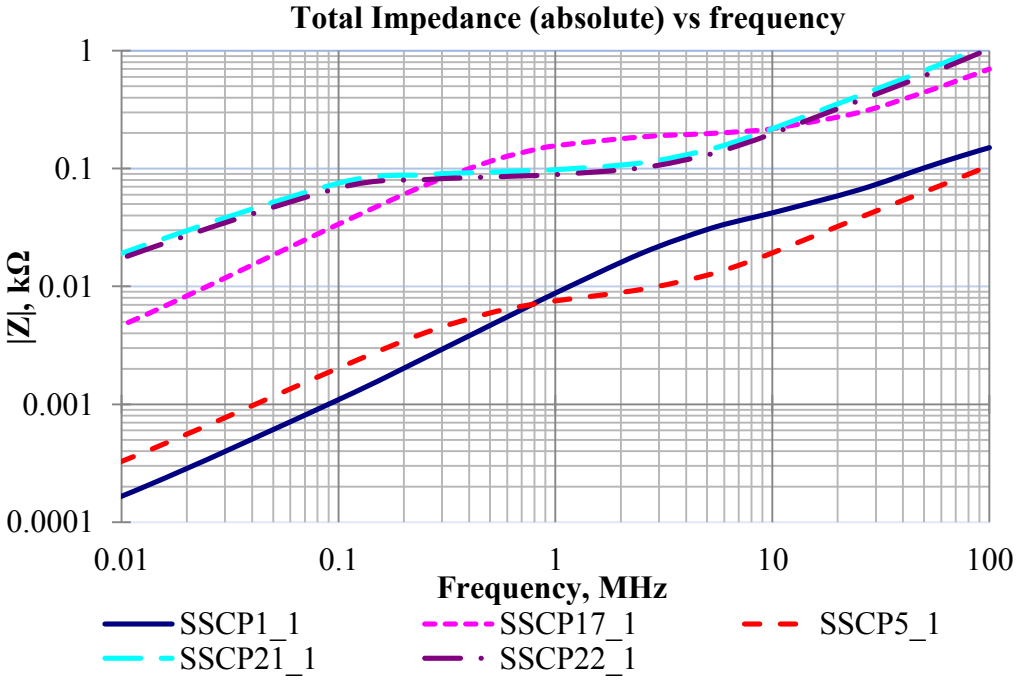

Figure 3.3: Parallel sensors impedance characteristics obtained from simulation results

For the series sensors, the absolute impedance value calculated from Eq. 3.25 reveals that all series sensors impedance values decrease as the frequency is increasing as shown in Figure 3.4. Therefore, the proper classification for all the sensors is capacitive. The introduction of ground plane in SECS21_1 and SECS22_1 causes the absolute impedance value to be less as compared to SECS17_1.

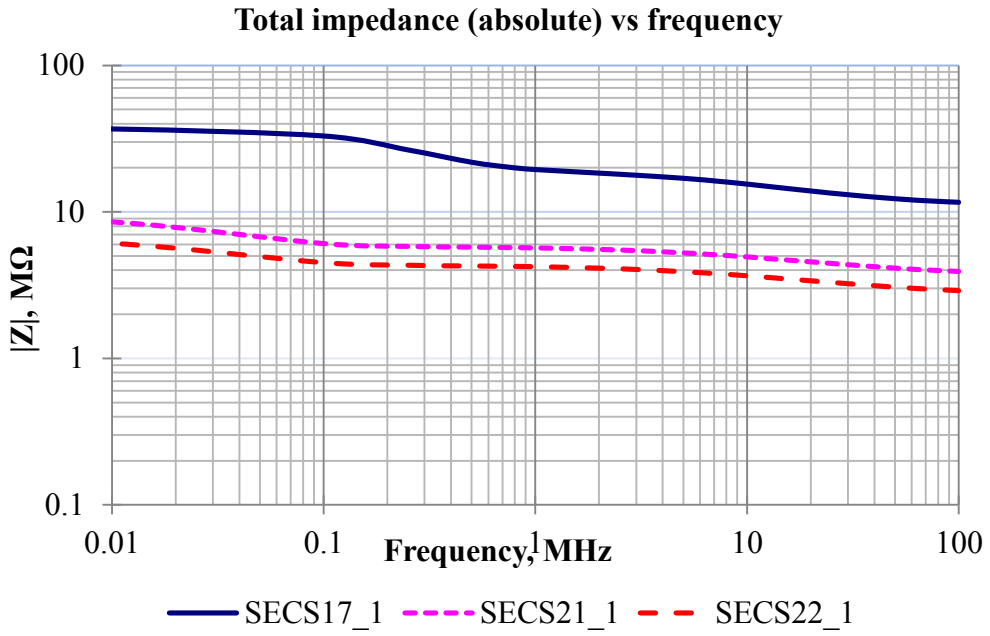

Figure 3.4: Series sensors impedance characteristics obtained from simulation results

3.4 Electromagnetic Fields Simulation and the Effect of Changes in the Electrical Properties of Environment Domain.

In this section, 3D simulations of the sensors using quasi-static time harmonic analysis were established to serve two objectives: the first objective is to understand the coupling phenomena of electric and magnetic fields, and the second objective is to observe the sensor response when the environment domain is set to pure water condition (Milli-Q) while the rest of the properties remains the same as the first one. SECS22_1 was chosen as the sensor of interest as it has been proven the best sensor for nitrate detection in chapter 5.

3.4.1 Sensors' description for electromagnetic fields simulation and electrical properties changes.

As usual there are four physical variables: the scalar electrical potential $\tilde{V}$ and the three components of magnetic vector potentials ($\tilde{A}$) $\tilde{A}_x$, $\tilde{A}_y$, and $\tilde{A}_z$. The sensor's model has also four subdomains, which are PCB copper tracks, insulating layer (Polytetrafluoroethylene

or Teflon), environment domain (air/ pure water) [121, 122], and Incralac coating film. All the subdomains are shown in Figure 3.5 with the same and unique system, Eq. 3.14, at this point. The domain properties for the sensor models are given in Table 3.1.

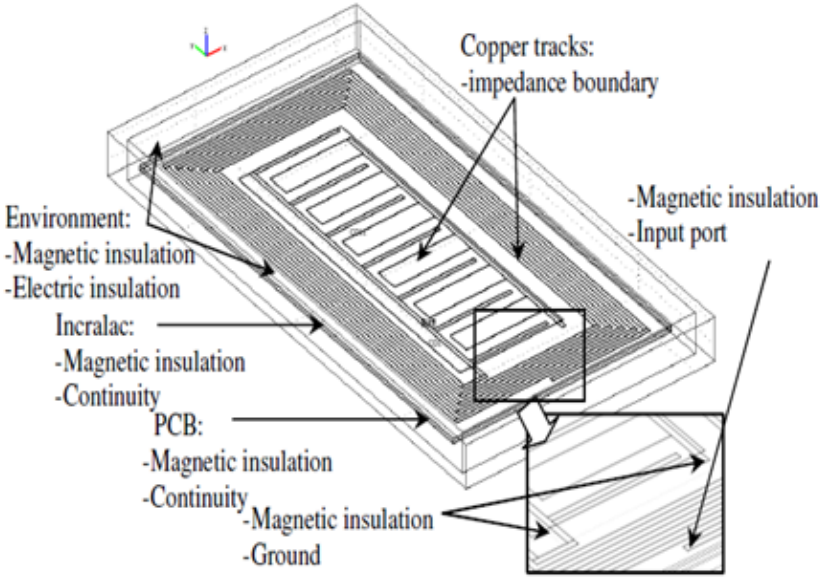

Figure 3.5: 3D-drawing and the boundary condition of SECS22_1

The PCB copper tracks are subjected to impedance boundary condition, given by Eq. 3.19. Insulating layer dielectric is treated with continuity boundary equations given by Eq. 3.17 and 3.18. The magnetic insulation and electric insulation equations are given by Eq. 3.20 and Eq. 3.21, respectively. The other boundaries for SECS22_1 sensor are the input and output boundaries as shown in the inset picture of Figure 3.5. The input boundary requires magnetic insulation equation and port boundary condition. Magnetic insulation equation and ground is applied on the opposite end of the input (output) and ground plane. The calculation of total impedance is given by Eq. 3.25.

3.4.2 Simulation Results for the Simulations of Electromagnetic Fields and Electrical Properties Changes

The magnetic flux density, B and the electric field intensity, E are expressed with respect of $\tilde{A}$ given by Eq. 3.15 and 3.16, respectively. The model was simulated between 1 kHz and 100 MHz. Figures 3.6 and 3.7 depict the solution of the sensor model for 500 kHz, Figure 3.6 shows that the electric potential distribution on the sensor and the magnetic

flux density distribution around the sensor represented by the “tube streamline”. As shown in Figure 3.6, the flux is largest around the meander planar turns. Figure 3.7 depicts the electric field distribution of electric field around the sensor where the electric field is represented by the “tube streamlines”.

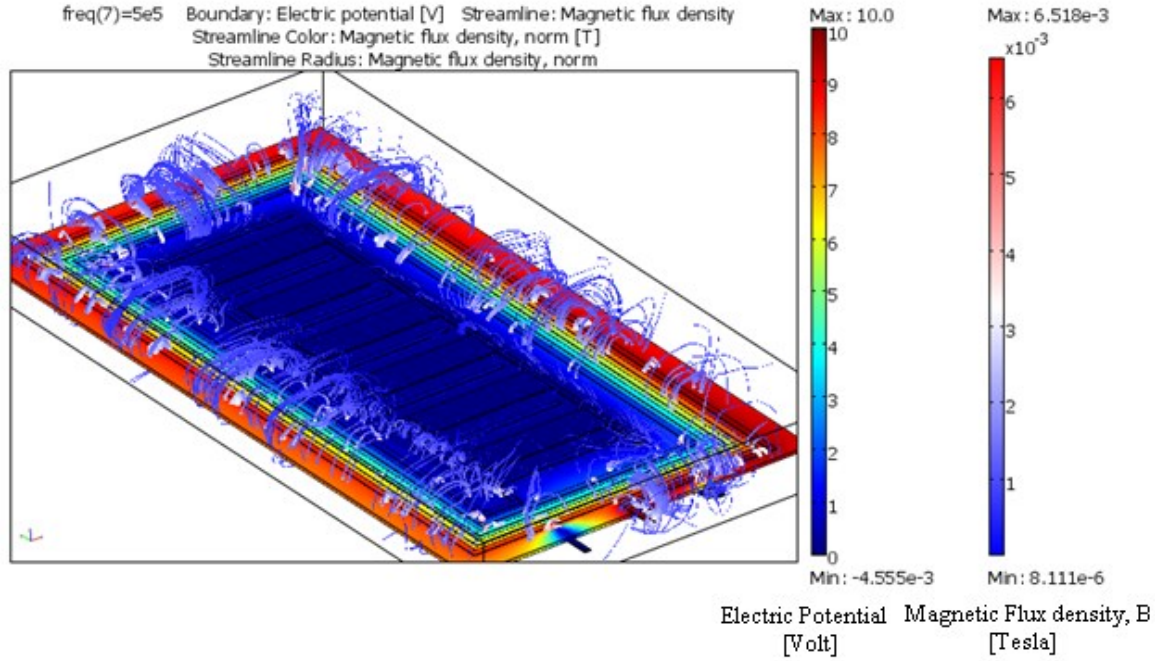

Figure 3.6: Electric potential and magnetic field distributions

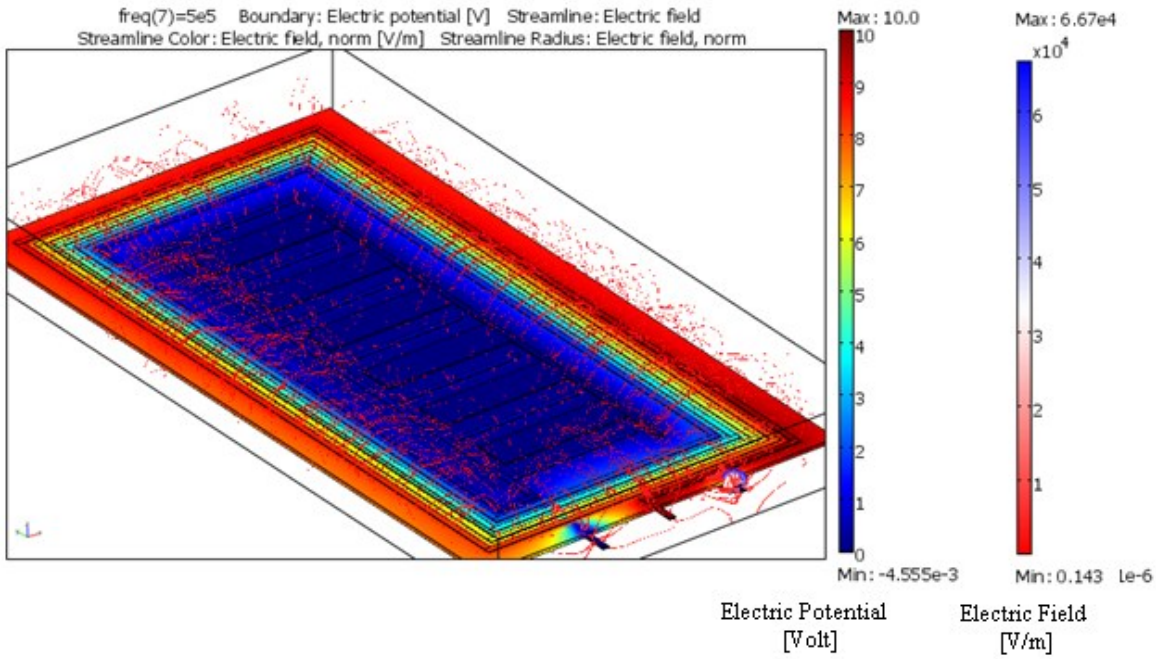

Figure 3.7: Electric potential and electric field distribution

The electric field lines are abundantly available and clearly visible on the surface of the meander turns. The electric fields terminate at the interdigital sensor area where the electric potential distribution value is the lowest. The low potential distribution of the sensor in the middle is being contributed by the ground back plane as can be seen from Figure 3.7.

The environment domain was set as pure water (σ = 0.8 and ε_r = 82) for the simulation of the effect of electrical properties of the environment domain. The simulation was also conducted at a frequency range between 1 kHz and 100 MHz. The Nyquist (complex impedance plane) plot in Figure 3.8 shows that the real part (Z') decreases with the increasing frequency, and the imaginary part (Z'') has a peak at 30 kHz. The simulation to calculate the response of the sensor to the decrease of electrical conductivity while the relative permittivity remains the same, and to the increase of relative permittivity while the electrical permittivity remains the same, have been conducted using the above model. However, it was difficult to get a good response because of the dominance of the inductive part as the capacitance part (electric field) is expressed with respect to magnetic vector potentials, $\tilde{A}$ (Eq. 3.16).

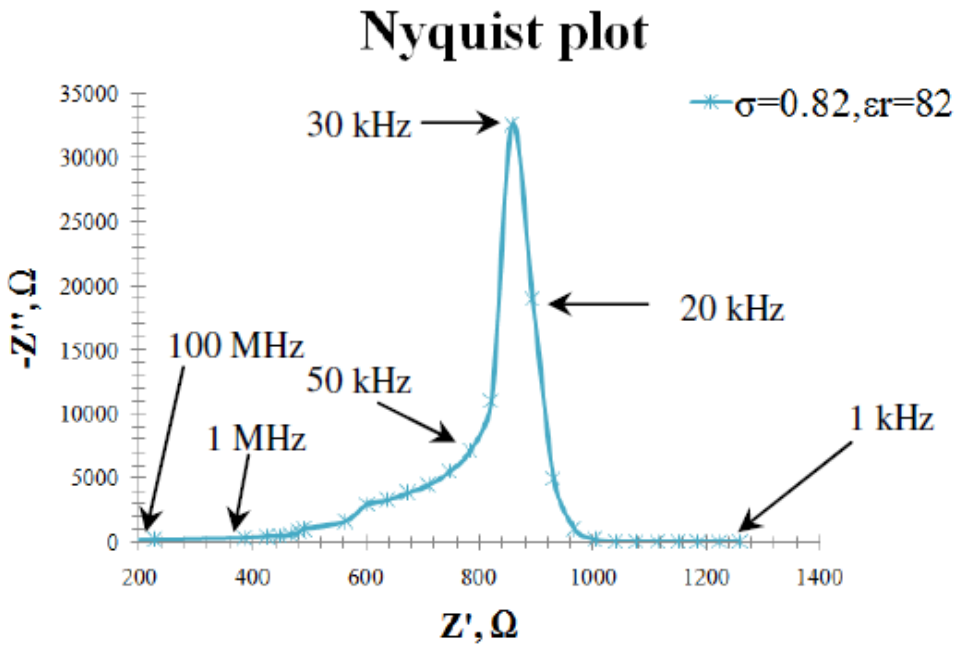

Figure 3.8: Impedance response of the sensor to water using electric and induction currents model on a Nyquist plot

Therefore the model was reduced by taking into account of the effect of electric field (electric current) only. As a result, the electric field is curl free and can be assign a scalar potential V when induction is disregarded. The equation of the subdomains then becomes:

$$-\nabla \cdot \left(\left(\sigma + j\omega \varepsilon_r \varepsilon_0 \right) \nabla V \right) = 0 \qquad \textbf{3.26}$$

The PCB copper tracks, insulating layer, and coating layer are subjected to continuity boundary condition of equation (8). The input boundary requires port boundary, and the output boundary was set to ground. The impedance is calculated as discussed in section 3.4.1. The electric field is obtained from the gradient of scalar potential, V:

$$\vec{\mathrm{E}} = -\nabla \mathrm{V} \qquad \textbf{3.27}$$

The addition of aqueous solution into the environment results in changes of permittivity and conductivity of the environment. The aqueous solution will respond to the applied electric field by redistributing its electrons and protons, positive charges being attracted towards the negative electrode and vice-versa, thus changing the total impedance of the sensor. Therefore, the total impedance of the sensor will be determined by the content of aqueous solution involved. Figure 3.9 depicts the Nyquist plot when the environment was set to pure water and a capacitive semicircle can be seen from the Figure. When ε_r is fixed at 82 and σ is decreased between 1.45×10^{-12} (set to be the lowest conductivity, i.e. coating film) and 145, the complex spectra shrink to a smaller semicircle as illustrated in Figure 3.10. The change of the electrical conductivity value seems to have a significant effect on the sensor's response. Under the situation when σ is fixed at 1.45×10^{-12} and ε_r is decreased between 82 and 16, there is a slight deviation on the rest of the spectra as a comparison to the initial value ($\sigma = 1.45\times10^{-12}$ and $\varepsilon_r = 82$). There is a significant change when the relative permittivity value was changed from 82 to 42 and lower. However, the changes between $\varepsilon_r = 41$ and $\varepsilon_r = 16$ are not proportional as illustrated in Figure 3.11.

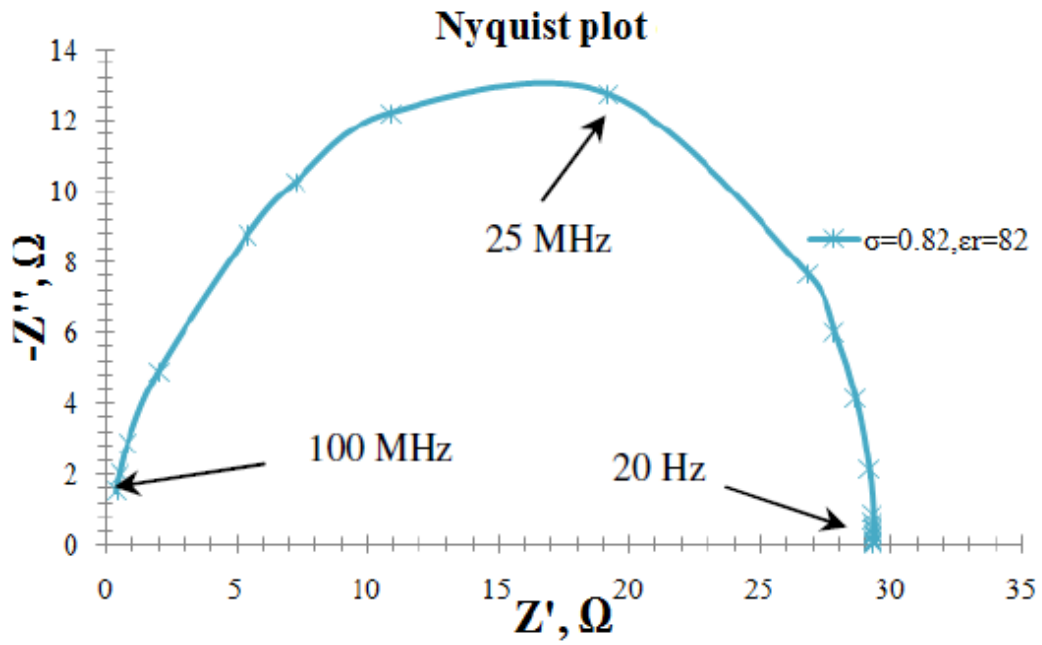

Figure 3.9: Nyquist plot of impedance curve of pure water using electric current model

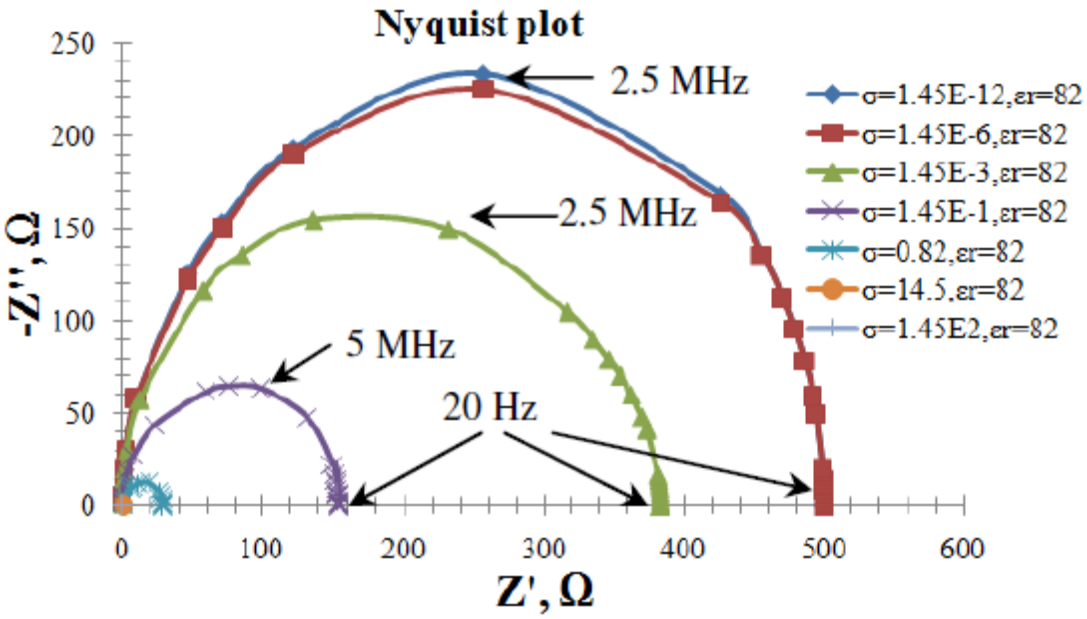

Figure 3.10: Nyquist plot of impedance curves with different water different σ values

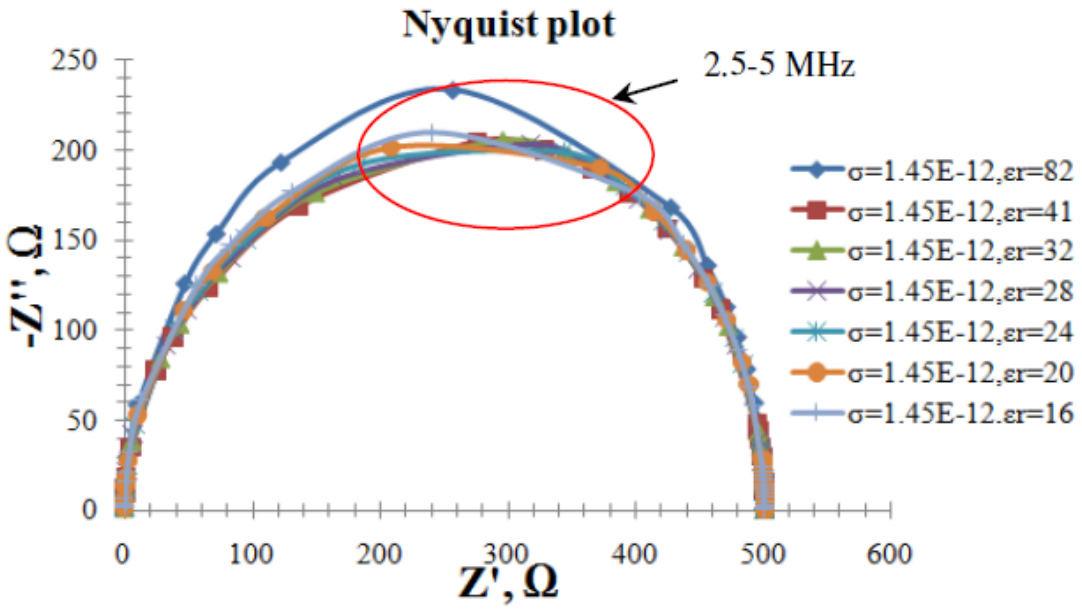

Figure 3.11: Nyquist plot of impedance curves with different water different ε_r values

3.5 Conclusion

In this chapter, the modelling of the sensor based on quasi-statics electromagnetic time harmonic analysis is presented. The effect of different parameter designs has been investigated, the results concluded, there are strong relationships between the sensors' characteristic and the sensors' response with connection type, number of meander turns, interdigital electrode configuration, and the introduction of negative back plane. Therefore, in the future, optimal design can be made based on the simulation results. The electromagnetic field simulation has shown that the combination of meander and interdigital element formed a different distribution of electrical field as compared to independent interdigital sensor. At first, it was expected that the electrical field will only be distributed in the intergital area (between the interdigital electrodes), but it was not the case, because SECS22_1's meander coils also act as an extended drive electrode, while the negative back plane also extended the ground electrode. The simulation of the response of SECS22_1, which has been determined as the best from the experiment with electrical properties changes has been discussed. The results have shown that the variation of electrical conductivity values of the environment domain greatly change the output response of the sensor.

CHAPTER 4

Characterization of the Sensors and the Experimental Setup

4.1 Introduction

All the fabricated sensors are described in chapter 2. The sensors characteristics of the sensors were determined by calculating the total impedance (absolute) of the sensors at different frequencies between 100 Hz and 100 MHz when no material is placed near the sensor (air).

4.2 Experimental Setup and LabView Program

The experimental setup involved a frequency waveform generator where the standard sinusoidal waveform with 10 Volts peak-to-peak value was set as the input signal for the sensors. An old microscope was used as a platform for the sensors. The Agilent 54622D mixed signal oscilloscope was interfaced to a PC, and then, the output signals and the sensors' impedance were recorded and calculated consecutively using developed programs using the *LabView* software. The Figures of the experimental setup and the caption of the developed *LabView* program are shown in Figures 4.1 and 4.2, respectively.

The *LabView* program consists of five parts: (a) the main controls, (b) the oscilloscope controls, (c) the function generator controls, (d) the displays, and (e) the controls to save the recorded data as can be seen in Figure 4.2. Figure 4.3 shows the *LabView* block function to calculate the impedance and phase shift.

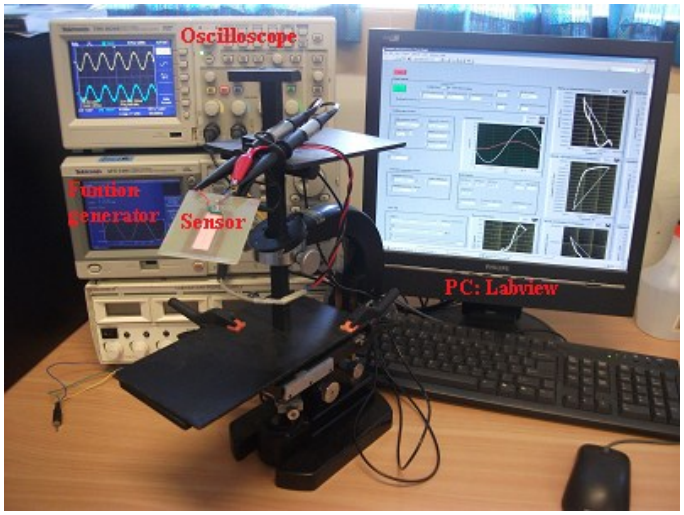

Figure 4.1: The experimental setup

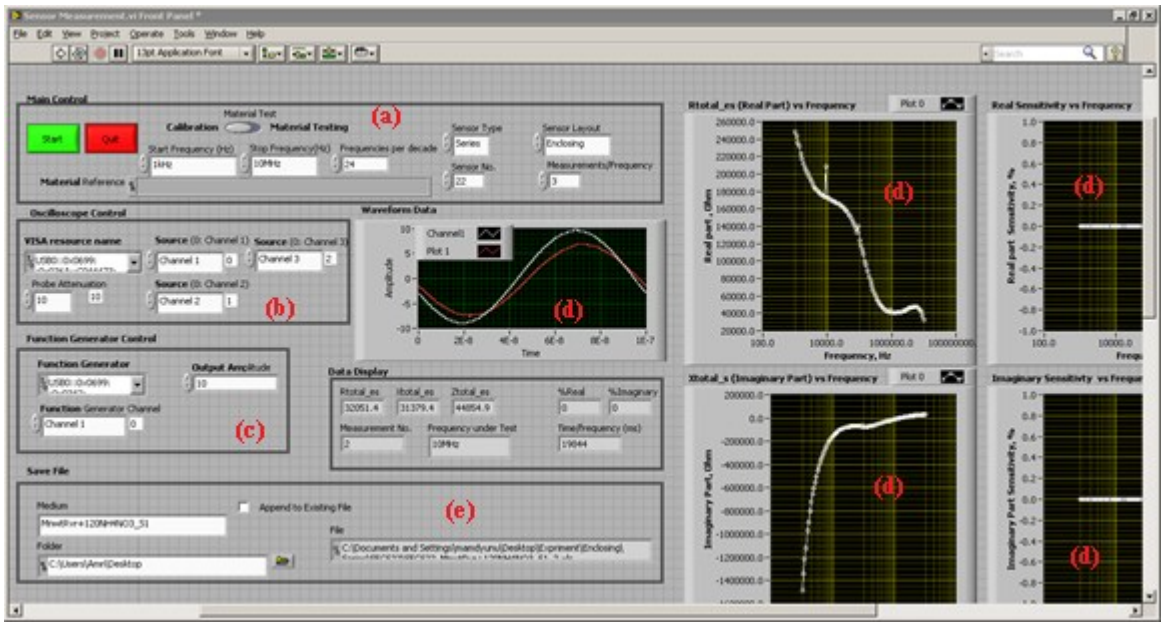

Figure 4.2: The front panel of the LabView program

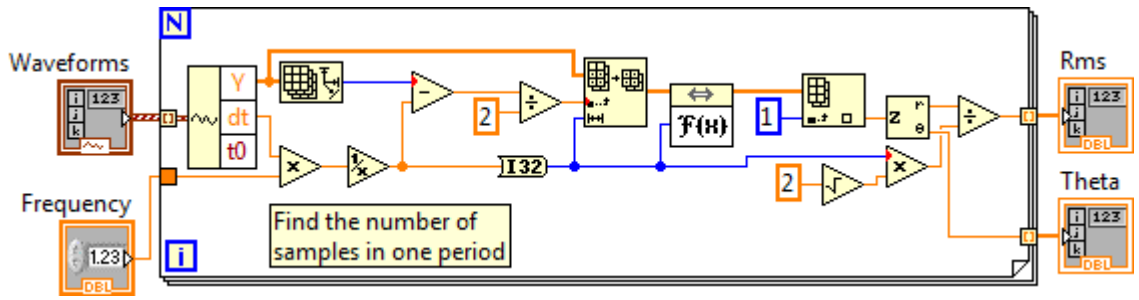

Figure 4.3: Block function to calculate the waveform's amplitude in RMS and phase angle in radian

Given a wave form, the phase angle, θ and V amplitude given in root mean square (*RMS*) of a given frequency are found by calculating the number of samples in a single period of the desired frequency according to the following equation:

$$\frac{Samples}{cycle} = \frac{1}{t_{samplerate} \times f_{desiredfrequency}} \qquad \textbf{4.1}$$

Then, one wave cycle is extracted from the waveform by taking half the number of samples per cycle from each side of the centre. Fourier transform is applied on the result. Because the window size covers exactly one period of the given frequency, it represents the fundamental frequency. This is element 1 in the Fourier transform results, (Element 0 is the DC component of the signal), as described by the following equation:

$$F_n = \sum_{k=0}^{N-1} f_k e^{-\frac{2\pi i n k}{N}} \qquad \textbf{4.2}$$

Where N is the number of sample and f_k is the data point (where $k = 0,\ldots,N-1$). The result is expressed in amplitude and phase by converting it into polar form, and then scaled by $1/\sqrt{2}\,\mathrm{N}$ to convert them to *RMS*. Scaling the result is not actually necessary as it cancels out later because we are only interested in the gain. Once the amplitude and phase angle have been found for the input (V_1) and output (V_2/V_3), the gain and phase shift to calculate the impedance can be found. An array of V amplitudes (RMS) and phase angle (θ) are passed to the *LabView* function to calculate the impedance as shown in Figure 4.4. The input voltage, V_1 and output voltage, V_2/V_3 are split up, and the output (V_2/V_3) is scaled with the calibration value found for the particular frequency that is being measured.

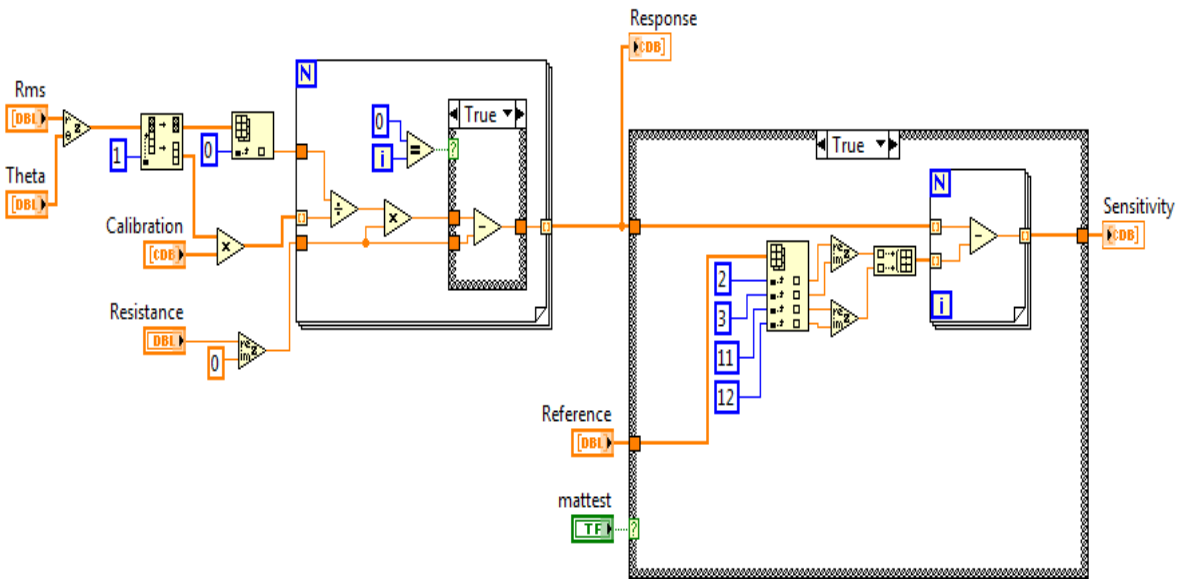

Figure 4.4: Block function to calculate the impedance

Finally, the total impedance in polar form can be calculated from:

$$Z\angle\theta = \left(V_{input}\angle\theta_{input} / V_{output}\angle\theta_{ouput}\right) \times R \qquad \textbf{4.3}$$

where, V_{input} = the *RMS* value of the input signal (V_1).

θ_{input} = the phase angle of the input signal.

V_{output} = the *RMS* value of the output signal measured across the series resistor (V_2/V_3).

θ_{output} = the phase angle of the output signal measured across the series resistor.

R = the resistance value of the series resistor.

4.3 Characteristics of the Sensors with Parallel Connection

Figures 4.5 and 4.6 illustrate the the impedance characterization of SSCP1_1 to SSCP24_1 and SECP1_1 to SECP24_1, respectively. In general, for each of the meander and interdigital sensor connected in parallel, the impedance increases with the increasing frequency and drops after a high frequency point, making the meander sensor with inductive characteristic as dominant and the capacitive part starts to appear after a high-frequency point.

As for SSCP1_1 to SSCP16_1, the maximum impedance amplitudes, which represent the transition points from inductive state to capacitive state, can be found at around 70 MHz. The magnitude of the impedance is basically increased when the number of meander turns increased, as can be seen between Figure 4.5 (a) and Figure 4.5 (b). The different maximum impedance values between the sensors of SSCP1_1 to SSCP16_1 are caused by the different designs of interdigital sensors and the introduction of the negative backplane. For SSCP17_1 to SSCP24_1, the maximum impedance values are consistently reduced between just over 300 Ω and 400 Ω, when the meander sensor with the total number of turns of five was introduced, as illustrated by Figure 4.5(c). For every sensor (SSCP17_1 to SSCP24_1), the transition point is moved to the same frequency between 40 MHz and 50 MHz.

However, the different designs of SECP1_1 to SECP24_1, have no significant systematic changes to the impedance values response and transition points, as can be seen in Figure 4.6.

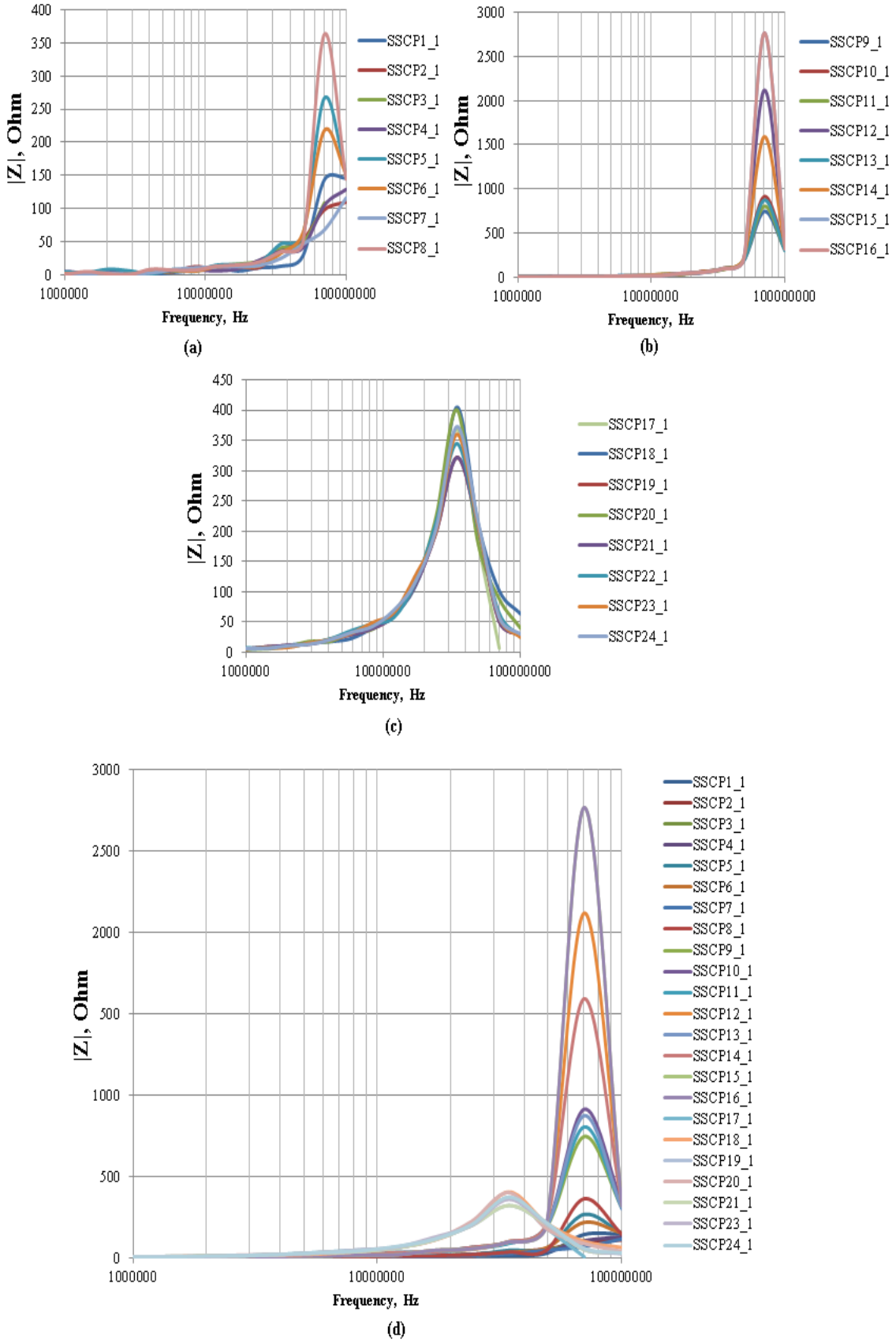

Figure 4.5: Impedance characterization of (a) SSCP1_1 to SSCP8_1, (b) SSCP9_1 to SSCP16_1, (c) SSCP17_1 to SSCP24_1, and (d) SSCP1_1 to SSCP24_1

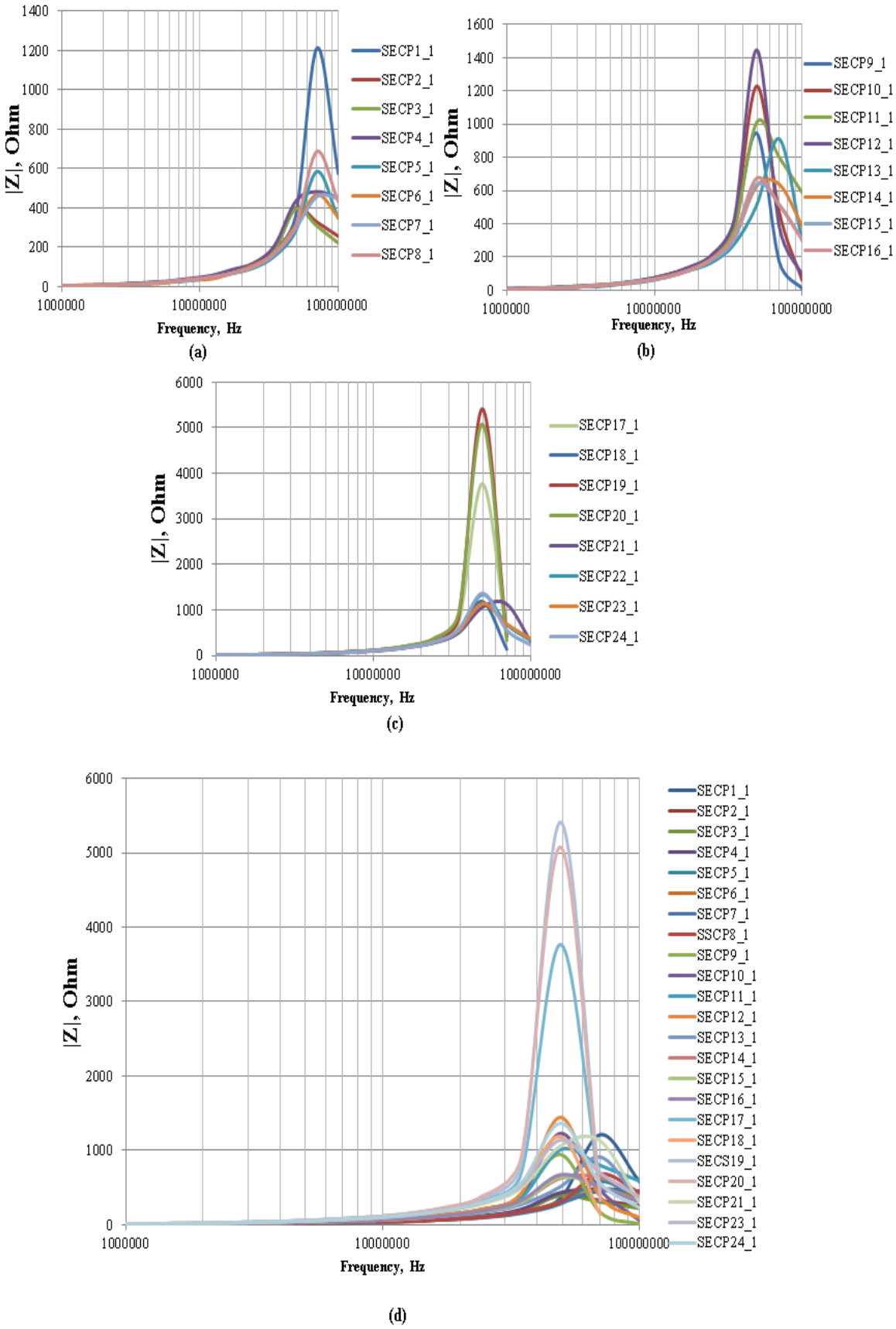

Figure 4.6: Impedance characterization of (a) SECP1_1 to SECP8_1, (b) SECP9_1 to SECP16_1, (c) SECP17_1 to SECP24_1, and (d) SECP1_1 to SECP24_1

The effect of the designs of the sensors on the electrical parameters of the sensors, is investigated by establishing an equivalent electrical circuit as can be seen in Figure 4.7 [126]. The circuit consists of total inductance (L), total capacitance (C), total resistive losses (R_1) and total resistance (R_2). The values of the electrical parameters in Figure 4.7 are estimated for each sensor from the real part and imaginary part responses using the EIS spectrum analyser software [127].

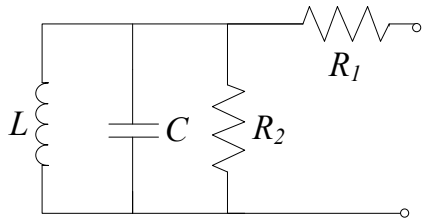

Figure 4.7: Circuit representation of the sensors combined in parallel

Tables 4.1 and 4.2 summarize the electrical parameters values of SSCP and SECP, respectively. For all the SSCP and SECP sensors, the average total resistive losses, R_1 value is relatively low, i.e. between 1.4×10^{-6} Ω to just below 10 Ω. The total resistance average value, R_2 is basically increased with the number of meander turns but significantly reduced when the negative backplane is introduced for SSCP sensors as summarized in Table 4.1. Moreover, the inductance value and capacitance value are relatively high for the sensors that have the most number of meander turns and negative backplane. However, SECP sensors show inconsistency, where most of the electrical parameters seems to be uncorrelated with the improvement in the designs.

It has been proven in [128, 129] that the signal strength and sensitivity of the planar electromagnetic sensors can be improved by achieving a design with the highest electrical parameter (total effective capacitance). Therefore, the best parallel connected planar electromagnetic sensors are among SSCP21_1 to SSCP24_1, as suggested by the data in Table 4.1, where the capacitance and inductance values are the highest as compared to other planar electromagnetic sensors connected in parallel.

Table 4.1: Electrical parameters values of SSCP1_1 to SSCP24_1

		Meander: One turn		Meander: Three turns		Meander: Five turns	
		No negative backplane	With negative backplane	No negative backplane	With negative backplane	No negative backplane	With negative backplane
Interdigatal: type 1		**SSCP1_1**	**SSCP5_1**	**SSCP9_1**	**SSCP13_1**	**SSCP17_1**	**SSCP21_1**
	R_1, Ω	0.729833333	0.9269	0.98301	0.30663	1.371	1.384
	R_2, Ω	190.4933333	176.1	493.7	115.5	1289	902
	C, F	4.91E-11	5.99E-11	1.92E-11	3.26E-11	9.70E-13	3.79E-11
	L, H	1.32E-08	6.59E-08	2.20E-07	1.35E-07	5.20E-07	9.51E-07
Interdigatal: type 2		**SSCP2_1**	**SSCP6_1**	**SSCP10_1**	**SSCP14_1**	**SSCP18_1**	**SSCP22_1**
	R_1, Ω	1.009	0.76603	1.085	0.0015997	1.349	1.676
	R_2, Ω	93.26	167.8	1591	230	1331	608.6
	C, F	2.38E-11	1.49E-10	1.00E-10	2.05E-11	1.49E-11	3.68E-11
	L, H	8.45E-08	3.07E-08	2.15E-07	1.05E-07	5.36E-07	1.08E-06
Interdigatal: type 3		**SSCP3_1**	**SSCP7_1**	**SSCP11_1**	**SSCP15_1**	**SSCP19_1**	**SSCP23_1**
	R_1, Ω	0.8475	0.50674	0.23508	1.199	0.51715	1.747
	R_2, Ω	379.4	19.08	116.1	2849	1378.2	608.1
	C, F	9.66E-11	2.03E-10	2.57E-11	1.18E-10	2.56E-11	1.95E-10
	L, H	3.76E-08	4.15E-08	4.54E-08	1.91E-07	3.23E-07	6.25E-07
Interdigatal: type 4		**SSCP4_1**	**SSCP8_1**	**SSCP12_1**	**SSCP16_1**	**SSCP20_1**	**SSCP24_1**
	R_1, Ω	1.347	0.46755	0.63147	1.371	1.369	1.684
	R_2, Ω	90.48	177.9	594	641.2	1071	447
	C, F	3.22E-11	1.31E-10	8.07E-12	1.88E-11	1.15E-11	2.39E-11
	L, H	7.44E-08	4.35E-08	2.80E-07	2.22E-07	7.09E-07	7.67E-07

Table 4.2: Electrical parameters values of SECP1_1 to SECP24_1

		Meander: One turn		Meander: Three turns		Meander: Five turns	
		No negative backplane	With negative backplane	No negative backplane	With negative backplane	No negative backplane	With negative backplane
Interdigatal: type 1		**SECP1_1**	**SECP5_1**	**SECP9_1**	**SECP13_1**	**SECP17_1**	**SECP21_1**
	R_1, Ω	7.20E+00	0.30245	0.1251	1.264	0.2497	0.12348
	R_2, Ω	328.1	195.8	50.57	1775	182.8	174.1
	C, F	3.33E-11	3.16E-12	8.31E-11	7.61E-12	1.71E-11	1.10E-11
	L, H	1.31E-07	2.37E-07	1.49E-07	9.92E-07	3.76E-07	1.64E-07
Interdigatal: type 2		**SECP2_1**	**SECP6_1**	**SECP10_1**	**SECP14_1**	**SECP18_1**	**SECP22_1**
	R_1, Ω	1.081	0.2358	1.184	0.52311	1.59	1.61
	R_2, Ω	824.1	112.5	1058	208.1	1552	1299
	C, F	1.57E-11	1.53E-11	9.76E-12	5.16E-12	8.77E-12	6.71E-12
	L, H	6.32E-07	1.45E-07	1.07E-06	3.95E-07	1.63E-06	1.51E-06
Interdigatal: type 3		**SECP3_1**	**SECP7_1**	**SECP11_1**	**SECP15_1**	**SECP19_1**	**SECP23_1**
	R_1, Ω	1.064	0.25094	1.274	0.10133	1.45	0.23678
	R_2, Ω	617.1	129.6	3703	70.46	1892	186.5
	C, F	1.84E-11	1.14E-12	8.04E-12	5.64E-12	9.24E-12	7.01E-13
	L, H	5.34E-07	1.54E-07	1.07E-06	1.16E-07	1.58E-06	2.64E-07
Interdigatal: type 4		**SECP4_1**	**SECP8_1**	**SECP12_1**	**SECP16_1**	**SECP20_1**	**SECP24_1**
	R_1, Ω	1.077	1.344	1.40E-06	0.24561	1.827	1.36
	R_2, Ω	4987	510.5	52.03	121.6	1157	952.7
	C, F	1.35E-11	1.02E-11	4.35E-12	8.62E-12	9.01E-12	7.12E-12
	L, H	6.36E-07	5.35E-07	3.77E-06	1.79E-07	1.85E-06	1.61E-06

4.4 Characteristics of the Sensors with Series Connection

Figures 4.8 and 4.9 depict the the impedance characterization of SSCS1_1 to SSCS24_1 and SECS1_1 to SECS24_1, respectively. In general, for most of the meander and interdigital sensor connected in series, a U-shaped impedance characteristic was obtained as shown in Figure 4.8 and 4.9. The right-half and left–half curves show that most of the sensors are capacitive at a low-frequency range and inductive at a high-frequency range, respectively. It is seen that, within a certain frequency range, the sensor shows the combined effect of inductive and capacitive response.

As for SSCS1_1 to SSCS24_1, the frequency range, which represents the combined effect of inductive and capacitive response, can be found at between around 100 kHz to 30 MHz. The introduction of negative backplane basically causes the frequency range of inductive-capacitive state to be narrower, and the impedance values to be increased as can be seen from Figure 4.8 (a), (b), and (c).

Similar results are obtained for SECP sensors as compared to SSCS sensors, where the differentiation between the sensors with and without the negative backplane can be clearly seen as shown in Figure 4.9.

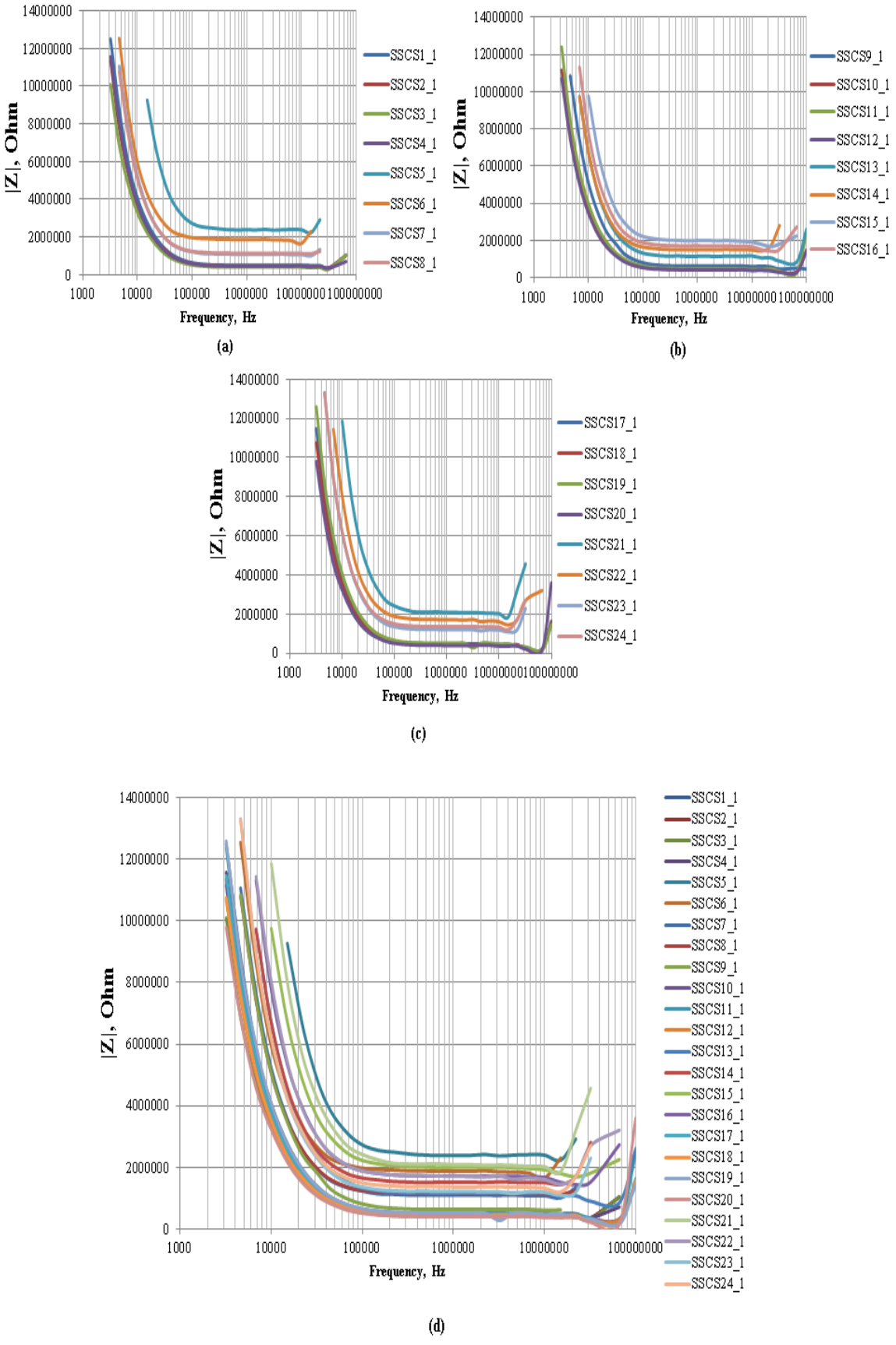

Figure 4.8: Impedance characterization of (a) SSCS1_1 to SSCS8_1, (b) SSCS9_1 to SSCS16_1, (c) SSCS17_1 to SSCS24_1, and (d) SSCS1_1 to SSCS24_1

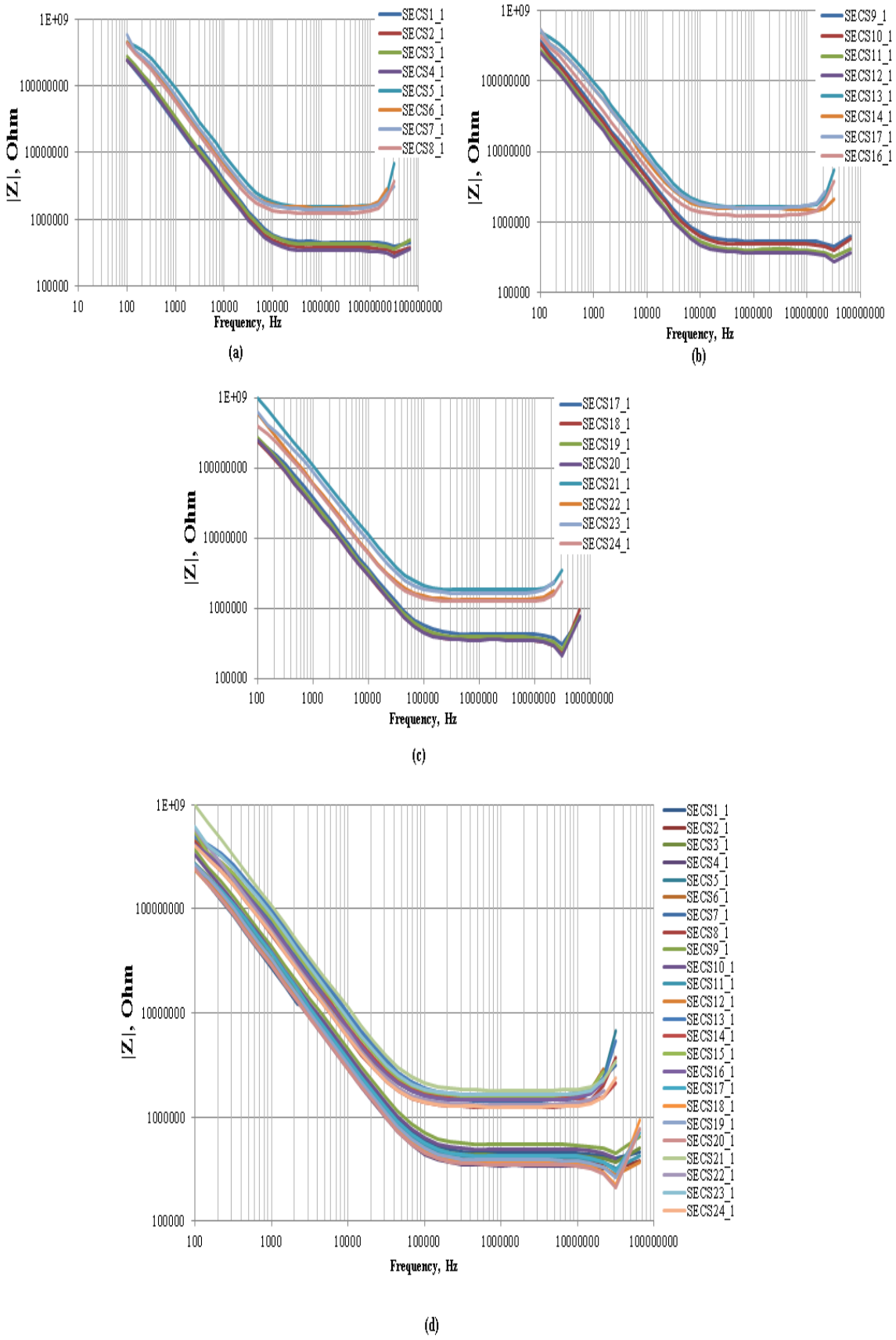

Figure 4.9: Impedance characterization of (a) SECS1_1 to SECS8_1, (b) SECS9_1 to SECS16_1, (c) SECS17_1 to SECS24_1, and (d) SECS1_1 to SECS24_1.

The SSCS and SECS sensors are modelled as an electrical circuit as can be seen in Figure 4.10 [124, 126]. The circuit consists of total inductance (L), total capacitance (C), total resistance (R_1) and total resistive losses (R_2). The values of electrical parameters in Figure 4.10 are also estimated for each sensor from the real part and imaginary part responses using EIS spectrum analyser software [127].

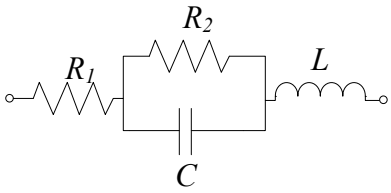

Figure 4.10: Circuit representation of the sensors combined in series.

Tables 4.3 and 4.4 summarize the electrical parameters values of SSCP and SECP, respectively. For all the SSCP and SECP sensors, the average total resistive losses, R_2 value is relatively high, i.e. between around 2.0×10^7 Ω to 2.0×10^{18} Ω. The total resistance average value, R_1 is basically increases when the negative backplane is introduced for SSCP and SECP sensors as summarized in Tables 4.3 and 4.4. Moreover, there is no significant improvement of capacitance and inductance values except for the sensors of SECS21_1 to SECS24_1. Therefore, the best series connected planar electromagnetic are SECS21_1 to SSCP24_1, as can be seen in Table 4.4, where the capacitance and inductance values are the highest as compared to other planar electromagnetic sensors connected in series.

Table 4.3: Electrical parameters values of SSCS1_1 to SSCS24_1.

		Meander: One turn		Meander: Three turns		Meander: Five turns	
		No negative backplane	With negative backplane	No negative backplane	With negative backplane	No negative backplane	With negative
Interdigatal: type 1		**SSCS1_1**	**SSCS5_1**	**SSCS9_1**	**SSCS13_1**	**SSCS17_1**	**SSCS21_1**
	R_1, Ω	495950	2.25E+06	580850	1.09E+06	465860	2.23E+06
	R_2, Ω	9.52E+08	5.72E+07	2.03E+18	1.20E+08	1.14E+08	3.36E+15
	C, F	3.95E-12	1.25E-12	3.60E-12	2.44E-12	4.85E-12	1.41E-12
	L, H	2.49E-04	7.22E-03	6.10E-04	1.11E-03	9.63E-04	1.08E-03
Interdigatal: type 2		**SSCS2_1**	**SSCS6_1**	**SSCS10_1**	**SSCS14_1**	**SSCS18_1**	**SSCS22_1**
	R_1, Ω	448500	1.72E+06	450980	1.47E+06	465860	1.47E+06
	R_2, Ω	1.05E+09	1.19E+08	1.28E+12	1.39E+08	2.09E+08	1.11E+08
	C, F	4.41E-12	1.95E-12	4.71E-12	2.45E-12	4.52E-12	2.22E-12
	L, H	9.49E-05	1.55E-03	1.78E-03	9.00E-04	1.91E-03	1.37E-03
Interdigatal: type 3		**SSCS3_1**	**SSCS7_1**	**SSCS11_1**	**SSCS15_1**	**SSCS19_1**	**SSCS23_1**
	R_1, Ω	395150	1.04E+06	379600	1.75E+06	377830	1.14E+06
	R_2, Ω	2.62E+08	1.62E+08	2.78E+08	1.06E+08	2.40E+08	1.49E+09
	C, F	4.87E-12	3.14E-12	5.01E-12	1.75E-12	5.51E-12	2.66E-12
	L, H	3.13E-05	7.54E-04	4.12E-03	1.19E-03	2.91E-03	8.97E-04
Interdigatal: type 4		**SSCS4_1**	**SSCS8_1**	**SSCS12_1**	**SSCS16_1**	**SSCS20_1**	**SSCS24_1**
	R_1, Ω	447110	1.08E+06	418610	1.67E+06	268700	1.24E+06
	R_2, Ω	1.76E+15	1.15E+08	1.35E+13	5.96E+19	1.95E+07	2.09E+08
	C, F	4.25E-12	3.27E-12	5.00E-12	2.10E-12	5.73E-12	2.72E-12
	L, H	3.72E-04	1.11E-03	1.72E-03	2.58E-03	4.68E-03	1.00E-03

Table 4.4: Electrical parameters values of SECS1_1 to SECS24_1.

		Meander: One turn		Meander: Three turns		Meander: Five turns	
		No negative backplane	With negative backplane	No negative backplane	With negative backplane	No negative backplane	With negative backplane
Interdigatal: type 1		**SECS1_1**	**SECS5_1**	**SECS9_1**	**SECS13_1**	**SECS17_1**	**SECS21_1**
	R_1, Ω	306140	1.55E+06	501430	1.68E+06	432790	1.89E+06
	R_2, Ω	1.66E+10	1.00E+08	4.98E+10	1.00E+08	4.69E+10	3.14E+10
	C, F	1.50E-12	2.06E-12	3.78E-12	1.76E-12	4.42E-12	5.95E-12
	L, H	1.03E-04	1.54E-03	3.77E-04	3.27E-03	3.17E-04	1.67E-02
Interdigatal: type 2		**SECS2_1**	**SECS6_1**	**SECS10_1**	**SECS14_1**	**SECS18_1**	**SECS22_1**
	R_1, Ω	320510	1.59E+06	3.03E+06	4.59E+06	323630	1.41E+06
	R_2, Ω	1.88E+10	8.54E+08	4.02E+10	1.18E+09	6.39E+08	1.82E+06
	C, F	5.40E-12	2.43E-12	7.03E-13	2.59E-12	2.64E-12	7.90E-12
	L, H	2.36E-04	1.46E-03	1.97E-03	1.12E-03	1.97E-04	6.54E-03
Interdigatal: type 3		**SECS3_1**	**SECS7_1**	**SECS11_1**	**SECS15_1**	**SECS19_1**	**SECS23_1**
	R_1, Ω	384540	1.54E+06	384760	1.69E+06	375450	1.68E+06
	R_2, Ω	2.91E+10	1.15E+09	5.18E+10	3.92E+10	1.25E+11	3.93E+10
	C, F	4.76E-12	2.26E-12	4.94E-12	2.13E-12	1.94E-12	5.51E-12
	L, H	2.24E-04	1.46E-03	3.19E-04	1.65E-03	2.45E-04	2.12E-03
Interdigatal: type 4		**SECS4_1**	**SECS8_1**	**SECS12_1**	**SECS16_1**	**SECS20_1**	**SECS24_1**
	R_1, Ω	325100	1.35E+06	335280	1.63E+00	325570	1.34E+06
	R_2, Ω	3.90E+10	1.00E+08	7.38E+08	7.84E+08	2.74E+10	7.19E+08
	C, F	2.93E-12	2.93E-12	5.41E-12	2.39E-12	5.65E-12	5.62E-12
	L, H	2.45E-04	2.14E-03	1.73E-04	2.07E-03	1.98E-04	4.75E-03

4.5 Conclusion

In this chapter, the characteristic of all the planar electromagnetic sensors and the effects of different designs to the electrical parameters of the sensors were discussed. The best parallel (SSCP21_1 to SSCP24_1) and series connected planar electromagnetic sensors (SECS21_1 to SECS24_1) were determined based on the highest capacitance and inductance compared to other similar sensors.

CHAPTER 5

Experiments, Results, and Discussions

5.1 Introduction

In this chapter, firstly, experiments are conducted to obtain the impedance characterization for the selected sensors from Chapter 4 and the results are compared with the simulation results obtained in Chapter 3. Then, the sensors are tested to detect nitrates contamination in distilled water from two set of experiments. Firstly, two nitrates forms namely; sodium nitrates ($NaNO_3$) and ammonium nitrates (NH_4NO_3), each of different concentration between 5 mg and 20 mg dissolved in 1 litre of distilled water were used to observe the sensor response. Secondly, $NaNO_3$ and NH_4NO_3 were mixed in several different ratios dissolved in 1 litre of distilled water and the responses of the sensors were observed. The best sensor has been determined based on the interpretation from both nitrates experiment results. Furthermore, the contamination level of water samples which were taken from various sources and locations in New Zealand have been determined using the ultimate best sensor and the results was compared with the results obtained using nuclear magnetic resonance (NMR) technique.

5.2 Description of the Selected Sensors

In the present study, electromagnetic sensors with meander and interdigital in parallel and series combination are tested. The sensors were designed using Altium and fabricated using simple printed circuit board (PCB) fabrication technology (0.25 mm thick) as described in Chapter 2. The objectives are to compare the impedance characteristic between the simulation and experiment results and to study the relationship between the generated electromagnetic fields with different combinations and geometries of planar electromagnetic sensors, thus finding the sensors that have the best performance for

detection of nitrates contamination and extend it for natural water sources quality monitoring.

The selected inductive-capacitive planar electromagnetic sensors connected in parallel are SSCP1_1, SSCP17_1, SSCP5_1, SSCP21_1, and SSCP22_1 respectively. Each sensor has a BNC connector and can be connected to an external function generator which provides an alternating 10 Volt peak-to-peak sine waveform signal.

The series combination sensors comprise of SECS17_1, SECS21_1, and SECS22_1. Each sensor consists of a meander coil spiralling inwards in rectangular form and the inner end is connected to an interdigital sensor completing a serial connection.

5.3 Experiment setup

The experimental setup for the sensors characteristic is discussed in Section 4.2 (Figure 4.1). The experimental setup for the water sample experiments is shown in Figure 5.1. The setup has a frequency waveform generator where a standard sinusoidal waveform with 10 Volts peak-to-peak value was set as the input signal for the sensors. An old microscope was used as a platform for the sample container and the sensors were partially immersed into the water sample. The Agilent 54622D mixed signal oscilloscope was interfaced to a PC where the output signals and the sensor's impedance was recorded and calculated using *LabView*.

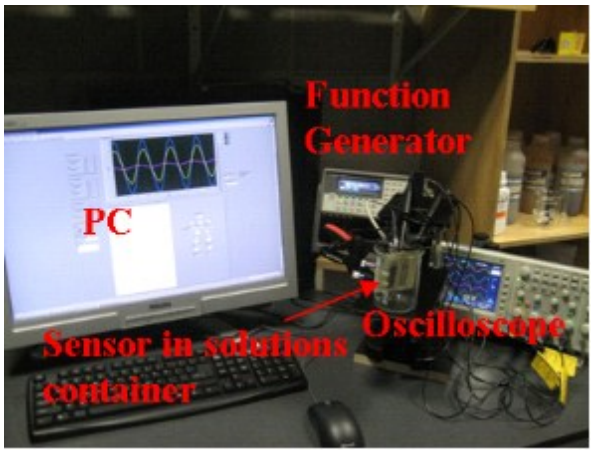

Figure 5.1: Experimental setup for the experiments

5.3.1 Characterization of the Sensors via Experiment

The simulation results and experimental results for the parallel sensors (as can be seen in Figure 5.2(a) and Figure 5.3(b), respectively) have number of similarities but from the experiments, it is revealed that the capacitive part starts to appear in SSCP17_1, SSCP21_1, and SSCP22_1 after approximately around 40 MHz. As for the series sensors, the impedance curves in Figure 5.3(b) seem to be steeper compared to the impedance curves obtained from simulation in Figure 5.3(a). It is also shown that the inductive becomes visible after around 10 MHz. In between state i.e. the combination of inductive and capacitive states can be seen from 500 kHz to 10 MHz and 400 kHz to 5 MHz for SECS17_1 and SECS21_1/SECS22_1, respectively.

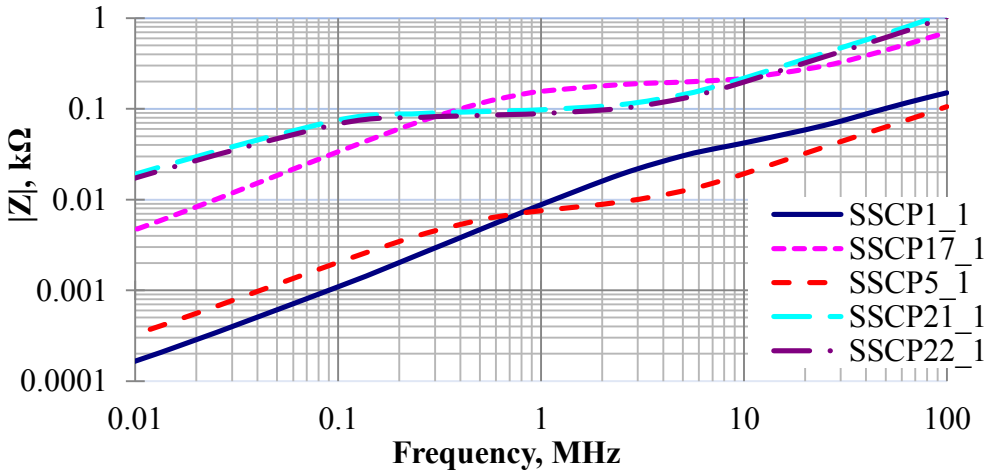

(a)

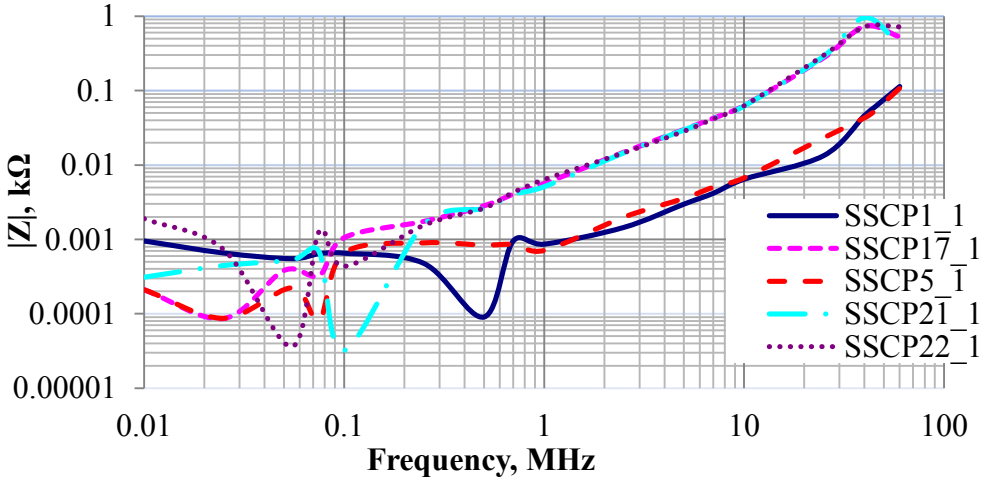

(b)

Figure 5.2: Parallel sensors impedance, |Z| characteristics obtained from (a) simulation results (b) experiment results

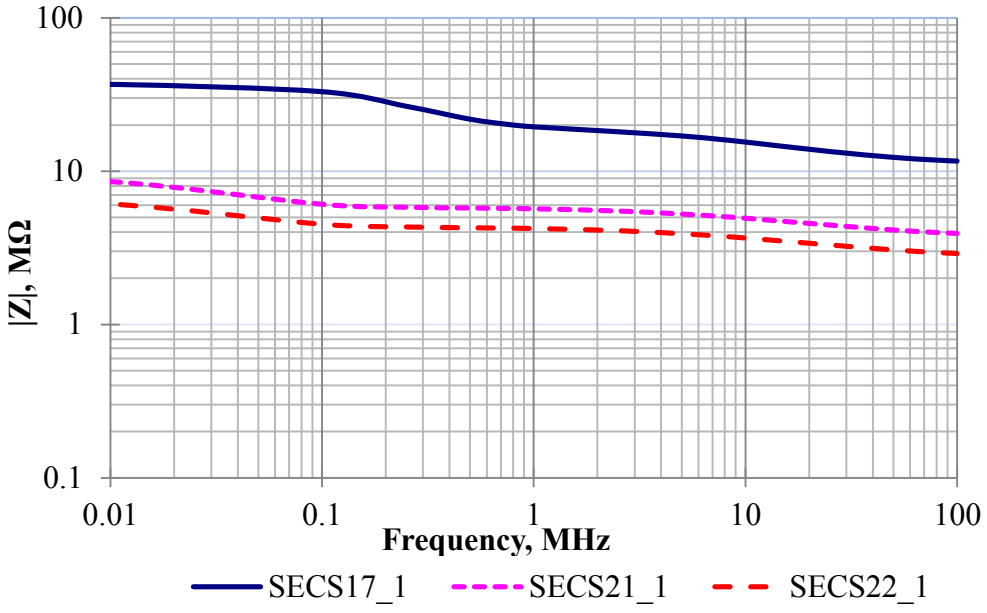

(a)

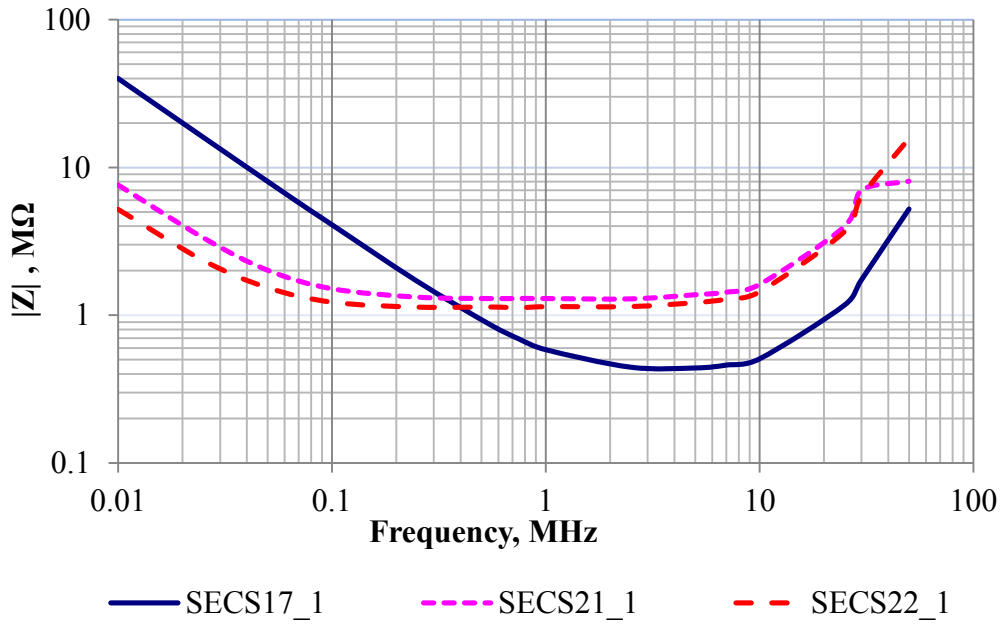

(b)

Figure 5.3: Series sensors impedance, |Z| characteristics obtained from (a) simulation results (b) experimental results

5.3.2 Experiment with Chemical Based on Nitrates and Water Samples: Single Frequency Operation

The operating frequencies for all parallel and series sensors during water sample experiments were set at 10 MHz and 500 kHz, respectively. Two sets of experiments were conducted to find the best sensor for further application as can be seen in Figure 6. Each of the sensors was sprayed with Wattyl Killrust Incralac to form an acrylic resin-based protective coating. The effect of the samples on the sensor's impedance was recorded and the sensitivities of the sensors are calculated from the real part and imaginary part as governed by the following equations:

$$\text{Real part sensitivity, } \%R = \frac{\left(\left(R_{total}\right)_{sample} - \left(R_{total}\right)_{distilled}\right)}{\left(R_{total}\right)_{distilled}} \times 100 \qquad \textbf{5.1}$$

$$\text{Imaginary part sensitivity, } \%X = \frac{\left(\left(X_{total}\right)_{sample} - \left(X_{total}\right)_{distilled}\right)}{\left(X_{total}\right)_{distilled}} \times 100 \qquad \textbf{5.2}$$

where, $(R_{total})_{distilled}$ = the real part of the impedance value when the sensor is immersed in the distilled water.

$(R_{total})_{sample}$ = the real part of the impedance value when the sensor is immersed in the water sample.

$(X_{total})_{distilled}$ = the imaginary part of the impedance value when the sensor is immersed in the distilled water.

$(X_{total})_{sample}$ = the imaginary part of the impedance value when the sensor is immersed in the water sample.

In this section, the first experiment involved the response of the sensors with different concentration of Nitrates samples in the form of sodium nitrate ($NaNO_3$) and ammonium nitrate (NH_4NO_3) mixture. Then, the sensors with the best sensitivities were chosen each from every combination for the next experiment (second experiment). Five different ratio mixes were prepared where the total weight of every single mix is given in 20 mg. Then, each mix is diluted in 1 Litre of distilled water into a container. The ratios of $NaNO_3$ to NH_4NO_3 were 1:1(Ratio_1), 1:2(Ratio_2), 2:1(Ratio_3), 1:3(Ratio_4) and 3:1(Ratio_5).

The second experiment objective was to test the chosen sensors with different concentration of nitrates samples (5 mg, 10 mg, 15 mg and 20 mg) in the form of sodium nitrate ($NaNO_3$) and ammonium nitrate (NH_4NO_3) diluted in 1 Litre of distilled water.

5.3.2.1 Experiment with Chemical Based on Nitrates

Figures 5.4 and 5.5 depict the real part and imaginary part sensitivities, respectively calculated for the parallel sensors. It is difficult to get a completely good indication of good response and relationship about the detection of nitrates in the water sample using parallel sensors. However, SSCP22_1 has been chosen since it seems to have a steady real part and imaginary sensitivities.

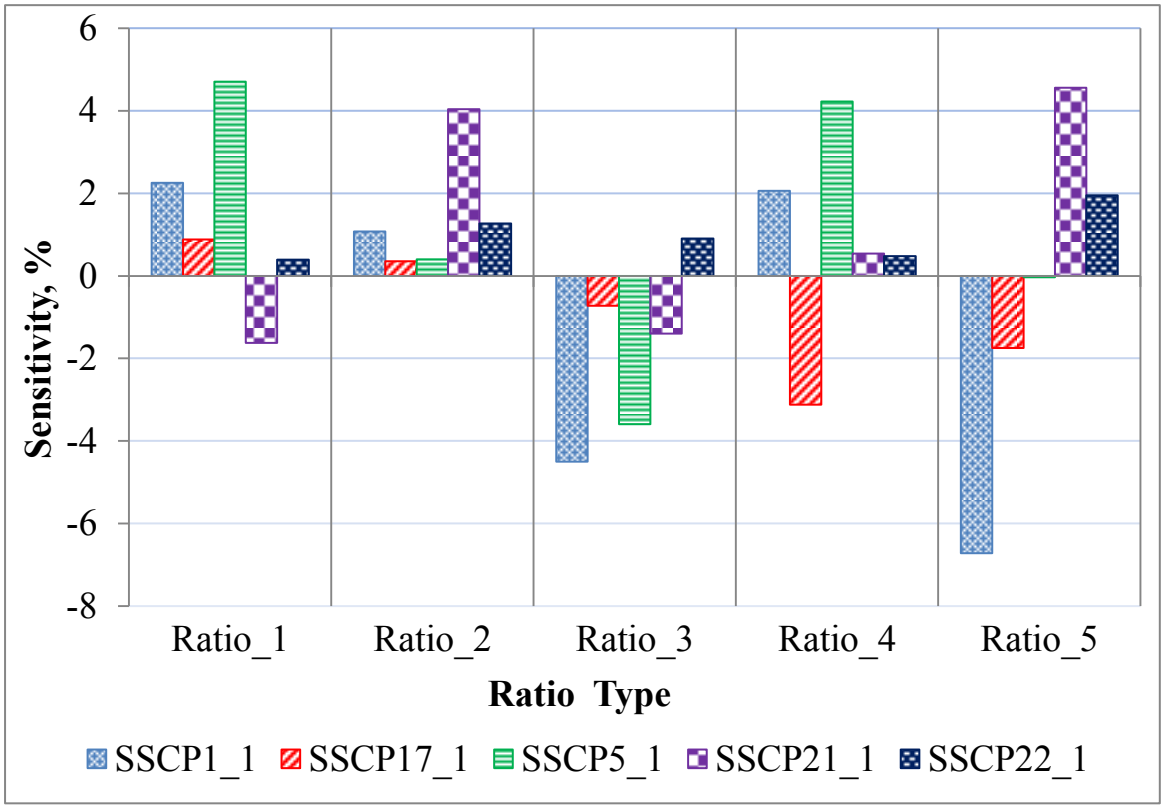

Figure 5.4: Parallel sensors real part sensitivity from experiment with nitrates mix (different ratio)

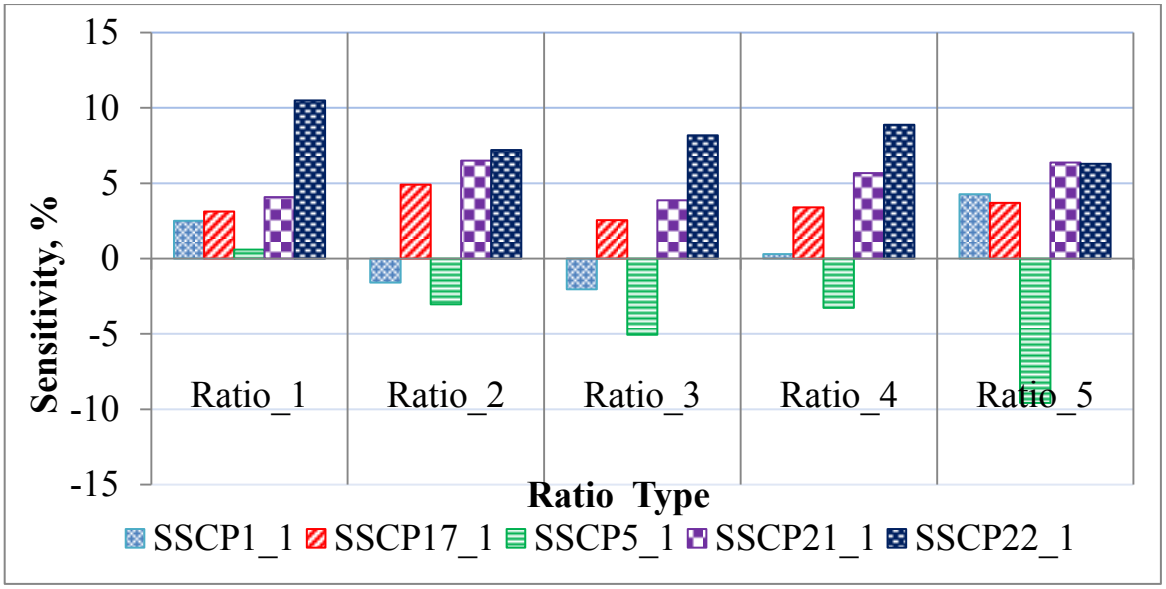

Figure 5.5: Parallel sensors imaginary part sensitivity from experiment with nitrates mix (different ratio)

Clear and better results can be seen using the series sensors as shown in Figures 5.6 and 5.7. The sensitivities of the real part values stay in the negative region and it is due to the increase of the conductivity level of the mixed solution. SECS22_1 has the best response amongst the series sensor and will be used for further application.

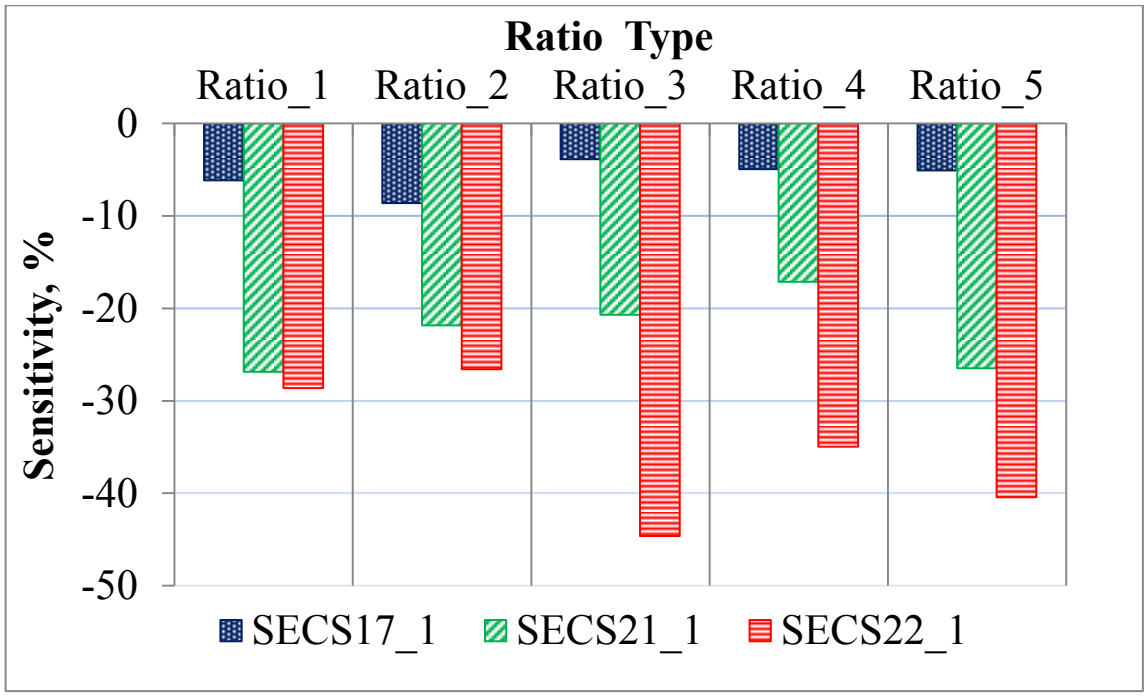

Figure 5.6: Series sensors real part sensitivity from experiment with nitrates mix (different ratio)

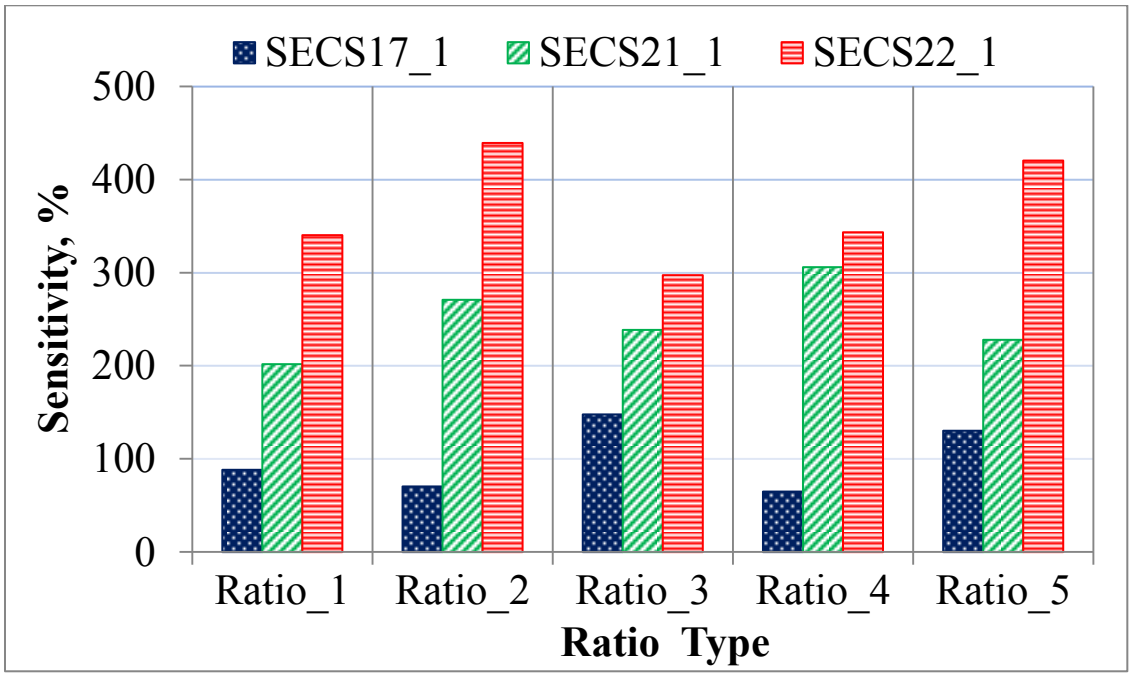

Figure 5.7: Series sensors imaginary part sensitivity from experiment with nitrates mix (different ratio)

5.3.2.2 Experiment with Different Concentrations of Nitrates

As SSCP22_1 was deployed in this experiment, there was no conclusive results can be given as the real part and the imaginary sensitivities values were randomly distributed without any positive relationship with the concentration of $NaNO_3$ or NH_4NO_3 as shown in Figure 5.8. This is mainly caused by the non-uniform electromagnetic fields generated by SSCP22_1.

Figures 5.9 shows the sensitivities value of SECS22_1 when tested with solution based on $NaNO_3$ and NH_4NO_3. A similar response can be observed for both solution types. The imaginary values are at range around 100% to around 200% and the values are independent of the total concentration showing that SECS22_1 is already able to detect contamination in the water sample. Moreover, the real part negatives values progressively decreases with the total concentration of the chemicals. This is true since the electrical conductivity; σ of the solution of water is highly dependent on its concentration of

dissolved salts where $NaNO_3$ and NH_4NO_3 were added in the distilled water. The purer the water samples, the lower the conductivity (the higher the resistivity) and vice versa. Therefore, the real part sensitivities give the indirect relationship of total amount of chemical concentrations with the quality level of the water samples. In previous work, it has been shown that with more negative electrodes, the field distribution become more uniform and that improves the sensitivities [67]. SECS22_1 comprises thick negative plane as shown in Figure 5.10 and this is similar to many negative electrodes.

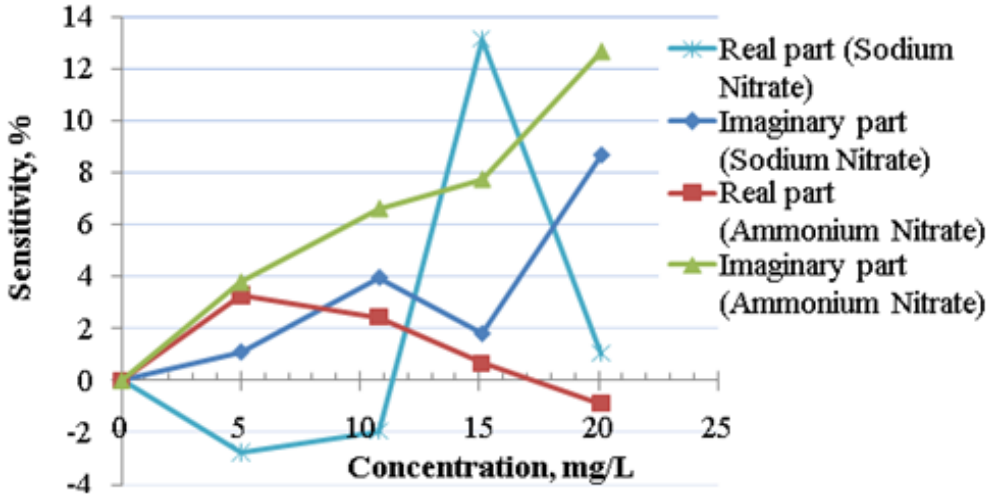

Figure 5.8: SSCP22_1 sensitivity from experiment with different concentration of sodium nitrate ($NaNO_3$)/ ammonium nitrate (NH_4NO_3)

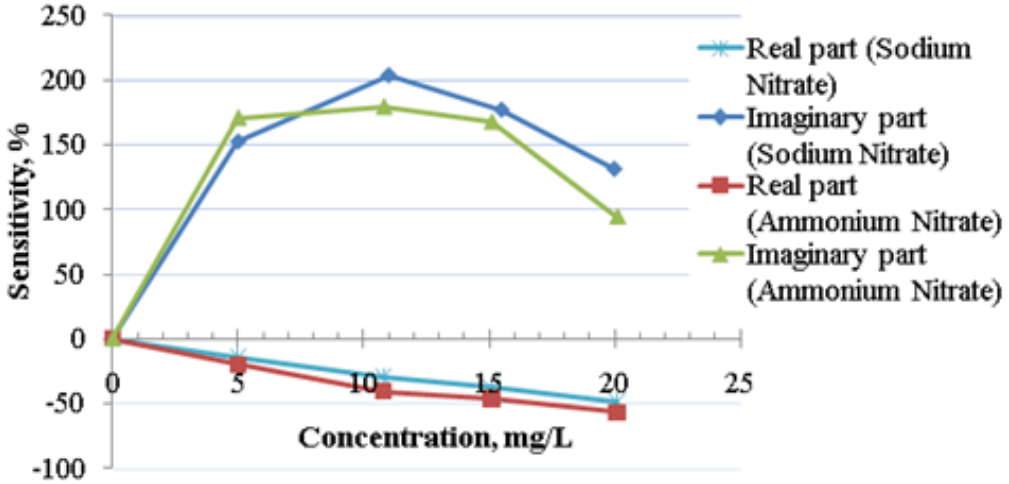

Figure 5.9: SESS22_1 sensitivity from experiment with different concentration of sodium nitrate ($NaNO_3$)/ ammonium nitrate (NH_4NO_3)

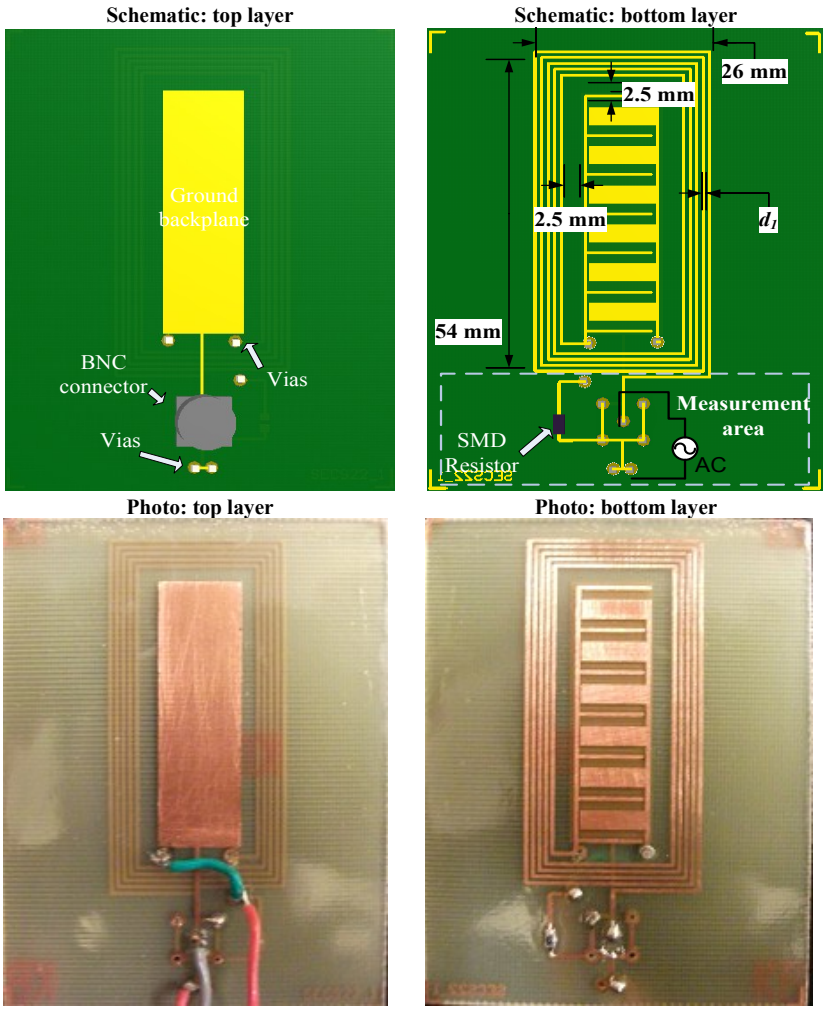

Figure 5.10: Schematic diagram and picture of SECS22_1

Figure 5.11 illustrates the re-plotted real part sensitivities using SECS22_1 for both chemical with the equivalent linear equation. The graphs in Figure 5.11 show very good correlation with R^2=0.9948 and R^2=0.9652, between SECS22_1's real part sensitivities with the chemical concentration and contamination level.

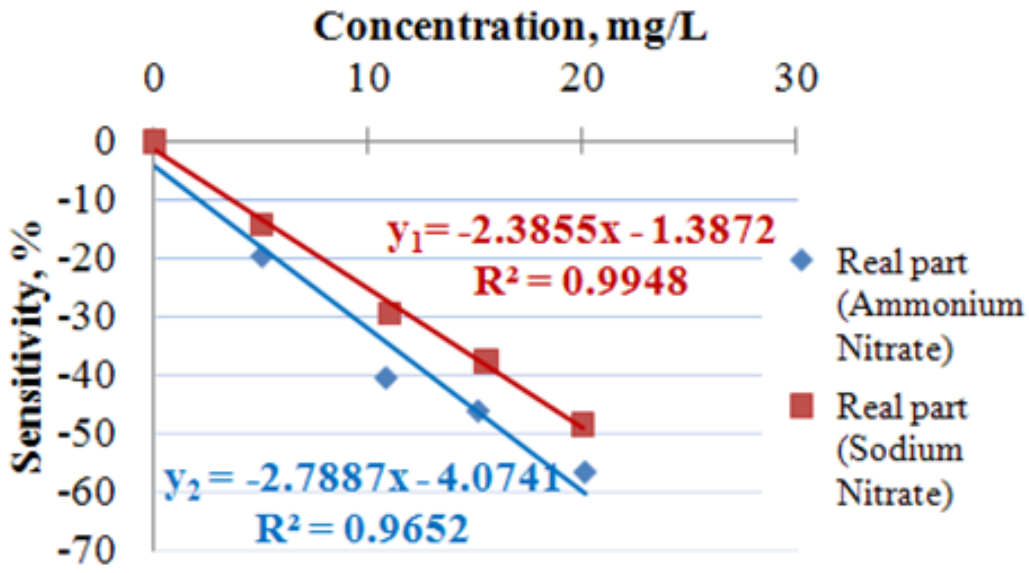

Figure 5.11: Graphs of SECS22_1 sensitivity from experiment with different concentration of sodium nitrate ($NaNO_3$)/ammonium nitrate (NH_4NO_3) with linear regression relationship

5.3.2.3 Effect of Experimental Variables (pH) on SECS22_1

In this section, the pH value for each solution was measured using Orion pH meter 420A. The effect of pH on SECS22_1 response was determined using a set of distilled water samples with different pH values which varied from 3.5 to 12. The pH value of the sample was adjusted with dilute HCl or NaOH solution. SECS22_1 response to the varying pH values can be seen in Figure 5.10. SECS22_1 is independent of pH in the range of 6.5 to 10. In the pH range below 6.5 where total amount of H^+ is basically increasing, the relatively bigger effective area of negative electrodes as compared to positive electrodes associated with SECS22_1, attempt to balance the increase of H^+ and try to put back the sensor response into the previous equilibrium state. It is seen that in Figure 5.12, a significant changes of SECS22_1 response was observed when the pH value is over 10, largely due to the increased of total amount of OH^-.

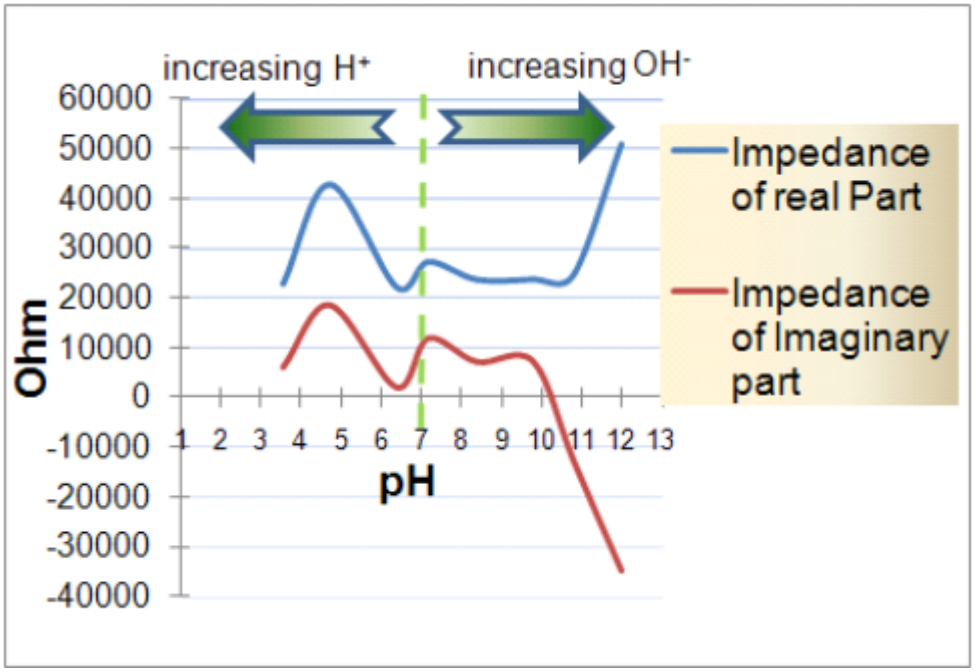

Figure 5.12: Sensitivity of SECS22_1 values plotted against pH value between the range of 3.5 and 12

5.3.2.4 Detection of Contamination in Water Samples using SECS22_1

Sensor SECS22_1 has been used to observe the response of the sensor with natural water mixed with contaminants. The samples of different bottles were taken from previous research by Karunanayaka in [130] is which related to the magnetic filtration technique of drinking and waste waters. The water samples were analysed using Nuclear Magnetic Resonance (NMR) analysis to check the amount of organic material in the sample and summarized in Table 5.1. Figure 5.13 shows the water samples collected from different places in the respective containers. Table 5.1 shows the amount of mineral in $g \cdot m^{-3}$ including the pH value. The experimental results as shown in Figure 5.14 suggested that the water samples to be divided into the following groups:

- Unsafe to consume.
- Use with caution.
- Safe to consume.

The unsafe to consume water sources are of 570-5 and 570-7. This can be explained from the lowest real part sensitivity (Figure 5.14(a)) and the highest imaginary part sensitivity (Figure 5.14(b)). The total amount of mineral in 570-5 and 570-7 as given in Table 5.1, validate the decision. As for the safe to consume water samples, 570-8, 570-9 and 570-10 are included. It has been postulated that the low imaginary sensitivity i.e. just below 2000 % (Figure 5.14(b)) as the main reason for the selection where the total amount of mineral for each sample in Table 5.1 confirms the selection.

Table 5.1: Content of water samples from NMR test results

Sample	pH	Ca (gm^{-3}-Ca)	Mg (gm^{-3}-Mg)	Fe (gm^{-3}-Fe)	$CaCO_3$ (gm^{-3}-$CaCO_3$)	Sulphate (gm^{-3}-SO_4)	Total mineral (gm^{-3})
570-1,Matakana raw	8.69	3.3	0.54	0.036	8	0.63	12.506
570-2,Matakana magnetic circle tank	8.06	3	0.51	0.039	10	0.24	13.789
570-3,IPL Mixed water UV	8.38	1.7	0.32	0.027	4	0.09	6.137
570-4, Edgecumbe raw	7.529	11.6	11.8	3.33	77	0.02	103.75
570-5, McCains D119 raw	6.62	17.3	24.8	2.62	150	0.23	194.95
570-6, Matakana raw2	7.8	3	0.51	0.036	8	0.63	12.176
570-7, McCains treated	8.2	4.6	3	0.334	24	606	637.934
570-8, Tauranga tapwater	7.27	2.8	0.56	0.005	8	1.8	13.165
570-9, Techical water system potable	7.16	5.3	0.56	0.11	14	2.17	22.14
570-10, Edgecumbe magnetic treatment	8.58	14.4	8.1	0.014	70	0.02	92.534

Figure 5.13: Water samples in containers, arranged in ascending order from left to right

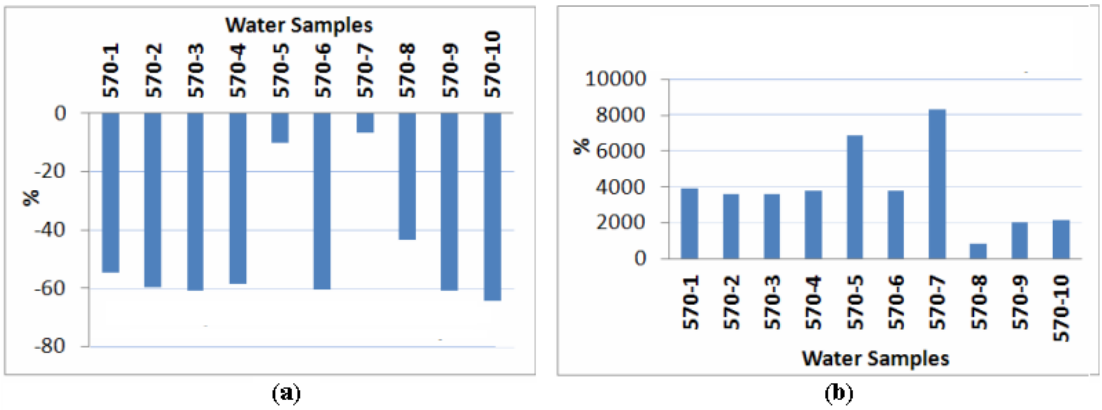

Figure 5.14: Sensitivity of SECS22_1 to water samples: (a) real part (b) imaginary part

Finally, 570-1, 570-2, 570-3, 570-4 and 570-6 are all group together in consume with caution group as the imaginary sensitivity has just passed 2000 % and just below 4000 %. Although some of the samples appear to be in low total amount of mineral, the visual tests experienced by the researcher indicate that there are some discolorations caused by certain kind of algae or living organism inside the water samples, thus changing the electrical properties of the water samples as can be seen from Figure 5.13. This may have cause the sensitivity to be significantly high as compared to the total amount of mineral given in Table 5.1.

5.3.2.5 Stability Test of SECS22_1

Long-term response stability has been identified as one of the important factors of a chemical sensor performance. In order to evaluate the response stability of the SECS22_1, one reference response value of distilled water was recorded. Then, the experiments involving the solutions with different ratio mix as well as the water samples were repeated separately where the sensors output response to each solution was recorded at an equal interval between approximately 550s to determine the real part and imaginary part sensitivities. The outcomes from Figure 5.15 and Figure 5.16 are the extensions of those that have been obtained in Figure 5.6, Figure 5.7, and Figure 5.14. As a whole, the previous results are still valid and significant. Moreover, the real part sensitivities remained constant as shown in Figures 5.15(a) and 5.16(a) while the imaginary part sensitivities moderately varied as can be seen in Figures 5.15(b) and 5.16(b).

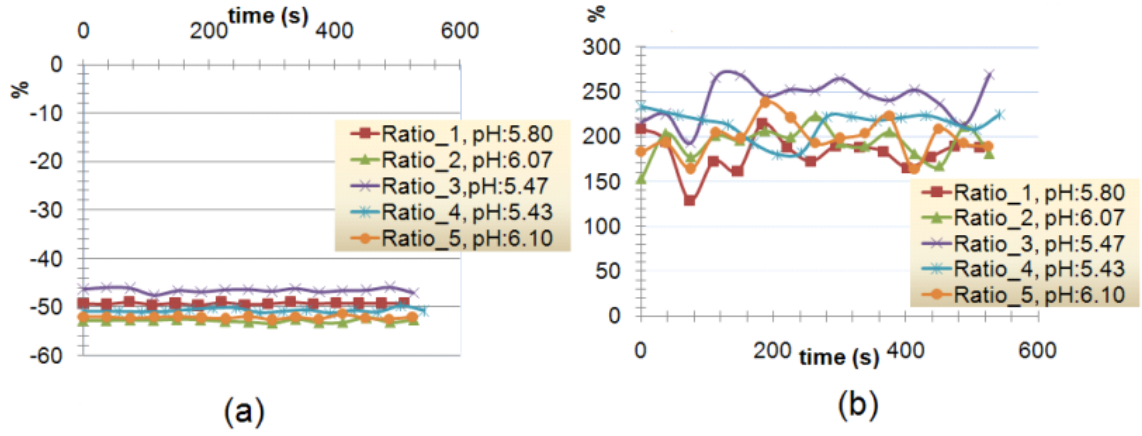

Figure 5.15: Sensitivity of SECS22_1 to nitrate solutions: (a) real part (b) imaginary part

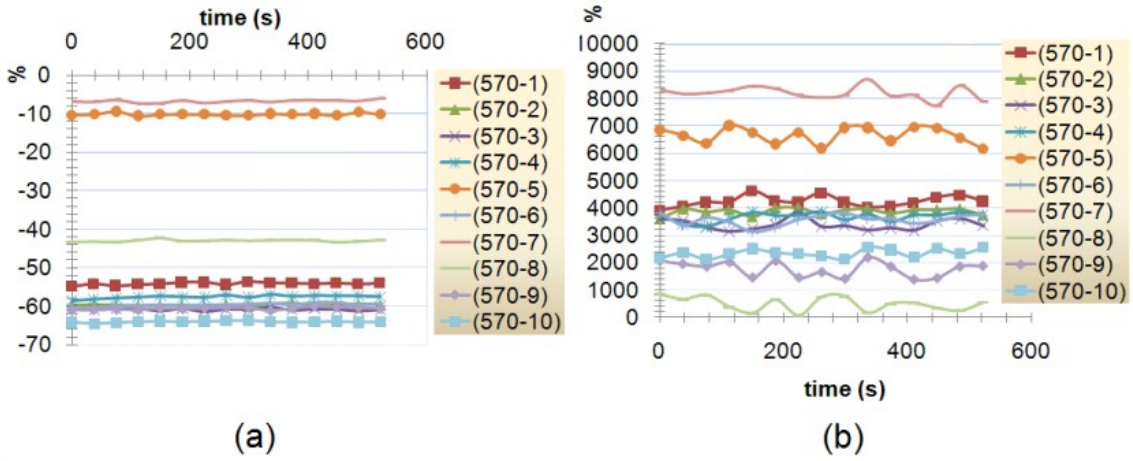

Figure 5.16: Sensitivity of SECS22_1 to water samples: (a) real part (b) imaginary part

5.3.3 Experiment with Chemical Based on Nitrates and Water Samples: Multivariate Frequency Operation

The next experiment involved the response of SECS22_1 sensor with distilled water, different concentration of nitrates samples in the form of Sodium Nitrate ($NaNO_3$) diluted in 1 litre of distilled water and different concentration of Nitrates samples in the form of ammonium nitrate (NH_4NO_3) diluted in 1 litre of distilled water. The operating frequency range was between 25 Hz and 1 MHz. The experimental setup is the same as shown in Figure 5.1.

5.3.3.1 Experiment with Distilled water, Different concentration of $NaNO_3$ and NH_4NO_3 and Results

The electrochemical impedance spectroscopy approach was used to estimate qualitatively the reaction of the sensor with water samples. The response in the frequency domain of an electrochemical reaction can be used to estimate the contamination in the water. Figure 5.17 describes a system for coated electrodes response to aqueous solution [123, 124, 131]. The circuit composed of the solution resistance (R_s), coating resistance (R_c), and coating capacitance (C_c). In this research, an additional meander inductance (L) has been added to represent the system. The coating capacitance (C_c) is assumed to be mainly contributed by the interdigital part and represented by the following equation [31]:

$$C_c = (\varepsilon_r \varepsilon_o A)/d \qquad \textbf{5.3}$$

where, ε = the relative permittivity of the coating.

ε_0 = the permitiivity of the vacuum(8.85×10^{-4} F/cm).

A = the effective area (cm^2).

d = the effective distance of electrode (cm).

C_c is commonly used to evaluate the changes in the relative permittivity caused by water absorption or changes in the pigment/polymer proportions of the protective/decorative coatings [124]. R_c is used to evaluate the protection level provided by the coating [123].

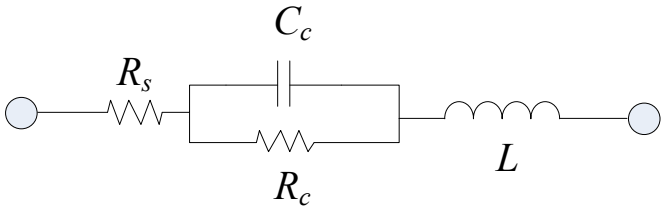

Figure 5.17: An equivalent electrochemical system for sensor's surface with intact coating

Figures 5.18 and 5.19 show the response of the sensor to the different concentration of sodium nitrate ($NaNO_3$) diluted in 1 litre of distilled water and different concentration of ammonium nitrate (NH_4NO_3) diluted in 1 litre of distilled water, respectively. Both Figures contain the response of the sensor to distilled water. The

simulated response of SECS22_1 with distilled water in Figure 3.8 as comparison to Figure 5.18 or 5.19 (0 mg/L) showing an obvious peak. This is postulated that the total inductance and total capacitance value as produced in the simulation model are largely and smaller, respectively than that are actually existed in the experiment result.

In general, the sensor shows a capacitive loop and an inductive loop at low frequency and high frequency, respectively. A typical electrochemical spectroscopy response with aqueous solution often show both capacitive and inductive semicircle [132]. However, our sensor shows significant deviation of the loops as can be seen in Figures 5.18 and 5.19. This is caused by the presence of inductive characteristic [131] of the meander sensor, especially at high frequency. The impedance curve is shrinking and becoming smaller as the concentration is increased, the results suggest that it is caused by the reduction of σ value and is confirmed in the simulation results in Chapter 3.

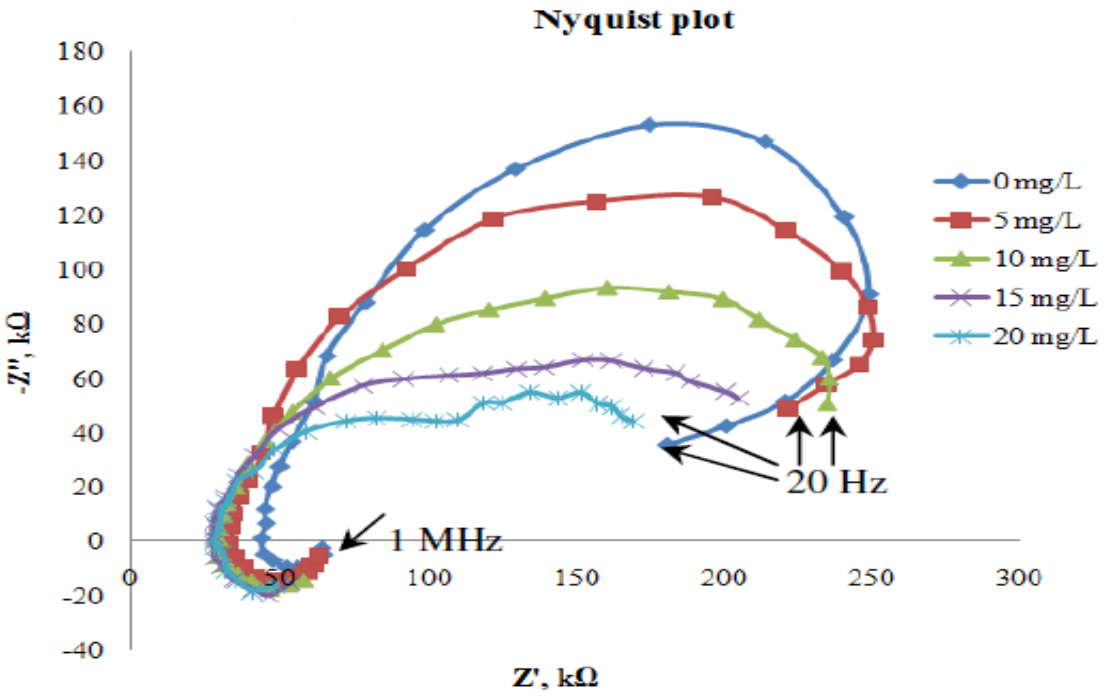

Figure 5.18: Nyquist plot for experiment involving different concentration of dissolved $NaNO_3$

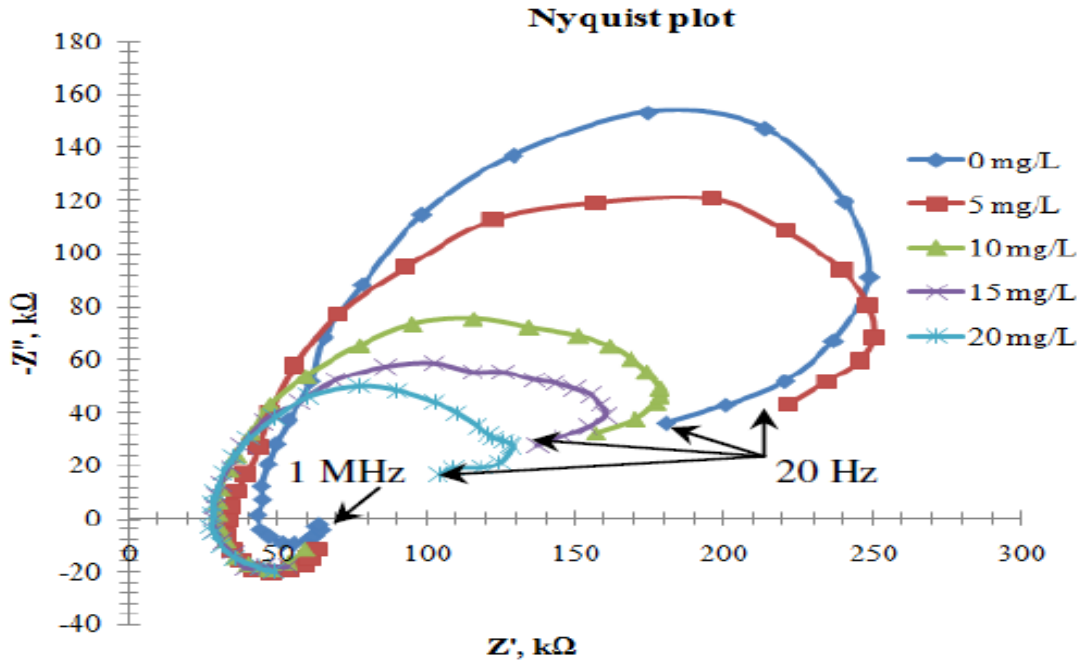

Figure 5.19: Nyquist plot for experiment involving different concentration of dissolved NH_4NO_3

For quantitative results, the sensitivities of the sensors are calculated from the real part as taking the value from the distilled value as reference in the following equation:

$$\%\text{Real\_part} = \sum_f \left[\frac{(R_{total})_{sample} - (R_{total})_{distilled}}{(R_{total})_{distilled}} \times 100 \right] \qquad \textbf{5.4}$$

In the simulation results in Figure 3.11, the imaginary part showed a response other than linear, therefore the absolute difference value is used to calculate the imaginary part sensitivity as shown in the following equation:

$$\%\,\text{Imaginary\_part} = \sum_f \left[\frac{\left|(X_{total})_{sample} - (X_{total})_{distilled}\right|}{\left|(X_{total})_{distilled}\right|} \times 100 \right] \qquad \textbf{5.5}$$

where, $(R_{total})_{distilled}$ = the real part of the impedance value when the sensor is immersed in the distilled water.

$(R_{total})_{sample}$ = the real part of the impedance value when the sensor is immersed in the water sample.

$(X_{total})_{distilled}$ = the imaginary part of the impedance value when the sensor is immersed in the distilled water.

$(X_{total})_{sample}$ = the imaginary part of the impedance value when the sensor is immersed in the water sample.

f = the frequency value.

Figure 5.20 shows the sensitivities value when tested with solution based on $NaNO_3$ and NH_4NO_3. Similar response can be observed for both solution types, except the real part sensitivity and the imaginary part sensitivity of NH_4NO_3 are much higher than $NaNO_3$.

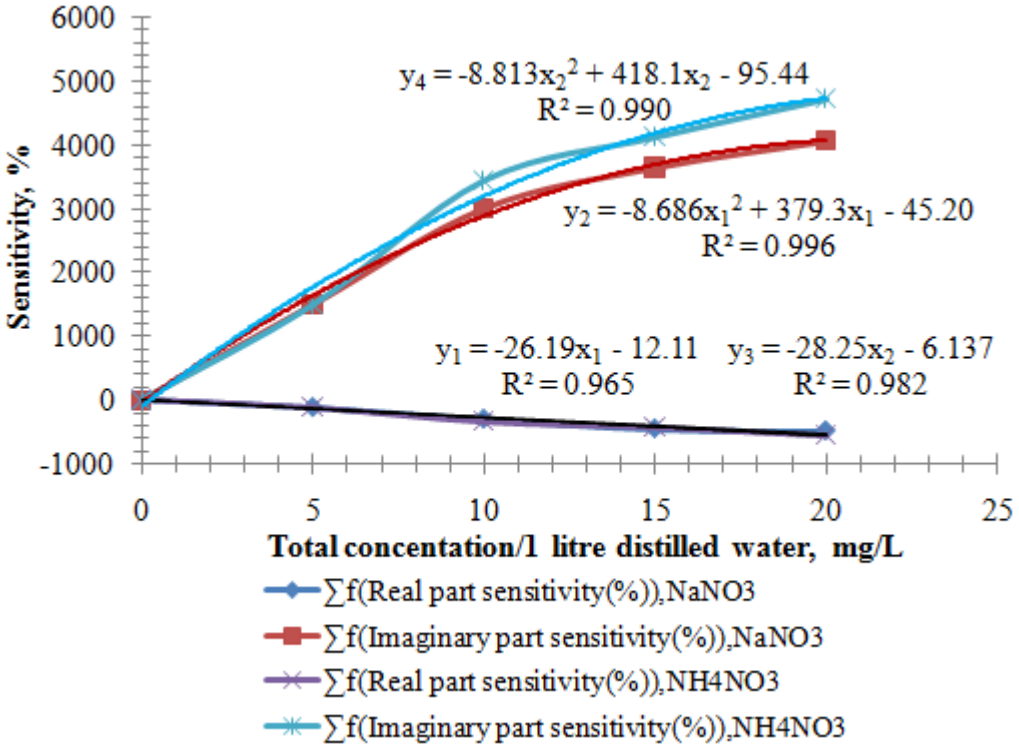

Figure 5.20: Sensitivity of SECS22_1 sensor to the different concentration of $NaNO_3$/NH_4NO_3

The real part negatives values progressively decreases with the total concentration of the chemicals. The linear equations y_1 and y_3 represent the real part sensitivity of $NaNO_3$ and NH_4NO_3, respectively where x_1 and x_2 signify the total concentration of $NaNO_3$ and NH_4NO_3, respectively. This indicates that the conductivity of the water has increased as can be seen from the simulation result (Figure 3.10). Good linear correlation

with R^2=0.965 and R^2=0.982, between the real part sensitivities with the chemical concentration of $NaNO_3$ and NH_4NO_3, respectively.

The sensitivity of the imaginary part for both type of aqueous solution increased when the concentrations were increased in polynomial order of two as can be seen in Figure 5.20. The linear equation y_2 and y_4 represent the imaginary part sensitivity of $NaNO_3$ and NH_4NO_3, respectively where x_2 and x_4 signify the total concentration of $NaNO_3$ and NH_4NO_3, respectively. The total sensitivities give good polynomial order of 2 correlation with R^2=0.996 and R^2=0.990. The coating capacitance, C_c is commonly used to evaluate the changes in the relative permittivity caused by the changes in the pigment/polymer proportions of the protective/decorative coatings [124] so the small change of C_c will be apparent in the imaginary part of the impedance response. The value of the double layer capacitance depends on many variables such as temperature, ionic concentrations, types of ions, oxide layers, electrode roughness, dielectric properties/relative permittivity [133, 134], etc. The change of the imaginary sensitivity is caused by the decrease in C_c, resulting from the change of the relative permittivity value is due to the effect of polymer changes with increasing chemical concentration.

5.3.3.2 Experiment with Water Samples

The sensor (SECS22_1) has been used to observe the response of the sensor with natural water mixed with contaminants. From the Nyquist plot and calculated sensitivities, the qualitative and qualitative responses are studied. The samples of different bottles were taken from previous research by Karunanayaka in [130]. Figure 5.13 shows the water samples collected from different places in the respective containers. The water samples were analysed using the Nuclear Magnetic Resonance (NMR) technique to check the amount of organic material in the sample and summarized in Table 5.1. Table 5.1 shows the amount of mineral in $g \cdot m^{-3}$ including the pH value

In this experiment the Milli-Q water was used as a reference, Milli-Q refers to water that has been purified and deionized to a high degree by a water purification system where the operating frequency is between 20 Hz and 1 MHz. Figure 5.21 illustrates that

similar curve obtained when the sensor tested with Milli-Q water when compared with the curve for distilled water in Figure 5.21 but with a larger curve. This proves that Milli-Q water is purer than distilled water. As a whole, all the water samples produced a significantly smaller complex plane curves compared to the Milli-Q curve.

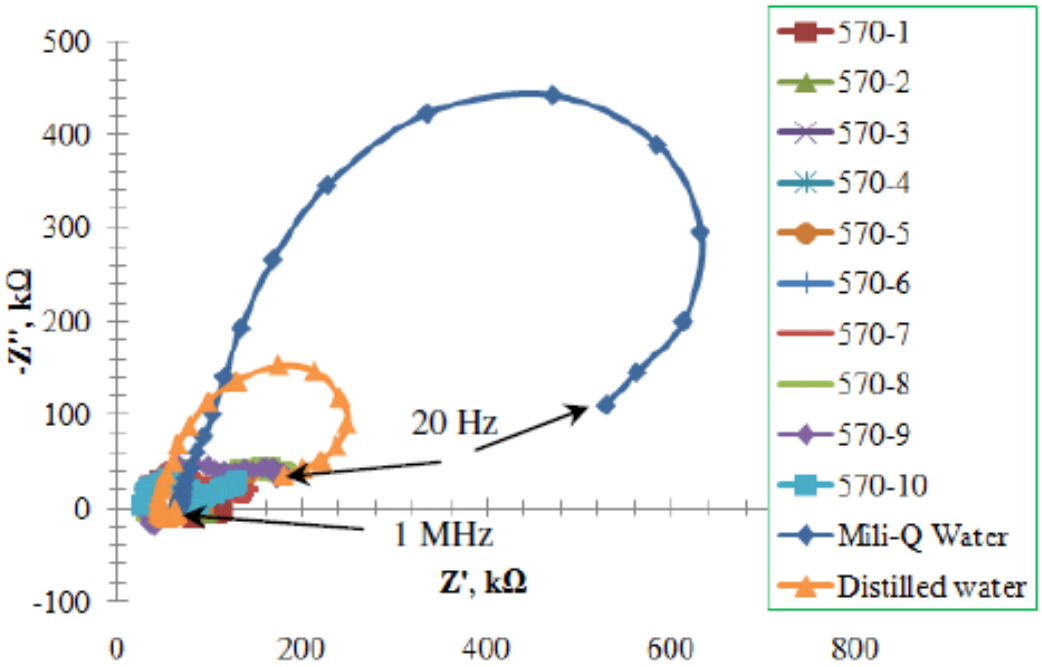

Figure 5.21: Nyquist plot for experiment involving water samples

Typically, pure water has a relative permittivity of 81 and electrical conductivity of 0.8 at room temperature. Any addition of other substance will reduce the relative permittivity of the aqueous solution and increase the electrical conductivity. Therefore, we can say that the curves that deviate further inside the Milli-Q curve have more contamination. From Figure 5.22, the most deviated curves are 570-1, 570-2, 570-3, 570-4, 570-5, 570-7, and 570-10.

The sensitivities were calculated using equations 5.4 and 5.5, taking the values from Milli-Q as reference. The sensitivity values calculated for the water samples as shown in Figure 5.23 suggested that the water samples to be divided into three groups of unsafe to consume, use with caution and safe to consume. The unsafe to consume water sources are of 570-5 and 570-7. This can be explained from the highest imaginary

sensitivities over 10000% and this condition is caused by high the total amount of mineral in 570-5 and 570-7 as given in Table 5.1.

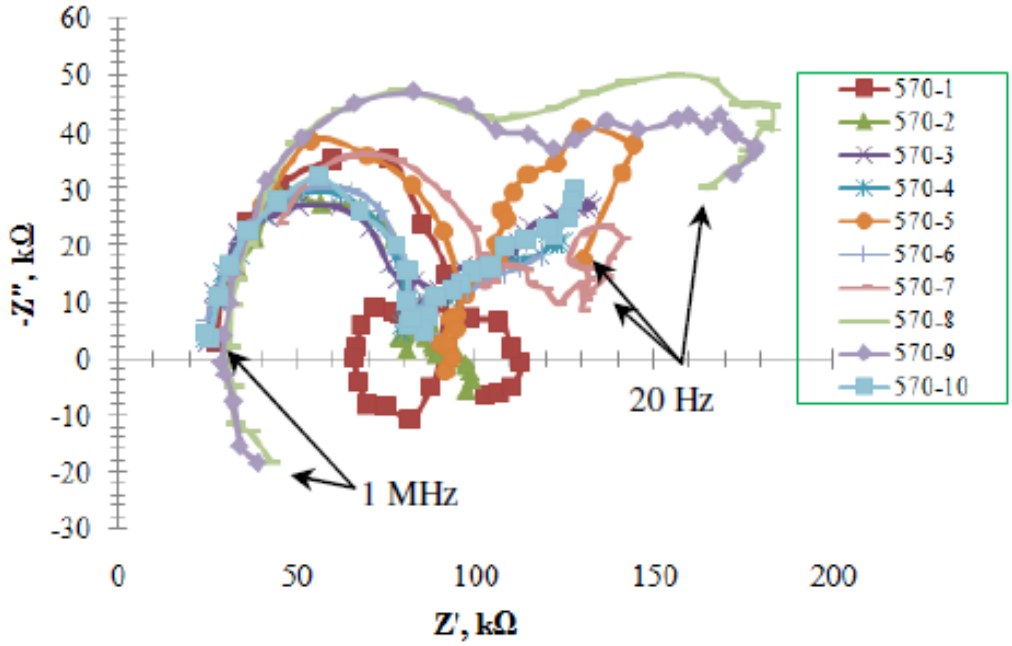

Figure 5.22: Nyquist plot for experiment involving water samples excluding the response from Milli-Q water and distilled water

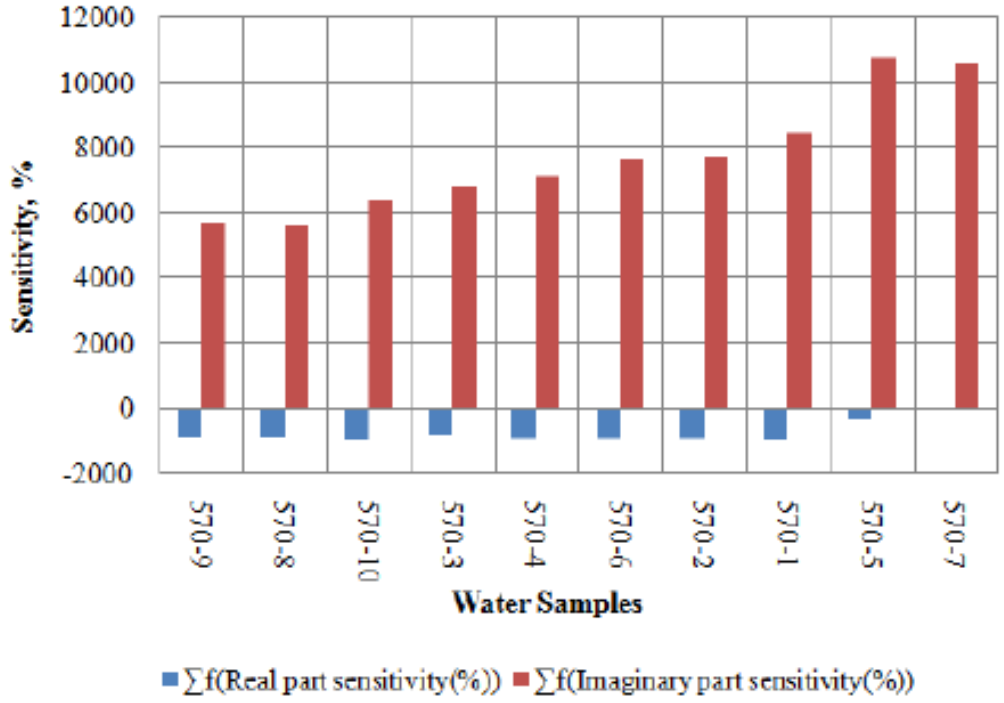

Figure 5.23: Sensitivity of the sensors to the aqueous solution arranged in order of increasing total mineral (gm^{-3}) in Table 5.1

As for the safe to consume water samples, 570-8 and 570-9 are included giving the imaginary sensitivities just above 4000% where the total amount of mineral for each sample in Table 5.1 confirms the selection. Finally, 570-1, 570-2, 570-3, 570-4, 570-6 and 570-10 are all group together in consume-with-caution group as the total sensitivity has just passed 6000 % and just above 8000 %. Although some of the samples in the cautious group appear to be in low total amount of mineral, there are some discolorations caused by certain kind of algae or living organism inside the water samples, thus changing the electrical properties of the water samples as shown in Figure 5.13. This may have cause the imaginary sensitivity to be significantly high as compared to the total amount of mineral given in Table 5.1. As a conclusion, if we combine the qualitative data interpreted form the impedance spectra and the quantitative data from the total sensitivities, only water samples of 570-8 and 570-9 are of acceptable high quality standard drinking water and safe to be consumed. This is indeed a better way to describe the contamination rather than single frequency result as has been described in [135].

5.4 Conclusion

The studies in this Chapter show that a very distinct differentiation of nitrates concentration can be achieved using a planar electromagnetic sensor with meander sensor and an interdigital sensor combined in series (SECS22_1). The process of selection of the sensor is also discussed. It can be used as a tool for water sources monitoring in farm where the nitrate level should not exceed 100 mg·$(NO_3)^-$−N/L. The SECS22_1 sensor has also been tested with drinking water samples and has shown very promising results to be a sensing tool of contamination detection in drinking water. Furthermore, the sensor has been re-tested using the same sets of test/water samples but using electrochemical impedance spectroscopy analysis method to understand the response between the sensors and aqueous solution. The outcomes verified the results in the latter experiment (single frequency operation).

CHAPTER 6

Multilinear Regression Analysis and Independent Component Analysis

6.1 Introduction

In this chapter, two models based on multilinear regression method (*MLR*) and independent component analysis are considered to estimate the amount of nitrate in natural water sources.

6.2 Multilinear Regression Method

Multilinear regression method is a statistical technique that can be used to predict a variable on the value of chemical concentration in water from the correlation with several other variables. Suppose the concentration of nitrate in the water needed to be estimated. Variables such as the real part sensitivity and the imaginary part sensitivity at different frequencies might contribute to the prediction of the amount of nitrate in the water samples. If the data were collected from these variables, perhaps by surveying a few prepared water samples with different known values of nitrate concentrations, a model can be estimated based on this data. This model may be used to estimate nitrate in other water samples from the natural sources such as river. Furthermore, multilinear regression method (*MLR*) has been successfully applied to estimate the quality of ground water [136] and to estimate moisture in peanuts still in their shell [137]. This section will try to apply multilinear regression to estimate nitrate contamination in water supply using the output form SECS22_1 sensor.

6.2.1 Preparation of Water Samples

SECS22_1 is tested with nitrates forms namely; sodium nitrates ($NaNO_3$) and ammonium nitrates (NH_4NO_3), each of different concentration between 5 mg and 20 mg dissolved in 1 litre of Milli-Q water and the real part and imaginary part of the sensors' impedance are observed. For every aqueous solution type (sodium nitrates ($NaNO_3$) or ammonium nitrates (NH_4NO_3)) a semi-empirical equation based on multilinear regression model was determined from the percentage changes of real part and imaginary part values as compared to the mean real part, R_{total} and imaginary part, X_{total} calculated from Milli-Q water at two frequencies and known concentration (KC) values. The semi-empirical equation could be used to determine the predicted concentration (PC) values of nitrates contamination (sodium nitrate or ammonium nitrate form) in natural water source.

6.2.2 Results and Discussion

The experimental setup has been described in Section 5.3. The operating frequencies of 164 kHz, 260 kHz, 350 kHz and 800 kHz were used in this experiment. The first step is to find two operating frequencies that can give the best linear relationship between real part and imaginary part sensitivities versus nitrate samples concentration in mg/L. Then, the selected data set are used to develop semi-empirical multilinear regression equations to estimate nitrates contamination in natural water sources. The real part and imaginary part sensitivity are calculated using the following equations:

$$\%R_{total\_f} = \frac{R_{total\_sample\_f} - R_{total\_Milli-Q\_f}}{R_{total\_Milli-Q\_f}} \times 100 \qquad \textbf{6.1}$$

$$\%X_{total\_f} = \frac{X_{total\_sample\_f} - X_{total\_Milli-Q-Q\_f}}{X_{total\_Milli-Q\_f}} \times 100 \qquad \textbf{6.2}$$

In general, the real part sensitivity negatives values progressively decreases with the total concentration of the chemicals as shown in Figures 6.1 and 6.2. The electrical conductivity; σ of the solution of water is highly dependent on its concentration of dissolved salts where $NaNO_3$ and NH_4NO_3 were added in the Milli-Q water. The

conductivity is increased (the resistivity is decreased) as the concentrations is increased and vice versa. Therefore, the real part sensitivities give the indirect relationship of total amount of chemical concentrations with the quality level of the water samples. The sensitivity of the imaginary part for both type of aqueous solutions is increasing when the concentrations were increased at frequency of 164k Hz and 800 kHz in Figure 6.1(a), 6.1(d), 6.2(a), and 6.2(d). The change of the imaginary sensitivity is caused by the decrease in the sensor's coating capacitance C_c, resulting from a decreased in the relative permittivity of the water samples when the chemical concentration increased. It is also shown in Table 6.1 that the slope values of the $NaNO_3$ and NH_4NO_3 linear regressions of imaginary part are significantly larger. It can be concluded that the operating frequencies of 164 kHz and 800 kHz will be used to develop multilinear regression models. Both frequencies give the best linear plots of between real part and imaginary part sensitivities versus nitrate samples concentration in mg/L.

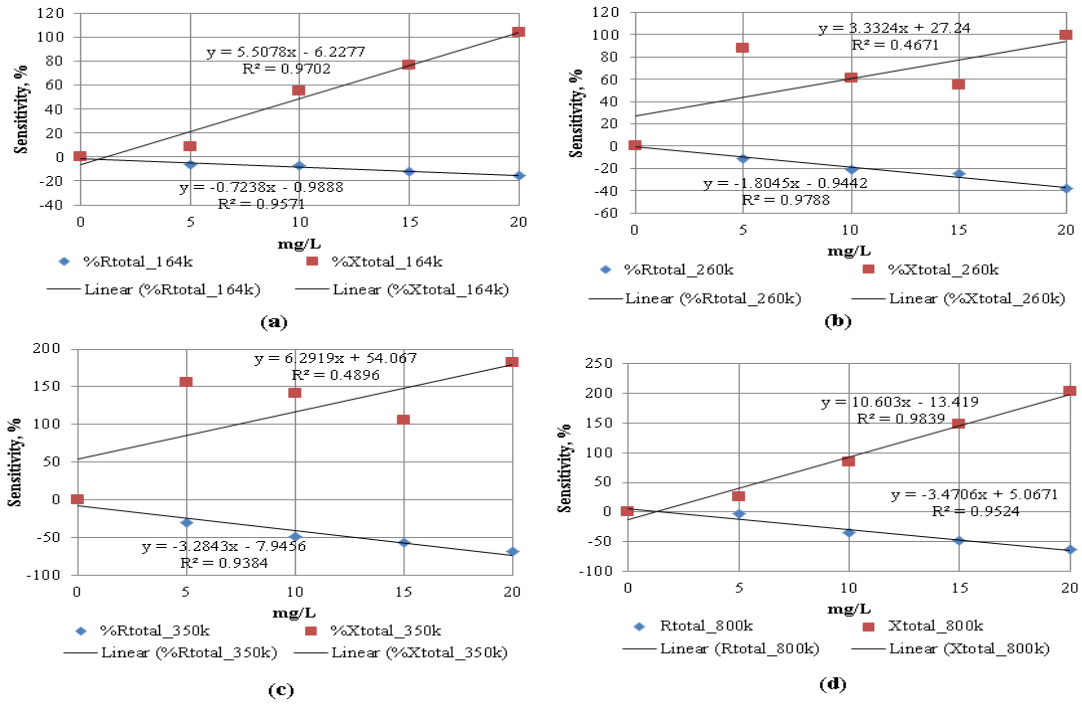

Figure 6.1: $NaNO_3$ sensitivities of real and imaginary: (a) 164 kHz, (b) 260 kHz, (c) 350 kHz, and (d) 800 kHz

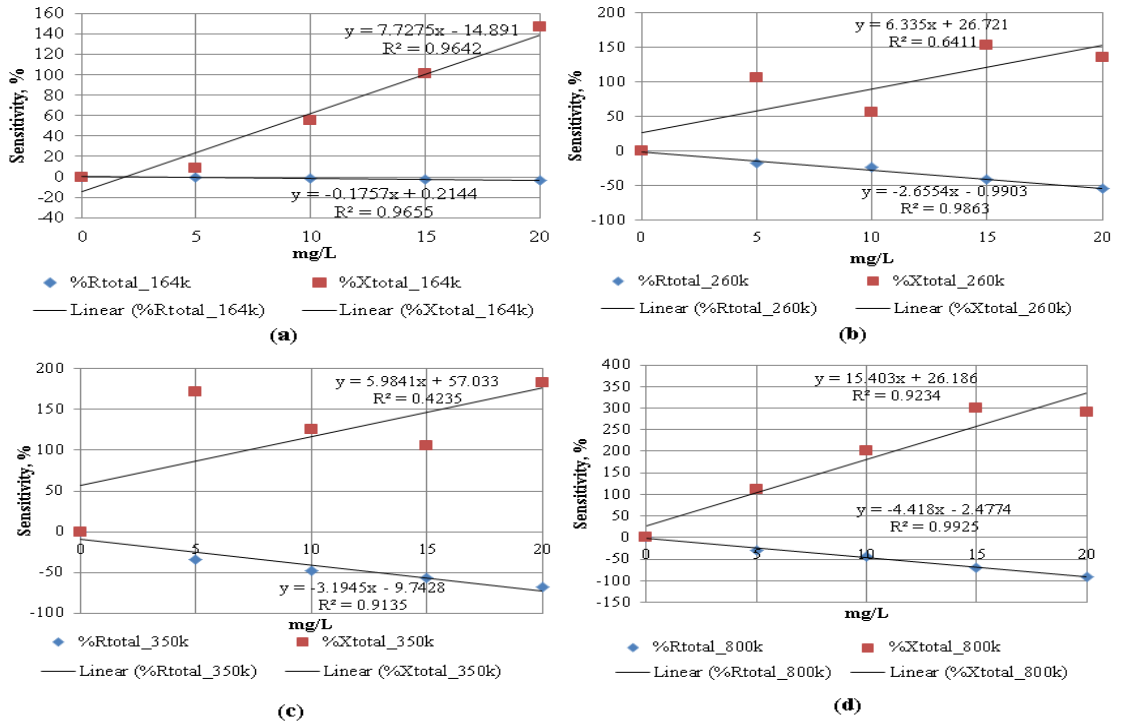

Figure 6.2: NH_4NO_3 sensitivities of real and imaginary: (a) 164 kHz, (b) 260 kHz, (c) 350 kHz, and (d) 800 kHz

Table 6.1: Summary of linear plots in Figures 6.1 and 6.2

SECS22_1	Linear regression of $\%R_{total\_f}$				Linear regression $\%X_{total\_f}$			
	$NaNO_3$		NH_4NO_3		$NaNO_3$		NH_4NO_3	
Freq, kHz	R^2	slope	R^2	slope	R^2	slope	R^2	slope
164	0.9571	-0.724	0.9655	-0.1757	0.9702	5.5078	0.9642	7.7275
260	0.9788	-1.805	0.9863	-2.6554	0.4671	3.332	0.6411	6.335
350	0.9384	-3.284	0.9135	-3.194	0.4896	6.292	0.4235	5.9841
800	0.9524	-3.4704	0.9925	-4.418	0.9839	10.603	0.9234	15.403

From the sensitivities of real part and imaginary part values at 164 kHz and 800 kHz and known concentration (*KC*) values in mg/L involving Milli-Q water and both $NaNO_3$ and NH_4NO_3 solutions. The multilinear regression (*MLR*) semi-empirical equations for $NaNO_3$ and NH4NO3 were developed using Excel given as the following equations:

$$\text{SECS22\_1 (mg/L}_{\text{NaN03}}) = 0.091 + 0.448\times \%R_{total\_f1} - 0.024\times\%R_{total\_f2} - 1.102\times\%X_{total\_f1} - 0.1062\times\%X_{total\_f2} \quad \textbf{6.3}$$

$$SECS22\_1(mg/L_{NH4N03}) = -0.083 + 0.3049\times \%R_{total\_f1} - 0.068\times\%R_{total\_f2} - 0.832\times\%X_{total\_f1} - 0.023\times\%X_{total\_f2} \quad \textbf{6.4}$$

where, $\%R_{total\_f1}$ = real part sensitivity at 164 kHz.

$\%X_{total\_f1}$ = imaginary part sensitivity at 164 kHz.

$\%R_{total\_f2}$ = real part sensitivity at 800 kHz.

$\%X_{total\_f2}$ = imaginary part sensitivity at 800 kHz.

For all models in equations 6.3 and 6.4, all independent values is highly correlated with the dependent value as the R^2 and Adjusted R^2 values are near to 1 as can be seen in Table 6.2. The standard error values in Table 2 represent the estimation of the standard deviation. The standard deviation value for SECS22_1(mg/L_{NaN03}) and SECS22_1(mg/L_{NH4N03}) are 0.4518 and 0.7191, respectively.

Table 6.2: Summary of MLR modes

Model	R^2	Adjusted R^2	Standard Error
SECS22_1 (mg/L_{NaN03})	0.9960	0.9959	0.4518
SECS22_1(mg/L_{NH4N03})	0.9900	0.9897	0.7191

SECS22_1(mg/L_{NaN03}) model is tested with water samples as following:

1) Manawatu river water samples.
2) Manawatu river water sample added with known concentration, *KC* of $NaNO_3$ (5.1 mg/L).
3) Manawatu river water sample added with known concentration, *KC* of $NaNO_3$ (10.7 mg/L),
4) Manawatu river water sample added with known concentration, *KC* of $NaNO_3$ (15.0 mg/L),
5) Manawatu river water sample added with known concentration, *KC* of $NaNO_3$ (20.00 mg/L),

Similarly, SECS22_1(mg/L_{NH4N03}) model is tested with water samples as following:

1) Manawatu river water samples.
2) Manawatu river water sample added with known concentration, *KC* of NH_4NO_3 (5.1 mg/L).
3) Manawatu river water sample added with known concentration, *KC* of NH_4NO_3 (10.7mg/L).
4) Manawatu river water sample added with known concentration, *KC* of NH_4NO_3 (15.0 mg/L).
5) Manawatu river water sample added with known concentration, *KC* of NH_4NO_3 (20.00 mg/L).

Figures 6.3 and 6.4 illustrate the results of SECS22_1(mg/L_{NaN03}) and SECS22_1(mg/L_{NH4N03}), respectively when tested with the water sample as listed above. The initial values for $NaNO_3$ and NH_4NO_3 are 2.49 mg/L and 18.693 mg/L, respectively. These values are estimated when SECS22_1(mg/L_{NaN03}) and SECS22_1(mg/L_{NH4N03}) are tested with Manawatu river water sample.

The outcomes concluded that the multilinear models cannot be used to estimate the amount of nitrate contamination of in river water samples as can be seen in Figures 6.3 and 6.4. The main reason is because the multilinear regression models in this experiment ware developed using ideal samples of nitrate ion. However, in the actual river water sample, there are more ion species and the SECS22_1 output is actually representing the combination of many ion species. Therefore, the next section will try to overcome the problem of interference of other ion species in estimating the amount of nitrate contamination.

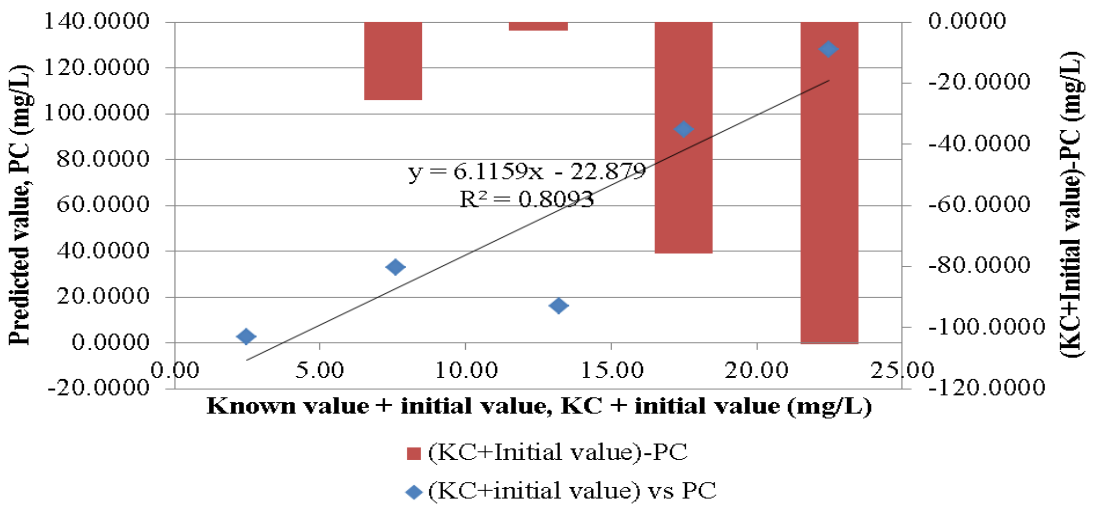

Figure 6.3: $NaNO_3$: KC+initial value versus PC and the difference between KC+initial and PC

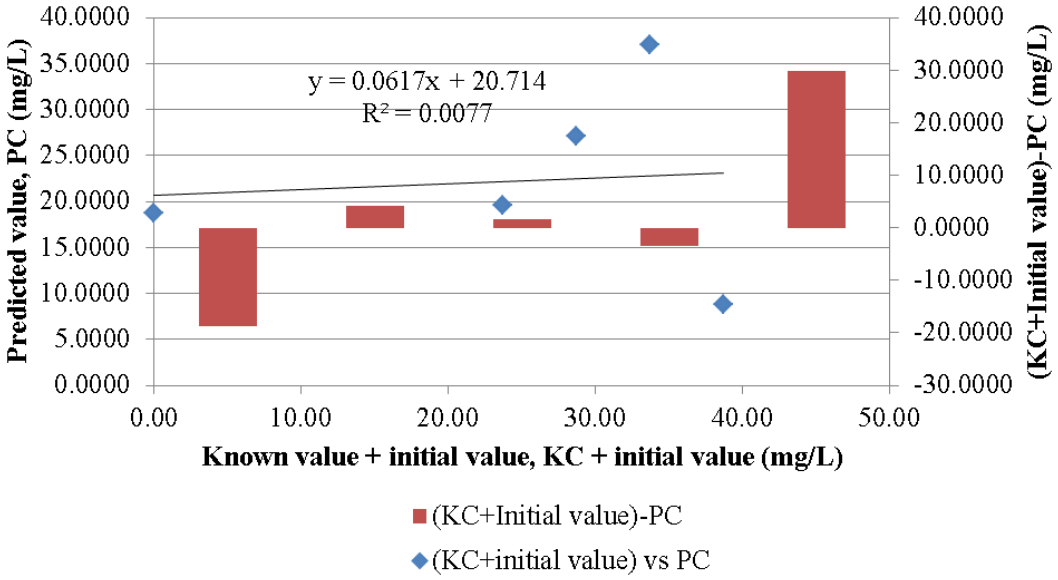

Figure 6.4: NH_4NO_3: KC+initial value versus PC and the difference between KC+initial and PC

6.3 Independent Component Analysis Method

In this section, the output parameters of SECS22_1 are analysed based on electrochemical impedance spectroscopy. An equivalent circuit is used to describe the interaction of the sensor output with different kind of water samples at different concentrations. The output parameters are derived and tested where the suitable signal forms are incorporated with independent component analysis (*ICA*). SCES22_1 is tested to estimate the amount of nitrate contamination in water samples with the assistance of independent component analysis based on *FastICA* fixed point algorithm under the contrast functions of *pow3*, *tanh*, *gauss*, and *skew*. Nitrates sample in the form of ammonium nitrates (NH_4NO_3), each of different concentration between 5 mg and 20 mg dissolved in 1 litre of deionized water (Milli-Q) was used as one of the main references. A model based on independent component analysis (*FastICA*: *pow3*, *tanh*, *gauss*, and *skew*) is developed to estimate nitrate contamination. The model was tested with eight sets of mixed NH_4NO_3 and $(NH_4)_2HPO_4$ water samples. The model is also tested with water samples were taken from Manawatu River nearby Hokowhitu campus, Massey University, New Zealand.

6.3.1 Preparation of Water Samples

In this section, two sets of water solutions were used as reference sets and initial test samples in the experiment. The other water samples involve the river water taken from the Manawatu River. The next section will discuss the preparation of the reference sets and initial test sample sets.

6.3.1.1 Reference Sets of Water Samples

The reference sets comprise of ammonium nitrate (NH_4NO_3) and diammonium phosphate ($(NH_4)_2HPO_4$) solutions at different concentration between 5 mg/L and 115 mg/L. Table 6.3 summarizes the water solutions for the reference sets. NH_4NO_3 and $(NH_4)_2HPO_4$ were chosen for the experiment because they are the two of the most common chemical

compounds used for the making of inorganic fertilizer [138, 139]. NH_4NO_3 water solutions serve as the main reference in measuring nitrate (NO_3^-). Basically, solid NH_4NO_3 is dissolved in water to produce an aqueous ammonium nitrate solution as follows:

$$NH_4NO_3\ (s) \rightarrow NH_4^+\ (aq) + NO_3^-\ (aq) \qquad \textbf{6.5}$$

The positive ion NH_4^+ is a weak base and NO_3^- is a strong acid. Furthermore, the ammonium nitrate is mixed with water, resulting:

$$NH_4NO_3 + H_2O \rightarrow NH_4OH + HNO_3 \qquad \textbf{6.6}$$

NH_4OH further dissolves to:

$$NH_4OH \rightarrow NH_3 + H_2O \qquad \textbf{6.7}$$

The NH_3 is the ammonia gas and it evaporates into the atmosphere. So the remaining HNO_3 remains as H^+ and NO_3^-. So basically, for the first reference set, the nitrate concentration is measured. $(NH_4)_2HPO_4$ water solutions were set as the other contamination and used to test the capability of the independent component analysis to estimate NO_3^- under the presence of other type of contaminations.

Table 6.3: Water samples as references

Sample Number	***Concentration of NH_4NO_3 (mg/L)***	***Sample Number***	***Concentration of $(NH_4)_2HPO_4$ (mg/L)***
1	5.5	7	5.0
2	10.6	8	10.0
3	15.1	9	15.0
4	21.0	10	21.2
5	61.0	11	61.7
6	110.0	12	113.5

6.3.1.2 Water Samples as Test Samples in Experiment

In this set, eight different groups of water samples were prepared where each group was divided into nine samples. The water sample groups are basically the combination of NH_4NO_3 and $(NH_4)_2HPO_4$ in the ratio of 1:1 from the range of 5mg/L:5mg/L to 100mg/L:100 mg/L. For example, three separate beakers were each filled with one litre of Milli-Q water. Then, each beaker was added with NH_4NO_3 and $(NH_4)_2HPO_4$ with the same amount of 5mg/L:5mg/L. Next, each beaker was divided into three samples. Therefore we have one group of water samples of nine. Table 2 summarizes the water sample group used in the experiment.

Table 6.4: Water Samples as test samples

Water Samples Group	***Concentration of NH_4NO_3 (mg/L)***	***Concentration of $(NH_4)_2HPO_4$ (mg/L)***
Group 1	5.0	5.0
Group 2	10.2	10.2
Group 3	15.3	15.4
Group 4	20.3	20.3
Group 5	40.1	40.1
Group 6	60.3	60.3
Group 7	80.2	80.4
Group 8	100.4	100.2

6.3.2 The Concept of Independent Component Analysis

Independent component analysis (*ICA*) is a powerful statistical tool to deal with issues related to separation of mixed signals problems. This concept was introduced in the end of 80's by Jutten and Herault [140]. One of the earliest demonstrations involved the recovering of the original speech signals of different speaker from mixed sound signals that are produced by different microphone [140, 141]. Two important aspects of *ICA* that made it so popular are it has the potential for blind-sources separation and feature extraction, where independent components (ICs) can be estimated from the mixed signals [140, 141]. In comparison with other methods such as Principal Component Analysis (*PCA*), *ICA* assumes that the inputs are statistically independent while the outputs are mutually independent and have non-Gaussian distribution [142].

The *ICA* method has been applied in many different areas, e.g. percentage estimation of fat content in meat [143], extraction of profiles from overlapping Gas Chromatography and Mass Spectra signals with background [144, 145], identifying constituents in commercial gasoline [146], estimation of compound distribution in spectral images for sorting tomatoes [147], monitoring and alert system for environment water [148], analysis of biomedical signals such as EEG, MEG and ECG [149, 150], identifying natural compound [151], and biomedical image processing [152, 153].

This section will discuss the basic concept of ICA. Consider linearly mixed signals given by the following equation:

$$X = AS \qquad \textbf{6.8}$$

Where X is an n×m matrix of mixture of source signals, A is an n×d mixing matrix, which characterizes the medium (material under test) through which the source signals transverse, and S is a d×m matrix of source signals. The main objective of ICA is to estimate mixing matrix A and/or the source matrix S from the observed matrix X. The components of matrix X are assumed statically independent, which can be concluded from non-Gaussianity. The in depth explanation of *ICA* concept is available in [140, 141].

In this research, a fixed point algorithm, *FastICA* developed using *Matlab* was used to implement ICA analysis [141, 154]. *FastICA* is based on the optimization of a nonlinear contrast function measuring the non-Gaussianity of the sources. There are two versions of the *FastICA* namely one-unit (deflation) algorithm and symmetric algorithm. In this study, one-unit (deflation) algorithm was employed. The weight vector was selected as random. The nonlinear contrast functions involved were *pow3*, *tanh*, *gauss*, and *skew* [141, 154].

The output responses of SECS22_1 sensor were analyzed and tested to suit with the application of ICA. Furthermore, to overcome the effect of interference of other major ions existed in natural water as commonly encountered in the other nitrate detection methods [17, 26], the output responses were decomposed into independent component

signals using FastICA. The independent component signals were matched with the reference spectra of nitrate before the concentration was estimated.

6.3.3 Experimental Setup and Data Analysis

The experimental setup is shown in Figure 5.1 (Section 5.3), the setup has a frequency waveform generator where standard sinusoidal waveform with 10 Volts peak-to-peak value was set as the input signal for the sensors. An old microscope was used as a platform for the sample container and the sensors were partially immersed into the water sample. A signal oscilloscope was interfaced to a PC where the output signals and the sensor's impedance was calculated using *LabView* software. The measurements were done at frequency range between 1 kHz and 10 MHz. Before the experiment, the sensor was sprayed with Wattyl Killrust Incralac to form an acrylic resin-based protective coating. The effect of the samples on the sensor's impedance was recorded.

6.3.3.1 Equivalent Circuit of the System

Electrochemical impedance spectroscopy approach was used to describe the reaction of the sensor with water samples based on the parameters of the equivalent circuit of electrochemical spectroscopy system with intact Wattyl Killrust Incralac coating. Figure 5.17 in Section 5.3.3.1 describes a system for coated sensor's surface response to aqueous solution as has been described as described in [124]. The total impedance is calculated from Eq. 2.6. The circuit composed of the solution resistance (R_s), coating resistance (R_c), and coating capacitance (C_c). An additional meander inductance (L) has been added to represent the system. The coating capacitance (C_c) is assumed to be mainly contributed by the interdigital part.

6.3.3.2 Response of the Sensor to Water Samples

Figure 6.5 shows the responses of the sensor to water samples as described in Section 6.3.1.1 calculated from Eq. 2.6. It can be seen form Figures 6.5(a) and 6.5(c) that the impedance values significantly decreasing from 10 kHz to 100 kHz when the chemical concentration is increasing. Furthermore, for chemical concentration higher than 0 mg/L, the impedance curve valley (the lowest point) is further shifting to the right with the increasing chemical concentration. A significant differentiation between concentrations can be observed from the phase plots in Figures 6.5(b) and 6.5(d).

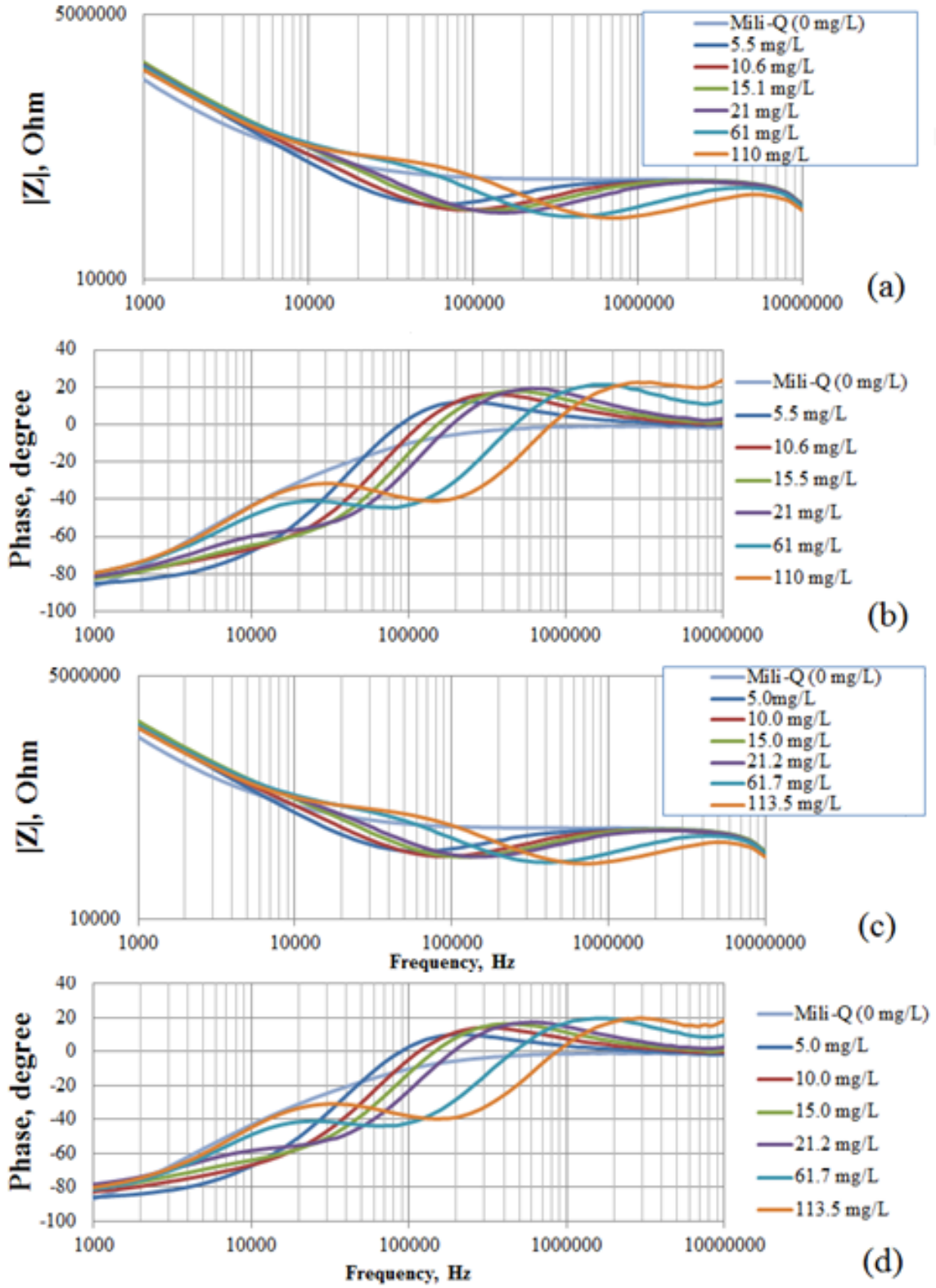

Figure 6.5: Impedance plots ((a) and (c)) and phase plots ((b) and (d)) of SECS22_1 for NH_4NO_3 and $(NH_4)_2HPO_4$ solutions, respectively

The parameter values in Figure 5.17 are estimated from the impedance responses in Figure 6.5 using a software called EIS spectrum analyser [127]. Figures 6.6(a)-(d) depict the estimated parameter values for NH_4NO_3/$(NH_4)_2HPO_4$ solutions at concentration values between 0 mg/L and 113.5 mg/L. In general, R_s is exponentially decreasing with the increasing chemical concentration for both NH_4NO_3 and $(NH_4)_2HPO_4$ solutions as can be on observed in Figure 6.6(a). R_s has inverse relationship with electrical conductivity of the solution e.g. water solution with high resistance has low electrical conductivity [116]. In low chemical concentration range, the low electrical conductivity is caused by a strong solvation effect and small mobility of solvated ions. The increasing chemical concentration encouraged the desolvation process and strong ion-ion interactions resulting in increase in conductivity level [155]. C_C is exponentially decreasing with the increasing chemical concentration for both NH_4NO_3 and $(NH_4)_2HPO_4$ solutions as can be seen in Figure 6.6(b). The change of the relative permittivity value is due to the effect of polymer changes with increasing chemical concentration. In the range of chemical value below 15 mg/L, *Rc* values increase from above 10^7 ohms to around 10^8 ohms for both NH_4NO_3 and $(NH_4)_2HPO_4$ solutions.

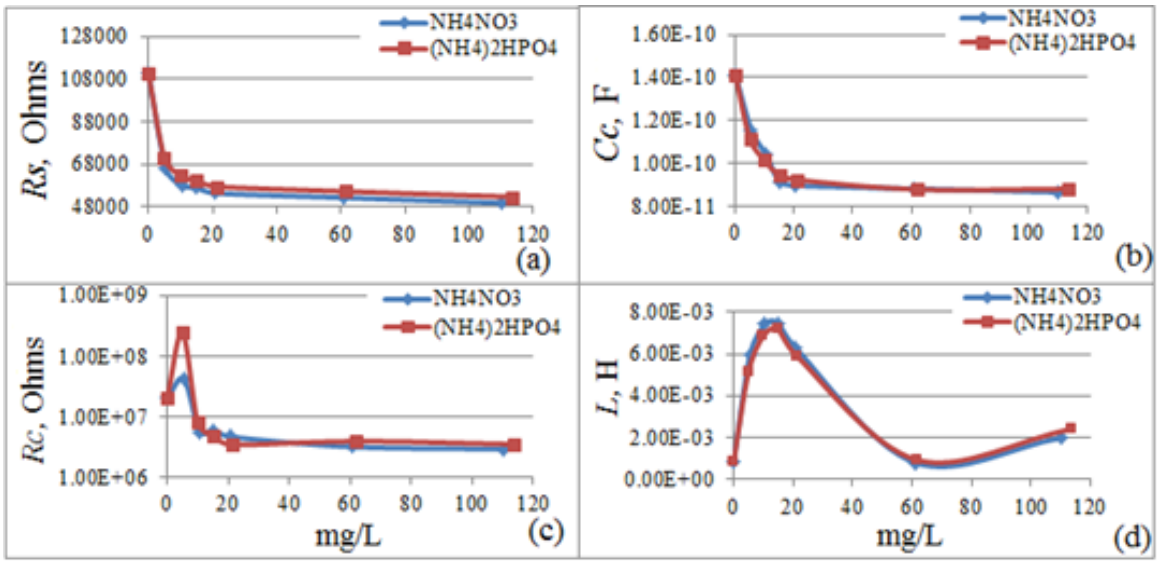

Figure 6.6: (a) The estimated solution resistance, R_s (b) The estimated coating capacitance, C_C (c) The estimated coating resistance, R_c (d) The effective Inductance, L at different concentration values between 0 mg/L and 113.5 mg/L of NH_4NO_3/$(NH_4)_2HPO_4$

There are significant decreases of values to around 3×10^6 ohms/cm^2 as can be seen in Figure 6.6(c) above 15 mg/L indicating the coating is still intact unless dropped to

value range below 10^6 ohms [123]. Figure 6.6(d) illustrates that the effective inductance has a nonlinear relationship with the chemical concentration values where the parameter *L* is associated with the inductance influenced by the resistive components of the meander sensor especially at high frequency [156].

6.3.3.3 Selection of Proper Signals for ICA

In this section, the approach to select the suitable signals for ICA analysis will be discussed. The signals are based on the sensitivities of the sensors which are calculated from the real part and imaginary part using Eq. 5.1 and 5.2, respectively. Another signal is introduced based on the output voltage, V_3 (the voltage across the series resistor) given by the following equation:

$$\text{Output sensitivity, } \%V = \frac{(V)_{sample} - (V)_{Milli-Q}}{(V)_{Milli-Q}} \times 100 \qquad \textbf{6.9}$$

where, $\%V$ = the output sensitivity.

$V_{Milli\text{-}Q}$ = the output voltage measured across the series resistor when the sensor is immersed in the Milli-Q.

V_{sample} = the output voltage measured across the series resistor when the sensor is immersed in the water sample.

Figures 6.7 (a), (c) and (e) illustrate the spectra of *%R*, *%X*, and *%V*, respectively of the sensor for NH_4NO_3 solutions at different concentration between 5.5 mg/L and 110 mg/L. Figures 6.7 (b), (d) and (f) show the spectra of *%R*, *%X*, and *%V*, respectively of the sensor for $(NH_4)_2HPO_4$ solutions at different concentration between 5.5 mg/L and 113.5 mg/L. Applying *ICA* directly with any of the data in Figure 6.7 is not suitable because the spectra in Figure 6.7 evidently have a baseline, which is not desired in ICA analysis [143]. Furthermore, it is hard to differentiate between the references spectrums having almost same concentration e.g. spectrum in Figure 6.7(e) with spectrum in Figure 6.7(f) etc. Therefore, a conventional approach to correct the baseline problem is to apply

second derivative spectra [143, 157] to all of the sensitivities forms. As for example, the second derivative for output sensitivity is given by the following equation:

$$\%V'' = \frac{d^2(\%V)}{df^2} \qquad \textbf{6.10}$$

Another important consideration in ICA, the scale of resulting signal (independent component) is not same as original data [141, 154], to overcome this problem, each resulting spectrum was normalized. Figures 6.8 (a) and (b) shows the second derivative spectra of *%R''* of NH_4NO_3 (5.5 mg/L) and *%R''* of $(NH_4)_2HPO_4$ (5.0 mg/L), respectively. Both spectra have a peak just after 1 kHz which overwhelming the information in the rest of the frequency ranges rendering disadvantages for differentiation process. Better results are obtained from the *%X''* in Figures 6.8(c) and (d), however, the active region is limited at around 400 kHz to 10 MHz. The best outcome can be concluded from *%V''* in Figures 6.8(e) and (f). Both spectra have the same maximum peak about 11 kHz but they are substantially different compared at the whole frequency range. It is clearly seen that the second derivative method (of *%V*) has not only removed the baseline but also greatly differentiate between different chemical species.

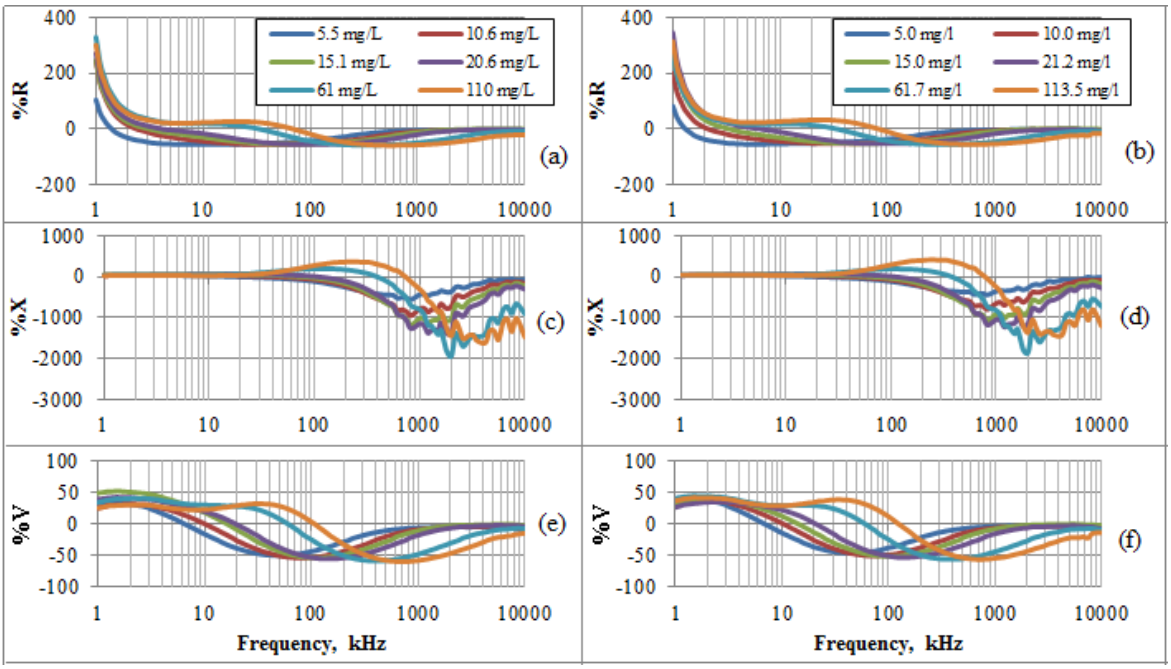

Figure 6.7: Sensitivities of sensor: NH_4NO_3 solutions: (a) %R (c) %X, (e) %V. $(NH_4)_2HPO_4$ solutions: (b) %R (d) %X, (f) %V

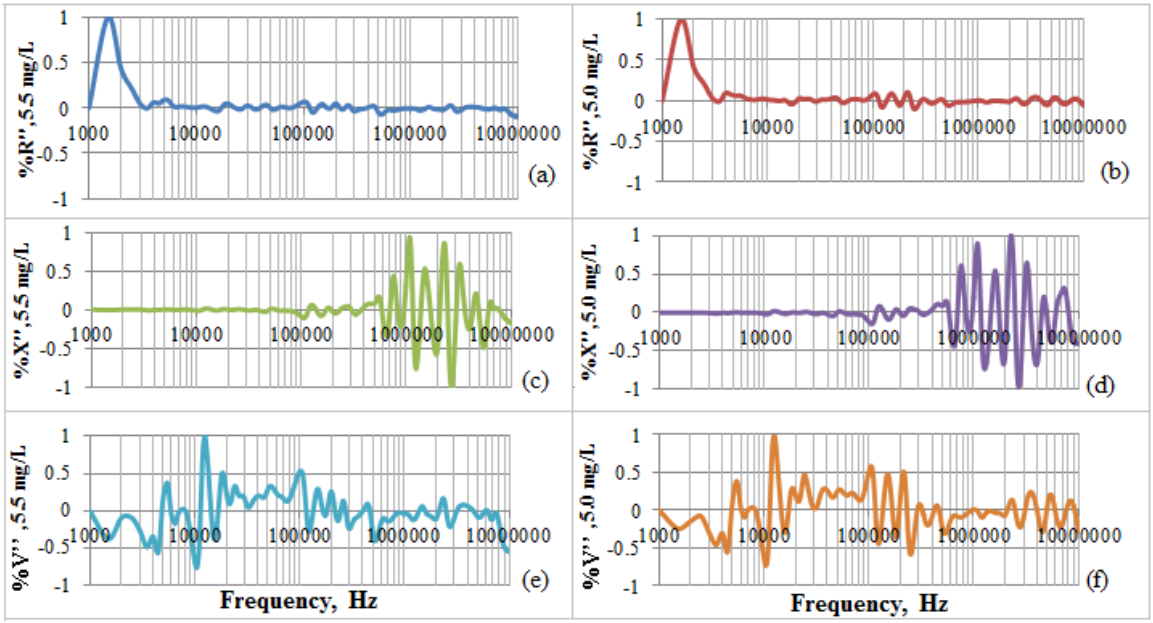

Figure 6.8: Second derivative of sensitivities of sensor: (a) %R'' of NH_4NO_3 with 5.5 mg/L (b) %R'' of $(NH_4)_2HPO_4$ with 5.0 mg/L (c) %X'' of NH_4NO_3 with 5.5 mg/L (d) %X'' of $(NH_4)_2HPO_4$ with 5.0 mg/L (e) %V'' of NH_4NO3 with 5.5 mg/L (f) %V'' of $(NH_4)_2HPO_4$ with 5.0 mg/L

Figures 6.9(a) shows the *%V* spectra of nine water samples of group 5 as explained in section 2.2. Each spectra consists the combination of NH_4NO_3 and $(NH_4)_2HPO_4$ in 40.1 mg/L and 40.4 mg/L, respectively. Each spectrum in Figure 6.9(a) is the weighted sum of the spectra of the two constituent components, i.e. NH_4NO_3 and $(NH_4)_2HPO_4$ and the weights depend on the concentration of each component. Figure 6.9(b) is the *%V''* of spectra in Figure 6.9(a). From Figure 6.9(b), it can be seen that the maximum peak has shifted further to the right as the chemical concentration is increased as compared to spectra of Figures 6.8 (e) and (f). The next steps will discuss the analysis method based on *ICA*.

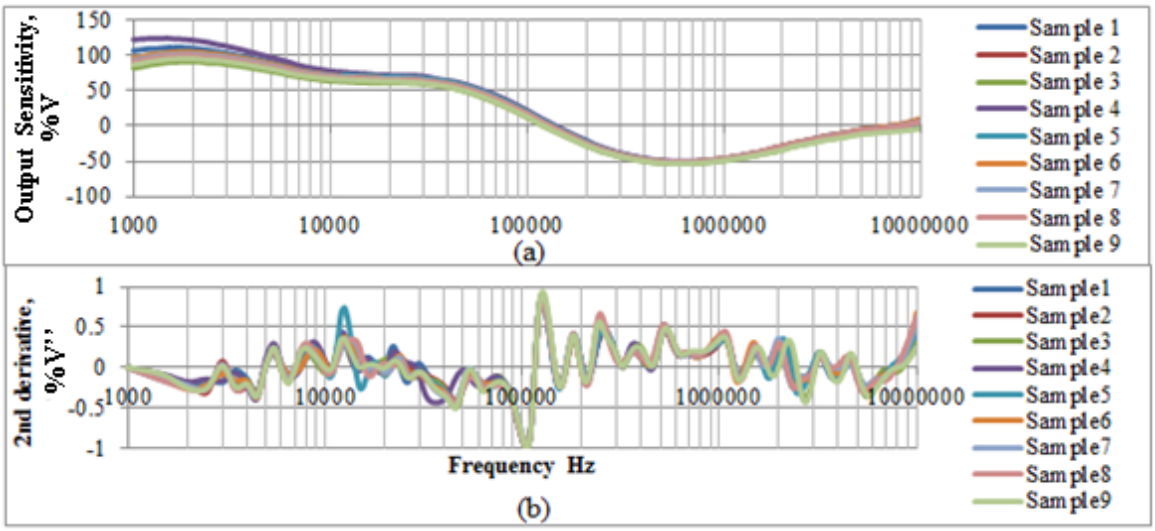

Figure 6.9: Samples of (a) Output sensitivities of the sensor and (b) Second derivative of the sensitivity of the sensor

6.3.4 Description of the Analysis Method

The analysis method consists of three main components: the application of fixed point algorithm (*FastICA*), spectral matching, and contamination calculation as summarized in Figure 6.10. In this study, eight different groups of water samples were tested where each group was divided into nine samples as described in Section 6.3.1.2. The second derivatives of all the samples in Section 6.3.1.2 are obtained. By default, the number of independent component is the same with the number of inputs. Therefore, in this experiment, nine independent components (ICs) were obtained. Figure 6.11 shows the resulting independent components (ICs) of second derivative spectra of the group 5 water samples (Figure 6.9(b)) under *pow3* contrast function setting. The ICs are assumed to be independent of the influence of any major ions combinations.

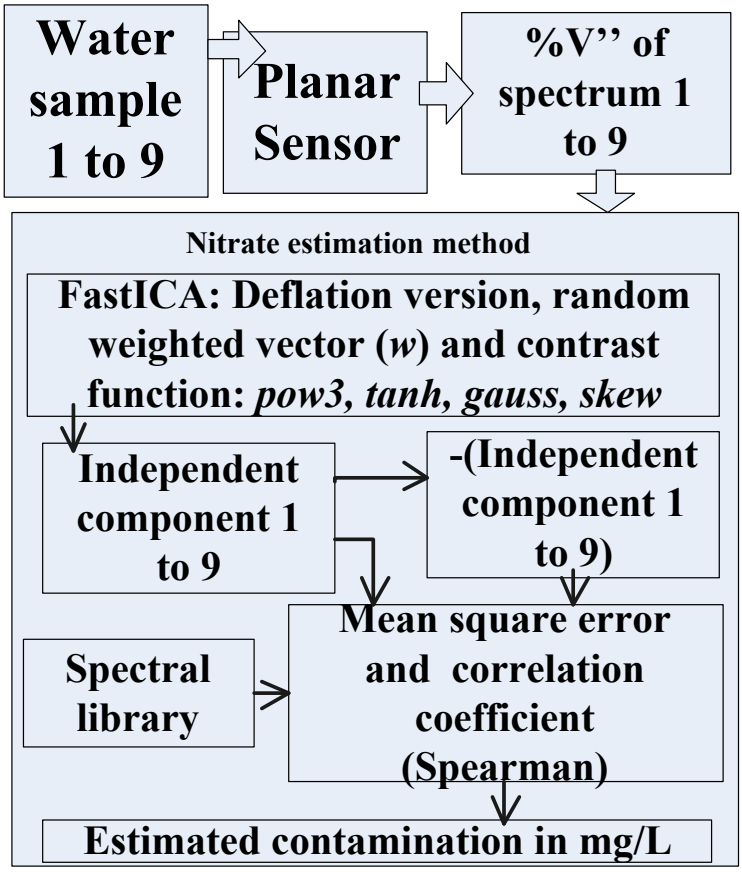

Figure 6.10: The schematic of the nitrate contamination estimation method

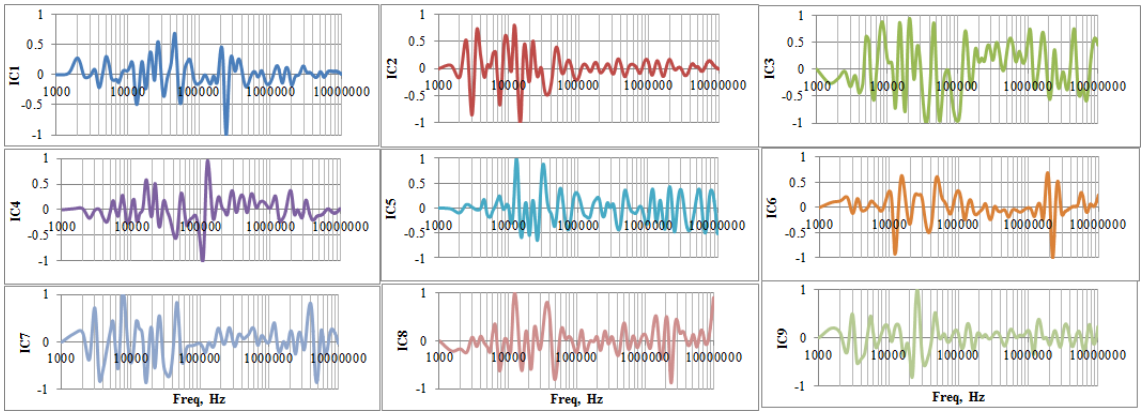

Figure 6.11: The independent components (ICs) resulting from Figure 6.9(b) using pow3 contrast function

The reference spectra in the spectral library consist of the second derivative of NH_4NO_3 and $(NH_4)_2HPO_4$ spectral in Figures 6.7 (e) and (f), respectively. Each of the resulting ICs is evaluated with the reference spectral using mean square error (*MSE*) and Spearman correlation coefficient (r^2) [158]. Another evaluation parameter given by the

ratio of r^2 to *MSE* called as defining factor value (*DFV*). However, another major problem of ICA analysis is some of the resulting ICs maybe “inverted" by x-axis [141]. Therefore, the evaluation process is repeated with ICs multiplied with -1 (-ICs). All the contrast functions have been tested in the experiment. The next section will discuss the calculation method for the contrast functions.

6.3.4.1 Calculation of Nitrate Contamination for *pow3* and *skew*

Tables 6.5 and Table 6.6 summarize the results from the evaluation of water sample of group 4 using *pow3*. Tables 6.7 and 6.8 summarize the results from the evaluation of water sample of group 5 using *pow3*. Referring to results in Table 6.5 which involve the evaluation of group 4 water samples with NH_4NO_3. All ICs and -ICs are referred to a specific reference value based on the highest *DFV* value yielded. For example, IC6 and IC7 are both referring to 5.5 mg/L of NH_4NO_3 in Table 6.5(a). Note that IC5 and IC9 are missing in Table 6.5(a) because the highest *DFV* value is in negative range, therefore they were omitted. The lowest value range and highest value range need to be identified for both ICs and –ICs e.g. the lowest values range in ICs of Table 6.5(a) are 5.5 mg/L and 110 mg/L.

Table 6.5:(a) ICs of group 4 for NH_4NO_3 using *pow3* (b)-ICs of group 4 for NH_4NO_3 using *pow3*

(a)

NH_4NO_3									
					IC3				
POW3	Reference, *mg/L*	r^2	*DFV*	Main Reference	Reference, mg/L	*MSE*	r^2	y_1, y_2	c_1
IC6	5.5	0.170	1.946		5.5	0.079	-0.108		
IC7	5.5	0.358	8.842		10.6	0.068	-0.031		
IC8	5.5	0.187	2.603		15.1	0.049	0.251	30.451	
IC4	10.6	0.598	8.102		20.6	0.025	0.364	13.102	
IC3	20.6	0.364	14.514	✓	61	0.032	0.327		21.776
IC1	61	0.336	11.451		110	0.077	0.486		
IC2	110	0.187	2.252						

(b)

NH_4NO_3										
					"-IC5"					
"-POW3"	Reference, *mg/L*	r^2	*DFV*	Main Reference	Reference, mg/L	*MSE*	r^2	y_1, y_2	c_1	*C*
"-IC1"	5.5	0.435	8.932		5.5	0.065	0.233			
"-IC2"	5.5	0.240	7.356		10.6	0.067	0.045			
"-IC3"	5.5	0.108	1.104		15.1	0.048	0.309	30.509		
"-IC5"	20.6	0.355	10.082	✓	20.6	0.035	0.355	13.287		
"-IC8"	20.6	0.247	4.294		61	0.033	0.208		21.900	21.838
"-IC4"	61	0.295	2.494		110	0.074	0.068			
"-IC6"	61	0.095	1.290							
"-IC7"	110	0.333	5.081							

Table 6.6:(a) ICs of group 4 for $(NH_4)_2HPO_4$ using *pow3* (b)-ICs of group 4 for $(NH_4)_2HPO_4$ using *pow3*

(a)

$(NH_4)_2HPO_4$									
					IC3				
POW3	Reference, *mg/L*	r^2	*DFV*	Main Reference	Reference, mg/L	*MSE*	r^2	y_1, y_2	c_1
IC5	5	0.135	4.238		5	0.053	0.312		
IC6	5	0.171	2.887		10	0.060	0.146		
IC4	10	0.535	6.505		15	0.041	0.465		
IC1	61.7	0.238	5.334		21.2	0.024	0.430	30.322	
IC3	61.7	0.535	20.045	✓	61.7	0.027	0.535	28.678	29.500
IC2	113.5	0.301	3.367		113.5	0.173	0.552		

(b)

$(NH_4)_2HPO_4$										
					"-IC8"					
"-POW3"	Reference, *mg/L*	r^2	*DFV*	Main Reference	Reference, mg/L	*MSE*	r^2	y_1, y_2	c_1	*C*
"-IC1"	5	0.194	7.831		5	0.022	0.581	2.095		
"-IC8"	5	0.581	26.185	✓	10	0.059	0.210	12.096		
"-IC6"	10	0.041	0.366		15	0.033	0.568			
"-IC2"	21.2	0.282	5.352		21.2	0.062	0.282			
"-IC5"	21.2	0.147	2.803		61.7	0.069	0.044		7.096	18.298
"-IC7"	61.7	0.378	6.595		113.5	0.187	0.178			
"-IC4"	113.5	0.283	1.858							

Table 6.7:(a) ICs of group 5 for NH_4NO_3 using *pow3*(b)-ICs of group 5 for NH_4NO_3 using *pow3*

(a)

NH_4NO_3									
					IC3				
POW3	Reference, *mg/L*	r^2	*DFV*	Main Reference	Reference, mg/L	*MSE*	r^2	y_1, y_2	c_1
IC9	15.1	0.352	5.966		5.5	0.307	-0.272		
IC7	20.6	0.591	5.632		10.6	0.306	-0.369		
IC2	61	0.125	3.151		15.1	0.248	-0.139		
IC4	61	0.066	1.925		20.6	0.186	0.205		
IC5	61	0.220	2.406		61	0.136	0.597	95.611	70.707
IC3	110	0.774	10.021	✓	110	0.077	0.774	24.904	
IC8	110	0.194	1.605						

(b)

NH_4NO_3										
					"-IC1"					
"-POW3"	Reference, *mg/L*	r^2	*DFV*	Main Reference	Reference, mg/L	*MSE*	r^2	y_1, y_2	c_1	*C*
"-IC1"	5.5	0.396	8.607	✓	5.5	0.046	0.396	3.632		
"-IC5"	5.5	0.267	2.182		10.6	0.051	0.170	8.800		
"-IC6"	5.5	0.294	4.390		15.1	0.047	0.172	6.216		
"-IC8"	5.5	0.388	7.797		20.6	0.035	0.244			
"-IC2"	10.6	0.267	5.733		61	0.031	0.087		6.220	38.464
"-IC3"	10.6	0.369	2.480							
"-IC7"	10.6	0.387	3.564							
"-IC4"	20.6	0.241	4.602							
"-IC9"	61	0.301	6.986							

Table 6.8:(a) ICs of group 5 for $(NH_4)_2HPO_4$ using *pow3*(b)-ICs of group 5 for $(NH_4)_2HPO_4$ using *pow3*

(a)

$(NH_4)_2HPO_4$									
					IC3				
POW3	Reference, *mg/L*	r^2	*DFV*	Main Reference	Reference, mg/L	*MSE*	r^2	y_1, y_2	c_1
IC5	5	0.410	5.825		5	0.218	-0.100		
IC9	5	0.335	10.388	×	10	0.250	-0.079		
IC6	15	0.207	3.068		15	0.173	0.301		
IC7	15	0.414	3.778		21.2	0.205	0.135		
IC2	61.7	0.155	2.881		61.7	0.151	0.490	91.945	64.524
IC4	61.7	0.233	6.308		113.5	0.095	0.758	27.422	
IC3	113.5	0.758	7.983	✓					
IC8	113.5	0.356	3.312						

(b)

$(NH_4)_2HPO_4$										
					"-IC2"					
"-POW3"	Reference, *mg/L*	r^2	*DFV*	Main Reference	Reference, mg/L	*MSE*	r^2	y_1, y_2	c_1	*C*
"-IC2"	5	0.302	14.589	✓	5	0.021	0.302	3.490		
"-IC3"	5	0.100	0.567		10	0.037	0.228	13.020		
"-IC4"	5	0.181	5.246		15	0.024	0.286			
"-IC8"	10	0.413	7.379		21.2	0.048	0.227			
"-IC1"	21.2	0.363	9.052		61.7	0.047	-0.155		8.255	36.390
"-IC6"	61.7	0.498	11.256		113.5	0.174	-0.075			
"-IC7"	61.7	0.053	0.444							
"-IC5"	113.5	0.033	0.158							

One primary IC/-IC is selected between the ICs/-ICs with the highest *DFV*. For example, IC3 and –IC5 are the primary reference in Table 6.5(a) and Table 6.5(b), respectively. The primary IC/-IC should be changed to another IC/-IC that has higher reference value considering the following conditions:

a) If there is another IC/-IC that has higher r^2 value and the difference between the *DFV* values is less than 50% e.g. compared to the original IC/-IC in Table 6.8(a). IC9 was the primary IC based on the highest *DFV* value (10.39) but changed to IC3 because it has higher r^2 and the *DFV* difference is 23.15% as compared to IC9.
b) If there is another IC/-IC that has r^2 difference less than 40% value and *DFV* difference less than 50% compared to the original IC/-IC.

For the selected primary IC/-IC, the values of r^2 corresponding to the reference spectral are studied as shown in right hand side of Table 6.5(a) for instance. The total estimated concentration; *C* is calculated from the average of estimated concentration (c_1) calculated from IC and –IC. If the primary IC/-IC is at the lowest range, therefore:

$$c_1 = (y_1 + y_2)/2 \qquad \textbf{6.11}$$

$$y_1 = RV + (r^2)_{RV} \times RV \qquad \textbf{6.12}$$

$$y_2 = RV' - (r^2)_{RV'} \times RV' \qquad \textbf{6.13}$$

where *RV* is the primary IC/-IC reference value in mg/L and $(r^2)_{RV}$ is the corresponding r^2 value, y_2 is selected at the next higher reference mg/L value. *RV'* is the reference value in mg/L of y_2 and $(r^2)_{RV'}$ is the corresponding r^2 value of y_2. If the primary IC/-IC is at between the lowest range and the highest range, y_2 is selected at the next lower reference mg/L value. If the primary IC/-IC is at the highest range, the following conditions are considered:

c) If the total number of independent components in the highest range are less than the number of independent components at the opposite side. For example, there are two ICs in Table 6.7(a) referring to 110 mg/L (highest range) while there are four –ICs referring to 5.5 mg/L in Table 6.7(b), therefore:

$$c_1 = (y_2 - y_1) \quad \textbf{6.14}$$

$$y_1 = RV - (r^2)_{RV} \times RV \quad \textbf{6.15}$$

$$y_2 = RV' + (r^2)_{RV'} \times RV' \quad \textbf{6.16}$$

where y_2 is selected at the next lower reference mg/L value.

d) For the condition that is contrary to the case in c) , c_1 is calculated from Eq. 6.11, y_1 from Eq. 6.12 and y_2 from Eq. 6.16 where y_2 is selected at the next lower reference mg/L value.

e) If the number of the independent components is the same, compare the r^2 value and if the IC/-IC that refers to the highest range has higher r^2 value, c_1 is calculated as in c). If not, c_1 is calculated by equations 6.11 to 6.13 where y_2 is selected at the next lower reference mg/L value.

f) If both primary IC and -IC are referring to the highest range, the c_1 in IC and –IC are calculated by equation 6.11 to 6.13 where y_2 is selected at the next lower reference mg/L value.

6.3.4.2 Calculation of Nitrate Contamination for *tanh*

Similarly, all ICs and -ICs are referred to a specific reference value based on the highest *DFV* value yielded like in *pow3*. The lowest value range and highest value range also need to be identified for both ICs and –ICs the same way in *pow3*.

One primary IC/-IC is selected between the ICs/-ICs with the highest r^2. Therefore, the primary IC/-IC is not expected to change. Then the following conditions are considered:

a) If the IC and –IC do not have the same independent number e.g. IC8 and –IC6, the total estimated concentration; C is calculated from the estimated concentration (c_1) calculated from IC or –IC that has the highest r^2. If it is at the lowest range, therefore c_1 is calculated from Eq. 6.11, y_1 and y_2 are given as following:

$$y_1 = \begin{cases} (r^2)_{RV'} \times RV, & if \quad (r^2)_{RV'} \geq 0.5 \\ RV - (r^2)_{RV'} \times RV, & if \quad (r^2)_{RV'} < 0.5 \end{cases} \qquad \textbf{6.17}$$

$$y_2 = \begin{cases} RV' + (r^2)_{RV} \times RV', & if \quad (r^2)_{RV} \geq 0.5 \\ RV' - (r^2)_{RV} \times RV', & if \quad (r^2)_{RV} < 0.5 \end{cases}, \qquad \textbf{6.18}$$

where RV is the primary reference value in mg/L and $(r^2)_{RV}$ is the corresponding r^2 value, y_2 is selected at the next higher reference mg/L value. RV' is the reference value in mg/L of y_2 and $(r^2)_{RV'}$ is the corresponding r^2 value of y_2. If the case between the lowest range and the highest range, c_1 is calculated from Eq. 6.11, y_1 and y_2 are given as following:

$$y_1 = \begin{cases} (r^2)_{RV'} \times RV, & if \quad (r^2)_{RV'} \geq 0.5 \\ RV + (r^2)_{RV'} \times RV, & if \quad (r^2)_{RV'} < 0.5 \end{cases} \qquad \textbf{6.19}$$

$$y_2 = \begin{cases} (r^2)_{RV} \times RV', & if \quad (r^2)_{RV} \geq 0.5 \\ RV' + (r^2)_{RV} \times RV', & if \quad (r^2)_{RV} < 0.5 \end{cases}, \qquad \textbf{6.20}$$

where y_2 is selected at the next lower reference mg/L value. If the primary IC or –IC is at the highest range, y1 is calculated as following:

$$y_1 = \begin{cases} RV + (r^2)_{RV'} \times RV, & if \quad (r^2)_{RV'} \geq 0.5 \\ RV - (r^2)_{RV'} \times RV, & if \quad (r^2)_{RV'} < 0.5 \end{cases} \qquad \textbf{6.21}$$

where y_2 is calculated using Eq. 6.18 and selected at the next lower reference mg/L value.

b) If the IC and –IC do have the same independent number e.g. IC8 and –IC8. The total estimated concentration; C is calculated from the average of y_1 (calculated using Eq. 6.12) from both IC and –IC.

6.3.4.3 Calculation of Nitrate Contamination for *gauss*

Similarly as *pow3*, all ICs and -ICs are referred to a specific reference value based on the highest *DFV* value yielded. The lowest value range and highest value range also need to be identified for both ICs and –ICs the same way in *pow3*.

One primary IC/-IC is selected between the ICs/-ICs with the highest *DFV* like in *pow3*. The primary IC/-IC should be changed to another IC/-IC that has higher reference value considering the following conditions:

a) There is another IC/-IC that has higher r^2 value and the difference between the *DFV* values is less than 45%.
b) If there is another IC/-IC that has r^2 difference less than 40% value and *DFV* difference less than 45% compared to the original IC/-IC.

If the IC and –IC do not have the same independent number e.g. IC8 and –IC6, the following conditions are considered:

a) If the IC and -IC are at the lowest range, C is considered from c_1, y_1, and y_2 calculated from Eq. 6.11, Eq. 6.15, and Eq. 6.13, respectively where y_2 is selected from the next higher reference mg/L value.
b) If the IC and -IC are in between the lowest and highest ranges. c_1 is calculated from Eq. 6.11. y_1, and y_2 are calculated from Eq. 6.12 and Eq. 6.13, respectively. However, if the value of $(r^2)_{RV}$ corresponds to IC is bigger $(r^2)_{RV}$ corresponds to –IC, y_2 for IC is selected from the next higher reference mg/L value. Therefore, y_2 for –IC is selected at the nearest lowest reference mg/L value.
c) If the IC/-IC is at the highest range, the total concentration is calculated from the following:
    a. If the opposite pair of IC/-IC is found to be at the lowest range, c_1 is calculated from Eq. (16). y_1, is calculated from:

$$y_1 = (r^2)_{RV'} \times RV \qquad \textbf{6.22}$$

y_2 is calculated using Eq. 6.13, where it was selected at the nearest lowest reference mg/L value. The other opposite pair; c_1, y_1, and y_2 are calculated from Eq. 6.11, Eq. 6.15, and Eq. 6.13, respectively.

b. If the opposite pair of IC/-IC is at the range between the highest and lowest, c_1 is calculated from Eq. 6.11. y_1 and y_2 are calculated from Eq. 6.11, Eq. 6.15, and Eq. 6.13, respectively. The other opposite pair; c_1, y_1, and y_2 are calculated from Eq. 6.11, Eq. 6.12, and Eq. 6.13, respectively where y_2 is selected at the nearest lowest reference mg/L value.

c. If both IC and –IC are at the highest ranges. For IC or –IC that has the highest $(r^2)_{RV}$. c_1, y_1, and y_2 are calculated from Eq. 6.11, Eq. 6.12, and Eq. 6.16, respectively. The other opposite pair; c_1, y_1, and y_2 are calculated from Eq. 6.11, Eq. 6.22, and Eq. 6.16, respectively.

If the IC and –IC do have the same independent number e.g. IC6 and –IC6. The total estimated concentration; C is calculated from the average of y_1 (calculated using Eq. 6.12) from both IC and –IC.

6.3.5 Results and Discussion

Figure 6.12 illustrates the graphs of the calculated contamination concentrations versus the estimated contamination (known value in Table 6.4) for the different contrast functions. In general, *pow3*, *tanh*, and *gauss* give the best and closest estimation of nitrate with the correlation function, R^2 of 0.9892, 0.9945, and 0.9862, respectively as can be seen in Table 6.9. For the estimation of nitrate contamination, the estimated values are very close to the predicted values with the correlation function, R^2 of 0.9921. Moreover, the contrast functions of *pow3*, *gauss*, and *gauss* generate maximum error of between just below 25% and 0.45% as can be seen in Figure 6.13 (b). The average errors for these functions in estimating nitrate contamination are between around 4% to just over 10% as shown in Table 6.10.

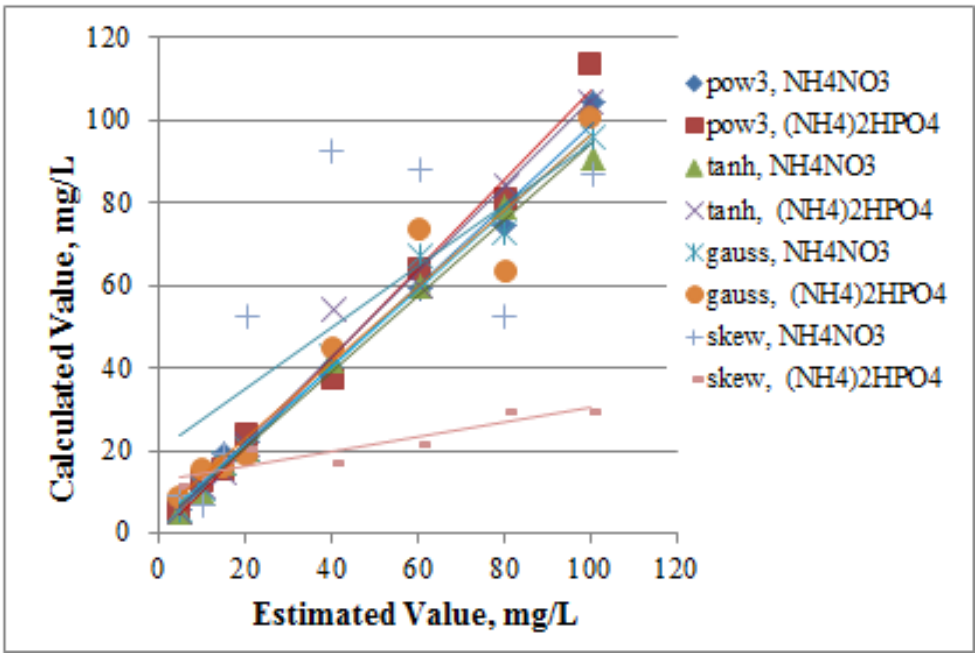

Figure 6.12: The graphs of contaminations concentration calculated values vs the estimated value for different contrast functions

Table 6.9: Correlation function, R^2 of plots in Figure 6.12

Contrast function	R^2, NH_4NO_3	R^2, $(NH_4)_2HPO_4$
pow3	0.9892	0.9921
tanh	0.9945	0.9849
gauss	0.9862	0.9424
skew	0.5334	0.8851

Table 6.10: Summary of Error for the contrast functions

Contrast function	Average Error (%), NH_4NO_3	Average Error (%), $(NH_4)_2HPO_4$
pow3	10.24004271	8.402481788
tanh	4.01985822	7.788128608
gauss	8.384853691	23.36170271
skew	64.75713615	52.08890138

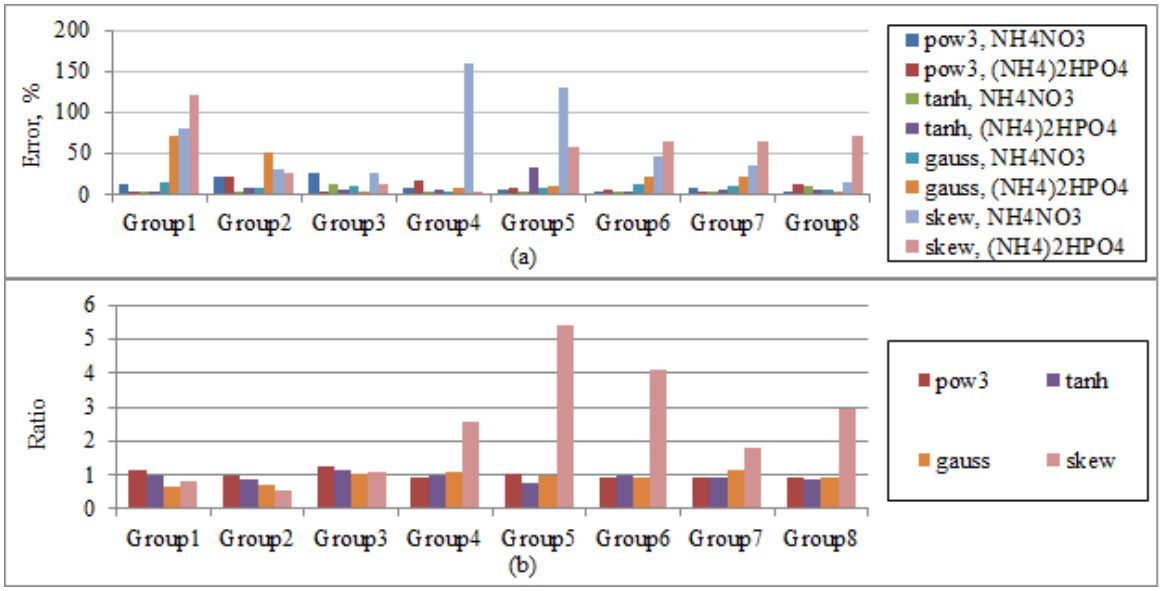

Figure 6.13: (a) The measurement error of contaminant projected along the water samples groups for different contrast function (b) Ratio of NH_4NO_3 to $(NH_4)_2HPO_4$ calculated along the water samples groups for different contrast function

In terms of discriminating other forms of contamination than nitrate, *pow3* and *tanh* are at the best with R^2 of 0.9921 and 0.9849, respectively as shown in Table 6.9. They also maintain accuracy between 7% to 8%, as shown in Table 6.10. The contrast function, *tanh* shows a slightly higher error percentage in detecting and discriminating other contamination other forms of contamination than nitrate. However, the ratio of NH_4NO_3 to $(NH_4)_2HPO_4$ projected along the water samples groups for different contrast for *pow3*, *tanh*, and *gauss* are found to be 1:1 as shown in Figure 6.13(b). In this experiment, contrast function of *skew* is found to be less accurate in estimating nitrate and discriminating nitrate with other type of contamination. This is explained from the less accurate results as can be seen in Table 6.9, Table 6.10, and Figure 6.13.

6.4 Nitrate Contamination Estimation in Natural Water Source using Independent Component Analysis Method

For the experiment in this section, water samples were taken from the Manawatu River near the Hokowhitu campus, Massey University were tested and the nitrate concentrations are estimated using the ICA method as discussed in the previous sections. Four different groups of water sample were prepared based on the river water samples. Each group was divided into nine samples and total volume of three litres. The water sample groups are:

1) Pure Manawatu river water samples.
2) Pure Manawatu river water sample added with NH_4NO_3 (5.6 mg/L).
3) Pure Manawatu river water sample added with NH_4NO_3 (20.4 mg/L).
4) Pure Manawatu river water sample added with NH_4NO_3 (120 mg/L).

The spectra of %V'' water sample group are used as inputs for FastICA. Figure 6.14(a) shows the second derivative of the reference spectrum of %V of NH_4NO_3 (20.6 mg/L). Figure 6.14(b) depicts the second derivative of the pure Manawatu river water samples, it can be clearly seen that the spectrum is different from the reference spectrum of the second derivative spectra of %V of NH_4NO_3 (20.6 mg/L) water solution.

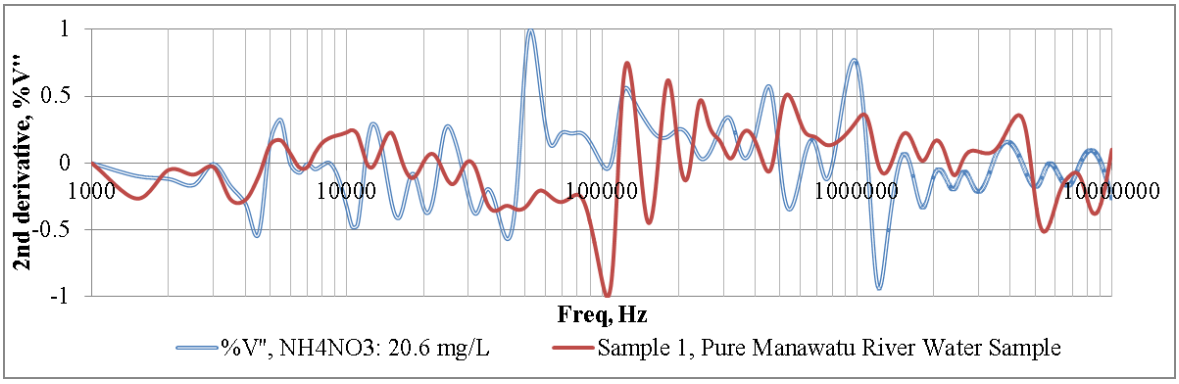

Figure 6.14: (a) %V'' of NH_4NO_3 (20.6 mg/L) water solution (b) %V'' of pure Manawatu river water sample

6.4.1 Results and Discussions

Initially, the estimated NH_4NO_3 in the Manawatu River is between 21.80 mg/L and 85.73 mg/L which comes to the average of 54.14 mg/L as can be seen from Figure 6.15. Under the chemical reaction NH_4NO_3 to water, Nitrate can be considered as the actual amount of contaminant that is calculated, thus, the average calculated value has exceeded the safe limit. This result is plausible because the site where the samples were taken is near to residential areas (possible sewage effluent) and Manawatu river has been reputed to have water quality issues for the past recent years [159]. *pow3*, *tanh* and *skew* had accurately estimated the nitrate value when 5.6 mg/L and 20.4 mg/L of NH_4NO_3 were added into the river water samples. These contrast functions have relatively low %error between -6% to 3% as can be seen from Figure 6.16. From Figure 6.16, *gauss* seems to have less accuracy. However, at the additional 120 mg/L of NH_4NO_3, all the contrast functions have given high error. This is because the reference spectra high limit is at 115 mg/L taking the consideration of naturally occurring levels of nitrate in the rivers are in the range of 17.32 and 38.97 mg/L [160]. This error can easily be fixed by providing reference spectra at higher values.

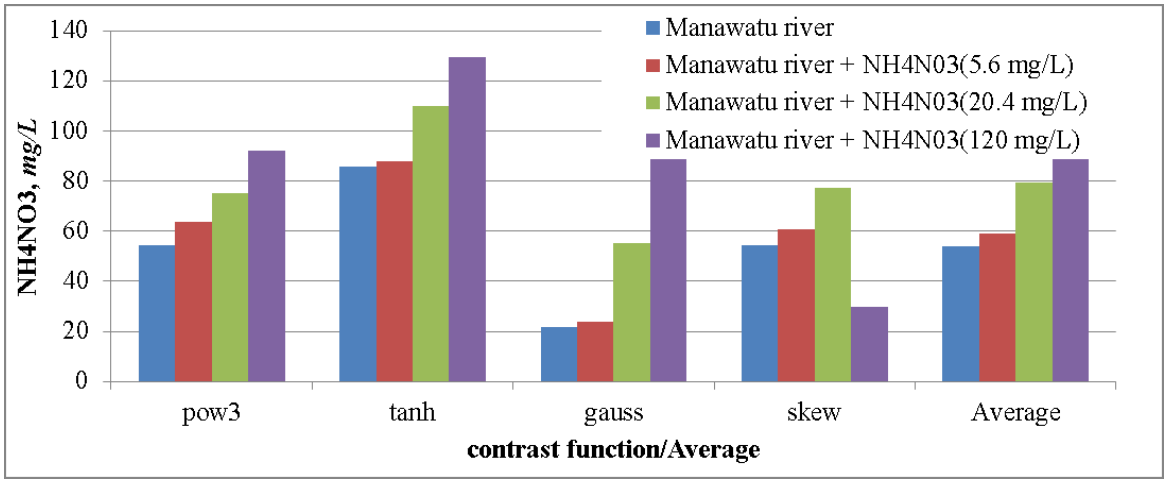

Figure 6.15: The graphs of contaminations concentration calculated values

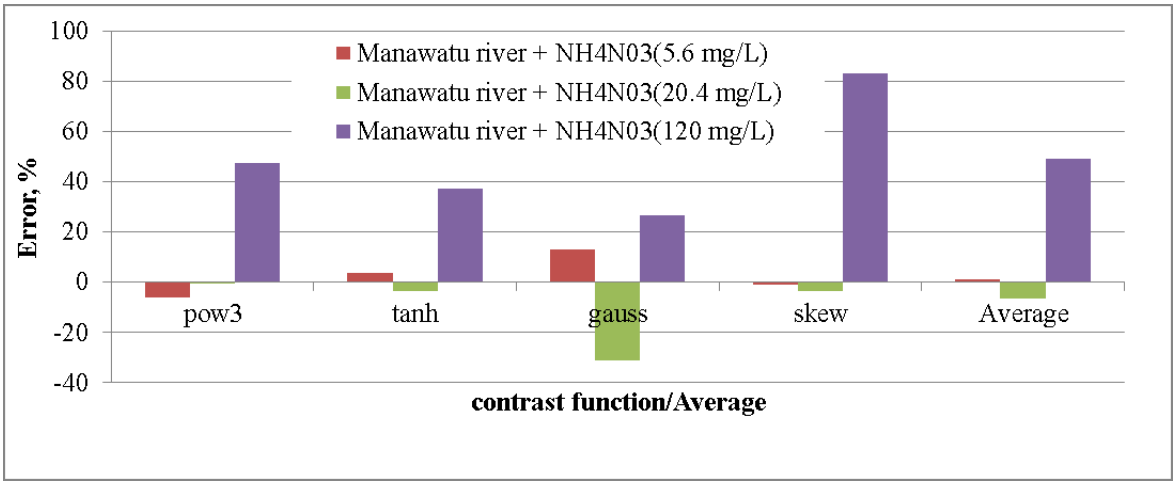

Figure 6.16: The graphs of %error of calculated values

6.5 Conclusion

The *MLR* models have been to estimate nitrates in the form of sodium nitrate and ammonium nitrate using SECS22_1 sensor. The results show that the models cannot accurately be used with the actual natural water samples. This problem is due to the inability of the models to discriminate the response from the other ions species that existed in the water samples. Therefore, the use of *MLR* is only suitable for problems that the estimated parameters are not influenced by untargeted parameters.

In the next experiments, the results of the sensor have been analysed based on the electrochemical spectroscopy and it has shown that the resistive, capacitive, and inductive elements of the sensor are responsive with the material change (chemical species and concentration). The output of the sensor (real part, imaginary part, and output voltage) also has been scrutinized and carefully derived so that it can be incorporated with the *ICA* analysis.

Based on the results of the studies in section 6.3.5, they show that an accurate discrimination and estimation of nitrates concentration can be achieved using the sensor with the assistance of *ICA* analysis under the setting of contrast function of *pow3*, *tanh*, and *gauss* with the relatively limited number of reference spectral. The contrast function

of *skew* has been discovered to be unsuitable for this study. Further investigation using Manawatu river water samples concluded that contrast function of pow3 and tanh are best used for future application.

The studies also show that an accurate estimation of NH_4NO_3 in natural water sources can be achieved using the sensor with the assistance of *ICA* and with the relatively limited number of reference spectra.

CHAPTER 7

Development of a Low-cost System

7.1 Introduction

The main objective of this chapter is to discuss the development a low-cost system for detection of nitrate and contamination in natural water resources based on SECS22_1. The performance of the system was observed where the sensor was tested with two aqueous solutions of nitrates namely, sodium nitrate ($NaNO_3$) and ammonium nitrate (NH_4NO_3), each of different concentration between 5 mg and 20 mg dissolved in 1 litre of Milli-Q water. Furthermore, it was also tested with various kinds of natural water samples taken from natural sources around New Zealand. The results from the first set of experiments show good linear correlations with the amount of concentration of nitrate forms in Milli-Q water. Favourably, the second experiment's outcome involving the water samples taken from various places around New Zealand also show a good correlation of contamination level as compared with results obtained from Nuclear Magnetic Resonance (NMR) measurement.

7.2 Motivation

The increase in nitrate concentration in groundwater arises mainly from natural and anthropogenic sources. However, extensive areas of some parts of the world have increasing nitrate concentration due to natural leaching [8]. The increase of agricultural fertilizers, manure and sludge application to land and streams with low water level is one of the main contributing causes to the nitrate increase in groundwater [10]. methemoglobinemia and fatal consequence in infants are caused by nitrate contamination [5]. Furthermore, livestock losses occurred often because of nitrate poisoning [6].

As has been discussed in Section 1.1, the farmers in New Zealand have to depend on laboratory based nitrate detection systems [21, 22]. These systems are usually expensive because they required many components. The methods often involved laborious measurement and inevitably consumes a lot of time. They also require controlled working condition. Moreover, the farmers may have been warned by the City Council for causing water contaminations (including Nitrates), even before they can get the water quality results from the laboratory.

Two recent indirect and in-situ methods for nitrate detection, as reported in [20, 161], involved nitrate measurement based on photometric device (the Pastel UV) [161] and the measurement of LED intensity emitted through a nitrate sensitive membrane using photo-detectors [20]. Both systems have good sensitivity and precision. However, the optical path has to be properly guided and aligned; requiring a regular repositioning to maintain the accuracy [20] and the output signal is susceptible to the interference from non-targeted ions[20, 161].

Therefore, because of the concerned with nitrates or any form of contamination in natural water sources, and the need of a low-cost, convenient, and suitable for in-situ measurement system for water quality monitoring, in this chapter a low-cost system based on a planar electromagnetic sensor is developed. The discussions of the preliminary results show that the system has the potential to be used with the ICA method in the future. For the convenient of the readers, some of the points in the previous chapters are re-presented in this Chapter.

7.3 Planar Electromagnetic Sensors

The planar electromagnetic sensor, SECS22_1 was designed using Altium Designer 6. The sensor was fabricated using simple printed circuit board (PCB) fabrication technology (thickness of 0.25 mm). The sensor is then coated using Wattyl Incralac

Killrust aerosol to form a coating layer in order to prevent any direct contact with water sample. Next section will discuss the construction and operating principle of the planar electromagnetic sensors.

7.3.1 Introduction, Construction and Operating Principle

Planar electromagnetic sensors have been used for many applications, some of the examples are moisture measurement in pulp [58], monitoring the change impedance caused by the growth of immobilized bacteria [59], human health confirmation based on the content of water in human skin [60], humidity sensors [61], food inspection for human safety [62], and estimation of material dielectric properties such as food, saxophone reeds and leather [65-67, 162].

Figure 7.1 shows the top and bottom layers of the planar electromagnetic sensor. The meander coil is connected in series with the interdigital coil and an ac voltage is applied across the combination of the coils. The meander coil produces a magnetic field and the interdigital coil produces an electric field. The combination of meander and interdigital coils produce electromagnetic field which interacts with the material under test. The purpose of providing a grounded backplane is to lessen the effect of background noise [135]. The total impedance is used as the characterization parameter for the sensor. The electrical equivalent circuit of the series combination sensor is shown in Figure 7.2. The sensor is connected to the output of the signal generator, R_1 denotes the series surface mount resistor connected to the sensor as shown in Figure 7.2.

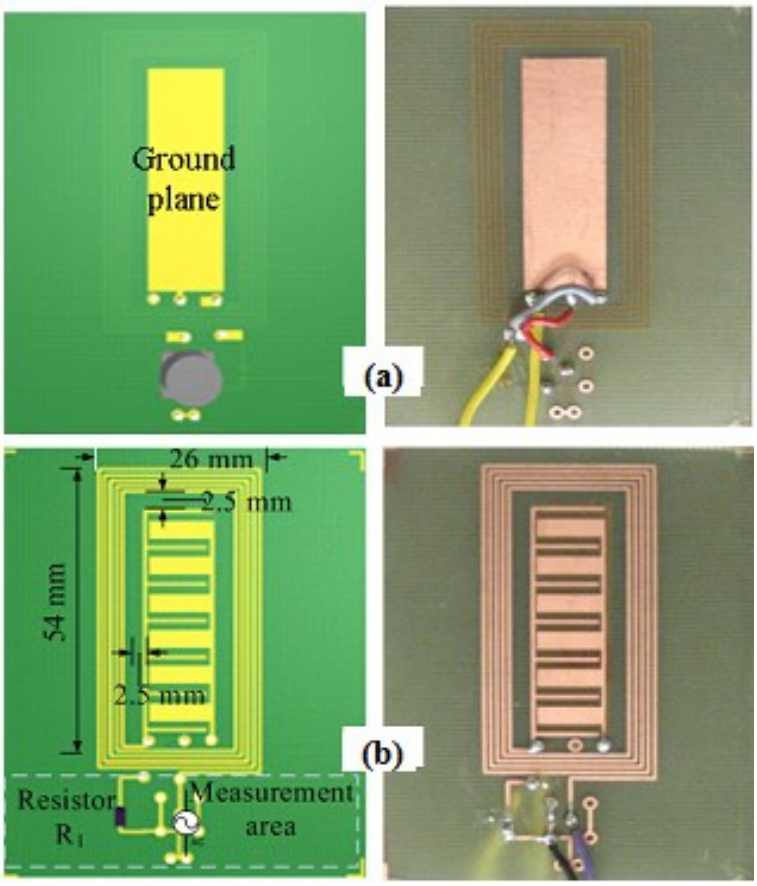

Figure 7.1: Left hand side: (a) schematic diagram of the top layer, (b) Schematic diagram of the bottom layer. Right hand side: (a) a picture of the top layer (b) a picture of the bottom layer

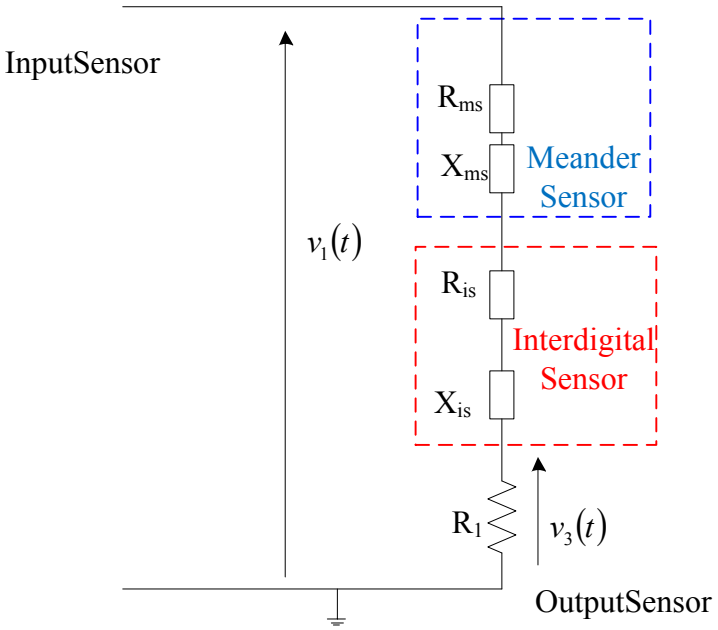

Figure 7.2: Electrical equivalent circuit of the planar electromagnetic sensor

7.3.2 Experimental Setup

The experimental setup is shown in Figure 7.3. The setup has a box containing the waveform generator circuit, signal conditioning circuit, phase and gain measurement circuit, frequency to voltage circuit and temperature circuit. The output signals from the circuits then captured the C8051F020 microcontroller which placed above the box. The microcontroller was interfaced with *LabView* through RS232 where the impedance calculation (real part, R_{total} and imaginary part, X_{total}), graphical display, and data storage are completed. The temperature sensor, LM335 was placed in the space created between the beaker and polystyrene. The next section will discuss the signal generator circuit, signal condition circuits, phase and gain measurement circuit, impedance (real part, R_{total} and imaginary part, X_{total}) and interface between C8051F020 microcontroller and *LabView*.

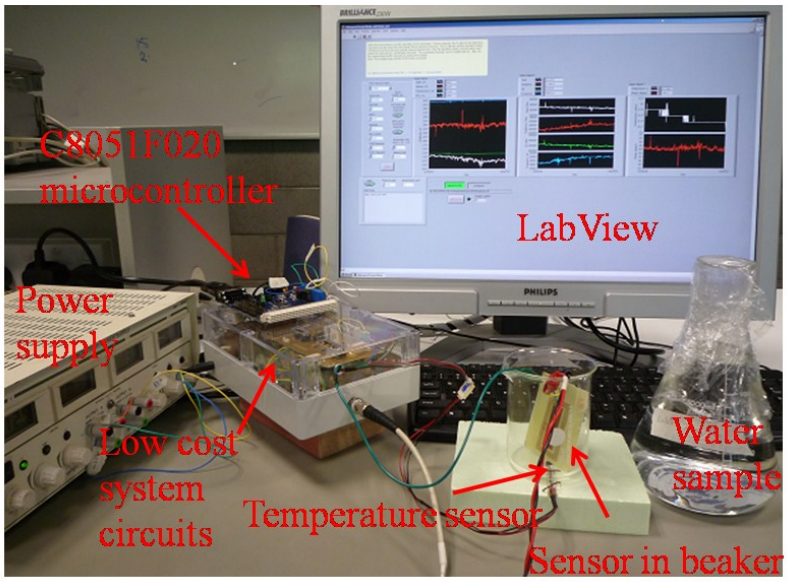

Figure 7.3: The experimental setup

7.4 The Low-cost System

The low-cost system comprises of five main parts: (a) waveform generator circuit, (b) signal conditioning circuit, (c) phase and gain measurement circuit, (d) frequency to

voltage circuit, (e) temperature circuit and (f) data acquisition system. The data acquisition system can be broken down into two significant components: (a) C8051F020 microcontroller and (b) *LabView* program. Next section will discuss about the low-cost system in detail.

7.4.1 Waveform Generator Circuit

The signal generator described here is based on high XR2206 IC [163] and the circuit schematic is illustrated in Figure 7.4. It provides sine around 1 Hz to 1 MHz, depending on the timing capacitors connected between pin 5 and pin 6. The amplitude can be varied from 1Volt peak-to-peak to 12 Volt peak-to-peak. Potentiometers R1p and R3 can be used to adjust the amplitude and frequency, respectively. The potentiometer, RA, adjusts the sine-shaping resistor, and RB provides the fine adjustment for the waveform symmetry. The operating frequency for the sensor during the experiments was set at 500 kHz and six volt peak-to-peak.

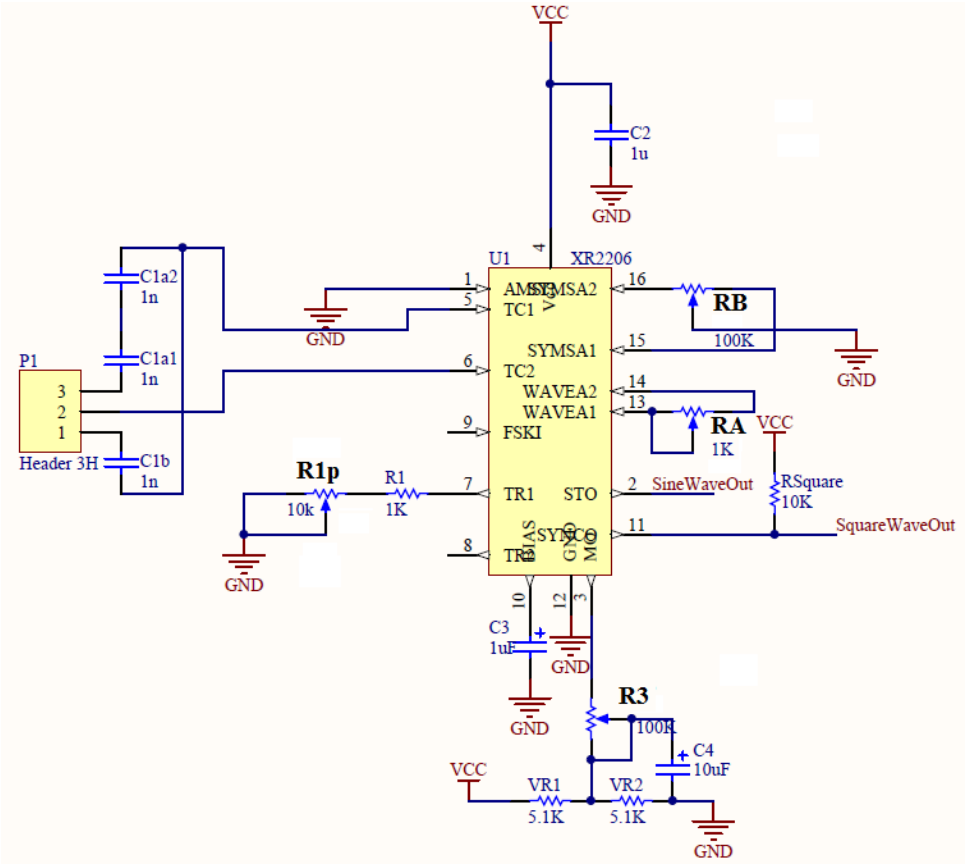

Figure 7.4: Waveform generator circuit

7.4.2 Signal Conditioning Circuit

The output signal from the waveform generator was connected to a buffer as can be seen in the right circuit of Figure 7.5 and the resulting signal, *InputSensor* from the buffer is then fed into the sensor (Figure 7.2). LF412 amplifier is chosen as voltage follower, which play a role in the impedance matching, reducing the loading effect as well as protection of the follow-up circuit.

At six Volt peak to peak, $v_1(t)$ gives maximum rating of 19.05 dBm in a 56 Ω system and $v_3(t)$/*Outputsensor* amplitude is always less than the maximum amplitude of $v_1(t)$/*InputSensor*. The signals of $v_1(t)$/*InputSensor* and $v_3(t)$/*Outputsensor* will be used to calculate the gain and phase which later to be calculate the impedance. However, the phase and gain chip (AD8302) for gain and phase measurement, only cater signals between -60 dBm and 0 dBm. Therefore, a pi network attenuator with attenuation level at 50 dBm was used to attenuate $v_1(t)$/*InputSensor* and $v_3(t)$/*Outputsensor* as can be seen in Figure 7.5 below.

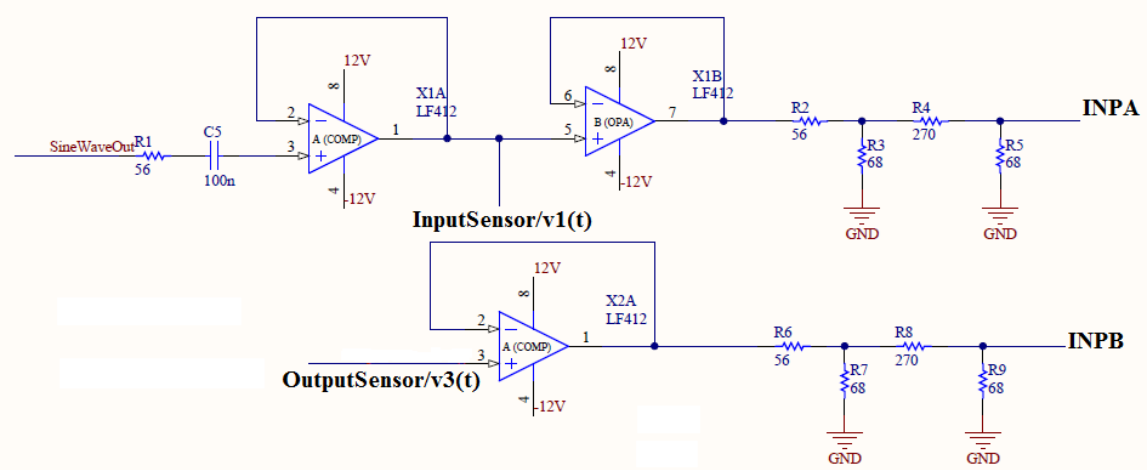

Figure 7.5: Buffer and attenuator of the input and output signals

7.4.3 Main Description of AD8302

The gain and phase measurements were realized using AD8302 chip [164]. It comprises a closely matched pair of demodulating logarithmic amplifiers where the difference of their

outputs, a measurement of the magnitude ratio or gain between the two input signals is available and a phase detector of the multiplier type. The indication of working system is provided by a precision 1.8 Volt reference voltage output. The scanning range of applied input signal is from -60 dBm to 0 dBm in a 50 Ω system. The outputs provide an accurate measurement of gain over a ±30dB range scaled to 30 mV/dB, and of phase over a 0°-180° range scaled to 10 mV/degree. Both gain and phase dc outputs should not be over 1.8 Volt. Table 7.1 summarizes the important information from the datasheet. The circuit of AD8302 can be seen in Figure 7.6.

Table 7.1: Specification of the AD8302 [20]

Parameters	Condition	Min	Typical	Max	Unit
Input frequency range		>0		<2.7	GHz
Input voltage range	Re = 50Ω	-60		0	dBm
Output voltage minimum	Phase different 180°		30		mV
Output voltage maximum	Phase different 0°		1.8		V
Slew rate			25		V/µs
Output bandwidth			30		MHz
1.8 V reference ouput	Load = 2 kΩ	1.7	1.8	1.9	V
	V_s = 2.7-5.5 V		0.25		mV/V

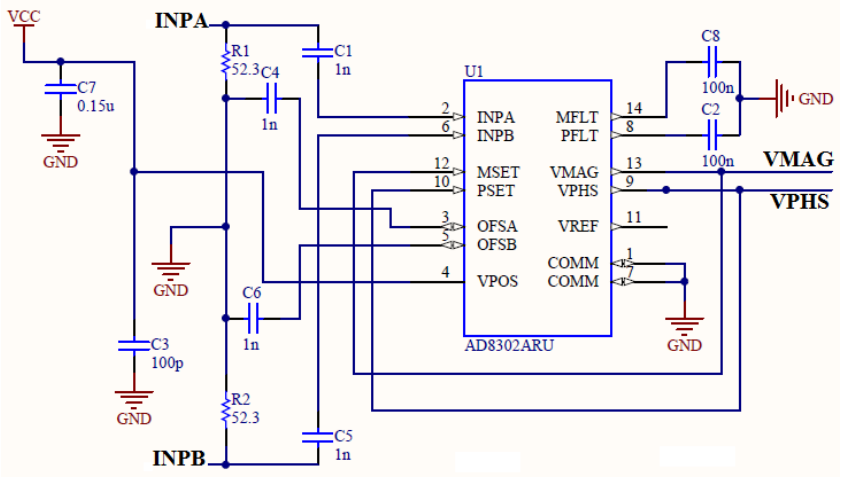

Figure 7.6: Connection of AD8302 in gain and phase measurement mode

7.4.4 Measurement of Impedance

The output signal from the waveform generator was connected to a buffer as can be seen in the circuit of Figure 7.5 and the resulting signal, *InputSensor* from the buffer is then fed into the sensor (Figure 7.2). The output voltage of the sensor, *OuputSensor* across the resistor, R_1 is connected to a buffer system as can be seen in Figure 7.5. The real part, R_{total} and the imaginary part, X_{total} of the sensor as can be seen in Figure 7.2 can be calculated from:

$$I_1 = \frac{V_3 \angle 0^\circ}{R_1} \qquad \textbf{7.1}$$

where, I_1 = the rms value of current through the sensor.

V_3 = the rms voltage across the surface mount resistor.

V_3 is considered as the reference so that its phase angle is 0°. R_1, with nominal value of 120 kΩ is the series surface mount resistor used to measure the total current through the sensor. The total impedance Z_{total} is given by:

$$Z_{total} = \frac{V_1 \angle \theta}{I_1 \angle 0} = \frac{V_1}{V_3} \angle \theta_1 \times R_1 \qquad \textbf{7.2}$$

where, V_1 = the rms values of input voltage, $v_1(t)$.

θ_1 = the phase difference between $v_1(t)$ and $v_3(t)$ in degree, taking $v_3(t)$ as reference.

The value from the terms V_1/V_3 and θ_1 are given by V_{mag} and V_{phase}, respectively, of AD8302. At 10 Volt peak to peak, $v_1(t)$/*InputSensor* gives maximum rating of 23.48 dBm in a 56 Ω system and $v_3(t)$/*Outputsensor* amplitude is always less than the maximum amplitude of $v_1(t)$/*InputSensor*. Since the range of input signal power of AD8302 is -60 dBm to 0 dBm, both $v_1(t)$/*InputSensor* and $v_3(t)$/*Outputsensor* signals (after the buffers) were both attenuated by 30 dBm using pi attenuators as shown in

Figure 7.5. The attenuated signals of $v_1(t)$/*InputSensor* and $v_3(t)$/*Outputsensor* are *INPA* and *INPB*, respectively. They were then inputted to the AD8302's pins of 2 and 6, respectively as illustrated in Figure 7.6.

For the gain measurement, the AD8302 takes the difference between the output two identical log amplifiers, each taking signals of the same frequency but at different amplitude values. Since the input signals ratio involved frequency domain, the resulting output of MSET pin becomes [164]:

$$V_{MAG} = V_{SLP} \log\left(\frac{V_1}{V_3}\right) + V_{CP} \qquad \textbf{7.3}$$

where, V_1 and V_3 = the input signals.

V_{MAG} = the dc output corresponding to the magnitude of the signal level difference.

V_{SLP} = the slope which is equivalent to 30 mV/dB.

V_{CP} = the offset voltage of 900 mV which was set internally to establish the centre point.

The output response based on Equation 7.3 is illustrated in Figure 7.7(a). The dc phase output, V_{PHS} is given by [164]:

$$V_{PHS} = -V_{\phi} \log\left(|\theta_1| - 90°\right) + V_{CP} \qquad \textbf{7.4}$$

where, θ_1 = the phase difference between $v_1(t)$ and $v_3(t)$.

V_{PHS} = the dc output corresponding to the magnitude of the signal level difference.

V_{ϕ} = equivalent to -10 mV/degree.

V_{CP} = the offset voltage of 900 mV which was set internally to establish the centre point.

The output response based on Equation 7.4 is illustrated in Figure 7.7(b).The total impedance, Z_{total} in Eq. 7.2 now can be calculated with the given values of V_1/V_3 and θ_1 from Eq. 7.3 and Eq. 7.4, respectively. Therefore, the real part, R_{total} and the imaginary part, X_{total} are given by:

$$R_{total} = Z_{total}\cos(\theta_1) - R_1 \quad \textbf{7.5}$$

$$X_{total} = Z_{total}\sin(\theta_1) \quad \textbf{7.6}$$

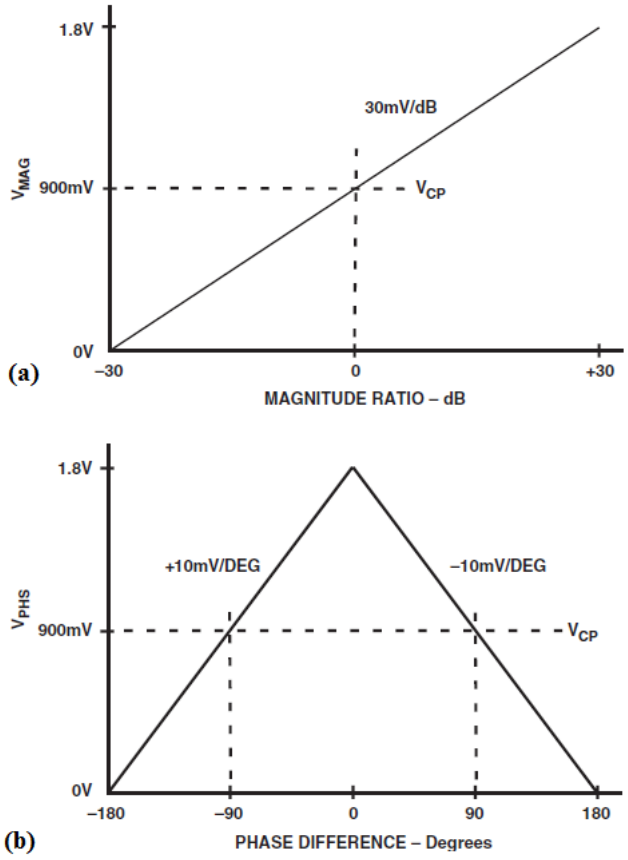

Figure 7.7: Idealized transfer characteristic for the (a) gain (b) phase [20]

7.4.5 Frequency to Voltage Converter Circuit

In order to display value the frequency of the waveform in Section 7.4.1, VFC110 chip was used. It has high maximum operating frequency of 4 MHz and a precision 5 Volt reference. For frequency-to-voltage conversion, *SineWaveOut* signal from the waveform generator circuit in figure 4 was tapped by frequency to voltage circuit as can be seen in Figure 7.8(a). The signal has to be converted into pulse signal [164], before that, *SineWaveOut* signal was buffered as can be seen in Figure 7.8 (a) and LM319N was used to convert the output signal from the buffer as shown in Figure 7.8 (b). The resulting pulse signal was applied to the comparator input in Figure 7.8 (c).

VFC110 operates by averaging (filtering) the reference current pulses triggered on every falling edge at the frequency input. Voltage ripple with a frequency equal to the input will be present in the output voltage. The magnitude of this ripple voltage is inversely proportional to the integrator capacitor, C10 as shown in Figure 7.8 (c). The output signal was limited between 0 and 2.4 Volt using a differential amplifier circuit as can be seen in Figure 7.8 (d). *Mc_A6* in Figure 7.8 (d) denotes the dc output signal in Volt.

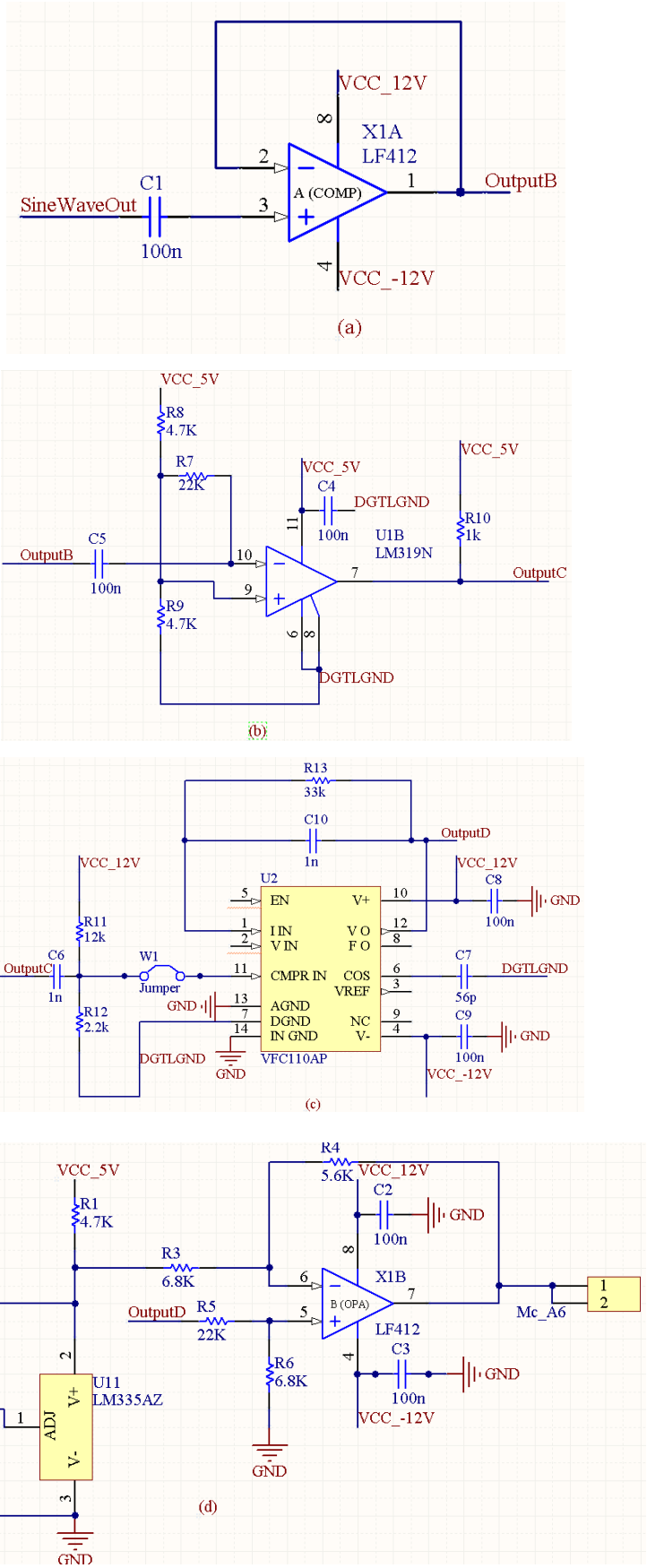

Figure 7.8: Frequency to voltage converter circuits

A calibration was performed by adjusting SineWaveOut and observing the frequency using an oscilloscope in the same time *Mc_A6* value was jotted down as measured by a digital multimeter. Figure 7.9 illustrates the frequency value versus Mc_A6 value and the relationship is given by the following equation.

$$Frequency\ (\text{Hz}) = -0.071(Mc\_A6)^5 + 0.890(Mc\_A6)^4 - 2.249(Mc\_A6)^3 + 2.381(Mc\_A6)^2 - 0.922(Mc\_A6) + 0.284 \quad \textbf{7.7}$$

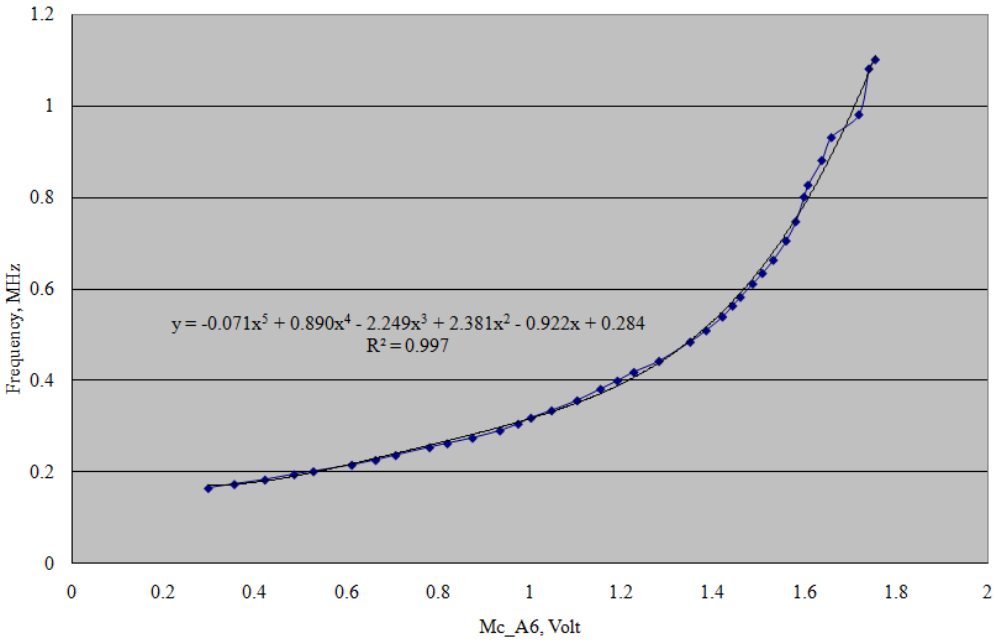

Figure 7.9: Calibration graph of frequency, MHz versus Mc_A6, volt

7.4.6 Temperature Circuit

Figure 7.10 depicts the circuit for temperature measurement. It consist of LM335 [165] which is used as a sensor to estimate the temperature of the solution. It also consists of a differential amplifier circuit to limit the signal between 0 to 2.4 Volts as the input of the data acquisition cannot exceed 2.4 Volts. The calibration to determine the relationship of *Mc_A7* output signal with the temperature was established by filling a 250 ml beaker with warm water and placing the sensor to the outside of the beaker wall as near as possible. In

the calibration process the temperature of the solution was measure using a typical laboratory thermometer while the *Mc_A7* output value was measured using a digital multimeter.

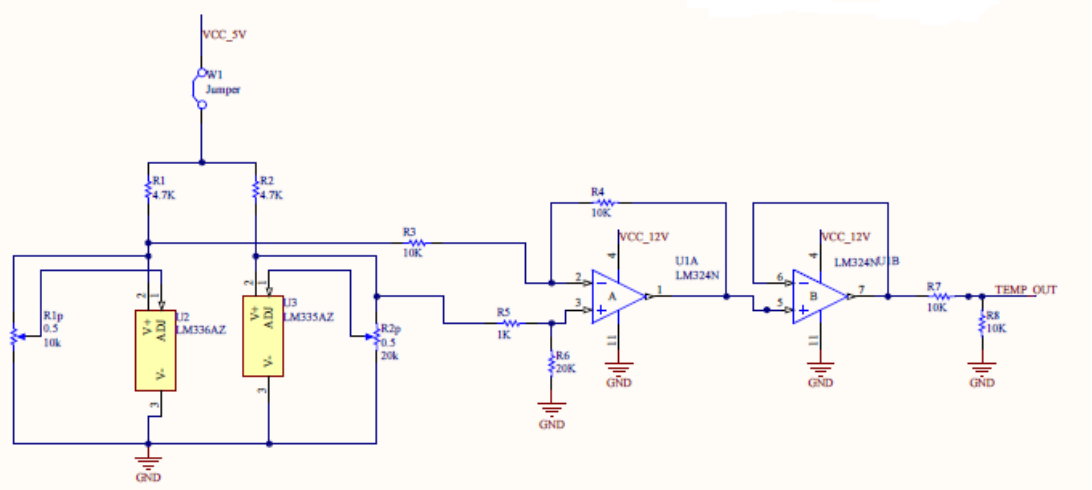

Figure 7.10: Temperature measurement circuit

Figure 7.11 illustrates the solution temperature value versus *Mc_A7* value and the relationship is given by the following linear equation.

$$Temperature\ (\text{Celsius}) = 218.9(Mc\_A7) - 223.6 \qquad \textbf{7.8}$$

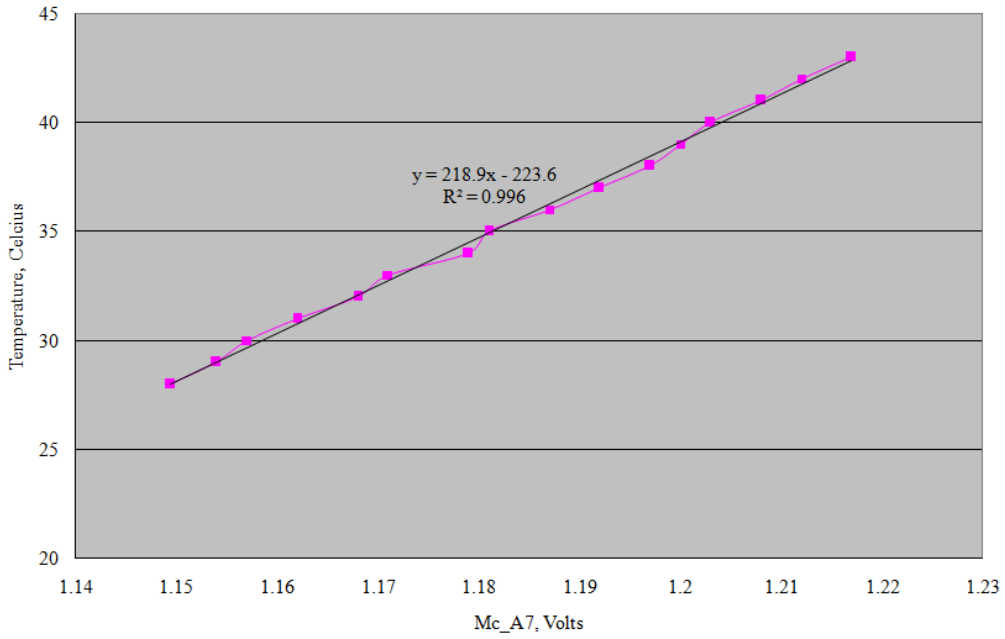

Figure 7.11: Calibration graph of solution temperature, Celsius versus Mc_A7, volt

7.4.7 Data Acquisition System

C8051F020 microcontroller is used to capture the output signals. The microcontroller has eight channels ADC with 12-bit resolution. Just four channels were used, ADC.0 and ADC.1 were connected to pin 13 (V_{MAG}) and pin 9 (V_{PHS}), respectively of AD8302 chip as shown in Figure 7.6. ADC.6 and ADC.7 were connected to temperature circuit output and frequency to voltage circuit output, respectively. All the channels maximum input level was set to 2.4 Volt. The channels are sequentially scanned and the results printed to a PC terminal program via the RS232.

LabView was chosen to calculate (R_{total} and imaginary part, X_{total}), graphical display, and data storage. The front panel of the *LabView* program can be seen from Figure 7.12. The *LabView* program comprises of five parts: (a) data transfer configuration (b) analog inputs display (V_{MAG}, V_{PHS}, V_{TEMP}, *and* V_{F2V}): the results were displayed in an array of string of characters. The output for each channel was obtained and separated from the array and converted from string into equivalent decimal value (c) R_{total}, X_{total}, $|Z|$, and θ_1 display which values have been realized using Eqs. 7.1 to 7.6, (d) temperature and frequency display, and (e) data storage control buttons.

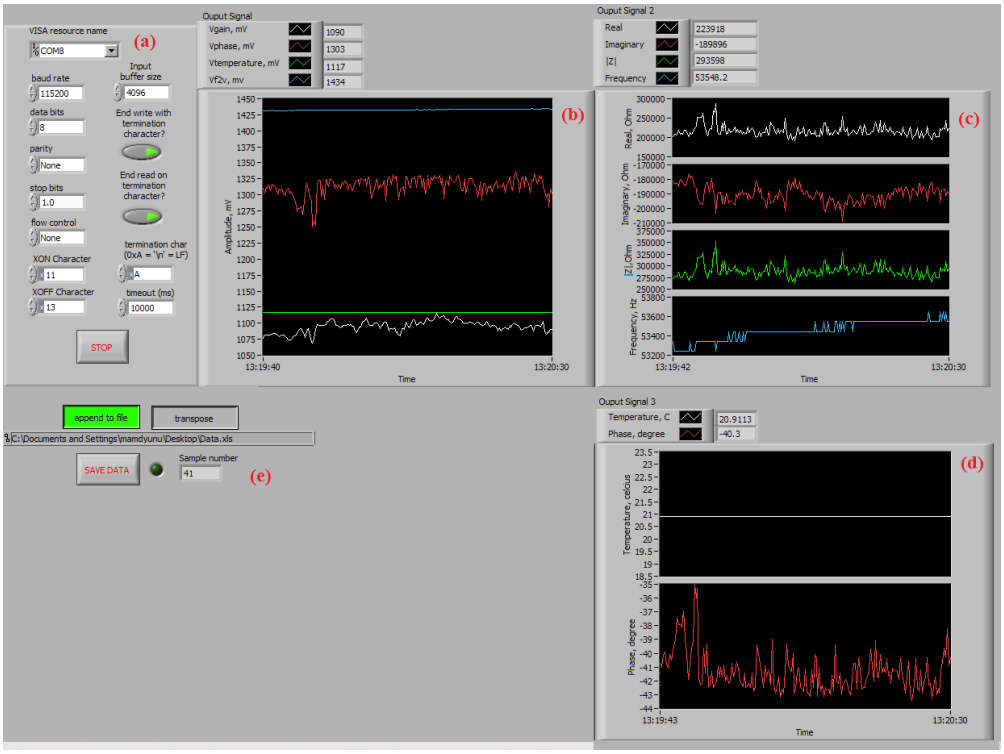

Figure 7.12: Front panel of the *LabView* program

7.5 Results and Discussion

The objective of first experiment was to test the system with different concentration of Nitrates samples between 5 and 20 mg in the form of Sodium Nitrate ($NaNO_3$) and Ammonium Nitrate (NH_4NO_3) diluted in 1 Litre of Milli-Q water. In the second experiment, the system was used to measure the contamination in water samples taken from different locations in New Zealand. The samples were obtained from previous research by Karunanayaka in [130] which related to magnetic filtration technique of drinking and waste waters. The water samples were analyzed using Nuclear Magnetic Resonance (NMR) analysis to check the amount of organic material in the sample and summarized in Table 7.2. The table shows the amount of mineral in $g \cdot m^{-3}$ including the pH value.

Table 7.2: Content of Water Samples from NMR Test Results

Sample	pH	Ca (gm^{-3}-Ca)	Mg (gm^{-3}-Mg)	Fe (gm^{-3}-Fe)	$CaCO_3$ (gm^{-3}- $CaCO_3$)	Sulphate (gm^{-3}-SO_4)	Total mineral (gm^{-3})
570-1,Matakana raw	8.69	3.3	0.54	0.036	8	0.63	12.506
570-2,Matakana magnetic circle tank	8.06	3	0.51	0.039	10	0.24	13.789
570-3,IPL Mixed water UV	8.38	1.7	0.32	0.027	4	0.09	6.137
570-4, Edgecumbe raw	7.529	11.6	11.8	3.33	77	0.02	103.75
570-5, McCains D119 raw	6.62	17.3	24.8	2.62	150	0.23	194.95
570-6, Matakana raw2	7.8	3	0.51	0.036	8	0.63	12.176
570-7, McCains treated	8.2	4.6	3	0.334	24	606	637.934
570-8, Tauranga tapwater	7.27	2.8	0.56	0.005	8	1.8	13.165
570-9, Techical water system potable	7.16	5.3	0.56	0.11	14	2.17	22.14
570-10, Edgecumbe magnetic treatment	8.58	14.4	8.1	0.014	70	0.02	92.534

The sensitivities of the sensors are calculated from the real part as taking the value from the Milli-Q water value as reference in the following equation:

$$\%\text{Real\_part} = \frac{(R_{total})_{sample} - (R_{total})_{Milli-Q}}{(R_{total})_{Milli-Q}} \times 100 \qquad \textbf{7.9}$$

In the simulation results as had been conducted in Section 3.4.2, it can be concluded that the imaginary part showed a response other than linear i.e. the difference between water sample output and Milli-Q output of imaginary parts may not be in positive value on the whole operating frequency range. Therefore to the absolute difference value is used to calculate the imaginary part sensitivity as shown in equation:

$$\%\,\text{Imaginary\_part} = \frac{\left|(X_{total})_{sample} - (X_{total})_{Milli-Q}\right|}{\left|(X_{total})_{Milli-Q}\right|} \times 100 \qquad \textbf{7.10}$$

where, $(R_{total})_{Milli\text{-}Q}$ = the real part of the impedance value when the sensor is immersed in the Milli-Q water.

$(R_{total})_{sample}$ = the real part of the impedance value when the sensor is immersed in the water sample.

$(X_{total})_{Milli\text{-}Q}$ = the imaginary part of the impedance value when the sensor is immersed in the Milli-Q water.

$(X_{total})_{sample}$ = the imaginary part of the impedance value when the sensor is immersed in the water sample.

Figure 7.13 shows the graphs of sensitivities value of the system tested with solution based on $NaNO_3$ and NH_4NO_3. Similar response can be observed for both solution types. The imaginary values are steadily increase with the increasing value of chemical concentration diluted in the Milli-Q water, showing good linear correlation with R^2=0.939 and R^2=0.920 corresponding to $NaNO_3$ and NH_4NO_3, respectively. Moreover, the real part negatives values progressively decreases with the total concentration of the chemicals. This is true since the electrical conductivity; σ of the solution of water is highly dependent on its concentration of dissolved salts where $NaNO_3$ and NH_4NO_3 were added in the Milli-Q water. High quality water samples which safe to consume has lower electrical conductivity (high resistivity) and conversely. Therefore, the real part sensitivities give the indirect relationship of total amount of chemical concentrations with the quality the water samples. The graphs in Figure 7.13 show good correlation with R^2=0.934 and R^2=0.971, between the real part sensitivities with the chemical concentration of $NaNO_3$ and NH_4NO_3, respectively.

The sensitivity values calculated for the water samples as shown in Figure 7.14 and Figure 7.15 recommended the water samples of 570-1 to 570-7 should never be consumed. This can be explained from the low real sensitivity values range and the high imaginary sensitivity values range which are between -223% to 20611% and 442% to 16362%, respectively. The most contaminated water sample is 570-7 as shown in Figure 7.14 and Figure 7.15 and this is caused by high the total amount of mineral in 570-7 as given in Table 7.2.

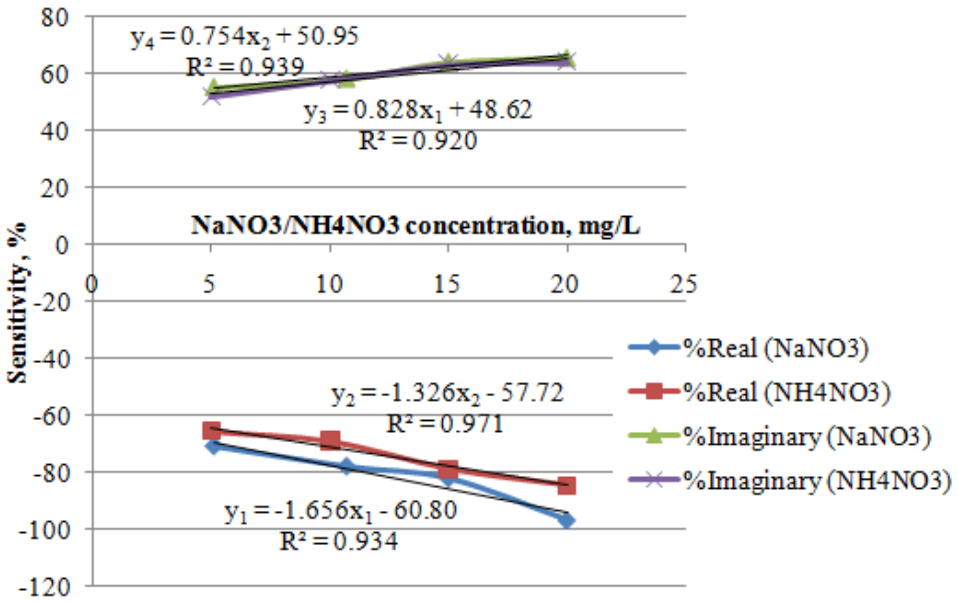

Figure 7.13: Graphs of sensitivity from experiment with different concentration of Sodium Nitrate ($NaNO_3$)/ Ammonium Nitrate (NH_4NO_3) with linear regression relationship

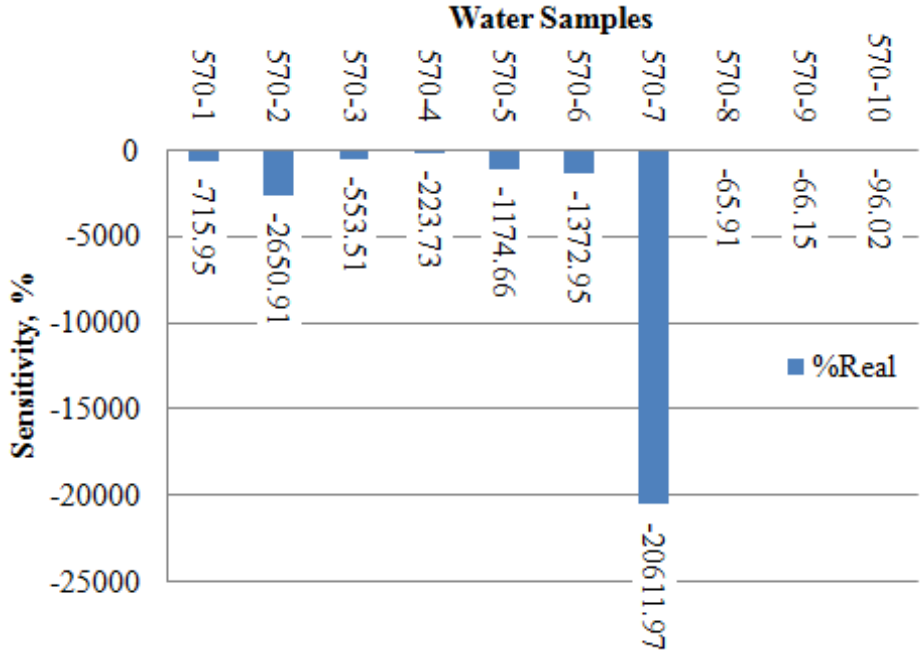

Figure 7.14: Real part sensitivity to the water samples

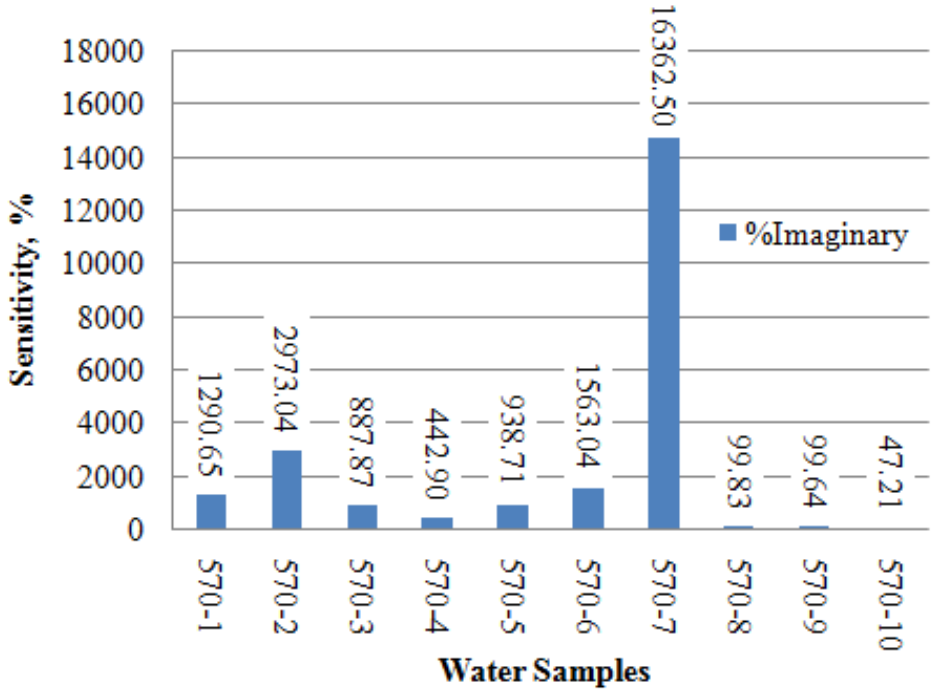

Figure 7.15: Imaginary part sensitivity to the water samples

As for the safe to consume water samples, 570-8, 570-9 and 570-10 are included where the real sensitivity values range and the imaginary sensitivity values range are between -65% to -96% and 47% and 99%, respectively. Although 570-10 is in the safe group, there are some discolorations caused by certain algae or living organism inside the water samples, thus changing the electrical properties of the water samples as shown in Figure 5.13. Caution should be considered in consuming 570-10.

7.6 Conclusion

The work above shows that a very distinct detection of nitrates and contamination in water can be achieved using a low-cost system. It can be used as a tool for water sources monitoring in farm where the nitrate level should not exceed 44.3 mg/L in New Zealand. The system has also been tested with drinking water samples and has shown promising results to be a sensing tool of contamination detection in drinking water.

CHAPTER 8

Conclusions and Future Research

8.1 Conclusions

This thesis contained the important information about the processes in designing, characterizing, simulating, testing, data analysing, and introducing a low-cost system based on a novel planar electromagnetic sensor for the estimation of Nitrate contamination and water quality. Ultimately, the works in this thesis have successfully demonstrated the estimation of Nitrate contamination and water quality estimation using novel planar electromagnetic sensors based on the combination of meander sensor and interdigital sensor. The problem formulation in Chapter 1 has outlined the topic and objectives of this research. The discussion of the recent progress of planar sensors, which utilized the effects of capacitive and inductive sensing has been covered. Furthermore, the advantages and disadvantages of different types of existing nitrate sensing system have been discussed.

In Chapter 2, the design structures of meander sensor and interdigital sensors have been described. The connection types and principle of measurement have also been explained. The attempts in improving the sensors performance have been conducted by changing the meander and interdigital sensors designs and the introduction of negative back plane. In total, 96 planar electromagnetic sensors have been fabricated in this research. The characteristic of all the planar electromagnetic sensors and the effect of different design to the electrical parameters of the sensors form the experiment were discussed in Chapter 4. An equivalent electrical circuit was established for each the parallel and series combined meander and interdigital sensors. Sensors with higher capacitance and inductance values tend to have better electric and magnetic fields distribution. In addition, they have better output response. Therefore, the best parallel (SSCP21_1 to SSCP24_1) and series connected planar electromagnetic sensors

(SECS21_1 to SECS24_1) were determined based on the highest capacitance and inductive compared to other similar sensors.

The modelling of the selected sensors in Chapter 4 was initially based on simplified electric current and induction models current based on gauge transformation. It was important to use the gauge transformation because the original electrical current and induction current models will make a huge demand of computation power especially in term of simulation machines memory and processor speed. The results of impedance characteristics of the sensors were compared with the experimental results. The outcomes showed similarity, however, from the simulation results, the effect capacitance component was reduced into the definition of the magnetic vector potential causing the transition points to be absented below 100 MHz. Based on the best sensor (SECS22_1) selected in Chapter 4, the distribution of electric field and magnetic field were observed. Furthermore, the effect of environment properties changes (electrical conductivity and relative permittivity) was investigated to determine the expected output. It can be concluded that the current model was not the closest to the actual sensor (but share acceptable similarities) because of inductance component dominance, therefore, new model was applied based on only electric current. The results from the latter simulation show that the changes in the electrical conductivity values of the environment have a high effect to SECS22_1 output.

The studies in Chapter 5, the initial studies with water samples of $NaNO_3$, NH_4NO_3 and drinking water samples taken from water treatment plants have showed that series connected sensors have better response when compared to parallel connected sensors. Furthermore, a planar electromagnetic sensor with meander sensor and interdigital sensor combined in series (SECS22_1) had the best real part sensitivity and imaginary part sensitivity and was chosen and used in the next experiments for further analysis. The comparison between simulation and experimental results showed that the real part sensitivity is linearly correlated with the electrical conductivity; σ of the solution of the water samples. The concept of electrochemical impedance spectroscopy was also considered interpreting the results based on an equivalent electrochemical system for the sensor's surface with intact coating. The model had been used to understand the output response of SECS22_1 on the Nyquist plot. It can be deduced that SECS22_1 gave

capacitive loop and inductive loop at low frequency and high frequency, respectively. The inductance element of the meander sensor had also caused a significant deviation of the loops especially at high frequency. Apart from that, the impedance curve is shrinking and smaller as the concentration is increased, the results suggest that it caused by the reduction of σ value and confirmed in the simulation results in Chapter 3.

The attempt of using models based on *MLR* to estimate nitrates contamination in Manawatu River had been unsuccessful because of the oversimplification of the problem. Water samples proved to be containing other major ions that could be interfering with the measurement and had caused inaccuracy to the measurement.

Alternatively, a method for the estimation of Nitrate concentration in water sources was established based on the Independent Component Analysis (*ICA*). The general idea was, for any given water sample, nine sets of multivariate measurements were recorded. Then, the nine sets of multivariate data were analysed using *FastICA* (Independent Component Analysis program). By default, nine independent components were obtained, and each independent component is assumed to be independent to the combination effect of ions in the water sample. This means that one independent component may strongly represent the output response of Nitrate ion. The method was carefully constructed by taking into account the *ICA* limitations. To estimate the amount of different nitrate concentrations, all the independent components were evaluated in the spectral matching process with the reference spectral using *MSE* and Spearman correlation function for every *FastICA* contrast function. The nitrate estimation equation for every *FastICA* function was established statistically based on the results. From the experiment with water samples of the combination of NH_4NO_3 and $(NH_4)_2HPO_4$, the results show that *pow3*, *gauss*, and *gauss* gave the best and closest estimation of nitrate with the correlation function, R^2 of 0.9892, 0.9945, and 0.9862, from the linear plots of the calculated value versus the estimated value. Moreover, the contrast functions of *pow3*, *tanh*, and *gauss* generate maximum error of between just below 25% and 0.45%. The average errors for these functions in estimating nitrate contamination are between around 4% to just over 10%. From the experiment that involved Manawatu River water samples, the results revealed that the contrast function of *pow3*, *tanh* and *skew* have shown the best accuracy in the estimation of NH_4NO_3 added into the river water samples with low

%error between -6% to 3%. This showed that at least the contrast functions of *pow3* and *tanh* can reliably be used to estimate nitrate contaminations in natural water samples.

The works that involved the development of a low-cost system in Chapter 7 proved that a system based on a novel planar electromagnetic sensor can be used as a tool for the estimation of nitrate contamination and water quality measurement. The low-cost system used a microcontroller, a waveform generator circuit, a signal conditioning circuit, a phase and gain measurement circuit, a frequency to voltage circuit, a temperature circuit, a data acquisition system based on C8051F020 microcontroller and a user friendly *LabView* program.

8.2 Future Research

Further research works need to be conducted using the estimation method based on the *ICA* for the detection of other major ions that commonly existed in natural water sources such as sodium: Na^{+}, Potassium: K^{+}, Calcium: Ca^{2+}, Magnesium: Mg^{2+}, Fluoride: F^{-}, Chloride: Cl^{-}, Sulphate: SO_4^{2-}, Bicarbonate: HCO_3^{-}, Carbonate: CO_3^{2-}, and Phosphate: PO_4^{3-}. Because of the flexibility of the estimation method based on the *ICA*, this proposed study can be done by preparing the standard samples, thus providing the relevant reference spectral of the aforementioned other major ions. This will help to develop a better system with a multi-sensing capability.

For further improvements, the sensor will be miniaturized to reduce the overall cost. Furthermore, the concept of ion selective electrode (*ISE*) polymerised with pyrolle doped with nitrate which will increase the selectivity. The process roughly will involve the replacement of copper track with graphite and polymerization of pyrolle doped with nitrate on the graphite through electrolysis to form polypyrolle.

On top of that, another set of miniaturized sensor can be constructed based on gold electrodes, a nitrate selective membrane based on biological/biological-synthesized

material (bio-sensor), and substrate with higher dielectric constant to improve the output response of the sensor.

The model based on the *ICA* will be improved by investigating other methods or algorithms of evaluations in the spectral matching such as Wavelet, Fourier Transform, and phase-based waveform matching.

The low-cost system will be improved by upgrading the waveform generator into Direct Digital Synthesis (*DDS*) function generator. This is important to allow better control of the frequency values and to realize the application of the model based on the *ICA* with the low-cost system. Since the low-cost system is targeted to be used in the open field, the study on the effect on temperature on the sensors sensitivities (real part and imaginary part) and the accuracy of the estimation method based on the *ICA* is important when the low-cost system is deployed.

As this thesis is completed, a research is already being conducted to incorporate the low-cost system with wireless technologies such as Zigbee to allow remote monitoring of environmental parameters.

.

References

[1] C. J. Vorosmarty, P. Green, J. Salisbury, and R. B. Lammers, "Global Water Resources: Vulnerability from Climate Change and Population Growth," *Science,* vol. 289, pp. 284-288, July 14, 2000 2000.

[2] http://www.unep.org/dewa/assessments/ecosystems/water/vitalwater/10.htm.

[3] http://www.grid.unep.ch/product/publication/freshwater_europe/ecosys.php.

[4] http://www.nzinstitute.org/index.php/nzahead/measures/water_quality/.

[5] N. F. Metcalf, W. K. Metcalf, and X. Wang, "The Differing Sensitivities of the Hemoglobin of Fetal and Adult Red-Cells to Oxidation by Nitrites in Man - the Role of Plasma," in *Proceedings of the Physiological Society*, Cambridge Meeting: Poster Communications, 1987, p. 44.

[6] L. P. Donald and D. F. Charles, "Water Quality for Livestock Drinking," *MU Extension Publication, University of Missouri-Columbia,* vol. EQ 381, pp. 1-4, 2001.

[7] J. Reichard and C. Brown, "Detecting groundwater contamination of a river in Georgia, USA using baseflow sampling," *Hydrogeology Journal,* vol. 17, pp. 735-747, 2009.

[8] A. P. S. Terblanche, "Health hazards of nitrate in drinking water," *Water Sa,* vol. 17, pp. 77-82, 1991.

[9] M. H. Ward, B. A. Kilfoy, P. J. Weyer, K. E. Anderson, A. R. Folsom, and J. R. Cerhan, "Nitrate Intake and the Risk of Thyroid Cancer and Thyroid Disease," *Epidemiology,* vol. 21, pp. 389-395 2010.

[10] H. J. Di and K. C. Cameron, "Nitrate leaching losses and pasture yields as affected by different rates of animal urine nitrogen returns and application of a nitrification inhibitor - a lysimeter study," *Nutrient Cycling in Agroecosystems,* vol. 79, pp. 281-290, Nov 2007.

[11] H. J. Di and K. C. Cameron, "Nitrate leaching in temperate agroecosystems: sources, factors and mitigating strategies," *Nutrient Cycling in Agroecosystems,* vol. 64, pp. 237-256, Nov 2002.

[12] E. M. Stanley, *Fundamental of Environmental Chemistry*, 3rd ed. Boca Raton: CRC Press, Taylor and Francis Group, 2009.

[13] http://www.reopure.com/nitratinfo.html.

[14] S. S. M. Hassan, "Ion-selective electrodes in organic functional group analysis. Microdetermination of nitrates and nitramines with use of the iodide electrode," *Talanta,* vol. 23, pp. 738-740, 1976.

[15] R. Bartzatt and L. Donigan, "The colorimetric determination of nitrate anion in aqueous and solid samples utilizing an aromatic derivative in acidic solvent," *Toxicological & Environmental Chemistry,* vol. 86, pp. 75 - 85, 2004.

[16] M. I. C. Monteiro, F. N. Ferreira, N. M. M. de Oliveira, and A. K. Ávila, "Simplified version of the sodium salicylate method for analysis of nitrate in drinking waters," *Analytica Chimica Acta,* vol. 477, pp. 125-129, 2003.

[17] S.-J. Cho, S. Sasaki, K. Ikebukuro, and I. Karube, "A simple nitrate sensor system using titanium trichloride and an ammonium electrode," *Sensors and Actuators B: Chemical,* vol. 85, pp. 120-125, 2002.

[18] M. A. Ferree and R. D. Shannon, "Evaluation of a second derivative UV/visible spectroscopy technique for nitrate and total nitrogen analysis of wastewater samples," *Water Research,* vol. 35, pp. 327-332, 2001.

[19] N. J. Gumede, "Harmonization of internal quality tasks in analytical laboratories case studies : water analysis methods using polarographic and voltammetric techniques," Masters Degree in Technology, Faculty of Applied Sciences, Durban University of Technology, Durban, 2008.
[20] F.-R. Maria Dolores and et al., "The use of one-shot sensors with a dedicated portable electronic radiometer for nitrate measurements in aqueous solutions," *Measurement Science and Technology,* vol. 19, p. 095204, 2008.
[21] M. T. Downes, "An improved hydrazine reduction method for the automated determination of low nitrate levels in freshwater," *Water Research,* vol. 12, pp. 673-675, 1978.
[22] http://www.mfe.govt.nz/publications/ser/technical-guide-new-zealand-environmental-indicators/html/page4-12.html.
[23] D. Connolly and B. Paull, "Rapid determination of nitrate and nitrite in drinking water samples using ion-interaction liquid chromatography," *Analytica Chimica Acta,* vol. 441, pp. 53-62, 2001.
[24] T. Kjær, L. Hauer Larsen, and N. P. Revsbech, "Sensitivity control of ion-selective biosensors by electrophoretically mediated analyte transport," *Analytica Chimica Acta,* vol. 391, pp. 57-63, 1999.
[25] T. A. Bendikov and T. C. Harmon, "A Sensitive Nitrate Ion-Selective Electrode from a Pencil Lead. An Analytical Laboratory Experiment," *Journal of Chemical Education,* vol. 82, pp. 439-441, 2005.
[26] M. J. Moorcroft, J. Davis, and R. G. Compton, "Detection and determination of nitrate and nitrite: a review," *Talanta,* vol. 54, pp. 785-803, Jun 21 2001.
[27] B. Hull and V. John, *Non-destructive testing*: Springer-Verlag New York Inc.,New York, NY, 1988.
[28] M. B. Mesina, T. P. R. de Jong, and W. L. Dalmijn, "Automatic sorting of scrap metals with a combined electromagnetic and dual energy X-ray transmission sensor," *International Journal of Mineral Processing,* vol. 82, pp. 222-232, Jun 2007.
[29] A. Srinivasan, *Handbook of Precision Agriculture*. New York: The Haworth Press, 2006.
[30] D. Schlicker, A. Washabaugh, I. Shay, and N. Goldfine, "Inductive and capacitive array imaging of buried objects," *Insight,* vol. 48, pp. 302-306, May 2006.
[31] A. R. Mohd Syaifudin, K. P. Jayasundera, and S. C. Mukhopadhyay, "A low cost novel sensing system for detection of dangerous marine biotoxins in seafood," *Sensors and Actuators B: Chemical,* vol. 137, pp. 67-75, 2009.
[32] A. V. Mamishev, K. Sundara-Rajan, F. Yang, Y. Q. Du, and M. Zahn, "Interdigital sensors and transducers," *Proceedings of the 2006 IEEE Sensors Applications Symposium,* vol. 92, pp. 808-845, May 2004.
[33] A. Guadarrama-Santana and A. Garcia-Valenzuela, "Principles and Methodology for the Simultaneous Determination of Thickness and Dielectric Constant of Coatings With Capacitance Measurements," *Instrumentation and Measurement, IEEE Transactions on,* vol. 56, pp. 107-112, 2007.
[34] B. George, H. Zangl, T. Bretterklieber, and G. Brasuer, "A Combined Inductive-Capacitive Proximity Sensor and Its Application to Seat Occupancy Sensing," presented at the I2MTC-International Instrumentation and Measurement, Singapore, 2009.
[35] N. Kirchner, D. Hordern, D. K. Liu, and G. Dissanayake, "Capacitive sensor for object ranging and material type identification," *Sensors and Actuators a-Physical,* vol. 148, pp. 96-104, Nov 4 2008.

[36] H. M. Greenhou, "Design of Planar Rectangular Microelectronic Inductors," *IEEE Transactions on Parts Hybrids and Packaging,* vol. 10, pp. 101-109, 1974.
[37] H. Y. Hwang, S. W. Yun, and I. S. Chang, "A design of planar elliptic bandpass filter using SMD type partially metallized rectangular dielectric resonators," *2001 IEEE Mtt-S International Microwave Symposium Digest, Vols 1-3,* pp. 1483-1486, 2001.
[38] K. Um and B. An, "Design of rectangular printed planar antenna via input impedance for supporting mobile wireless communications," *Proceeedings IEEE 55th Vehicular Technology Conference, Vtc Spring 2002, Vols 1-4,* pp. 948-951, 2002.
[39] J. Yunas, N. A. Rahman, L. T. Chai, and B. Y. Majlis, "Study of coreless planar inductor at high operating frequency," *Proceedings 2004 IEEE International Conference on Semiconductor Electronics,* pp. 606-610, 2004.
[40] J. Fava and M. Ruch, "Design, construction and characterisation of ECT sensors with rectangular planar coils," *Insight,* vol. 46, pp. 268-274, May 2004.
[41] J. L. Quirarte, M. J. M. Silva, and M. S. R. Palacios, "Software for analysis and design of rectangular planar arrays," *2004 1st International Conference on Electrical and Electronics Engineering (ICEEE),* pp. 90-95, 2004.
[42] D. Valderas, J. Melendez, and I. Sancho, "Some design criteria for UWB planar monopole antennas: Application to a slotted rectangular monopole," *Microwave and Optical Technology Letters,* vol. 46, pp. 6-11, Jul 5 2005.
[43] L. W. Li, Y. N. Li, and J. R. Mosig, "Design of a novel rectangular patch antenna with planar metamaterial patterned substrate," *2008 IEEE International Workshop on Antenna Technology : Small Antennas and Novel Metamaterials - Conference Proceedings,* pp. 119-122, 2008.
[44] H. Oraizi and M. T. Noghani, "Design and Optimization of Linear and Planar slot Arrays on Rectangular Waveguides," *2008 European Microwave Conference, Vols 1-3,* pp. 1468-1471, 2008.
[45] J. O. Fava, L. Lanzani, and M. C. Ruch, "Multilayer planar rectangular coils for eddy current testing: Design considerations," *Ndt & E International,* vol. 42, pp. 713-720, Dec 2009.
[46] N. J. Goldfine, "Magnetometers for Improved Materials Characterization in Aerospace Applications," *Materials Evaluation,* vol. 51, pp. 396-405, Mar 1993.
[47] N. J. Goldfine and D. Clark, "Near-surface material property profiling for determination of SCC susceptibility," presented at the in 4th EPRI Balance-of-Plant Heat Exchanger NDE Symp, 1996.
[48] S. Yamada, H. Fujiki, M. Iwahara, S. C. Mukhopadhyay, and F. P. Dawson, "Investigation of printed wiring board testing by using planar coil type ECT probe," *IEEE Transactions on Magnetics,* vol. 33, pp. 3376-3378, Sep 1997.
[49] S. C. Mukhopadhyay, S. Yamada, and M. Iwahara, "Experimental determination of optimum coil pitch for a planar mesh-type micromagnetic sensor," *IEEE Transactions on Magnetics,* vol. 38, pp. 3380-3382, Sep 2002.
[50] S. C. Mukhopadhyay, "Quality inspection of electroplated materials using planar type micro-magnetic sensors with post-processing from neural network model," *IEEE Proceedings-Science Measurement and Technology,* vol. 149, pp. 165-171, Jul 2002.
[51] M. A. Md Yunus and S. C. Mukhopadhyay, "Novel planar electromagnetic sensors for detection of nitrates and contamination in natural water sources," *IEEE Sensors Journal,* Accepted for publication 24 Sept 2010.

[52] S. C. Mukhopadhyay, "A novel planar mesh-type microelectromagnetic sensor - Part II: Estimation of system properties," *IEEE Sensors Journal,* vol. 4, pp. 308-312, Jun 2004.
[53] S. C. Mukhopadhyay, "High Performance Planar Electromagnetic Sensors-A Review of Few Applications," in *New Zealand National Conference on Non-Destructive Testing*, 2004, pp. 33-41.
[54] S. C. Mukhopadhyay, "Novel planar electromagnetic sensors: Modeling and performance evaluation," *Sensors,* vol. 5, pp. 546-579, Dec 2005.
[55] Y. Sheiretov, D. Grundy, V. Zilberstein, N. Goldfine, and S. Maley, "MWM-Array Sensors for In Situ Monitoring of High-Temperature Components in Power Plants," *IEEE Sensors Journal,* vol. 9, pp. 1527-1536, Nov 2009.
[56] K. D. AnimAppiah and S. M. Riad, "Analysis and design of ferrite cores for eddy-current-killed oscillator inductive proximity sensors," *IEEE Transactions on Magnetics,* vol. 33, pp. 2274-2281, May 1997.
[57] D. Karunanayaka, Gooneratne, C. P., Mukhopadhyay, S. C., and Sen Gupta G. , "A Planar Electromagnetic Sensors Aided Non-destructive Testing of Currency Coins," *NDT.net* vol. 11, pp. 1-12, Sept 2006.
[58] K. Sundara-Rajan, L. Byrd, and A. V. Mamishev, "Moisture content estimation in paper pulp using fringing field impedance Spectroscopy," *IEEE Sensors Journal,* vol. 4, pp. 378-383, Jun 2004.
[59] S. M. Radke and E. C. Alocilja, "Design and fabrication of a microimpedance biosensor for bacterial detection," *IEEE Sensors Journal,* vol. 4, pp. 434-440, Aug 2004.
[60] N. Sekiguchi, T. Komeda, H. Funakubo, R. Chabicovsky, J. Nicolics, and G. Stangl, "Microsensor for the measurement of water content in the human skin," *Sensors and Actuators B-Chemical,* vol. 78, pp. 326-330, Aug 30 2001.
[61] P. Furjes, A. Kovacs, C. Ducso, M. Adam, B. Muller, and U. Mescheder, "Porous silicon-based humidity sensor with interdigital electrodes and internal heaters," *Sensors and Actuators B-Chemical,* vol. 95, pp. 140-144, Oct 15 2003.
[62] S. M. Radke and E. C. Alocilja, "A microfabricated biosensor for detecting foodborne bioterrorism agents," *IEEE Sensors Journal,* vol. 5, pp. 744-750, 2005.
[63] A. R. M. Syaifudin, K. P. Jayasundera, and S. C. Mukhopadhyay, "A low cost novel sensing system for detection of dangerous marine biotoxins in seafood," *Sensors and Actuators B-Chemical,* vol. 137, pp. 67-75, Mar 28 2009.
[64] A. R. M. Syaifudin, M. A. Yunus, S. C. Mukhopadhyay, and K. P. Jayasundera, "A novel planar interdigital sensor for environmental monitoring," in *Sensors, 2009 IEEE*, Christchurch, New Zealand, 2009, pp. 105-110.
[65] S. C. Mukhopadhyay, C. P. Gooneratne, S. Demidenko, and G. S. Gupta, "Low Cost Sensing System for Dairy Products Quality Monitoring," *Proceedings of the IEEE Instrumentation and Measurement Technology Conference, 2005. IMTC 2005. ,* vol. 1, pp. 244-249, May 2005.
[66] S. C. Mukhopadhyay, G. Sen Gupta, J. D. Woolley, and S. N. Demidenko, "Saxophone reed inspection employing planar electromagnetic sensors," *IEEE Transactions on Instrumentation and Measurement,* vol. 56, pp. 2492-2503, Dec 2007.
[67] S. C. Mukhopadhyay and C. P. Gooneratne, "A novel planar-type biosensor for noninvasive meat inspection," *IEEE Sensors Journal,* vol. 7, pp. 1340-1346, Sep-Oct 2007.
[68] S. C. Mukhopadhyay, S. D. Choudhury, T. Allsop, V. Kasturi, and G. E. Norris, "Assessment of pelt quality in leather making using a novel non-invasive sensing

approach," *Journal of Biochemical and Biophysical Methods,* vol. 70, pp. 809-815, 2008.

[69] M. A. M. Yunus, V. Kasturi, S. C. Mukhopadhyay, and G. Sen Gupta, "Sheep skin property estimation using a low-cost planar sensor," in *Instrumentation and Measurement Technology Conference, 2009. I2MTC '09. IEEE*, 2009, pp. 482-486.

[70] K. G. Ong, C. A. Grimes, C. L. Robbins, and R. S. Singh, "Design and application of a wireless, passive, resonant-circuit environmental monitoring sensor," *Sensors and Actuators a-Physical,* vol. 93, pp. 33-43, Aug 25 2001.

[71] K. G. Ong, J. Wang, R. S. Singh, L. G. Bachas, and C. A. Grimes, "Monitoring of bacteria growth using a wireless, remote query resonant-circuit sensor: application to environmental sensing," *Biosensors & Bioelectronics,* vol. 16, pp. 305-312, Jun 2001.

[72] K. G. Ong, J. S. Bitler, C. A. Grimes, L. G. Puckett, and L. G. Bachas, "Remote query resonant-circuit sensors for monitoring of bacteria growth: Application to food quality control," *Sensors,* vol. 2, pp. 219-232, Jun 2002.

[73] M. C. Hofmann, F. Kensy, J. Buchs, W. Mokwa, and U. Schnakenberg, "Transponder-based sensor for monitoring electrical properties of biological cell solutions," *Journal of Bioscience and Bioengineering,* vol. 100, pp. 172-177, Aug 2005.

[74] E. L. Tan, W. N. Ng, R. Shao, B. D. Pereles, and K. G. Ong, "A wireless, passive sensor for quantifying packaged food quality," *Sensors,* vol. 7, pp. 1747-1756, Sep 2007.

[75] J. B. Ong, Z. P. You, J. Mills-Beale, E. L. Tan, B. D. Pereles, and K. G. Ong, "A Wireless, Passive Embedded Sensor for Real-Time Monitoring of Water Content in Civil Engineering Materials," *IEEE Sensors Journal,* vol. 8, pp. 2053-2058, Nov-Dec 2008.

[76] B. Sharavanan, P. Jung-Rae, M. Tarisha, A. Niwat, A. Alkim, R. Tenneti, and R. N., "Conformal Passive Sensors for Wireless Structural Health Monitoring," in *Material and devices for smart systems III*, Boston, 2009, pp. 341-348.

[77] E. W. Stanley and et al., "Wireless temperature sensing using temperature-sensitive dielectrics within responding electric fields of open-circuit sensors having no electrical connections," *Measurement Science and Technology,* vol. 21, p. 075201, 2010.

[78] S. E. Woodard, "SansEC sensing technology - A new tool for designing space systems and components," in *Aerospace Conference, 2011 IEEE*, 2011, pp. 1-11.

[79] E. Dickey, O. Varghese, K. Ong, D. Gong, M. Paulose, and C. Grimes, "Room Temperature Ammonia and Humidity Sensing Using Highly Ordered Nanoporous Alumina Films," *Sensors,* vol. 2, pp. 91-110, 2002.

[80] K. V. Oomman and A. G. Craig, "Metal Oxide Nanoarchitectures for Environmental Sensing," *Journal of Nanoscience and Nanotechnology,* vol. 3, pp. 277-293, 2003.

[81] J. Garcia-Canton, A. Merlos, and A. Baldi, "High-Quality Factor Electrolyte Insulator Silicon Capacitor for Wireless Chemical Sensing," *Electron Device Letters, IEEE,* vol. 28, pp. 27-29, 2007.

[82] J. García-Cantón, A. Merlos, and A. Baldi, "A wireless LC chemical sensor based on a high quality factor EIS capacitor," *Sensors and Actuators B: Chemical,* vol. 126, pp. 648-654, 2007.

[83] R. N. Sah, "Nitrate-nitrogen determination—a critical review," *Communications in Soil Science and Plant Analysis,* vol. 25, pp. 2841-2869, 1994/11/01 1994.

[84] R. Desai, M. Marti Villalba, N. S. Lawrence, and J. Davis, "Green Approaches to Field Nitrate Analysis: An Electroanalytical Perspective," *Electroanalysis,* vol. 21, pp. 789-796, 2009.
[85] A. R. Asghari, M. K. Amini, H. R. Mansour, and M. Salavati-Niasari, "A tetra-coordinate nickel(II) complex as neutral carrier for nitrate-selective PVC membrane electrode," *Talanta,* vol. 61, pp. 557-563, 2003.
[86] M. M. Ardakani, A. Dastanpour, and M. Salavati-Niasari, "A highly selective nitrate electrode based on a tetramethyl cyclotetra-decanato-nickel(II) complex," *Journal of Electroanalytical Chemistry,* vol. 568, pp. 1-6, 2004.
[87] R. K. Mahajan, R. Kaur, H. Miyake, and H. Tsukube, "Zn(II) complex-based potentiometric sensors for selective determination of nitrate anion," *Analytica Chimica Acta,* vol. 584, pp. 89-94, 2007.
[88] T. Bolanca, S. Cerjan-Stefanovic, G. Srecnik, Z. Debeljak, and M. Novic, *Development of an ion chromatographic method for monitoring fertilizer industry wastewater quality* vol. 27. Colchester, ROYAUME-UNI: Taylor & Francis, 2004.
[89] R. Michalski and I. Kurzyca, "Determination of Nitrogen Species (Nitrate, Nitrite and Ammonia Ions) in Environmental Samples by Ion Chromatography," *Polish Journal of Environmental Studies,* vol. 15, pp. 5-18, 2006.
[90] D. Kim, I. Goldberg, and J. W. Judy, "Micromachined Amperometric Nitrate Sensor with Integrated Microfluidics," in *Proceedings of the Sixth International Symposium on Chemical and Biological Sensors and Analytical Systems*, Hawaii, 2004, pp. 223-231.
[91] S. Ward-Jones, C. E. Banks, A. O. Simm, L. Jiang, and R. G. Compton, "An In Situ Copper Plated Boron-Doped Diamond Microelectrode Array for the Sensitive Electrochemical Detection of Nitrate," *Electroanalysis,* vol. 17, pp. 1806-1815, 2005.
[92] K. Soropogui, M. Sigaud, and O. Vittori, "Alert Electrodes for Continuous Monitoring of Nitrate Ions in Natural Water," *Electroanalysis,* vol. 18, pp. 2354-2360, 2006.
[93] M. J. A. Shiddiky, M.-S. Won, and Y.-B. Shim, "Simultaneous analysis of nitrate and nitrite in a microfluidic device with a Cu-complex-modified electrode," *Electrophoresis,* vol. 27, pp. 4545-4554, 2006.
[94] T. R. L. C. Paixão, J. L. Cardoso, and M. Bertotti, "Determination of nitrate in mineral water and sausage samples by using a renewable in situ copper modified electrode," *Talanta,* vol. 71, pp. 186-191, 2007.
[95] S. Aravamudhan and S. Bhansali, "Development of Micro-Fluidic Nitrate-Selective Sensor Based on Polypyrrole Nanowires," in *Solid-State Sensors, Actuators and Microsystems Conference, 2007. TRANSDUCERS 2007. International*, 2007, pp. 1059-1062.
[96] Y. Li, J. Sun, C. Bian, J. Tong, and S. Xia, "Electrodeposition of copper nano-clusters at a platinum microelectrode for trace nitrate determination," *Procedia Engineering,* vol. 5, pp. 339-342, 2010.
[97] E. Andreoli, V. Annibaldi, D. A. Rooney, K.-S. Liao, N. J. Alley, S. A. Curran, and C. B. Breslin, "Electrochemical Conversion of Copper-Based Hierarchical Micro/Nanostructures to Copper Metal Nanoparticles and Their Testing in Nitrate Sensing," *Electroanalysis,* pp. 2164–2173, 2011.
[98] D. Albanese, M. Di Matteo, and C. Alessio, "Screen printed biosensors for detection of nitrates in drinking water," in *Computer Aided Chemical*

Engineering. vol. Volume 28, S. Pierucci and G. B. Ferraris, Eds., ed: Elsevier, 2010, pp. 283-288.
[99] C. J. Taylor, L. A. Bain, D. J. Richardson, S. Spiro, and D. A. Russell, "Construction of a whole-cell gene reporter for the fluorescent bioassay of nitrate," *Analytical Biochemistry,* vol. 328, pp. 60-66, 2004.
[100] L. F. Capitán-Vallvey, E. Arroyo-Guerrero, M. D. Fernández-Ramos, and F. Santoyo-Gonzalez, "Disposable Receptor-Based Optical Sensor for Nitrate," *Analytical Chemistry,* vol. 77, pp. 4459-4466, 2005.
[101] T. Taniai, A. Sakuragawa, and T. Okutani, "Monitoring of Hydrogen Peroxide, Nitrate and Nitrite in Rain Water," *Analytical Sciences,* vol. 16, pp. 275-281, 2000.
[102] L. Monser, S. Sadok, G. M. Greenway, I. Shah, and R. F. Uglow, "A simple simultaneous flow injection method based on phosphomolybdenum chemistry for nitrate and nitrite determinations in water and fish samples," *Talanta,* vol. 57, pp. 511-518, 2002.
[103] Z. Legnerová, P. Solich, H. Sklenárová, D. Satínský, and R. Karlícek, "Automated simultaneous monitoring of nitrate and nitrite in surface water by sequential injection analysis," *Water Research,* vol. 36, pp. 2777-2783, 2002.
[104] C. Gal, W. Frenzel, and J. Möller, "Re-Examination of the Cadmium Reduction Method and Optimisation of Conditions for the Determination of Nitrate by Flow Injection Analysis," *Microchimica Acta,* vol. 146, pp. 155-164, 2004.
[105] C. A. G. P. Paula, Jos, eacute, L. F. C. Lima, M.L, uacute, and M. F. S. S. cia, "An enzymatic flow analysis methodology for the determination of nitrates and nitrites in waters," *International Journal of Environmental and Analytical Chemistry,* vol. 85, pp. 29-40, 2005.
[106] B. Haghighi and S. F. Kurd, "Sequential flow injection analysis of ammonium and nitrate using gas phase molecular absorption spectrometry," *Talanta,* vol. 64, pp. 688-694, 2004.
[107] P. Nagaraja, M. Hemantha Kumar, H. Yathirajan, and J. Prakash, "Highly Sensitive Reaction of Nitrate with Brucine and 3-Methyl-2-benzothiazolinone Hydrazone Hydrochloride for the Determination of Nitrate in Environmental Samples," *Analytical Sciences,* vol. 19, pp. 961-963, 2003.
[108] P. Mikuska and Z. Vecera, "Simultaneous determination of nitrite and nitrate in water by chemiluminescent flow-injection analysis," *Analytica Chimica Acta,* vol. 495, pp. 225-232, 2003.
[109] N. Beda and A. Nedospasov, "A spectrophotometric assay for nitrate in an excess of nitrite," *Nitric Oxide,* vol. 13, pp. 93-97, 2005.
[110] S. A. Mir, "A rapid technique for determination of nitrate and nitric acid by acid reduction and diazotization at elevated temperature," *Analytica Chimica Acta,* vol. 620, pp. 183-189, 2008.
[111] X. Tu, B. Xiao, J. Xiong, and X. Chen, "A simple miniaturised photometrical method for rapid determination of nitrate and nitrite in freshwater," *Talanta,* vol. 82, pp. 976-983, 2010.
[112] H. Kodamatani, S. Yamazaki, K. Saito, T. Tomiyasu, and Y. Komatsu, "Selective determination method for measurement of nitrite and nitrate in water samples using high-performance liquid chromatography with post-column photochemical reaction and chemiluminescence detection," *Journal of Chromatography A,* vol. 1216, pp. 3163-3167, 2009.
[113] H. Kodamatani, S. Yamazaki, K. Saito, Y. Komatsu, and T. Tomiyasu, "Rapid Method for Simultaneous Determination of Nitrite and Nitrate in Water Samples

Using Short-Column Ion-Pair Chromatographic Separation, Photochemical Reaction, and Chemiluminescence Detection," *Analytical Sciences,* vol. 27, p. 187, 2011.
[114] M. Akyüz and S. Ata, "Determination of low level nitrite and nitrate in biological, food and environmental samples by gas chromatography-mass spectrometry and liquid chromatography with fluorescence detection," *Talanta,* vol. 79, pp. 900-904, 2009.
[115] P. Griess, "Bemerkungen zu der Abhandlung der HH. Weselsky und Benedikt Ueber einige Azoverbindungen," *Berichte der deutschen chemischen Gesellschaft,* vol. 12, pp. 426-428, 1879.
[116] M. A. M. Yunus and S. C. Mukhopadhyay, "Novel Planar Electromagnetic Sensors for Detection of Nitrates and Contamination in Natural Water Sources," *Sensors Journal, IEEE,* vol. 11, pp. 1440-1447, 2011.
[117] A. V. Mamishev, B. C. Lesieutre, and M. Zahn, "Optimization of multi-wavelength interdigital dielectrometry instrumentation and algorithms," *IEEE Transactions on Dielectrics and Electrical Insulation,* vol. 5, pp. 408-420, Jun 1998.
[118] S. C. Mukhopadhyay, C. P. Gooneratne, G. Sen Gupta, and S. Yamada, "Characterization and comparative evaluation of novel planar electromagnetic sensors," *IEEE Transactions on Magnetics,* vol. 41, pp. 3658-3660, Oct 2005.
[119] A. R. Mohd Syaifudin, S. C. Mukhopadhyay, and P. L. Yu, "Modelling and fabrication of optimum structure of novel interdigital sensors for food inspection," *International Journal of Numerical Modelling: Electronic Networks, Devices and Fields,* pp. 456-466, 2011.
[120] "COMSOL AC/DC Module, User's Guide," *Version 3.5a,* November 2008.
[121] O. A. Stafford, B. R. Hinderliter, and S. G. Croll, "Electrochemical impedance spectroscopy response of water uptake in organic coatings by finite element methods," *Electrochimica Acta,* vol. 52, pp. 1339-1348, Nov 12 2006.
[122] T. S. Light, S. Licht, A. C. Bevilacqua, and K. R. Morash, "The fundamental conductivity and resistivity of water," *Electrochemical and Solid State Letters,* vol. 8, pp. E16-E19, 2005.
[123] C. J. McNamara, M. Breuker, M. Helms, T. D. Perry, and R. Mitchell, "Biodeterioration of Incralac used for the protection of bronze monuments," *Journal of Cultural Heritage,* vol. 5, pp. 361-364, Oct-Dec 2004.
[124] E. Cano, D. Lafuente, and D. M. Bastidas, "Use of EIS for the evaluation of the protective properties of coatings for metallic cultural heritage: a review," *Journal of Solid State Electrochemistry,* vol. 14, pp. 381-391, March 2010.
[125] http://www.conservationresources.com/Main/section_40/section40_08.htm.
[126] C. R. Paul, "Analysis of Linear Circuits," in *Analysis of Linear Circuits B2 - Analysis of Linear Circuits*, ed. New York: McGraw-Hill, 1989.
[127] A. S. Bondarenko and G. A. Ragoisha, "EIS Spectrum Analyser," *http://www.abc.chemistry.bsu.by/vi/analyser/*.
[128] V. Kasturi and S. C. Mukhopadhyay, "Estimation of Property of Sheep Skin to Modify the Tanning Process Using Interdigital Sensors." vol. 21, S. C. Mukhopadhyay and R. Y. M. Huang, Eds., ed: Springer Berlin Heidelberg, 2008, pp. 91-110.
[129] V. M. Kasturi, "Quality inspection of leather using novel planar sensor," Master of Engineering, School of Engineering and Advanced Technology, Massey University, New Zealand, Palmerston North, 2008.

[130] D. Karunanayaka, "Studies of Magnetic Filtration Techniques to Purify Potable Water and Waste Water," Master of Engineering, School of Engineering and Advanced Technology, Massey University, New Zealand, Palmerston North, 2007.
[131] Y. J. Tan, S. Bailey, and B. Kinsella, "An investigation of the formation and destruction of corrosion inhibitor films using electrochemical impedance spectroscopy (EIS)," *Corrosion Science,* vol. 38, pp. 1545-1561, 1996.
[132] M. Itagaki, A. Taya, K. Watanabe, and K. Noda, "Deviations of Capacitive and Inductive Loops in the Electrochemical Impedance of a Dissolving Iron Electrode," *Analytical Sciences,* vol. 18, pp. 641-644, 2002.
[133] C. Jeyaprabha, S. Sathiyanarayanan, S. Muralidharan, and G. Venkatachari, "Corrosion inhibition of iron in 0.5 mol L-1 H2SO4 by halide ions," *Journal of the Brazilian Chemical Society,* vol. 17, pp. 61-67, 2006.
[134] R. Ravichandran, S. Nanjudan, and N. Rajendran, *Corrosion inhibition of brass by benzotriazole derivatives in NaCl solution* vol. 52. Bradford, ROYAUME-UNI: Emerald, 2005.
[135] M. A. Md Yunus, S. C. Mukhopadhyay, and G. Sen Gupta, "A new planar electromagnetic sensor for quality monitoring of water from natural sources," *ICST 2010. 4th International Conference on Sensing Technology, 2010,* pp. 554-559, June 3 – 5 2010.
[136] I. Chenini and S. Khemiri, "Evaluation of ground water quality using multiple linear regression and structural equation modeling," *International Journal of Environmental Science and Technology,* vol. 6, pp. 509-519, Sum 2009.
[137] C. V. Kandala and J. Sundaram, "Nondestructive Measurement of Moisture Content Using a Parallel-Plate Capacitance Sensor for Grain and Nuts," *Sensors Journal, IEEE,* vol. 10, pp. 1282-1287, 2010.
[138] M. Van der Perk, *Soil and water contamination: from molecular to catchment scale*. Leiden, The Netherland: Taylor and Francis/Balkema, 2006.
[139] M. E. Ortiz-Santaliestra, A. Marco, M. J. Fernández-Benéitez, and M. Lizana, "Effects of ammonium nitrate exposure and water acidification on the dwarf newt: The protective effect of oviposition behaviour on embryonic survival," *Aquatic Toxicology,* vol. 85, pp. 251-257, 2007.
[140] C. Jutten and J. Herault, "Blind separation of sources, part I: An adaptive algorithm based on neuromimetic architecture," *Signal Processing,* vol. 24, pp. 1-10, 1991.
[141] A. Hyvärinen and E. Oja, "Independent component analysis: algorithms and applications," *Neural Networks,* vol. 13, pp. 411-430, 2000.
[142] G. Wang, Q. Ding, and Z. Hou, "Independent component analysis and its applications in signal processing for analytical chemistry," *TrAC Trends in Analytical Chemistry,* vol. 27, pp. 368-376, 2008.
[143] J. Chen and X. Z. Wang, "A New Approach to Near-Infrared Spectral Data Analysis Using Independent Component Analysis," *Journal of Chemical Information and Computer Sciences,* vol. 41, pp. 992-1001, 2001.
[144] X. Shao, G. Wang, S. Wang, and Q. Su, "Extraction of Mass Spectra and Chromatographic Profiles from Overlapping GC/MS Signal with Background," *Analytical Chemistry,* vol. 76, pp. 5143-5148, 2004.
[145] Z. Liu, W. Cai, and X. Shao, "Sequential extraction of mass spectra and chromatographic profiles from overlapping gas chromatography-mass spectroscopy signals," *Journal of Chromatography A,* vol. 1190, pp. 358-364, 2008.

[146] N. Pasadakis and A. A. Kardamakis, "Identifying constituents in commercial gasoline using Fourier transform-infrared spectroscopy and independent component analysis," *Analytica Chimica Acta,* vol. 578, pp. 250-255, 2006.
[147] G. Polder, G. W. A. M. van der Heijden, and I. T. Young, "Tomato sorting using independent component analysis on spectral images," *Real-Time Imaging,* vol. 9, pp. 253-259, 2003.
[148] B. Ling, M. Zeifman, and J. Hu, "Rugged early-warning spectroscopic system for real-time environment water monitoring," in *Conference on optically biological and chemical detection for defence III*, Stockholm, Sweden, 2006, pp. 42-50.
[149] R. Vigario, J. Sarela, V. Jousmiki, M. Hamalainen, and E. Oja, "Independent component approach to the analysis of EEG and MEG recordings," *Biomedical Engineering, IEEE Transactions on,* vol. 47, pp. 589-593, 2000.
[150] Y. Sevim and A. Atasoy, "Performance evaluation of nonparametric ICA algorithm for fetal ECG extraction," *Turkish Journal of Electrical Engineering and Computer Sciences,* vol. 19, pp. 657-666, 2011.
[151] G. Wang, Q. Ding, Y. Sun, L. He, and X. Sun, "Estimation of source infrared spectra profiles of acetylspiramycin active components from troches using kernel independent component analysis," *Spectrochimica Acta - Part A: Molecular and Biomolecular Spectroscopy,* vol. 70, pp. 571-576, 2008.
[152] A. Saalbach, O. Lange, T. Nattkemper, and A. Meyer-Baese, "On the application of (topographic) independent and tree-dependent component analysis for the examination of DCE-MRI data," *Biomedical Signal Processing and Control,* vol. 4, pp. 247-253, 2009.
[153] M. Jian and Z. Sun, "Exploring the intrinsic structure of magnetic resonance spectra tumor data based on independent component analysis and correlation analysis," vol. 4132 LNCS - II, ed, 2006, pp. 788-797.
[154] A. Hyvarinen, "Fast and robust fixed-point algorithms for independent component analysis," *Neural Networks, IEEE Transactions on,* vol. 10, pp. 626-634, 1999.
[155] S. Gadzuric, M. Vranes, and S. Dozic, "Electrical Conductivity and Density of Ammonium Nitrate + Formamide Mixtures," *Journal of Chemical & Engineering Data,* vol. 56, pp. 2914-2918, 2011.
[156] D. V. Franco, L. M. D. Silva, W. F. Jardim, and J. F. C. Boodts, "Influence of the electrolyte composition on the kinetics of the oxygen evolution reaction and ozone production processes," *Journal of the Brazilian Chemical Society,* vol. 17, pp. 446-757, 2006.
[157] F. Adar, R. Geiger, and J. Noonan, "Raman Spectroscopy for Process/Quality Control," *Applied Spectroscopy Reviews,* vol. 32, pp. 45 - 101, 1997.
[158] J. Ma and Z. Sun, "Exploring the Intrinsic Structure of Magnetic Resonance Spectra Tumor Data Based on Independent Component Analysis and Correlation Analysis Artificial Neural Networks – ICANN 2006." vol. 4132, S. Kollias, A. Stafylopatis, W. Duch, and E. Oja, Eds., ed: Springer Berlin / Heidelberg, 2006, pp. 788-797.
[159] *Manawatu River, http://en.wikipedia.org/wiki/Manawatu_River*.
[160] L. Fewtrell, "Drinking-water nitrate, methemoglobinemia, and global burden of disease: A discussion," *Environmental Health Perspectives,* vol. 112, pp. 1371-1374, Oct 2004.
[161] C. Gonzalez, S. Spinelli, J. Gille, E. Touraud, and E. Prichard, "Validation procedure for existing and emerging screening methods," *TrAC Trends in Analytical Chemistry,* vol. 26, pp. 315-322, 2007.

[162] M. A. M. Yunus, V. Kasturi, S. C. Mukhopadhyay, and G. Sen Gupta, "Sheep skin property estimation using a low-cost planar sensor," in *Proceedings of the IEEE Instrumentation and Measurement Technology Conference, 2009. I2MTC '09*, 2009, pp. 482-486.
[163] E. Inc. (1997). *XR-2206 Datasheet, 1997*. Available: http://http://www.exar.com/
[164] B.-B. Inc. (1993). *VFC110 Datasheet, 1993*. Available: http://www.burrbrown.info/
[165] *Data Acquisition Data Book*: National Semiconductor, 1993.

Research Outputs

Below are the research outputs in conjunction with the author's Ph.D candidacy:

Journal Publications

1. **M. A. Md Yunus**, S. C. Mukhopadhyay, and G. Sen Gupta, "A Review of Material Properties Estimation Using Eddy Current Testing and Capacitive Imaging," *Sensors & Transducers Journal,* vol. 100, pp.92-115, January 2009.
2. **M. A. M. Yunus** and S. C. Mukhopadhyay, "Development of planar electromagnetic sensors for measurement and monitoring of environmental parameters," *Measurement Science and Technology,* vol. 22, p. 025107, 18th January 2011.
3. **M. A. M. Yunus** and S. C. Mukhopadhyay, "Novel Planar Electromagnetic Sensors for Detection of Nitrates and Contamination in Natural Water Sources," *Sensors Journal, IEEE,* vol. 11, pp. 1440-1447, 19th April 2011.

Textbook Publications

Work is published in the New development and Applications in Sensing Technology book by Springer.

1. **M. A. M. Yunus** and S. C. Mukhopadhyay, "Planar Electromagnetic Sensor for the Detection of Nitrate and Contamination in Natural Water Sources Using Electrochemical Impedance Spectroscopy Approach," in *New Developments and Applications in Sensing Technology*. vol. 83, S. C. Mukhopadhyay, A. Lay-Ekuakille, and A. Fuchs, Eds., ed: Springer Berlin Heidelberg, 2011, pp. 39-63.

Work is submitted for publication in Francis and Taylor.

1. **M. A. M. Yunus** and S. C. Mukhopadhyay, “Design and application of low-cost system based on planar electromagnetic sensors and impedance spectroscopy for monitoring of nitrate contamination in natural water sources”.

Conference Publications

1. **M. A. M. Yunus**, V. Kasturi, S. C. Mukhopadhyay, and G. Sen Gupta, "Sheep skin property estimation using a low-cost planar sensor," in *Instrumentation and Measurement Technology Conference, 2009. I2MTC '09. IEEE*, Singapore, 5-7th May 2009, pp. 482-486.
2. **M. A. Md Yunus**, S. C. Mukhopadhyay, and G. Sen Gupta, “Material Properties Estimation Using a Low-cost Planar Electromagnetic Sensors”, The Second International Conference on Control, Instrumentation & Mechatronics Engineering (CIM '09), Malaysia, pp. 851-856, 2-3th June 2009.
3. **M. A. Md Yunus**, S. C. Mukhopadhyay, and G. Sen Gupta, "A new planar electromagnetic sensor for quality monitoring of water from natural sources," in ICST 2010. 4th International Conference on Sensing Technology, 2010, Lecce, Italy, 3-5th June 2010, pp. 554-559.
4. A. R. M. Syaifudin, **M. A. Yunus**, S. C. Mukhopadhyay, and K. P. Jayasundera, "A novel planar interdigital sensor for environmental monitoring," in Sensors, 2009 IEEE, Christchurch, New Zealand, 25-28th Oct 2009, pp. 105-110.
5. **M. A. Md Yunus**, S. C. Mukhopadhyay, and G. Sen Gupta, "Development of Planar Electromagnetic Sensors for Water Contamination sensing," in The 13-th International Meeting on Chemical Sensors, IMCS-13, Perth, Western Australia, 11-14th July 2010, p. 249.
6. **M. A. M. Yunus**, G. R. Mendez, and S. C. Mukhopadhyay, "Development of a low-cost system for nitrate and contamination detections in natural water supply based on a planar electromagnetic sensor," in Instrumentation and Measurement Technology Conference (I2MTC), 2011 IEEE, Hangzhou, Republic of China, 10-12 Mayth 2011, pp. 1-6.

7. **M. A. M. Yunus** and S. C. Mukhopadhyay . "A New Method for Monitoring Ammonium Nitrate Contamination in Natural Water Sources Based on Independent Component Analysis". IEEE Sensors 2011, Limerick, Limerick, Ireland 28-3th October.
8. **M. A. Md Yunus**, S. C. Mukhopadhyay, and A. D. Punchihewa "Application of Independent Component Analysis for Estimating Nitrate Contamination in Natural Water Sources Using Planar Electromagnetic Sensor". ICST2011, Palmerston North, New Zealand. 28th Nov to 1th Dec 2011.
9. G. R. Mendez, **M. A. M. Yunus**, and S. C. Mukhopadhyay A WiFi based Smart Wireless Sensor Network for an Agricultural Environment. ICST2011, Palmerston North, New Zealand. 28th Nov to 1st Dec 2011.

Presentations

1. **M. A. Md Yunus**, S. C. Mukhopadhyay, and G. Sen Gupta, IEEE Postgraduate Student Presentation Day, "Nondestructive Testing and Imaging for Material Characterization", Victoria University, Wellington, 28th August 2008.
2. **M. A. Md Yunus**. "Novel Planar Electromagnetic Sensors for Nondestructive Testing and Tomography". PhD confirmation seminar. 14th July 2009. Massey University, Palmerston North. New Zealand.
3. **M. A. Md Yunus**. "The Development of a New Sensing System for the Detection of Contamination in Natural Water Supplies". Electronics, Information and Communication System (*EICS*) Seminar, 17th May 2010. Massey University, New Zealand.
4. **M. A. M. Yunus** and S. C. Mukhopadhyay. "A Novel Planar Electromagnetic Sensor for Environmental Monitoring Application". IEEE Instrumentations and Measurement Society New Zealand Chapter Workshop, 1st – 2nd September 2010. Massey University, Wellington. New Zealand.
5. **M. A. M. Yunus** and S. C. Mukhopadhyay, "Design and application of low-cost system based on planar electromagnetic sensors and impedance spectroscopy for monitoring of nitrate contamination in natural water sources".

2011 IEEE (NZ) Sensors, Measurement and Instrumentation Workshop. AUT, Auckland. 10th – 11th March 2011.

6. **M. A. Md Yunus**. "Application of a detection system using a planar electromagnetic sensor for monitoring ammonium and nitrate contamination in natural water sources based on multilinear regression model and independent component analysis." Electronics, Information and Communication System (*EICS*) Seminar, 4th April 2011. Massey University, New Zealand.

Awards

1. One of the 10 best articles award from International Frequency Sensor Association (IFSA) and Sensor & Transducers Journal's Editorial Board for the article titled: A Review of Material Properties Estimation Using Eddy Current and Capacitor Imaging" published in Sensors & Transducers Journal (ISSN 1726-5479), Vol.100, January 2009, pp 92-112.
2. Student travel award for one of the best papers reviewed, titled: *Development of a low-cost system for nitrate and contamination detections in natural water supply based on a planar electromagnetic sensor*. The award was conferred at the 2011 IEEE International Instrumentation and Measurement Technology Conference Four Points by Sheraton Hangzhou Binjiang, Hangzhou, China, 2-5th May 2011.